# Measurement of the $^3$He Spin Structure Functions in the Resonance Region: A Test of Quark-Hadron Duality on the Neutron

---

A Dissertation
Submitted
to the Temple University Graduate Board

---

In Partial Fulfillment
of the Requirements for the Degree of
Doctor of Philosophy

---

by
Patricia H. Solvignon
August, 2006

*Dedicated to my parents*

# ABSTRACT

## Measurement of the $^3$He Spin Structure Functions in the Resonance Region: A Test of Quark-Hadron Duality on the Neutron

Patricia H. Solvignon

Doctor of Philosophy

Temple University, 2004

Advisor: Dr. Zein-Eddine Meziani

One of the biggest challenges in the study of the nucleon structure is the understanding of the transition from partonic degrees of freedom to hadronic degrees of freedom. In 1970, Bloom and Gilman noticed that structure function data taken at SLAC in the resonance region average to the scaling curve of deep inelastic scattering (DIS). Early theoretical interpretations suggested that these two very different regimes can be linked under the condition that the quark-gluon and quark-quark interactions are suppressed. Substantial efforts are ongoing to investigate this phenomenon both experimentally and theoretically.

Quark-hadron duality has been confirmed for the unpolarized structure function $F_2$ of the proton and the deuteron using data from the experimental Hall C at Jefferson Lab (JLab). Indications of duality have been seen for the proton polarized structure function $g_1$ and the virtual photon asymmetry $A_1$

at JLab Hall B and HERMES. Because of the different resonance behavior, it is expected that the onset of duality for the neutron will happen at lower momentum transfer than for the proton. Now that precise spin structure data in the DIS region are available at large $x$, data in the resonance region are greatly needed in order to test duality in spin-dependent structure functions.

The goal of experiment E01-012 was to provide such data on the neutron ($^3$He) in the moderate momentum transfer ($Q^2$) region, $1.0 < Q^2 < 4.0$ $(\mathrm{GeV/c})^2$, where duality is expected to hold. The experiment ran successfully in early 2003 at Jefferson Lab in Hall A. It was an inclusive measurement of longitudinally polarized electrons scattering from a longitudinally or transversely polarized $^3$He target. Asymmetries and cross section differences were measured in order to extract the $^3$He spin structure function $g_1$ and virtual photon asymmetry $A_1$ in the resonance region. A test of quark-hadron duality has then been performed for the $^3$He and neutron structure functions.

The study of spin duality for the neutron will provide a better understanding of the mechanism of the strong interaction. Moreover, if duality is well understood, our resonance data will bring information on the high $x$ region where theoretical predictions for $A_1$ are drastically different.

# ACKNOWLEDGEMENTS

I would like to thank my advisor Dr. Zein-Eddine Meziani for giving me the opportunity of coming in USA to do a Ph.D and for his support and advice all along these years. Also, at the origin of my adventure in USA, there is Pierre Bertin to who I would like to send all my appreciations. My years as a Temple graduate student were mostly spent at JLab where I had the great chance of being guided by Jian-Ping Chen. Along with Jian-Ping, I would like to thank Nilanga Liyanage for their confidence in my work and being always very encouraging. Seonho Choi has also been of great importance during my Ph.D from his help at the beginning of my analysis. In the polarized $^3$He collaboration, I had the opportunity of working with two great people as Todd Averett and Wolfgang Korsch.

I am very grateful to the Hall A staff members for their help during the running of this experiment and also for their availability to answer my questions when an analysis struggle came along.

During the intense work of a Ph.D, colleagues and friends are especially precious. Many people have been very patient and understanding during these years. So thank you to Vince Sulkosky, Alexandre Deur, Xiaochao Zheng, Alexandre Camsonne, Fatiha Benmokhtar, Stephanie Bailey, Ameya kolarkar, Aidan Kelleher and Jaideep Singh. Particularly, I would like to

thank my best friend in USA, Enka Lakuriqi, for opening her parents' house for me when I arrived in USA and for all her help.

My family has always been central in my life. My parents and my brother have always been very supportive with my decisions and I am very grateful to them for that. I enjoy each minute spent on the phone with my nephews, Joris, Alexis and Marie. They are my rainbow. My number one supporter, all these years at school, is my cousin Isabelle who could get more stressed than me before my exam. I miss her very much as I am finishing this manuscript.

Finally, I would like to thank Karl for all these great moments spent together.

# TABLE OF CONTENTS

# LIST OF TABLES

# LIST OF FIGURES

# CHAPTER 1

# INTRODUCTION

The structure of the nucleon has been extensively studied since the confirmation of the nucleon substructure from deep inelastic scattering (DIS) experiments performed at the Standford Linear Accelerator Center (SLAC) about thirty years ago [Friedman, 1972]. It was observed that the nucleon is composed of point-like particles, the partons. The partons were later associated with light mass quarks and the gluons, mediators of the strong interaction between quarks. But, even with the establishment of Quantum Chromodynamics (QCD) as the theory of the strong force, the behavior of the nucleon constituents is still not totally understood. Depending on the resolution of the electromagnetic probe, different pictures of the nucleon can be obtained. At high momentum transfer $Q^2 > 1$ GeV$^2$ and large invariant mass $W > 2$ GeV, the quarks inside the nucleons act as quasi-free particles and their interactions can be treated perturbatively in terms of partonic degrees of freedom: this is the deep inelastic scattering region where quarks exhibit the QCD property of asymptotic freedom. But as $Q^2$ and $W$ decrease, interactions between quarks and gluons make it difficult to access the properties of the nucleon such as, for example, the spin distribution among

its constituents. In this regime, quarks and gluons cannot be studied separately, and we talk of hadronic degrees of freedom. This is the resonance region where the nucleon goes through many hadronic excited states.

One of the key questions in understanding the internal mechanisms of the nucleon is how nucleon degrees of freedom transform from partonic to hadronic. To answer this question, one has to investigate the strongly non-perturbative regime of the resonances. With the advances in electrons beam and target techniques, deep inelastic scattering measurements have reached remarkable precision. But resonance data are also needed to help test QCD in the non-perturbative regime. One part of the answer could reside in the phenomenon of quark-hadron duality which was observed for the first time even before the formulation of QCD. Quark-hadron duality, which was observed for the first time even before the formulation of QCD, relates the resonance region to the DIS region, hinting to a common origin of these two very different regimes. This phenomenon has been intensively studied on spin-independent structure functions but spin-dependent data is lacking. The goal of this work is to test quark-hadron duality in the spin structure functions. It is the first experiment dedicated to study the onset of spin duality in the neutron.

# CHAPTER 2

# PROBING THE STRUCTURE OF THE NUCLEON

## 2.1 Formalism

The internal structure of the nucleon can be studied through lepton scattering which is well described under the theory of Quantum Electrodynamics (QED). In the Born approximation, the incoming electron scatters on the nucleon by exchanging a virtual photon, and only the outgoing electron is detected in an inclusive electron-nucleon scattering (Fig. 2.1). The relevant

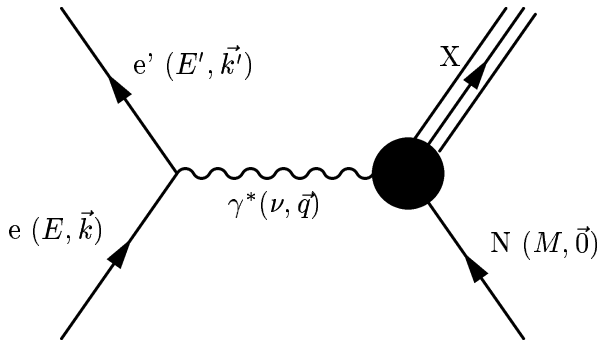


**Figure 2.1:** Lowest order diagram for inclusive scattering

kinematic variables of the reaction are the four-momenta $k^\mu = (E, \vec{k})$ and

$k'^{\mu} = (E', \vec{k'})$ of the incident and scattered electrons respectively, the scattering angle $\theta$ and the four-momentum of the target $p^{\mu} = (M, \vec{0})$. The exchanged photon carries the four-momentum $q^{\mu} = (k - k')^{\mu}$. The hadronic final state is described by $X$. The scattering process is a function of two invariants. A standard choice is the invariant mass of the hadronic final state and the four-momentum transfer $Q^2$ defined as:

$$W^2 = (q + p)^2 = M^2 + 2M\nu - Q^2 \tag{2.1}$$

$$\nu = E - E' \tag{2.2}$$

$$Q^2 = -q^2 = -(k - k')^2 \simeq 4EE' \sin^2 \frac{\theta}{2} \tag{2.3}$$

for $m_e \ll E, E'$.

Other variables are routinely employed such as:

$$x = \frac{Q^2}{2M\nu} \tag{2.4}$$

the Bjorken variable, and:

$$\nu = E - E' \tag{2.5}$$

the energy transfer $\nu$ to the nucleon.

## 2.2 Structure functions

The differential cross section for the process of Fig 2.1 is given by:

$$\frac{d^2\sigma}{d\Omega dE'} = \frac{\alpha^2}{Q^4} \frac{E'}{E} L_{\mu\nu} W^{\mu\nu} \tag{2.6}$$

where $\alpha$ is the fine structure constant. The expression of the leptonic tensor $L^{\mu\nu}$ for an incident electron of helicity $\pm 1/2$ can be written as:

$$L^{\mu\nu} = 2k^{\mu}k'^{\nu} + 2k'^{\mu}k^{\nu} + g^{\mu\nu}q^2 \mp 2i\epsilon^{\mu\nu\lambda\rho}k_{\lambda}k'_{\rho} \tag{2.7}$$

The symmetric part under the interchange $\mu \leftrightarrow \nu$ corresponds to an unpolarized lepton, while the anti-symmetric part contains the lepton spin information and thus corresponds to polarized lepton.

The structure of the hadron is described by response functions $W_{1,2}$ and $G_{1,2}$ in the hadronic tensor $W_{\mu\nu}$:

$$\begin{aligned} W_{\mu\nu} &= \left(\frac{q_\mu q_\nu}{q^2} - g_{\mu\nu}\right) W_1(\nu, Q^2) \\ &\quad + \left(p_\mu - \frac{p\cdot q}{q^2}q_\mu\right)\left(p_\nu - \frac{p\cdot q}{q^2}q_\nu\right)\frac{W_2(\nu,Q^2)}{M^2} \\ &\quad + i\epsilon_{\mu\nu\lambda\rho}q^{\lambda}\left[s^{\rho}G_1(\nu,Q^2) + (p\cdot q s^{\rho} - s\cdot q p^{\rho})\frac{G_2(\nu,Q^2)}{M^2}\right] \end{aligned} \tag{2.8}$$

where $s^{\rho}$ is the target spin vector. When probing the inelastic region, it is standard to work with the dimensionless spin-independent structure functions $F_{1,2}$ defined as follows:

$$F_1(x, Q^2) = MW_1(\nu, Q^2) \tag{2.9}$$

$$F_2(x, Q^2) = \nu W_2(\nu, Q^2) \tag{2.10}$$

and the spin- dependent structure functions $g_{1,2}$:

$$g_1(x, Q^2) = M\nu G_1(\nu, Q^2) \tag{2.11}$$

$$g_2(x, Q^2) = \nu^2 G_2(\nu, Q^2) \tag{2.12}$$

using the convention from [Thomas, 2001].

The structure functions can be accessed experimentally by measuring the cross section for different beam and target helicity states. Using an unpolarized target and an unpolarized electron beam, $F_1$ and $F_2$ can be determined as follows:

$$\frac{d^2\sigma_0}{d\Omega dE'} = \frac{\alpha^2 \cos^2\frac{\theta}{2}}{4E^2 \sin^4\frac{\theta}{2}} \left( \frac{2}{M} F_1(x,Q^2) \tan^2\frac{\theta}{2} + \frac{1}{\nu} F_2(x,Q^2) \right) \tag{2.13}$$

The multiplicative term in front of the parentheses is the Mott cross section,

$$\sigma_{Mott} = \frac{\alpha^2 \cos^2\frac{\theta}{2}}{4E^2 \sin^4\frac{\theta}{2}} \tag{2.14}$$

which describes scattering from a point-like particle. $F_1$ and $F_2$ take into account the composite nature of the nucleon. The unpolarized cross section can also be written in terms of longitudinal and transverse virtual photoabsorption cross sections $\sigma_L$ and $\sigma_T$:

$$\frac{d^2\sigma_0}{d\Omega dE'} = \Gamma(\sigma_T(x,Q^2) + \epsilon\sigma_L(x,Q^2)) \tag{2.15}$$

where

$$\epsilon = \frac{1}{1 + 2(1+\nu^2/Q^2)\tan^2\frac{\theta}{2}} \tag{2.16}$$

is the ratio of longitudinal to transverse polarization of the virtual photon and

$$\Gamma = \frac{\alpha}{2\pi^2 Q^2} \frac{E'}{E} \frac{K}{1-\epsilon} \tag{2.17}$$

is the flux of virtual photons. The factor $K$ is equal to $\nu(1-x)$ in Hand's convention [Hand, 1963].

Finally, $F_1$ and $F_2$ can be expressed as a function of $\sigma_L$ and $\sigma_T$:

$$F_1(x,Q^2) = \frac{K}{4\pi^2\alpha} M\sigma_T(x,Q^2) \tag{2.18}$$

$$F_2(x,Q^2) = \frac{K}{4\pi^2\alpha}\frac{\nu}{(1+\nu^2/Q^2)}\Big[\sigma_L(x,Q^2)+\sigma_T(x,Q^2)\Big] \tag{2.19}$$

and the ratio of longitudinal to transverse cross sections as:

$$R(x,Q^2) = \frac{\sigma_L(x,Q^2)}{\sigma_T(x,Q^2)} = \frac{F_2(x,Q^2)}{2xF_1(x,Q^2)}\Big(1+\frac{4M^2x^2}{Q^2}\Big) - 1 \tag{2.20}$$

The spin-dependent structure functions $g_1$ and $g_2$ of the nucleon can be accessed by using a polarized electron beam and a target which is polarized longitudinally or transversely with respect to the electron helicity:

$$\Delta\sigma_{\parallel} = \frac{4\alpha^2}{M\nu Q^2}\frac{E'}{E}\Big[(E+E'\cos\theta)g_1(x,Q^2) - 2Mxg_2(x,Q^2)\Big] \tag{2.21}$$

$$\Delta\sigma_{\perp} = \frac{4\alpha^2}{M\nu Q^2}\frac{E'^2}{E}\sin\theta\Big[g_1(x,Q^2)+\frac{2E}{\nu}g_2(x,Q^2)\Big] \tag{2.22}$$

with $\Delta\sigma_{\parallel} = \frac{d^2\sigma^{\downarrow\Uparrow}}{d\Omega dE'} - \frac{d^2\sigma^{\uparrow\Downarrow}}{d\Omega dE'}$ and $\Delta\sigma_{\perp} = \frac{d^2\sigma^{\downarrow\Leftarrow}}{d\Omega dE'} - \frac{d^2\sigma^{\uparrow\Leftarrow}}{d\Omega dE'}$. The $\uparrow$ or $\downarrow$ represents the beam helicity and $\Downarrow$ or $\Leftarrow$ the polarization direction of the target.

## 2.3 Virtual photon absorption asymmetries

At the photon-nucleon vertex, the absorption of the virtual photon by the nucleon is related to the imaginary part of the forward virtual Compton

scattering amplitude $f(\nu)$ through the optical theorem [Thomas, 2001]:

$$\sigma_{tot}(\nu) = \frac{4\pi}{\nu}\mathcal{I}m\ f(\nu) \tag{2.23}$$

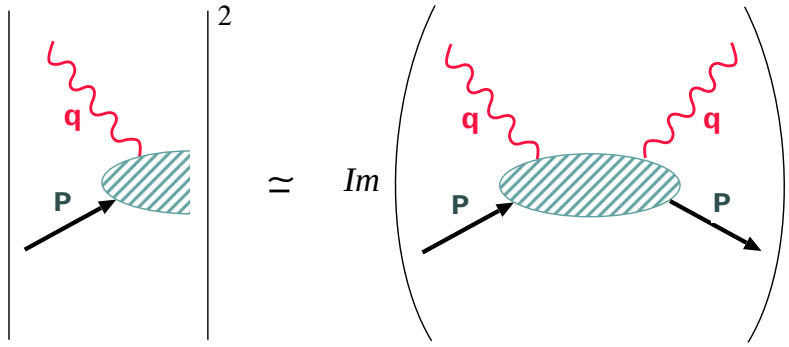


**Figure 2.2:** Illustration of the optical theorem.

A total of four independent Compton helicity amplitudes [Manohar, 1992], $A_{(a,b)\to(c,d)}$, can be derived from the three polarization states of the virtual photon combined with a spin-1/2 target. $a$ and $b$ are the incident photon and nucleon helicities, and $c$ and $d$ are the final photon and nucleon helicities. The virtual photoabsorption cross sections are defined as:

$$\sigma_{3/2} = \frac{4\pi^2\alpha}{MK}A_{(1,1/2)\to(1,1/2)} = \frac{4\pi^2\alpha}{MK}\left(F_1 - g_1 + \gamma^2 g_2\right) \tag{2.24}$$

$$\sigma_{1/2} = \frac{4\pi^2\alpha}{MK}A_{(1,-1/2)\to(1,-1/2)} = \frac{4\pi^2\alpha}{MK}\left(F_1 + g_1 - \gamma^2 g_2\right) \tag{2.25}$$

$$\sigma_{L} = \frac{4\pi^2\alpha}{MK}A_{(0,1/2)\to(0,1/2)} = \frac{4\pi^2\alpha}{MK}\left(-F_1 + \frac{(1+\gamma^2)}{2x}F_2\right) \tag{2.26}$$

$$\sigma_{LT} = \frac{4\pi^2\alpha}{MK}A_{(1,-1/2)\to(0,1/2)} = \frac{4\pi^2\alpha}{MK}\gamma\left(g_1 + g_2\right) \tag{2.27}$$

The virtual photon-nucleon asymmetries are defined by:

$$A_1(x,Q^2) = \frac{\sigma_{1/2} - \sigma_{3/2}}{\sigma_{1/2} + \sigma_{3/2}} = \frac{g_1(x,Q^2) - \gamma^2 g_2(x,Q^2)}{F_1(x,Q^2)} \tag{2.28}$$

$$A_2(x,Q^2) \;=\; \frac{2\sigma_{LT}}{\sigma_{1/2}+\sigma_{3/2}} = \frac{\gamma(g_1(x,Q^2)+g_2(x,Q^2))}{F_1(x,Q^2)} \tag{2.29}$$

with $\gamma^2 = Q^2/\nu^2$. The quantities $A_1$ and $A_2$ can be extracted from the longitudinal ($A_{\|}$) and transverse ($A_{\perp}$) polarization asymmetries:

$$A_{\|} = \frac{\frac{d^2\sigma^{\downarrow\Uparrow}}{d\Omega dE'} - \frac{d^2\sigma^{\uparrow\Uparrow}}{d\Omega dE'}}{\frac{d^2\sigma^{\downarrow\Uparrow}}{d\Omega dE'} + \frac{d^2\sigma^{\uparrow\Uparrow}}{d\Omega dE'}} \qquad\qquad A_{\perp} = \frac{\frac{d^2\sigma^{\downarrow\Leftarrow}}{d\Omega dE'} - \frac{d^2\sigma^{\uparrow\Leftarrow}}{d\Omega dE'}}{\frac{d^2\sigma^{\downarrow\Leftarrow}}{d\Omega dE'} + \frac{d^2\sigma^{\uparrow\Leftarrow}}{d\Omega dE'}} \tag{2.30}$$

as follows:

$$A_1(x,Q^2) = \frac{A_{\|}(x,Q^2)}{D(1+\zeta\eta)} - \frac{\eta A_{\perp}(x,Q^2)}{d(1+\zeta\eta)} \tag{2.31}$$

$$A_2(x,Q^2) = \frac{\zeta A_{\|}(x,Q^2)}{D(1+\zeta\eta)} + \frac{A_{\perp}(x,Q^2)}{d(1+\zeta\eta)} \tag{2.32}$$

Here, the different coefficient expressions are:

$$D \;=\; \frac{1-\frac{E'\epsilon}{E}}{1+\epsilon R(x,Q^2)} \tag{2.33}$$

$$d \;=\; D\sqrt{\frac{2\epsilon}{1+\epsilon}} \tag{2.34}$$

$$\eta \;=\; \frac{\epsilon\sqrt{Q^2}}{E-E'\epsilon} \tag{2.35}$$

$$\zeta \;=\; \eta\frac{1+\epsilon}{2\epsilon} \tag{2.36}$$

where $D$ is the photon depolarization factor.

The quantities $A_1$ and $A_2$ reflect the helicity correlation between the virtual photon and the nucleon (or the quarks in deep inelastic scattering). They must satisfy the positivity constraints [Soffer, 2000]:

$$|A_1| \le 1 \qquad \text{and} \qquad |\mathrm{A_2}| \le \sqrt{\mathrm{R}\frac{\mathrm{A_1}+1}{2}} \tag{2.37}$$

## 2.4 Description of nucleon (and nucleus) states

The virtual photon energy spectrum provides information on different properties of the nucleon: its charge and magnetic moment in elastic scattering, its spin and momentum excited states through inelastic region, and its substructure in the deep inelastic scattering region. Fig. 2.3 shows the evolution of the electroproduction cross section for $^3$He as the excitation photon energy increases.

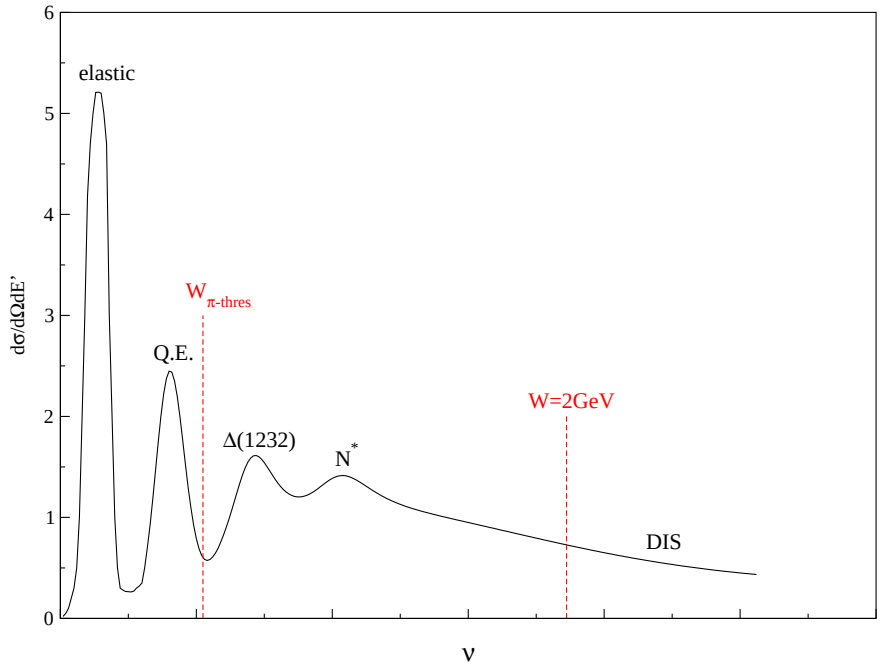


**Figure 2.3:** $^3$He absolute cross section. For nuclear targets like $^3$He, the nucleon elastic peak widens due to the Fermi motion of the nucleon. This peak is now called the quasi-elastic scattering (QE).

### 2.4.1 Elastic scattering

At $\nu = Q^2/2M$, the energy of the probe is not sufficient to excite or break the nucleon (or nucleus*). The reaction is elastic leaving the nucleon intact. Applying conservation of momentum and energy, the incident and the scattered energies can be related by:

$$E' = \frac{E}{1 + \frac{2E}{M}\sin^2\frac{\theta}{2}} \tag{2.38}$$

Here, $M$ is the mass of the nucleon or the target nucleus. The Rosenbluth cross section [Rosenbluth, 1950] contains information about the nucleon's composite nature:

$$\frac{d\sigma}{d\Omega} = \left(\frac{d\sigma}{d\Omega}\right)_{Mott}\left[\frac{G_E^2 + \tau G_M^2}{1+\tau} + 2\tau G_M^2 \tan^2\frac{\theta}{2}\right] \tag{2.39}$$

with $\tau = \frac{Q^2}{4M^2}$, and:

$$G_E(Q^2) = \mathcal{F}_1(Q^2) - \frac{\kappa Q^2}{4M^2}\mathcal{F}_2(Q^2) \tag{2.40}$$

$$G_M(Q^2) = \mathcal{F}_1(Q^2) + \kappa\mathcal{F}_2(Q^2) \tag{2.41}$$

are the Sachs form factors, also called the electric and magnetic form factors. $\mathcal{F}_1$ and $\mathcal{F}_2$ are the Dirac and Pauli form factors respectively. $G_E$ and $G_M$ can be extracted by measuring the ratio $\sigma/\sigma_{Mott}$ as a function of two scattering angle keeping $Q^2$ constant. This method is called Rosenbluth separation.

At $Q^2 = 0$, the nucleon charge and magnetic moment are given by:

$$G_E^p(0) = 1 \qquad \text{and} \qquad \mathrm{G_M^p}(0) = \mu_\mathrm{p} = 2.793 \tag{2.42}$$

*for $\nu = Q^2/2M_{nucleus}$

for the proton, and:

$$G_E^n(0) = 0 \qquad \text{and} \qquad \mathrm{G_M^n}(0) = \mu_\mathrm{n} = -1.913 \tag{2.43}$$

for the neutron. At low $Q^2$, a phenomenological fit to the world data shows that the form factors are well described by a dipole form as follows:

$$G_E^p(Q^2) \approx \frac{G_M^p(Q^2)}{\mu_p} \approx \frac{G_M^n(Q^2)}{\mu_n G_D(Q^2)} \approx G_D(Q^2) = \frac{1}{1 + \frac{Q^2}{Q_0^2}} \tag{2.44}$$

where $Q_0^2 = 0.84$ GeV$^2$. The charge and magnetization radii of the nucleon can then be extracted through the expansion of the form factors:

$$G_{E,M}(Q^2) = G_{E,M}(Q^2) - \frac{1}{6} Q^2 \left\langle r^2 \right\rangle_{E,M} + \mathcal{O}(Q^4) \tag{2.45}$$

It was found that $< r^2 >^{1/2} \approx 0.81$ fm for the proton electric and magnetic radii as well as for the neutron magnetic radius. The neutron electric radius is very small since the neutron has no net charge.

At large $Q^2$, according to predictions from perturbative Quantum Chromodynamics (pQCD) [Lepage, 1979], the elastic form factor varies as $G_M(Q^2) \sim 1/Q^4$. The transition region between the low and high $Q^2$ regions is of great interest in order to understand the non-perturbative structure of the nucleon and to determine the onset of perturbative behavior.

### 2.4.2 Quasi-elastic scattering

If the target is a nucleus, an intermediary process can be probed. Quasi-elastic scattering consists of knocking out a bound nucleon which can be

considered quasi-free. The virtual photon energy is $\nu = Q^2/2M$, and the width of the peak is determined by the Fermi momentum $p_F$,

$$\Delta\nu = \sqrt{2}qp_F/\sqrt{M^2+q^2}\ , \tag{2.46}$$

due to the motion of nucleons inside the nucleus.

### 2.4.3 Resonances

As the virtual photon energy increases, the nucleon goes through different excited states called the nucleon resonances. Traditionally, the resonance region is composed of mass states between the pion production threshold ($W_{\pi-thres} = M_N + M_\pi$) and $W = 2$ GeV. In inclusive scattering, many resonances contribute to the inelastic cross section as well as a non-resonant background, therefore individual resonances are difficult to isolate. However, in exclusive processes $e + N \rightarrow e' + R$ (R denoting the detected hadronic final state), the electroproduction of resonances can be described in terms of helicity amplitudes [Carlson, 1998]. For the three polarization states of the virtual photon (two transverse and one longitudinal), three helicity amplitudes are defined:

$$G_+ = \frac{1}{2M} < R, \lambda' = \frac{1}{2}|\epsilon_\mu^{(+)} \cdot j^\mu(0)|N, \lambda = \frac{1}{2} > \tag{2.47}$$

$$G_0 = \frac{1}{2M} < R, \lambda' = -\frac{1}{2}|\epsilon_\mu^{(0)} \cdot j^\mu(0)|N, \lambda = \frac{1}{2} > \tag{2.48}$$

$$G_- = \frac{1}{2M} < R, \lambda' = -\frac{3}{2}|\epsilon_\mu^{(-)} \cdot j^\mu(0)|N, \lambda = \frac{1}{2} > \tag{2.49}$$

where $\epsilon^{(\pm)} = (0, \pm 1, -i, 0)/\sqrt{2}$ and $\epsilon^{(0)} = (|\vec{q}|, 0, 0, \nu)/Q$ are the transverse and longitudinal polarization four-vectors respectively.

The structure functions for a single resonance of mass $M_R$ and width $\Gamma_R$ can be expressed as a function of the helicity amplitudes:

$$W_1 = \frac{M}{\pi M_R \Gamma_R} \left( |G_+|^2 + |G_-|^2 \right) \tag{2.50}$$

$$W_2 = \frac{1}{1 + \frac{\nu^2}{Q^2}} \frac{M}{\pi M_R \Gamma_R} \left( |G_+|^2 + 2|G_0|^2 + |G_-|^2 \right) \tag{2.51}$$

in the unpolarized case, and:

$$g_1 = \frac{1}{1 + \frac{Q^2}{\nu^2}} \frac{M^2}{\pi M_R \Gamma_R} \left[ |G_+|^2 - |G_-|^2 + (-1)^{s_R - 1/2} \eta_R \frac{Q\sqrt{2}}{\nu} G_0^* G_+ \right] \tag{2.52}$$

$$g_2 = -\frac{1}{1 + \frac{Q^2}{\nu^2}} \frac{M^2}{\pi M_R \Gamma_R} \left[ |G_+|^2 - |G_-|^2 - (-1)^{s_R - 1/2} \eta_R \frac{\nu\sqrt{2}}{Q} G_0^* G_+ \right] \tag{2.53}$$

in the polarized case. The quantities $s_R$ and $\eta_R$ are the spin and parity of the resonance.

The relation between exclusive and inclusive processes was observed in the early 1970s with the first observation of parton-hadron duality [Bloom, 1970]. Chapter 3 is dedicated to the description of this phenomenon.

### 2.4.4 Deep Inelastic Scattering

At large $Q^2$ and $\nu$, as the resonance strengths fall off, Bjorken [Bjorken, 1969] predicted that the behavior of the structure functions $W_1$ and $W_2$ becomes

dependent on only one dimensionless variable $x = Q^2/2M\nu$. In the limit where $Q^2/M$ and $\nu$ are much larger than typical hadron masses:

$$MW_1(\nu, Q^2) \rightarrow F_1(x) \tag{2.54}$$

$$\nu W_2(\nu, Q^2) \rightarrow F_2(x) \tag{2.55}$$

The fact that the structure functions are independent of $Q^2$ and $\nu$ at a given value of $x$ suggests that the electron scatters on free point-like particles. These particles were named partons by Feynman [Feynman, 1969]. Scaling of the structure function $\nu W_2$ (Fig. 2.4) was observed in data [Breidenbach, 1969] taken at SLAC down to surprisingly low $Q^2$ of 1 $(\mathrm{GeV/c})^2$. In the infinite-

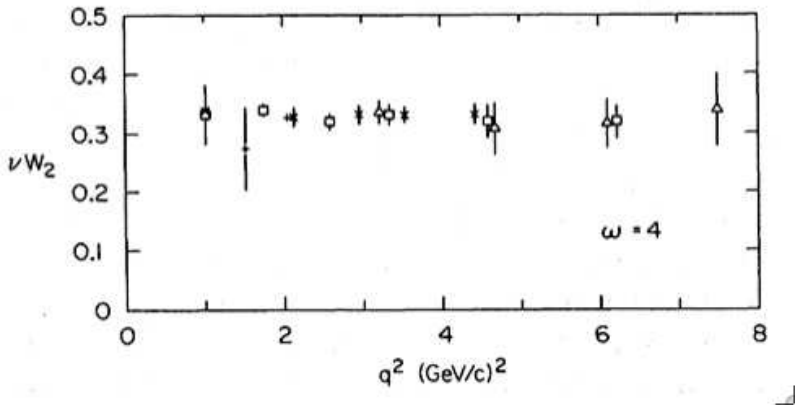


**Figure 2.4:** Observation of scaling on $\nu W_2$ for the proton. $\omega$ is equal to $1/x$. This work was awarded the Nobel Prize in 1990. Figure from [Kendall, 1991].

momentum reference frame defined by Feynman [Feynman, 1969], where $\nu$ and $Q^2$ go to infinity keeping $x$ finite, the virtual photon scatters on a quasi-free parton since it has no time to interact with the other partons. This is called the parton model and it exhibits the property of asymptotic freedom.

Deep inelastic scattering can be interpreted as the incoherent sum of elastic scattering on non-interacting partons. The struck parton carries a fraction $x$ of the nucleon momentum:

$$|\vec{p}_q| = x|\vec{P}| \tag{2.56}$$

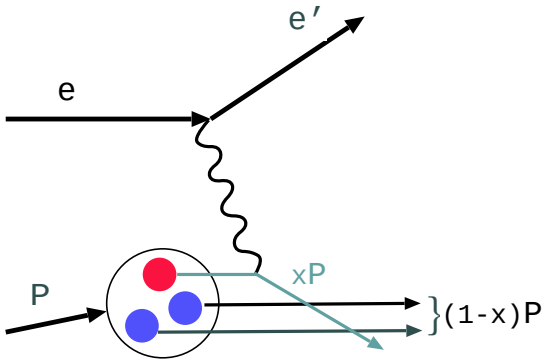


**Figure 2.5:** Illustration of deep inelastic scattering.

Defining $q(x)$ as the probability to find a quark of flavor $q$ and charge $e_q$ in the nucleon carrying the fraction $x$ of the nucleon momentum, the structure functions can be written as:

$$F_1(x) = \frac{1}{2}\sum_q e_q^2[q^{\uparrow}(x) + q^{\downarrow}(x) + \bar{q}^{\uparrow}(x) + \bar{q}^{\downarrow}(x)] \tag{2.57}$$

$$F_2(x) = 2xF_1(x) \tag{2.58}$$

$$g_1(x) = \frac{1}{2}\sum_q e_q^2[q^{\uparrow}(x) - q^{\downarrow}(x) + \bar{q}^{\uparrow}(x) - \bar{q}^{\downarrow}(x)] \tag{2.59}$$

$$g_2(x) = 0 \tag{2.60}$$

with the $\uparrow$ ($\downarrow$) representing the helicity of the quark or antiquark ($\bar{q}$) when it is parallel (antiparallel) to the nucleon polarization. Eq. (2.58) is called the Callan-Gross relation [Callan, 1969].

In the Bjorken scaling limit, the term $\gamma^2 g_2$ in Eq. (2.30) vanishes and the virtual photon absorption asymmetry $A_1$ becomes:

$$A_1(x) \approx \frac{g_1(x, Q^2)}{F_1(x, Q^2)} \tag{2.61}$$

The asymmetry $A_1$ is expected to have a weak $Q^2$-dependence if $g_1$ and $F_1$ show a similar behavior. Expressed as a function of parton distributions, $A_1$ gives access to the spin distribution of the partons in the nucleon.

The partons are currently associated with the quarks, antiquarks and gluons. The gluons are the carriers of the strong force between quarks. As an asymptotically free theory, Quantum Chromodynamics (QCD) is the established theory of strong interactions, with the strong coupling constant $\alpha_s(Q^2)$ becoming small as $Q^2$ increases.

At finite $Q^2$, quarks interact by exchanging spin-1 gluons at short distances. Soft gluons can be emitted before or after the electron scattering. All diagrams of Fig 2.6 must be taken into account in order to evaluate the cross section. These radiations of gluons generate a $Q^2$ logarithmic depen-

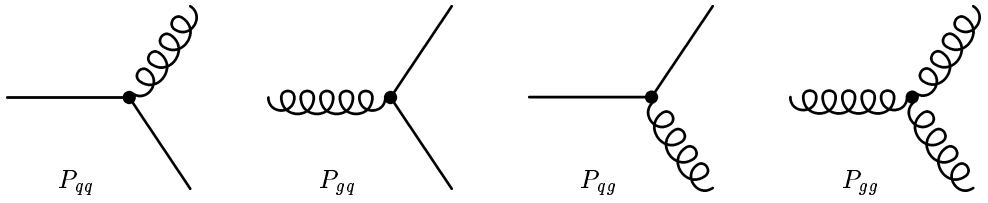


**Figure 2.6:** Feynman diagrams of the processes responsible for scaling violation. $P_{xx}$ are explained in the text.

dence of the parton distributions. Concretely it can be explained as follows: at low $Q^2$ the nucleon structure is dominated by valence quarks, defined as the excess of $u$ or $d$ quark distributions with respect to their anti-partner distributions ($q_v = q - \bar{q}$). At large $Q^2$, the resolution allows the observation of $q\bar{q}$ pairs and gluons which contribute to the DIS cross section.

From the DGLAP equations ([Gribov, 1972], [Dokshitzer, 1977] and [Altarelli, 1977]), the $Q^2$-evolution of the parton distributions can be calculated at leading order:

$$\frac{d\Delta q_v(x,Q^2)}{d(\ln\,Q^2)} = \frac{\alpha_s(Q^2)}{2\pi}\int_x^1 \frac{dy}{y} P_{qq}(x/y) q_v(y,Q^2) \tag{2.62}$$

for valence quark. $P_{qq}(x/y)$ is the probability that a quark with a nucleon momentum fraction $y$ will radiate a gluon and will then carry a momentum fraction $x$. The total number of valence quarks stays constant due to the fact that $\int_0^1 dz P_{qq}(z) = 0$ with $z = x/y$ and $y = \nu/E$. Gluon emission or $q\bar{q}$ creation doesn't affect the valence quark number. The contributions of $q\bar{q}$ pairs and gluons to the deep inelastic process are given by:

$$\begin{aligned}\frac{d\Delta q(x,Q^2)}{d(\ln\,Q^2)} &= \frac{\alpha_s(Q^2)}{2\pi}\int_x^1 \frac{dy}{y}(P_{qq}(x/y) f_i(y,Q^2) &(2.63)\\ &\quad + P_{qg}(x/y) f_i(y,Q^2) g(y,Q^2)) &(2.64)\end{aligned}$$

$$\begin{aligned}\frac{d\Delta G(x,Q^2)}{d(\ln\,Q^2)} &= \frac{\alpha_s(Q^2)}{2\pi}\int_x^1 \frac{dy}{y}(P_{gq}(x/y) f_i(y,Q^2) &(2.65)\\ &\quad + P_{gg}(x/y) f_i(y,Q^2) g(y,Q^2)) &(2.66)\end{aligned}$$

$P_{qg}(x/y)$ is the probability of quark with a nucleon momentum fraction $y$ will emit a gluon carrying a momentum fraction $x$, $P_{gq}(x/y)$ the probability

of a gluon producing a quark-antiquark pair, and $P_g g(x/y)$ the probability of gluon emitting two gluons. $P_{gq}(x/y)$ and $P_{gg}(x/y)$ corresponds to the evolution of the gluon distribution. Eqs. (2.62-2.66) are valid at leading order but can be generalized to next-to-leading order with $\alpha_s$ corrections:

$$P_{ij}(x) = P_{ij}^{(0)} + \frac{\alpha_s}{2\pi} P_{ij}^{(1)} + ... \tag{2.67}$$

The $Q^2$ behavior of the structure functions is extracted from the Operator Product Expansion (see Section 3.2), and the leading twist term can be evaluated for any $Q^2$ using the DGLAP equations.

# CHAPTER 3

# QUARK-HADRON DUALITY

## 3.1 Bloom-Gilman duality

In the early 1970s, Bloom and Gilman [Bloom, 1970] made a remarkable observation regarding the $W_2$ structure function: the scaling curve obtained at high $Q^2$ seems to be an accurate average of the resonances at low $Q^2$, when an appropriate scaling variable is chosen (see Fig. 3.1). This phenomenon is called "quark-hadron duality" and indicates a common origin for the resonances and the scaling region.

Assuming QCD is the correct theory of the strong interaction, all hadronic states must be described as a complex combination of strongly interacting quarks and gluons. However, a full QCD calculation is not possible due to the complication arising from the multiple quark-gluon couplings. The resonance region is a non-perturbative regime where quarks and gluons react as a whole under the effect of the electromagnetic probe. On the other hand, the scaling region is well described by perturbative QCD (pQCD) in terms of quark-gluon degrees of freedom as the incoherent sum over asymptotically free quarks. Quark-hadron duality states that, in a certain kinematic region, the average behavior of the hadronic processes can be described by pQCD

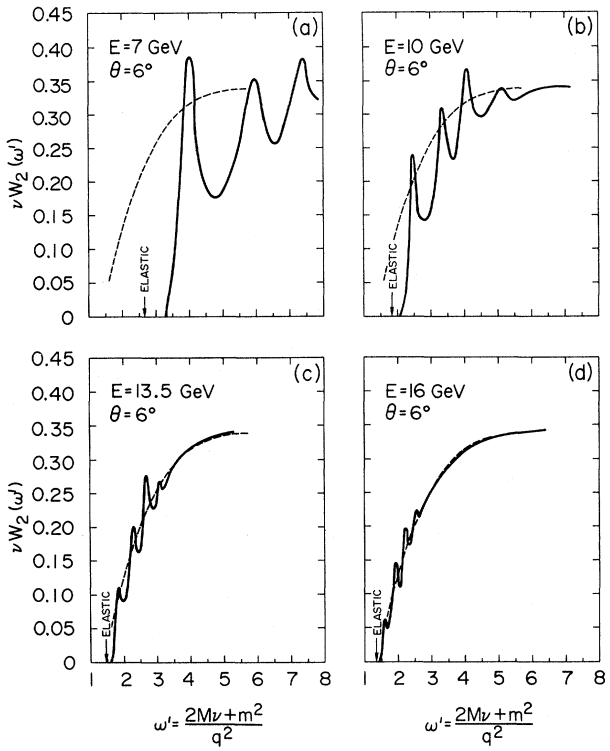


**Figure 3.1:** Observation of Bloom-Gilman duality: the resonance data oscillate around the smooth scaling curve and their fall off follow the scaling curve as the incident energy increases. Figure from [Bloom, 1970].

calculations. But, quark-hadron duality is also expected to break down at low $Q^2$ and in particular at $Q^2 = 0$. There, it is clear that the charge of the neutron, determined by the elastic form factors, cannot be expressed from the sum of the squared quark charges of pQCD. Therefore, the onset of quark-hadron duality will determine the limit of applicability of pQCD in the transition region.

Recent experimental data [Niculescu, 2000] for the unpolarized structure

function $F_2$ on the proton (see Fig. 3.2) and on the deuteron have confirmed Bloom-Gilman duality. Moreover it appears that, when averaging on individual resonances, the scaling behavior is reproduced. Thus, duality is also verified locally.

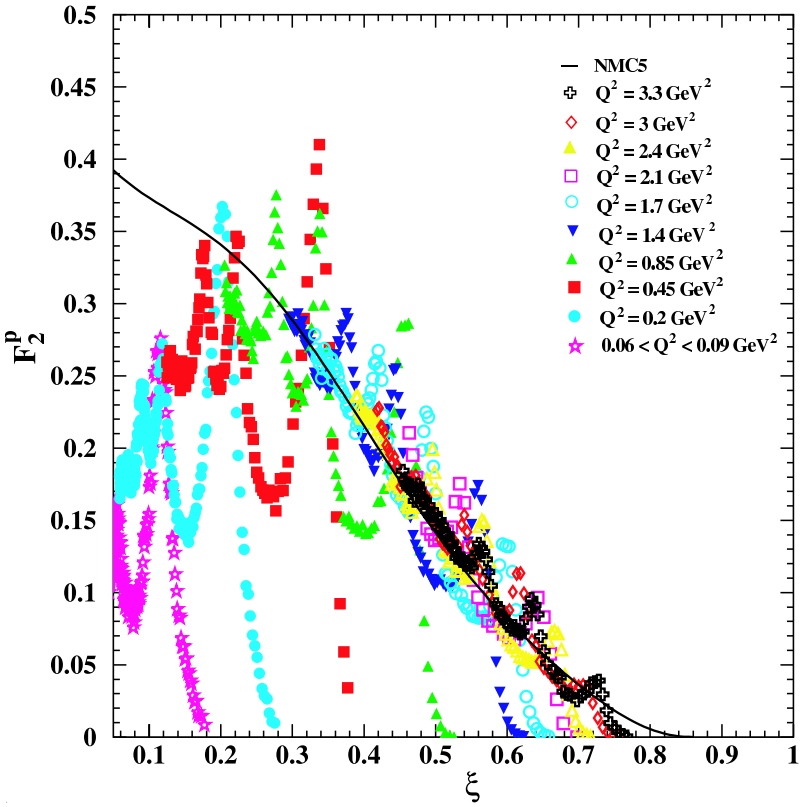


**Figure 3.2:** $F_2^p$ data from [Niculescu, 2000] as a function of the Nachtmann variable $\xi = 2x/(1+\sqrt{1+4M^2x^2/Q^2})$.

From the above results, a natural question arises whether quark-hadron duality exists for spin-dependent structure functions and under which conditions. The focus of this chapter is to give an overview on the theoretical

developments on quark-hadron duality for spin-dependent structure functions.

## 3.2 Operator Product Expansion

In the QCD framework, the behavior of the structure function moments can be interpreted through the Operator Product Expansion (OPE) down to the transition region. It is therefore an ideal theoretical framework to study quark-hadron duality [De Rujula, 1977].

At equal time, the product of two local fields $\mathcal{O}_a(l)$ and $\mathcal{O}_b(m)$ can be expanded as follows [Wilson, 1969]:

$$\lim_{l \to m} \mathcal{O}_a(l)\mathcal{O}_b(m) = \sum_n C_n(l-m)\mathcal{O}_n(m) \tag{3.1}$$

where $l$ and $m$ are four-vectors. The $C_n$ are the Wilson coefficient functions and can be computed in perturbative theory.

For a virtual photon scattering off a nucleon, the forward Compton amplitude can be written as:

$$T_{\mu\nu}(q) = < p, \lambda' | \int d^4x e^{iq\cdot x} T(J_\mu(x) J_\nu(0)) | p, \lambda > \tag{3.2}$$

In the asymptotic limit, the small $x$ behavior of the time-ordered product of the electromagnetic currents $J(0)$ and $J(z)$ dominates the integral, and Eq. (3.2) can be expressed as a sum of local operators:

$$T_{\mu\nu}(q) = \sum_n C_n(q) < p, \lambda' | \mathcal{O}_n(0) | p, \lambda > \tag{3.3}$$

At infinite $Q^2$, the matrix elements of the $\mathcal{O}_n$ are $q$-independent and the coefficients $C_n(q)$ contain the strength of the local fields. On the other hand, at finite $q$ both the coefficients and the local operators need to be computed to determine the contribution of the local field.

### The twist expansion

The forward Compton amplitude being related to the nucleon photo-absorption (see Eq. (2.23)), so the moments of nucleon structure functions can be expressed as a function of the coefficients $\mu_\tau^{(n)}$:

$$\Gamma_1^{(n)}(Q^2) \equiv \int_0^1 x^{n-1} g_1(x)\, dx = \sum_{\tau=2,4,\ldots}^{\infty} \frac{\mu_\tau^{(n)}(Q^2)}{Q^{\tau-2}}, \qquad n = 1, 3, 5, \ldots \tag{3.4}$$

Since $g_1$ is odd under the transformation $x \to -x$, $n$ must be positive and odd. The $\mu_\tau^{(n)}$ are related to the matrix elements of quark and gluon operators [Chen, 2005]. The twist $\tau$ is defined as the mass dimension minus the spin of an operator. Gauge invariance requires that the operators contain at least two quarks or two gluon fields. Hence, $\tau \geq 2$.

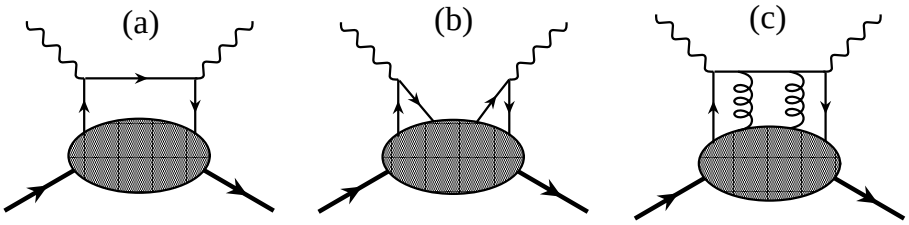


**Figure 3.3:** Leading (a) and higher twist (b-c) contributions to the structure functions. Figure reproduced from [Melnitchouk, 2005].

Following the reasoning in [De Rujula, 1977], Ji and Melnitchouk [Ji, 1997]

investigated quark-hadron duality using the twist expansion (Eq. 3.4). A similar work was done for the neutron in [Meziani, 2005]. As the leading twist contribution (diagram (a) of Fig. 3.3), $\mu_2^{(n)}(Q^2)$, to the n$^{th}$ moment of the spin structure function $g_1$ can be calculated, the higher twist terms ($\tau > 2$) are isolated as follows:

$$\Delta\Gamma_1^{(n)}(Q^2) = \Gamma_1^{(n)}(Q^2) - \mu_2^{(n)}(Q^2) = \frac{\mu_4^{(n)}(Q^2)}{Q^2} + \mathcal{O}(1/Q^4) \tag{3.5}$$

A strong $Q^2$ dependence of $\Gamma_1^{(n)}$ in Eq. (3.4) is expected at low $Q^2$ which is responsible for the violation of both duality and scaling. Quark-quark and quark-gluon correlations, also called the higher twists (see Fig. 3.3), are believed to be at the origin of the strong variation of the structure function moments. As $Q^2$ gets larger, the higher twists are suppressed and duality should be observed. Here the twist-2 term dominates the expansion and is responsible for the scaling of the structure functions.

The resonance contribution to the n$^{th}$ moment of $g_1$ can be defined as:

$$\Gamma_{1,res}^{(n)}(Q^2) = \int_{x_{thr.}}^{x_{2GeV}} x^{n-1} g_1(x, Q^2)\, dx \tag{3.6}$$

$x_{thr.}$ and $x_{2GeV}$ are the value of the Bjorken variable at the pion threshold and at $W$=2 GeV, respectively. When looking at the contribution of the resonance region in the full moments of $g_1$ [Edelmann, 2000], the resonance region can be a significant part of the moments (see Fig. 3.4). So observation of scaling in the full moments and in DIS implies scaling in the resonance region. At low $Q^2$, the dominant contribution to the higher moments ($n \geq 3$)

strength comes from the resonance region and therefore higher moments are more sensitive to higher twist effects.

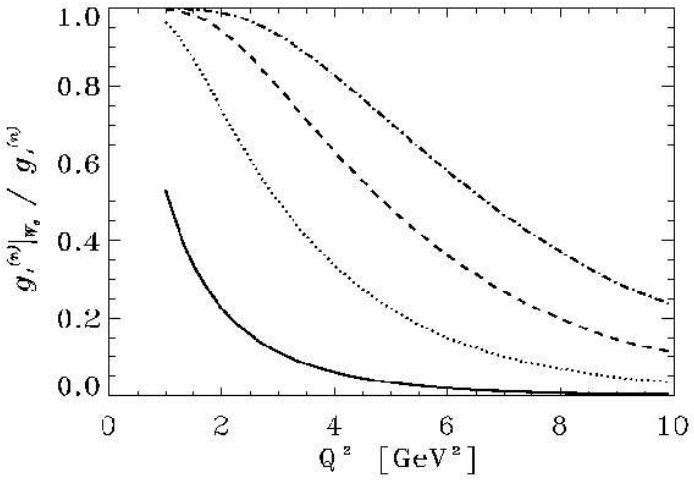


**Figure 3.4:** Contribution of the resonance region to the full moments of the structure function $g_1$. Plotted are the ratio for the 1st (solid), 3rd (dotted), 5th (dashed) and 7th (dash-dotted) moments. Figure reproduced from [Edelmann, 2000].

At leading order*, the twist-2 contribution to the first moment of $g_1$ can be written in term of parton distributions:

$$\mu_2^{(1)}(Q^2) = \frac{1}{2}\sum_q e_q^2 \int_0^1 \left[\Delta q(x,Q^2) + \Delta\bar{q}(x,Q^2)\right]\, dx \tag{3.7}$$

where $\Delta q = q^\uparrow - q^\downarrow$ and $\Delta\bar{q} = \bar{q}^\uparrow - \bar{q}^\downarrow$ and, $q^\uparrow$, $q^\downarrow$, $\bar{q}^\uparrow$ and $\bar{q}^\downarrow$ are the helicity-dependent quark distributions. The matrix element $\mu_4^{(1)}$ of Eq. (3.5) contains twist contributions from terms with $\tau \leq 4$ and can be written as:

$$\mu_4^{(1)}(Q^2) = \frac{1}{9}M^2\left[a_2(Q^2) + 4d_2(Q^2) + 4f_2(Q^2)\right] \tag{3.8}$$

*The coefficients $\mu_\tau^{(n)}$ can be calculated pertubatively as a power series in $\alpha_s(Q^2)$. The leading order contains no $\alpha_s$ factor.

The first term of Eq. (3.8), $a_2$, is given by the third moment of $g_1$, related to target mass correction corresponding to a twist-two contribution:

$$a_2(Q^2) = 2\int_0^1 x^2 \; g_1(x, Q^2) \; dx \tag{3.9}$$

The $d_2$ term is a twist-three matrix element and is given by the second moment of the leading-twist part of the structure functions $g_1$ and $g_2$:

$$d_2(Q^2) = \int_0^1 x^2 \left[2g_1(x, Q^2) + 3g_2(x, Q^2)\right] \; dx \tag{3.10}$$

Due to the $x^2$-weighting, the resonance region represents a large contribution to $d_2$ at low $Q^2$.

The twist-four term, $f_2$, contains both quark and gluon fields and has been extracted from a fit of experimental data. However, $f_2$ could also be accessed by measuring the spin structure function $g_3$ in an inclusive unpolarized electron scattering on a longitudinally polarized target:

$$f_2(Q^2) = \frac{1}{2}\int_0^1 x^2 \left[7g_1(x, Q^2) + 12g_2(x, Q^2) - 9g_3(x, Q^2)\right] \; dx \tag{3.11}$$

The quantities $d_2$ and $f_2$ determine the effects of the nucleon spin on the color electric and magnetic fields [Chen, 2005].

## 3.3 Resonance versus scaling in pQCD

At high $Q^2$, the helicity amplitudes defined in Section 2.4.3 follow the behavior defined by the counting rules [Brodsky, 1975]: one factor of $Q$ for each unbroken fermion line, one factor of $1/Q$ for each internal fermion propagator,

one factor of $1/Q^2$ for each gluon propagator and one factor of $1/Q$ for each helicity flip. At leading order, the calculation given in [Carlson, 1998] yields

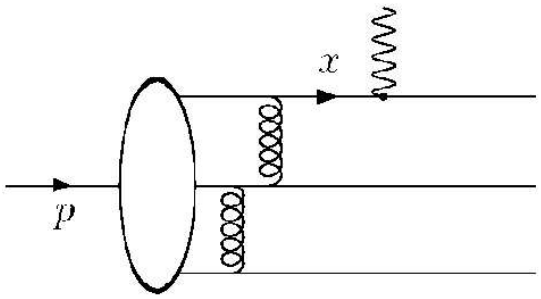


**Figure 3.5:** Leading order diagram for the transition amplitude $G_+$ (no spin flip).

to the transition amplitude $G_+ = g_+/Q^3$ represented in Fig. 3.5. In the case of the transition $G_0$, a quark must flip its helicity, leading to $G_0 = Mg_0/Q^4$. Finally, $G_- = M^2 g_-/Q^5$ in which two quarks have their helicities flipped. The coefficients $g_{\pm,0}$ are real constants in the Born approximation.

Thus, at the resonance peak, the structure function $g_1$ from Eq. (2.53) is dominated by $G_+$ and becomes:

$$g_1 = \frac{M^2}{\pi M_R \Gamma_R} \frac{g_+^2}{(M_R^2 - M^2)^3}(1-x)^3 \tag{3.12}$$

where, for $W \sim M_R$ and as $x \to 1$, $1/Q^2$ can be replaced by $(1-x)/(M_R^2 - M^2)$.

In the deep inelastic scattering region, it is understood that the quark carrying a large fraction of the nucleon momentum will very likely also carry the nucleon helicity [Farrar, 1975]. In this case, $g_1$ and $F_1$ are governed by $(1-x)^3$ behavior. The comparison of the DIS behavior to Eq. (3.12)

demonstrates quark-hadron duality for $g_1$.

## 3.4 SU(6) quark model

The SU(6) spin-flavor symmetric quark model provides a reasonable description of the nucleon excited state spectra. Quark-hadron duality is studied in the context of SU(6) symmetry breaking [Close, 2003]. Different scenarios with particular $N \rightarrow N^*$ transition suppressions are considered in order to obtain an agreement between resonance and DIS average behavior.

Working with the multiplets $\mathbf{56}^+(L=0)$ and $\mathbf{70}^-(L=1)$ of the SU(6) quark model, Close and Isgur [Close, 2001] write the ground state nucleon wave function as follows:

$$|N>=\cos\theta_w|\Psi_\rho>+\sin\theta_w|\Psi_\lambda> \tag{3.13}$$

The nucleon wave function is defined as a product of the flavor and the spin wave functions. The symmetric part is represented by $\Psi_\rho$ in Eq. (3.13) and the anti-symmetric part by $\Psi_\lambda$. Table 3.1 summarizes the resonance contributions to the structure functions $F_1$ and $g_1$ for the proton and the neutron. In the SU(6) limit, $\theta_w = \frac{\pi}{4}$, and the sum over all $\mathbf{56}^+$ and $\mathbf{70}^-$ representations gives [Close, 1972]:

$$A_1^p = \frac{5}{9} \quad \text{and} \quad \mathrm{A_1^n} = 0 \tag{3.14}$$

Here the assumption that the transition form factors have the same $Q^2$ dependence was made, which holds for $x < 1/3$.

| Structure functions | SU(6) representations $^2\mathbf{8}[\mathbf{56}^+]$ | $^4\mathbf{10}[\mathbf{56}^+]$ | $^2\mathbf{8}[\mathbf{70}^-]$ | $^4\mathbf{8}[\mathbf{70}^-]$ | $^2\mathbf{10}[\mathbf{70}^-]$ | Total |
|---|---|---|---|---|---|---|
| $F_1^p$ | $9\rho^2$ | $8\lambda^2$ | $9\rho^2$ | $0$ | $\lambda^2$ | $18\rho^2+9\lambda^2$ |
| $F_1^n$ | $\frac{(3\rho+\lambda)^2}{4}$ | $8\lambda^2$ | $\frac{(3\rho-\lambda)^2}{4}$ | $4\lambda^2$ | $\lambda^2$ | $\frac{29\rho^2+27\lambda^2}{2}$ |
| $g_1^p$ | $9\rho^2$ | $-4\lambda^2$ | $9\rho^2$ | $0$ | $\lambda^2$ | $18\rho^2-3\lambda^2$ |
| $g_1^n$ | $\frac{(3\rho+\lambda)^2}{4}$ | $-4\lambda^2$ | $\frac{(3\rho-\lambda)^2}{4}$ | $-2\lambda^2$ | $\lambda^2$ | $\frac{9\rho^2-9\lambda^2}{2}$ |

**Table 3.1:** Resonance contributions to the structure functions. $\rho = \cos\theta_w$ and $\lambda = \sin\theta_w$

In this context of SU(6) breaking, three scenarios for which transitions to specific resonances are removed from the summation are proposed in order to satisfy duality as $x \to 1$ ($\theta_W \to 0$). First the suppression of spin-$\frac{3}{2}$ states is considered which translates in the dominance of the magnetic coupling at high $Q^2$. Then helicity-$\frac{3}{2}$ transitions are eliminated corresponding, at large $Q^2$, to the pQCD restriction that the photons interact with the quarks having the same helicity as the nucleon. Finally the symmetric wave function is cut out reproducing the modifications of the spin-0 and spin-1 components of the nucleon due to spin-dependent forces. For all these cases, SU(6) breaking projects the spin asymmetries $A_1^{p,n} \to 1$ as $x$ goes to 1, as illustrated in Fig. 3.6.

## 3.5 Dynamical models

The dynamical quark models provide phenomenological descriptions of the dual nature of the strong interactions. Different assumptions are made

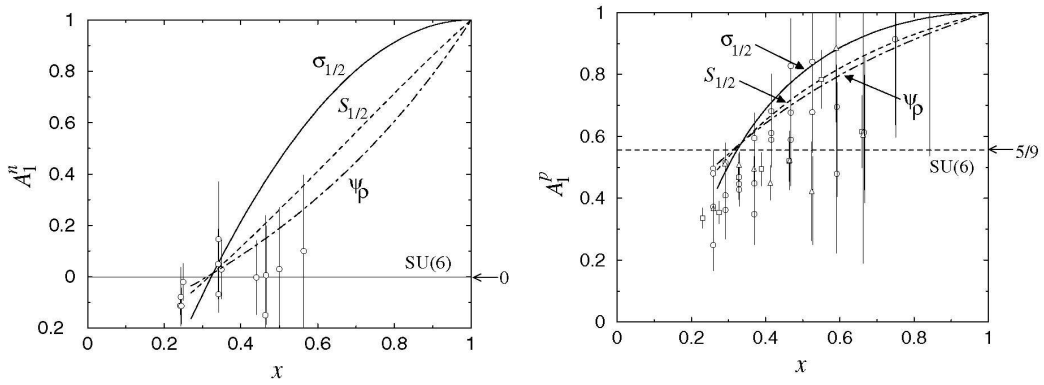


**Figure 3.6:** Spin asymmetries $A_1^n$ (right) and $A_1^p$ trends from the different scenarios of SU(6) breaking: spin-1/2 dominance ($S_{1/2}$), helicity-1/2 dominance ($\sigma_{1/2}$) and $\Psi_\rho$ dominance. Figure from [Close, 1972].

like an infinite number of colors ($N_c \to \infty$) translating to infinitely narrow resonances. Since DIS doesn't depend on $N_c$, working with $N_c \to \infty$ affects only the resonance region. Another assumption is to treat a light quark in an infinitely heavy anti-quark core. More details on phenomenological models can be found in the overview of Melnitchouk, Ent and Keppel [Melnitchouk, 2005].

A recent work by Matsui, Sato and Lee [Matsui, 2005] was devoted to study pion electroproduction near the $\Delta(1232)$ resonance, using the SL model defined in their earlier work [Sato, 1996]. Fig. 3.7 shows good agreement between the data on proton spin structure function $g_1^p$ and the SL model, but it also shows the striking deviations from the DIS trend. Therefore, this dynamical quark model predicts the violation of spin duality for the $\Delta$-transition at any $Q^2$. The observation of local duality in the $\Delta$ region would

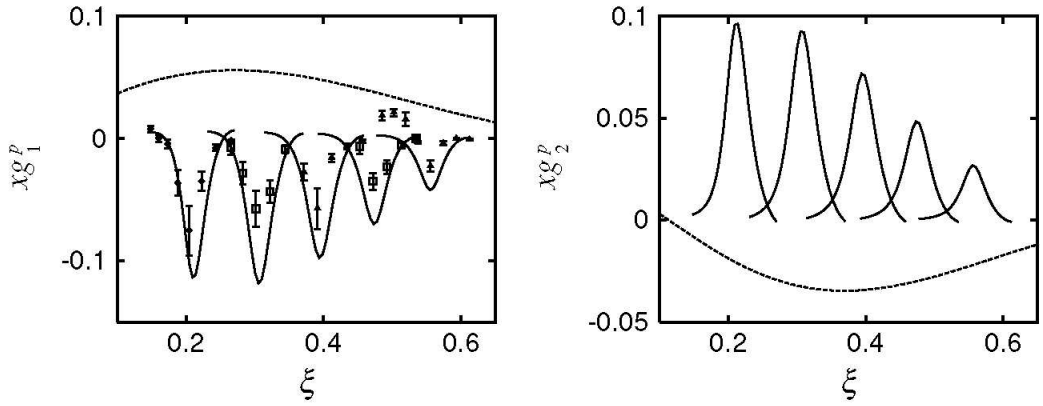


**Figure 3.7:** Extended SL model predictions for $g_{1,2}$ (solid line) in the delta region at $Q^2 = 0.21$, 0.35, 0.62, 0.92, 1.37 $(\mathrm{GeV/c})^2$. The data are from [Fatemi, 2003] and the dashed curved are fits of DIS data. Figure from [Matsui, 2005].

imply that the non-resonant background is the dominant contribution to the cross section.

## 3.6 Experimental overview of spin duality

Recently, an intense effort was made at Jefferson Lab was made to experimentally study the spin structure functions in the resonance region. Data were collected on the proton and the deuteron in Hall B, and on $^3$He in Hall A[†]. In this section, an overview of the recent resonance data or in particular, their behavior with respect to quark-hadron duality is presented.

Proton and deuteron resonance spin structure functions were measured

[†]The neutron spin structure functions can be extracted from the deuteron or $^3$He by subtracting the proton contribution

in Hall B with the CLAS detector [Mecking, 2003] from experiment EG1b [Prok, 2004, Dharmawardane, 2004]. Fig. 3.8 shows the test of global quark-hadron on the deuteron spin structure function $g_1^d$. To do so, partial moments of $g_1$ in the resonance and DIS regions are evaluated from the pion threshold to $W = 2$ GeV, and their ratio is calculated. If it is found equal to 1, duality is then verified. As can be seen in Fig. 3.8, the onset of global duality for the deuteron seems to be for $Q^2 \approx 1.2$ GeV$^2$.

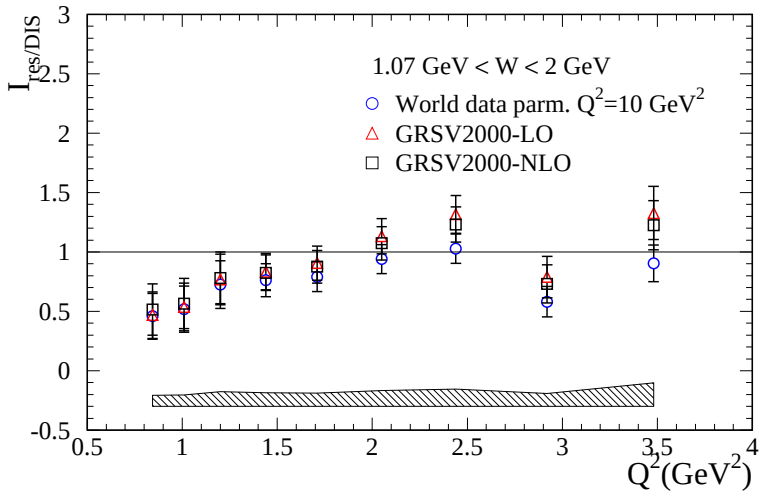


**Figure 3.8:** Test of global quark-hadron duality on the deuteron spin structure function $g_1^d$. The ratio was evaluated using several DIS parametrizations. Figure from [Dharmawardane, 2004].

Fig. 3.9 shows a test of global and local duality for the proton. Local duality in the $\Delta(1232)$ is shown to be violated for all the $Q^2$. But in the $S_{11}(1535)$ and $F_{15}(1680)$ regions, local duality is verified down to $Q^2 \approx 0.5$ GeV$^2$. The same local behavior was observed for the deuteron [Dharmawardane, 2004]. However, the onset of global duality on the proton seems to occur at a larger

$Q^2$ ($\approx 1.7$ GeV$^2$) than for the deuteron.

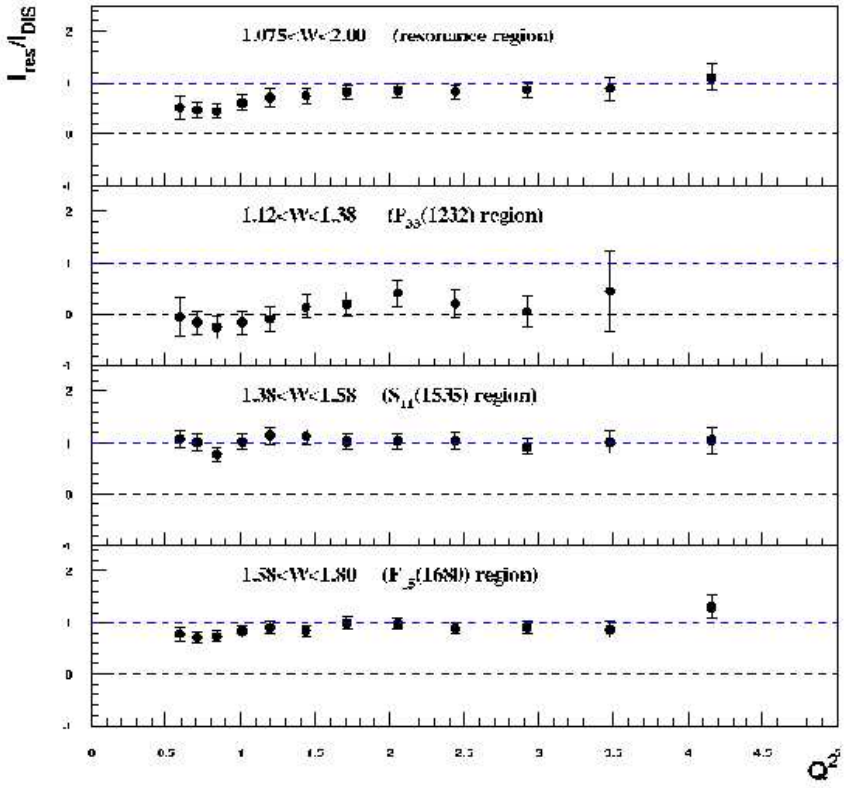


**Figure 3.9:** Test of global and local quark-hadron duality on the proton spin structure function $g_1^p$. The ratio was evaluated using several DIS parametrizations. Figure from [Dodge, 2005].

In Hall A, experiment E94-010 measured the spin structure functions $g_1$ and $g_2$ on $^3$He [Slifer, 2004]. Moments of the $^3$He structure functions were evaluated. Also the neutron moments were then extracted. A dedicated study [Meziani, 2005] on the higher twist effects was performed for the neutron and the results are shown in Fig. 3.10. The quantity plotted is defined in

Eq. (3.5) and contained twist-2, twist-3 and twist-4 contributions. The twist-2 part is responsible for the scaling of structure functions and is well known. However, the $Q^2$ evolution of the higher twists is difficult to parametrize. From this analysis, the authors showed that the quark-gluon interaction effects are small or cancel between neutron resonances for $Q^2$ as low as 0.5 GeV$^2$.

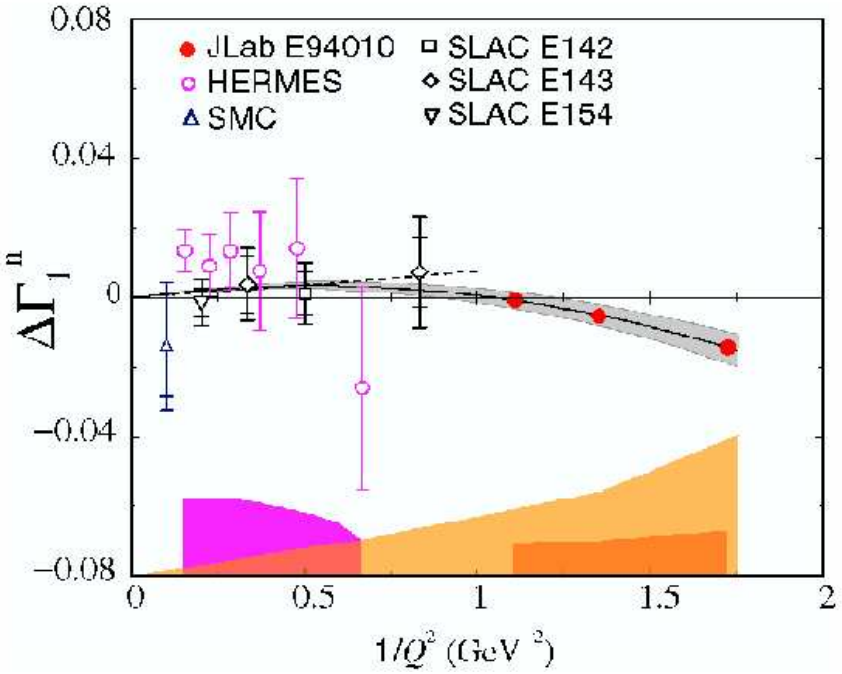


**Figure 3.10:** Extraction of the higher twist contribution to $\Gamma_1^n$.

Fig. 3.11 shows a qualitative indication of quark-hadron duality on the $g_1$ spin structure function for $^3$He, where the resonance data oscillate around the DIS data.

The recent resonance data combined with the data from this experiment

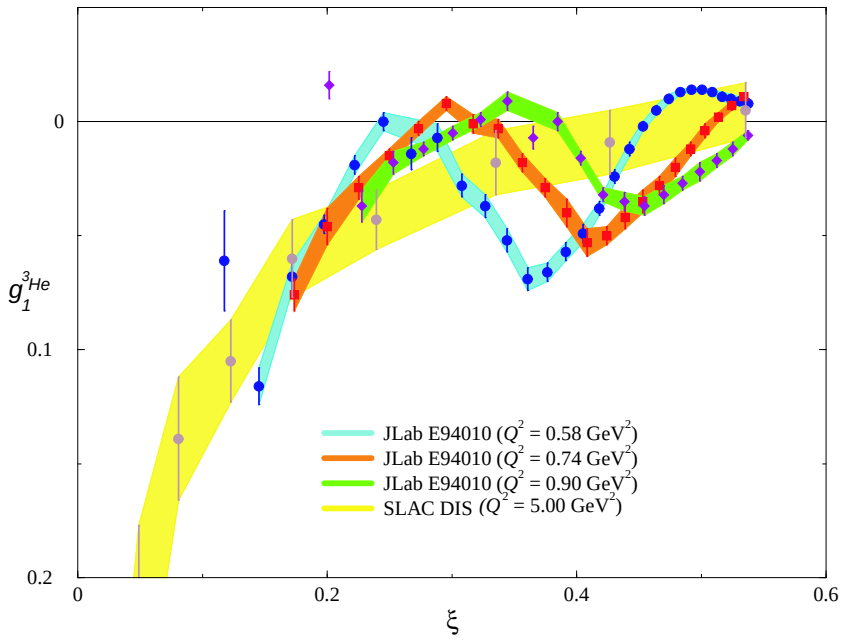


**Figure 3.11:** $g_1^{^3\mathrm{He}}$ from E94-010 measured in the resonance region and compared to DIS data measured at SLAC. Figure from [Choi, 2003].

should increase our understanding of the origins of spin duality, and ultimately the structure of the nucleon.

# CHAPTER 4

# THE EXPERIMENT

Experiment 01-012 took place at the Jefferson Laboratory in the experimental Hall A in January-February 2003. The polarized electron beam scattered off a polarized $^3$He target in order to access the spin-dependent structure functions $g_1$ and $g_2$, and the virtual photon asymmetries $A_1$ and $A_2$.

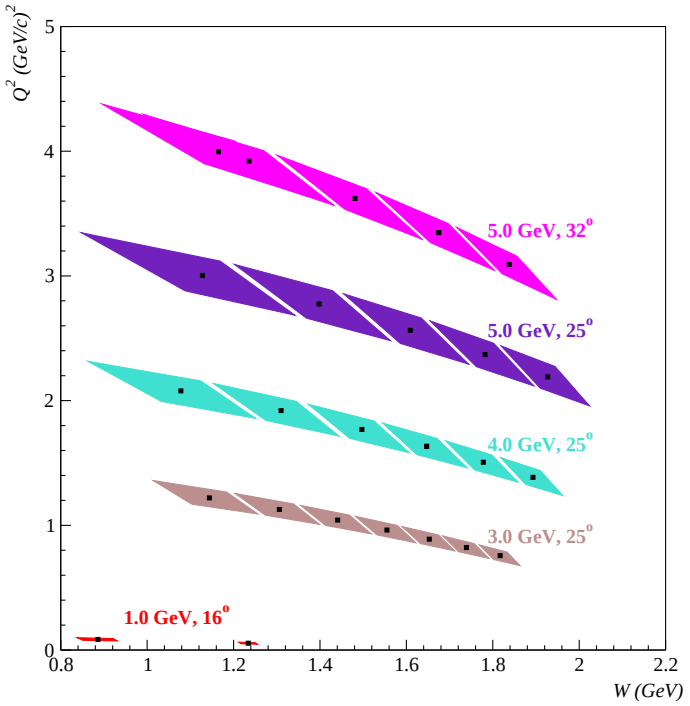


**Figure 4.1:** Kinematic coverage of E01-012. The black points represent the central spectrometer settings, and the parallelograms around these points correspond to the momentum and angular acceptance.

The goal of the experiment was to measure these structure functions in the resonance region and then compare their behavior to deep inelastic data and theoretical predictions. The kinematic coverage (Fig. 4.1) was chosen in a region where the onset of quark-hadron duality is expected to be observed. For these measurements, the two Hall A High Resolution Spectrometers (HRS) were set in symmetric configuration. Elastic scattering data (E = 1.046 GeV, $\theta = 16°$) were used to check the product of beam and target polarizations and the spectrometer acceptances. In order to cover the resonance region for $1.0 < Q^2 < 4.0$ $(\mathrm{GeV/c})^2$, three incident beam energies (E = 3.028, 4.018 and 5.009 GeV) and two spectrometer angles ($\theta = 25°$ and $32°$) were chosen.

## 4.1 The Jefferson Lab polarized electron beam

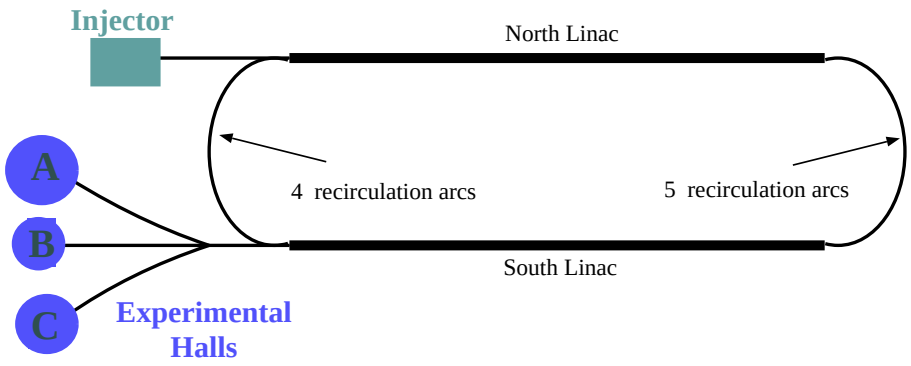


**Figure 4.2:** Accelerator schematic.

The polarized electron beam (Fig. 4.2) is generated in the injector with pulses at 1497 MHz. Each hall receives a pulse every 2 ns (exactly at 499

MHz). The electrons exit the injector with an energy of about 45 MeV. Each linac is composed of series of superconducting cavities designed to accelerate the electrons to a maximum of 4.0 GeV after 5 passages. Due to the high performance of the cavities, the maximum energy achieved is 6.0 GeV.

Polarized electrons are produced by illuminating a gallium arsenide (GaAs) cathode with circularly polarized photons [Grames, 2000]. In order to achieve high polarization, a GaAsP (phosphorus strained gallium arsenide) crystal is inserted between two layers of GaAs. This creates a perturbation in the crystal potential and removes the degeneracy of the GaAs valence band. The photon wavelength is tuned to excite the electron from the $P_{3/2}$ level to the $S_{1/2}$ level (Fig. 4.3). In the conduction band, electrons need an extra 4 eV in

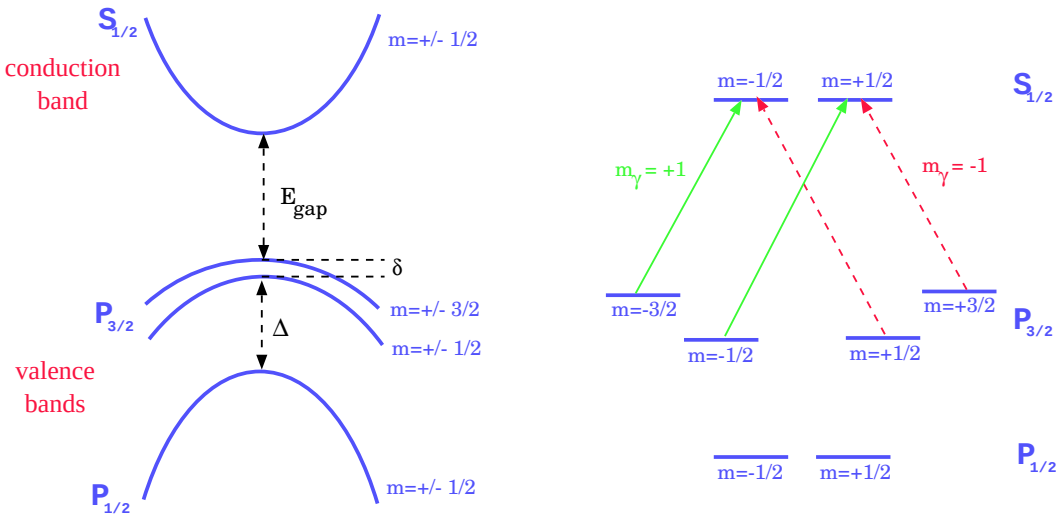


**Figure 4.3:** Energy level structure of strained GaAs. The incident photon of energy $E_\gamma$ will induce the transition from the $P_{3/2}$ level to the $S_{1/2}$ level with $E_{gap} < E_\gamma < E_{gap} + \delta$.

order to access the electron affinity. In order to lower this potential barrier, a thin layer of cesium-phosphor is added at the surface of the GaAs crystal (Fig. 4.4). This caused the electron affinity to become negative, meaning that the vacuum level is now accessible with a lower photon energy than needed to access the conduction band. A beam polarization of 85% is typical.

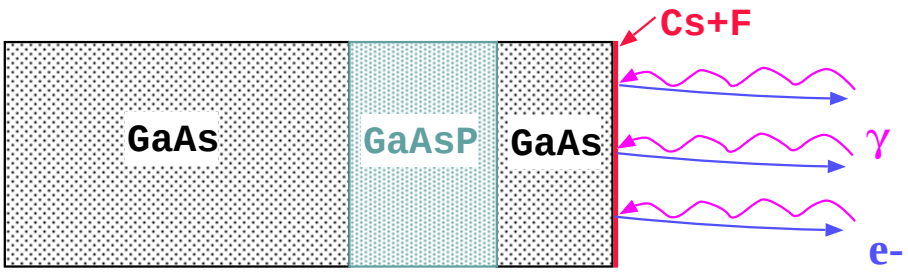


**Figure 4.4:** Simplified sketch of electron extraction from the GaAs crystal.

### 4.1.1 Electron beam helicity

The transformation from linearly to circularly polarized photons is accomplished with the insertion of a Pockels cell in the optical path. The Pockels cell is a crystal for which the refractive index can be changed by an applied electric field. The helicity of the incident electron is inverted at a frequency of 30Hz by switching the sign of the voltage in the Pockels cell. In addition, a half-wave plate can be inserted before the Pockels cell in order to generate an electron beam with helicity opposite to the helicity signal of the accelerator.

During the experiment E01-012, a special helicity scheme (Fig. 4.5) was required by the experimental Hall C for the $G_0$ experiment [Pitt, 2001]. The

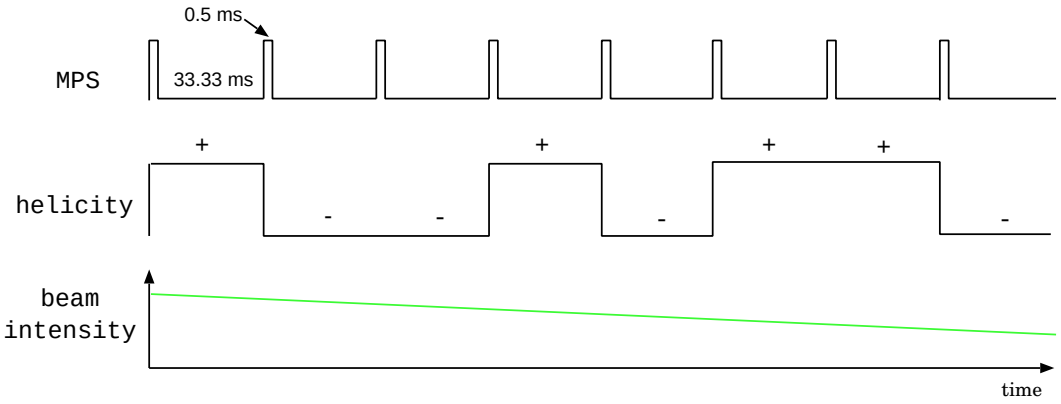


**Figure 4.5:** Helicity sequence used during E01-012 with a hypothetical linear drift of the beam intensity.

characteristics of this scheme are:

- The helicity sequence is organized in quartet ($+\ -\ -\ +$ or $-\ +\ +\ -$). This has the advantage to cancel inside each quartet the false asymmetry created by the linear drift of the beam intensity.

- The helicity information sent by the source to the Hall data acquisition (DAQ) is delayed by 8 macropulses (MPS) in order to remove any correlations in the helicity extraction.

The helicity decoding was implemented in the analysis software ESPACE [The Jlab HallA Collaboration, 2002] by a collaborator [Choi, 2003].

### 4.1.2 Beam charge asymmetry feedback

Imperfections of the Pockels cell crystal generate a small linear component in the circularly polarized light. Therefore the polarization becomes elliptical.

When flipping the helicity of the beam, the angle of the ellipse changes, creating a helicity correlated asymmetry. This effect is called Polarization Induced Transport Asymmetry (PITA) [Cates, 1991].

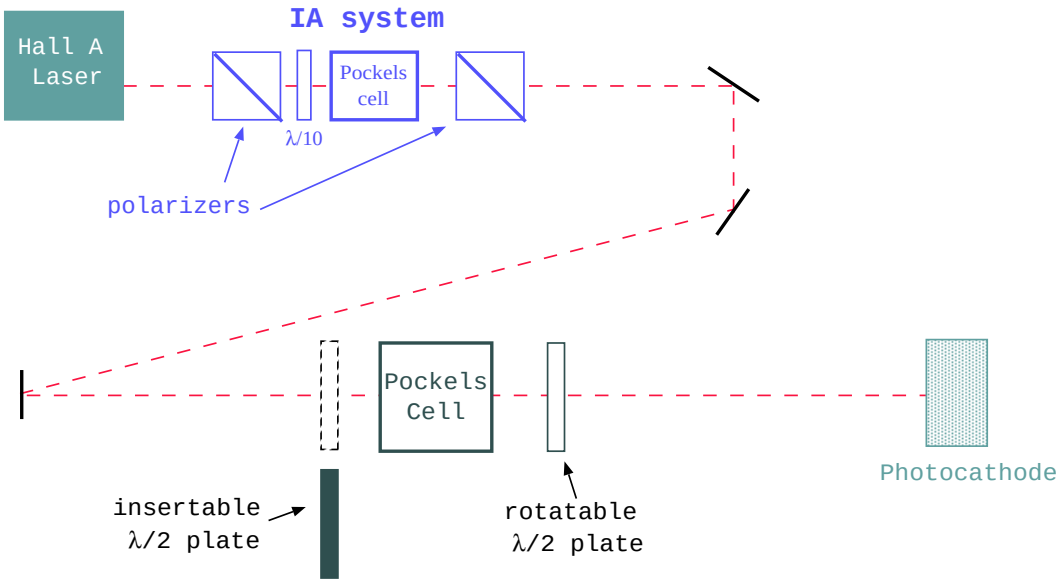


**Figure 4.6:** The polarized beam system including the charge asymmetry control elements.

In order to minimize this effect [Humensky, 2003], the Hall A Proton Parity Experiment (HAPPEx) data acquisition system monitors the charge asymmetry and adjusts the Pockels voltage accordingly. In addition, a rotatable half-waveplate is inserted downstream of the Pockels cell in order to control the orientation of the residual linear component with respect to the photocathode bifringent axis. Finally, the intensity of the laser beam can be attenuated by using the IA system upstream of the Pockels cell (Fig. 4.6). The IA system is composed of $\lambda/10$-plate and a secondary Pockels cell placed

between two polarizers. The $\lambda/10$-plate induces a change of phase to the linearly polarized laser light which can be compensated by changing the voltage in the secondary Pockels cell. This tuning generates an attenuation of the light intensity which can be applied to each helicity gate.

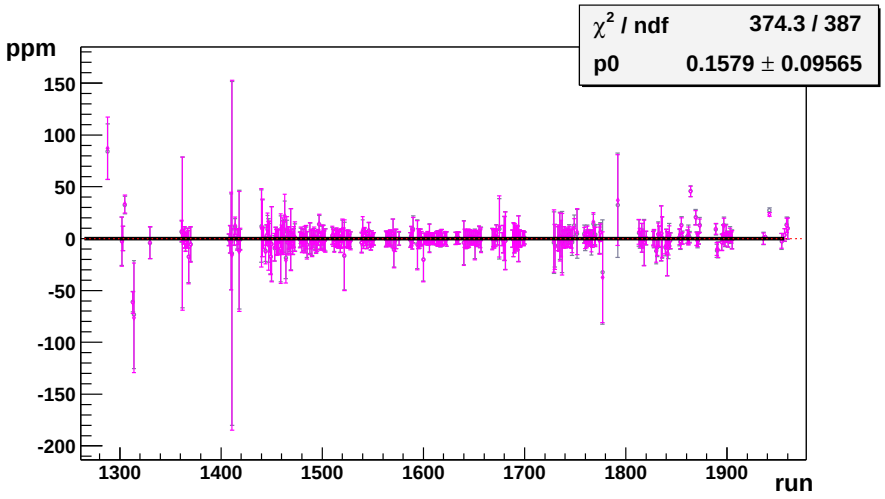


**Figure 4.7:** Beam charge asymmetry controlled by the IA system. Figure from Ref. [Vacheret, 2004b].

The parity DAQ ran during this entire experiment in order to test the IA system for the future HAPPEX [Cates, 1999, Armstrong, 2000] running. The analysis results [Vacheret, 2004a] can be seen in Fig. 4.7. The average charge asymmetry is 0.158 ppm.

### 4.1.3 Beam energy

The momentum of an electron deflected by a magnetic field is proportional to field integral as follows:

$$p = k\frac{\int \vec{B} \cdot \vec{dl}}{\theta} \tag{4.1}$$

Here, $\theta$ is the deflection angle and is equal to 34.3°. The proportionality constant $k$ is equal to 0.299792 GeV rad/(T·m·c)

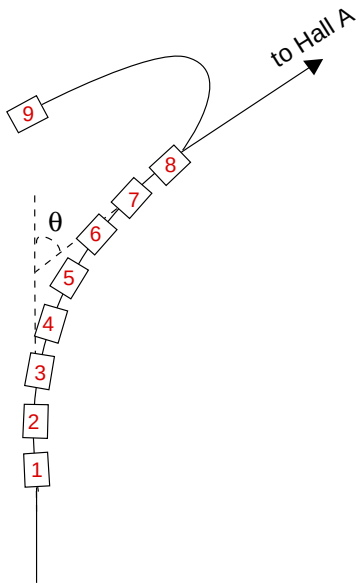


**Figure 4.8:** Illustration of the arc section of Hall A beamline.

The beam energy was monitored continuously using the Tiefenback measurement method [Tiefenback, 2006]. This non-invasive measurement uses the relation between the field integral value and the current setpoint in the eight dipoles of the arc section of the Hall A beamline (Fig. 4.8). In addition, energy corrections are applied depending on the beam position read by the

beam position monitors (BPMs) and using the magnetic transfer functions along the Hall A line. Conversions are done with a lookup table providing the basic translation between current setpoint and field integral.

The average measurements for each energy setting are summarized in Table 4.1. The accuracy of this method is approximately $5 \times 10^{-4}$.

| Beam energy in MeV |
|---|
| 1046.1 |
| 3028.1 |
| 4017.9 |
| 5008.7 |

**Table 4.1:** Beam energy from Tiefenback measurements.

### 4.1.4 Beam polarization

The polarization of the beam was measured using a Møller polarimeter [Alcorn, 2004]. This is an invasive measurement and dedicated time was allocated to this purpose at the beginning and at the end of an energy setting. In a Møller measurement, the electron beam collides with the polarized electrons from a magnetized iron foil. The Møller scattering cross section depends on the beam and the target polarization:

$$\sigma = \sigma_0 \Big[ 1 + \sum_{i=X,Y,Z} P_b^i \; A_{ii} \; P_t^i \Big] \tag{4.2}$$

The $A_{ii}$ are the analyzing powers of the different polarization projections, and $\sigma_0$ is the unpolarized Møller cross section. $P_b^i$ and $P_t^i$ are the polarizations

of the beam and the target respectively along the $i^{\text{th}}$-axis. The analyzing powers depends on the scattering angle in the center of mass frame:

$$A_{ZZ} = \frac{\sin^2\theta_{cm}(7+\cos^2\theta_{cm})}{(3+\cos^2\theta_{cm})^2} \tag{4.3}$$

$$A_{XX} = -A_{YY} = \frac{\sin^4\theta_{cm}}{(3+\cos^2\theta_{cm})^2} \tag{4.4}$$

The longitudinal polarization of the beam can be extracted from $A_{ZZ}$ which reaches a maximal value of 7/9 at $\theta_{cm}$=90° and from the knowledge of the target polarization.

All the Møller measurements [Chudakov, 2003] performed during the experiment are listed in Table 4.2. The statistical and systematic uncertainties are absolute.

| Date | Energy (MeV) | $P_b \pm$ stat. $\pm$ syst. (%) |
|---|---|---|
| 01/07/2003 | 1046.05 | 63.1 ± 0.4 ± 2.1 |
| 01/09/2003 | 4017.92 | 70.2 ± 0.2 ± 2.4 |
| 01/13/2003 | 4017.92 | 72.5 ± 0.2 ± 2.5 |
| 01/17/2003 | 5008.68 | 78.6 ± 0.2 ± 2.7 |
| 01/28/2003 | 5008.68 | 77.4 ± 0.2 ± 2.6 |
| 02/03/2003 | 5008.68 | 79.1 ± 0.2 ± 2.7 |
| 02/07/2003 | 3028.13 | 78.4 ± 0.2 ± 2.7 |
| 02/12/2003 | 5008.68 | 84.9 ± 0.2 ± 2.9 |

**Table 4.2:** Beam polarization from Møller polarimetry [Chudakov, 2003].

### 4.1.5 Beam charge measurement

In order to determine the number of incident electrons, two beam current monitors (BCMs) were placed 25 m upstream of the target [Alcorn, 2004].

BCMs are RF resonant cavities tuned to the frequency of the beam (1497 MHz). Inside the cavities, the beam creates an electromagnetic field which induces a current in a coil. The coil response is proportional to the beam current. The outputs of the two cavities are converted to frequency using a voltage-to-frequency converter (V-to-F) and then sent to VME scalers. The relation between beam current and extracted scalers is linear for beam current between 5 and 200$\mu$A, but the linearity can be extended down under 5$\mu$A by amplifying the cavities output by gain factors of 3 and 10. Finally, an Unser monitor [Unser, 1981] placed between the two BCMs can perform an absolute measurement of the current and is used to calibrate them.

These beam cavity monitors have been determined to be stable over periods of months. The scaler outputs were calibrated two months before the experiment [Jones, 2002]. The conversion of the V-to-F scalers to current is done as follows:

$$\mathrm{I_{avg}} = \frac{\frac{\mathrm{scaler}}{\mathrm{time}} - \mathrm{offset}}{\mathrm{k}} \tag{4.5}$$

Table 4.3 gives the value of the constant $k$ as a function of the amplification gain factor.

| Amplification | upstream | downstream |
|---|---|---|
| 1x | 1333.3 | 1345.1 |
| 3x | 4101.6 | 4165.6 |
| 10x | 12474.3 | 13122.2 |

**Table 4.3:** BCM calibration constant [Jones, 2002].

### 4.1.6 Beam position measurement

The beam position monitors (BPMs) are located 7.353 and 1.122 meters upstream of the target in order to measure the beam position in a non-invasive way. They are composed of four antennae placed in a cylinder parallel to the direction of the beam. The passage of the beam through the cylinder induces a signal in the antennae inversely proportional to the distance from the beam.

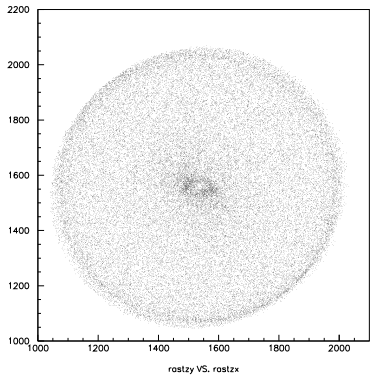


**Figure 4.9:** The circular pattern of the raster.

Experiment E01-012 used a glass target cell in which the pressure can rise to about 14 atm under running conditions. To avoid overheating the very thin glass window, the beam was rastered using two air core dipoles (one vertical, one horizontal) located 23 m upstream of the target [Chen, 2001]. Both dipoles oscillate at 18 kHz with a phase of 90° between them. This creates a circular pattern (Fig. 4.9) with a radius modulated at 1 kHz. The beam position was corrected if drifts are seen.

## 4.2 Experimental Hall A

### 4.2.1 The data acquisition (DAQ)

The signal outputs of each component of the experiment are collected and processed by a combination of hardware and software forming CODA (CEBAF Online Data Acquisition) [The JLab CODA Group , 1995]. CODA extracts information from the read-out controllers (ROCs) which gather the data from analog-to-digital converters (ADCs), time-to-digital converters (TDCs) and scalers in buffers. The buffers are sent to the event builder (EB) through the network. In the EB, the collected data from each event are organized with respect to the CODA data structure. Finally, the data are written on a storage disk by the event recorder (ER). Associated with the ROCs, each event is recorded by the trigger supervisor (TS) which synchronizes the data coming into the ROCs and is not affected by the DAQ dead-time.

In addition to CODA, a slow control software called EPICS (Experimental Physics and Industrial Control System) [The Controls Software Group, 2004] reads out many characteristics of experimental devices such as the spectrometer magnet currents, the beam half-wave plate status, the target temperature sensor. Information from EPICS can then be injected into the datastream.

### 4.2.2 The spectrometers

The standard configuration of Hall A consists of two high resolution spectrometers. The magnet setup is a QQDQ configuration as shown in Fig. 4.10. This arrangement of three quadrupoles and a dipole allows to reach a high

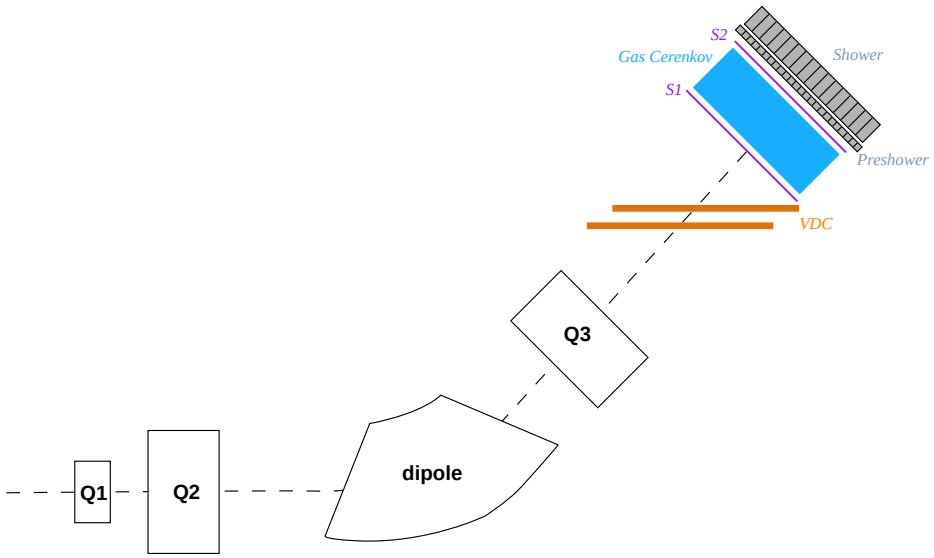


**Figure 4.10:** Schematic layout of the HRS spectrometer. Also shown is the detector package.

momentum resolution at the order of $10^{-4}$, and provides the 45° bending for the transport of the scattered electrons to the detectors. The momentum range of the spectrometers is $0.3 - 4.0$ GeV/c. The main characteristics of the two spectrometers are summarized in Table 4.4.

| | |
|---|---|
| Configuration | QQDQ |
| Bending angle | 45° |
| Momentum range (GeV/c) | $0.3 - 4.0$ |
| Momentum acceptance (%) | $\lvert\delta_p/p\rvert < 4.5$ |
| Momentum resolution | $10^{-4}$ |
| Angular range | |
| HRS-L | $12.5 - 150°$ |
| HRS-R | $12.5 - 150°$ |
| Angular acceptance (mrad) | |
| horizontal | $\pm 30$ |
| vertical | $\pm 60$ |
| Angular resolution (mrad) | |
| horizontal $\phi$ | 0.5 |
| vertical $\theta$ | 1.0 |
| Solid angle $\Delta\Omega$ at $\delta_p/p = 0, y_0 = 0$ | 6 msr |
| Transverse length acceptance | $\pm 5$ cm |
| Transverse position resolution | 1 mm |

**Table 4.4:** Main characteristics of the Hall A high resolution spectrometer. From [Alcorn, 2004].

### 4.2.3 Detector package

In order to fully characterize the scattered particles, different types of counters and detectors are used (Fig. 4.11). The first device in the scattered electron's path is the vertical drift chambers (VDCs). These provide the tracking of the event for the vertex reconstruction process. Then the particles encounter two scintillator planes which trigger the data acquisition. Finally, a $CO_2$ gas Čerenkov counter is placed between the two scintillator planes, and provides particle identification. The PID performance can be improved with the two-layered electromagnetic calorimeters.

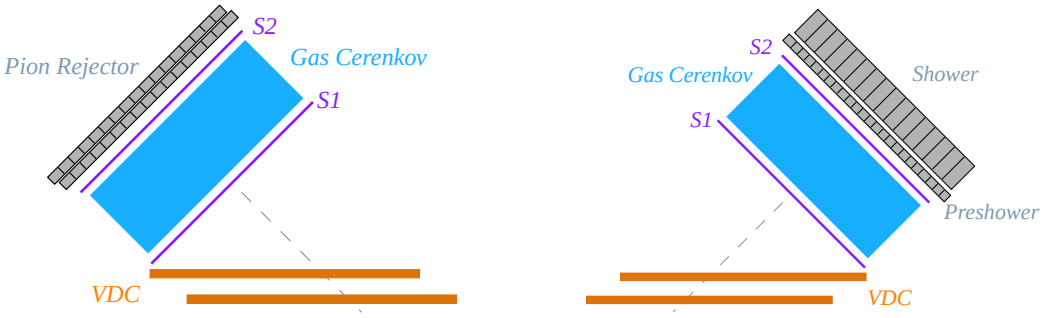


**Figure 4.11:** Illustration of the left and right HRS detector packages

### Vertical Drift Chambers

In order to achieve a good resolution in position and angle, each spectrometer contains two vertical drift chambers (VDC) [Alcorn, 2004]. Each drift chamber is made of two sensing wire planes (368 wires per plane) in a configuration shown in Fig. 4.12. An electric field is created by gold-plated Mylar planes powered at -4.0 kV and placed above and below each sensing wire plane. The drift chambers are filled with 62% argon providing the ionizing medium, and 38% ethane acting as a buffer gas.

Primary ionization happens when incident particles (mostly electrons and pions) collide with gas molecules ejecting electrons. These electrons then drift along the field lines. Close to the wire the electric field becomes purely radial and accelerates the primary ionization electrons. This gain of energy makes multiple ionizations possible and a signal in the sensing wire is then

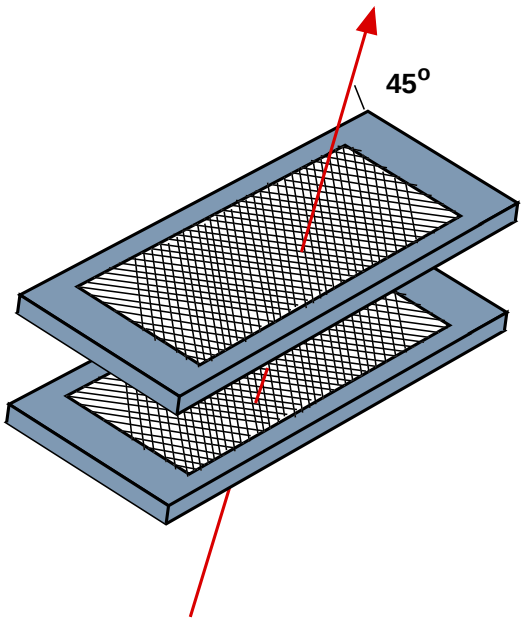


**Figure 4.12:** Schematic layout of the pair of VDCs.

detectable. The position of the incident particle can be evaluated from the time between the primary ionization and the signal which is proportional to the distance [Leo, 1987].

The first multi-wire plane in the particle trajectory is at the focal plane of the spectrometer. The electrons cross the wire chambers with an angle between approximately 38 and 52°. On average, five wires per plane fire and the trajectory of the electrons can be reconstructed very accurately. Position and angular resolutions are about 100 $\mu$m and 0.5 mrad respectively.

### Scintillators

Both spectrometers are composed of two scintillators planes (denoted S1 and S2) [Alcorn, 2004] used for the triggering of the data acquisition system. Each plane is composed of 6 overlapping plastic paddles with one photomultiplier (PMT) at each paddle end.

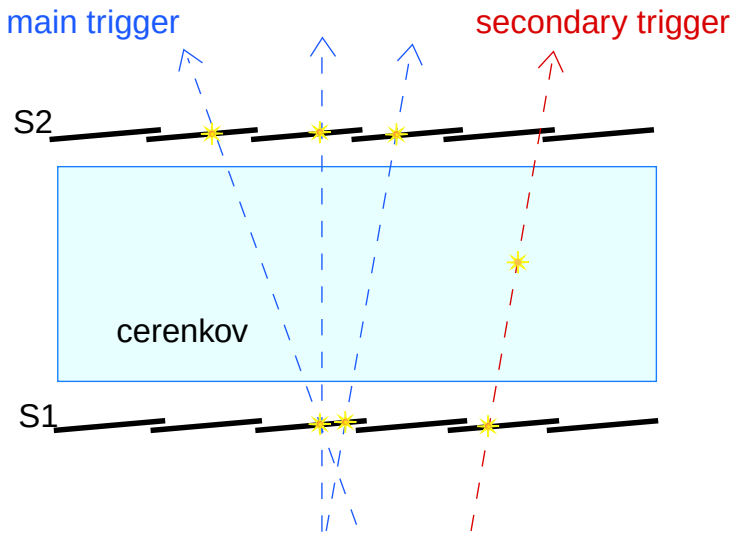


**Figure 4.13:** Illustration of trigger selections from the scintillators.

Different trigger types are associated with specific scenarios as illustrated in Fig. 4.13. An event is considered "good" if it triggers a paddle in both S1 and S2 with both PMTs of each paddle having fired and if the angle of its trajectory is small enough. That is, if the event triggers paddle $n$ of S1 then to be accepted as a good event it will have to trigger paddle $n$ or $n-1$ or $n+1$ of S2. The good event is called type 1 for the right arm and type 3 for the left arm and is the main trigger.

A secondary trigger (type 2 for the right HRS and type 4 for the left HRS) might be a good electron but failed one of the previous tests. However it has fired the Čerenkov counter.

The various trigger signals are sent to the trigger supervisor which starts the data acquisition. Another use of the scintillators is for the determination of the particle speed (Fig. 6.5) by measuring the time-of-flight between S1 and S2.

### Čerenkov counter

The Čerenkov counter [Alcorn, 2004] is filled with $CO_2$ gas, which has an index of refraction $n = 1.00041$ at STP, allowing the separation of electrons and pions. The Čerenkov radiation is detected by ten spherical mirrors and reflected to ten PMTs (Fig. 4.14).

The Čerenkov radiation is emitted when the velocity of a charged particle is greater than $1/n$. With $n = 1.00041$, the momentum threshold for a particle of mass $m$ can be calculated as follows:

$$P = \frac{mc}{\sqrt{n^2 - 1}} \tag{4.6}$$

Therefore the momentum threshold for electron detection is about 18 MeV/c and for pion detection about 4.9 GeV/c. In the momentum range that the HRS operates (less than 4GeV/c), pions cannot trigger the $CO_2$ gas Čerenkov detector.

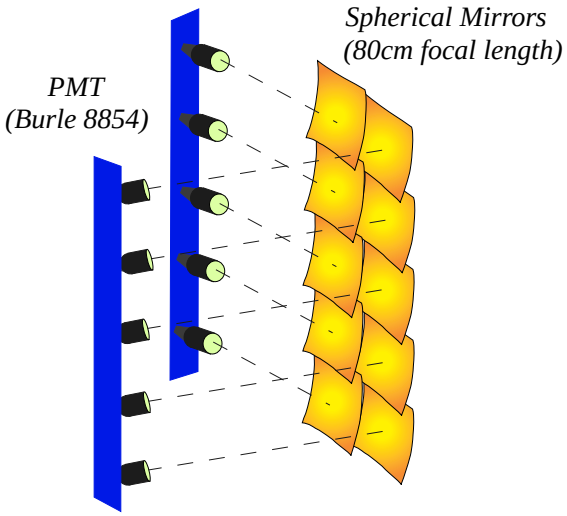


**Figure 4.14:** Layout of the PMTs and mirrors of the Čerenkov detector.

### Electromagnetic calorimeters

The particle identification performance can be improved by using an electromagnetic calorimeter in addition to the gas Čerenkov counter. The propagation of an energetic particle through dense material generates cascades of photons and $e^-$-$e^+$ pairs. The light emitted from the electromagnetic cascade is detected by photomultipliers.

Both HRS contain two-layer shower counters (Fig. 4.15) composed of lead-glass blocks of which the main components are PbO and $SiO_2$. The right spectrometer is furnished with a total absorber. In the momentum range covered by the spectrometer, the total lead-glass thickness is sufficient to contain the electromagnetic shower produced by the incident particle. It consists of two columns of 24 lead-glass blocks forming the preshower

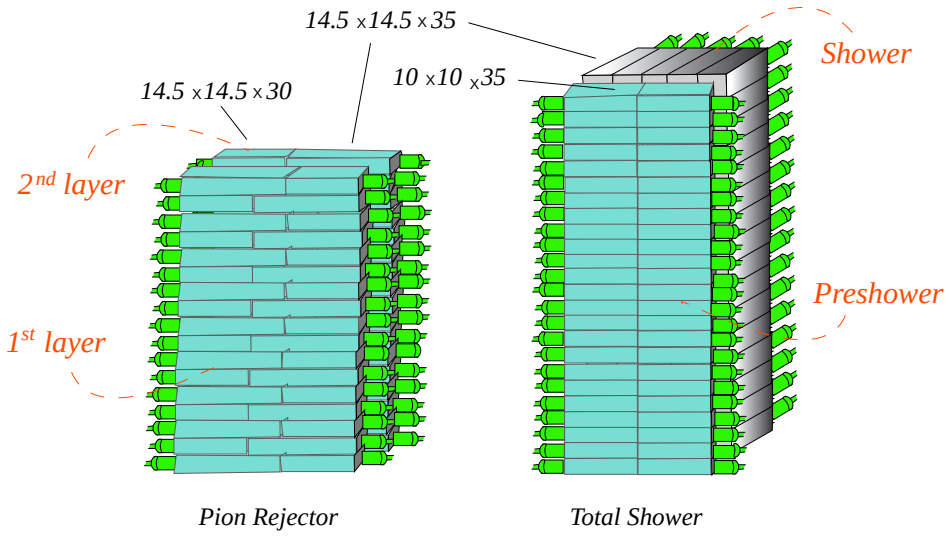


**Figure 4.15:** Configuration of the electromagnetic calorimeters in left (pion rejector) and right (total shower) HRS.

placed in front of the shower composed of 5 columns of 16 blocks. In the left spectrometer, the electromagnetic calorimeter is called the pion rejector. The two layers are identical with two columns of 17 blocks each. The pion rejector is not a total absorber.

# CHAPTER 5

# THE POLARIZED $^3$HE TARGET

A schematic of the Jefferson Lab polarized $^3$He target system is shown in Fig. 5.1. The cell is placed in the center of the system. The pumping chamber sits in an oven heated to 170°C to vaporize the alkali metal (Rubidium). The target chamber is centered in the holding field. Two sets of Helmholtz coils produce the holding field in any desired in-plane direction. Three coherent diode-array lasers for each configuration (longitudinal or transverse) are tuned at a wavelength of 795 nm which is required for the optical pumping of the Rubidium. The laser light goes through a series of optical elements in order to convert it from linear to circular polarization.

Two independent polarimetry systems monitor the polarization of the target. The Nuclear Magnetic Resonance (NMR) signal is detected by two pick-up coils placed parallel to the target chamber during the RF excitation of the $^3$He spins. The Electron Paramagnetic Resonance technique looks at the change in the Zeeman frequency of the Rubidium as the $^3$He spins are flipped.

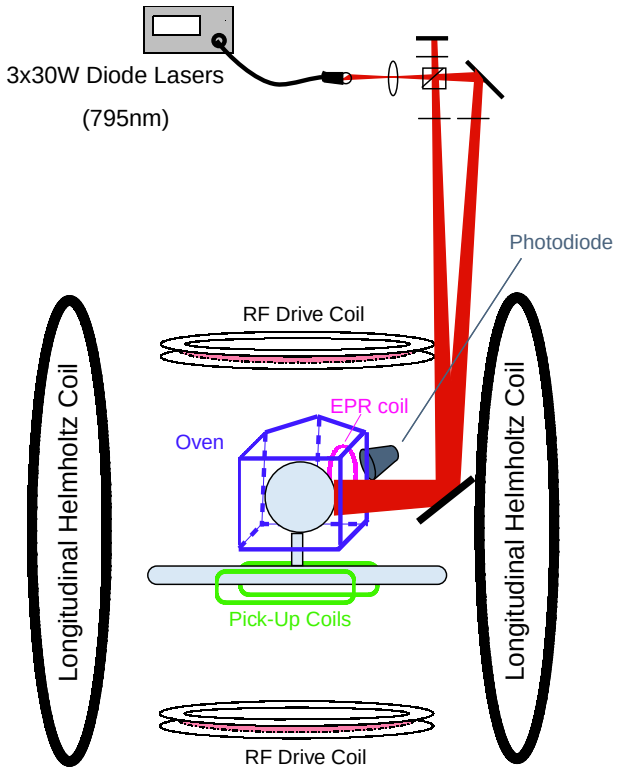


**Figure 5.1:** Polarized $^3$He target system. Only the longitudinal Helmholtz coils are shown for clarity.

## 5.1 Optical pumping

The polarization of the $^3$He nuclei is based on a two-step process: Rubidium vapor is optically pumped [Happer, 1972] with a circularly polarized light and then the Rb electron transfers its polarization to the $^3$He nucleus by spin-exchange interactions. If we neglect the spin of the Rb nucleus, the principle of optical pumping on the Rb ground state sublevels can be illustrated by Fig. 5.2. In a magnetic field, right hand circularly polarized light of

794.8 nm can induce the D1 transition, depopulating the ground state Zeeman sublevel (5 $^2S_{1/2}$,$m$=-1/2) in favor to the excited state Zeeman sublevel (5 $^2P_{1/2}$,$m$=+1/2). This transition follows the angular momentum selection rules $\Delta m = \pm 1$. The electrons may decay, emitting photons isotropically

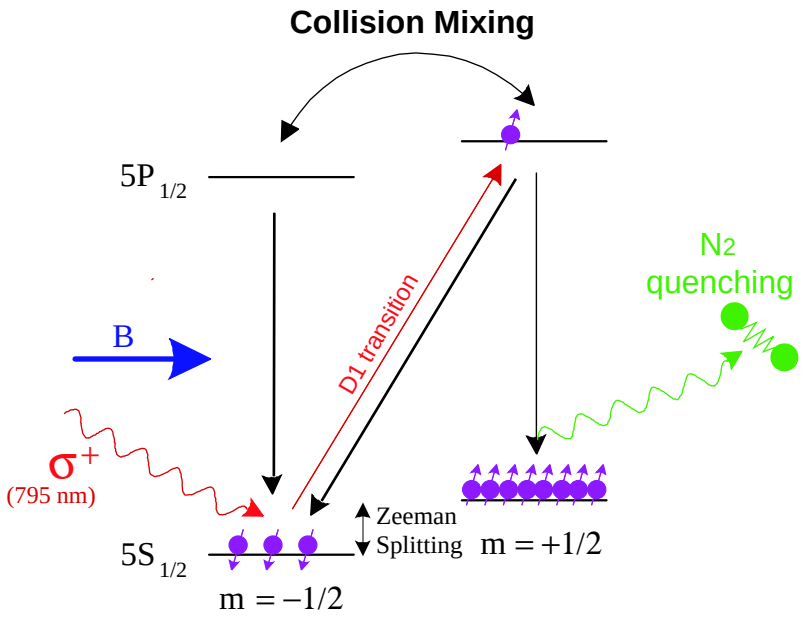


**Figure 5.2:** Optical pumping principle

that could limit the efficiency of the optical pumping. To reduce this effect, a small amount of $N_2$ buffer gas is added to the cell.

The average polarization obtained by optical pumping can be estimated by:

$$P_{\mathrm{Rb}} = \frac{\mathcal{R}}{\mathcal{R} + \Gamma_{SD}} \tag{5.1}$$

$\mathcal{R}$ is the optical pumping rate: $\mathcal{R} = \int \Phi(\nu)\sigma(\nu)d\nu$ where $\Phi(\nu)$ is the photon flux per frequency unit and $\sigma(\nu)$ is the light absorption cross section. $\Gamma_{SD}$ is the electron spin depolarization rate which is mostly caused by spin rotation interactions happening during the collisions: Rb-Rb, Rb-$^3$He and Rb-$N_2$.

The Rb spin depolarization rate is therefore proportional to the densities of each species:

$$\Gamma_{SD} = k_{\mathrm{Rb-^3He}}[^3\mathrm{He}] + \mathrm{k_{Rb-N_2}[N_2]} + \mathrm{k_{Rb-Rb}[Rb]} \tag{5.2}$$

The spin destruction constants are [Wagshul, 1994]:

$$k_{\mathrm{Rb-^3He}} \leq 2 \times 10^{-18}\mathrm{cm}^3/\mathrm{s} \tag{5.3}$$

$$k_{\mathrm{Rb-N_2}} = 8 \times 10^{-18}\mathrm{cm}^3/\mathrm{s} \tag{5.4}$$

$$k_{\mathrm{Rb-Rb}} = 8 \times 10^{-13}\mathrm{cm}^3/\mathrm{s} \tag{5.5}$$

For the experiment E01-012, the $^3$He density in the pumping chamber was on average equal to $2.0 \times 10^{20}\mathrm{cm}^{-3}$ (= 7.4 amagats), the nitrogen density is about 0.9% of the $^3$He density and the Rubidium density (in $\mathrm{cm}^{-3}$) can be estimated using Killian's formula [Killian, 1926]:

$$[Rb] = \frac{1.507 \times 10^{(26-\frac{4040}{T})}}{T} \tag{5.6}$$

The rubidium is vaporized at the target oven temperature of 170°C. Finally, $\Gamma_{SD} = 1172\ \mathrm{s}^{-1}$. The other causes of Rb spin depolarization are the collisions with the walls and spin-exchange interaction which are described in the next section. In a high pressure cell the rate of the collisions with the walls are

only significant within 0.1mm of the walls [Romalis, 1997]. The Rubidium can reach a polarization better than 90%.

## 5.2 Spin-exchange interaction and $^3$He relaxation rates

The Rubidium electron transfers its polarization to the $^3$He by "hyperfine like" interaction. The spin-exchange coefficient has been measured recently [Chann, 2002] to be $k_{SE} = 6.7 \times 10^{-20}\text{cm}^3/\text{s}$. The polarization of $^3$He increases exponentially with time as shown in Fig. 5.3:

$$P_{^3\text{He}}(t) =< P_{\text{Rb}} > \frac{\gamma_{SE}}{\gamma_{SE} + \Gamma}[1 - e^{-(\gamma_{SE}+\Gamma)t}] \tag{5.7}$$

$\gamma_{SE}$ is the $^3$He spin-exchange rate: $\gamma_{SE} = k_{SE}[\text{Rb}]$. $\Gamma$ is $^3$He nuclear spin relaxation and $< P_{\text{Rb}} >$ is the volume average Rb polarization. $\gamma_{SE}$ is quite small, on the order of $10^{-5}\ \text{s}^{-1}$, so care must be taken to minimize the nuclear relaxation rate.

The polarization loss of the $^3$He nucleus comes from several sources:

- The $^3$He-$^3$He magnetic dipolar interaction due to the coupling of the nuclear spins to the angular momentum of the $^3$He atoms has been measured in [Newbury, 1993]:

$$\Gamma_{dipole} = \frac{[^3\text{He}]}{744}\ \text{h}^{-1} \tag{5.8}$$

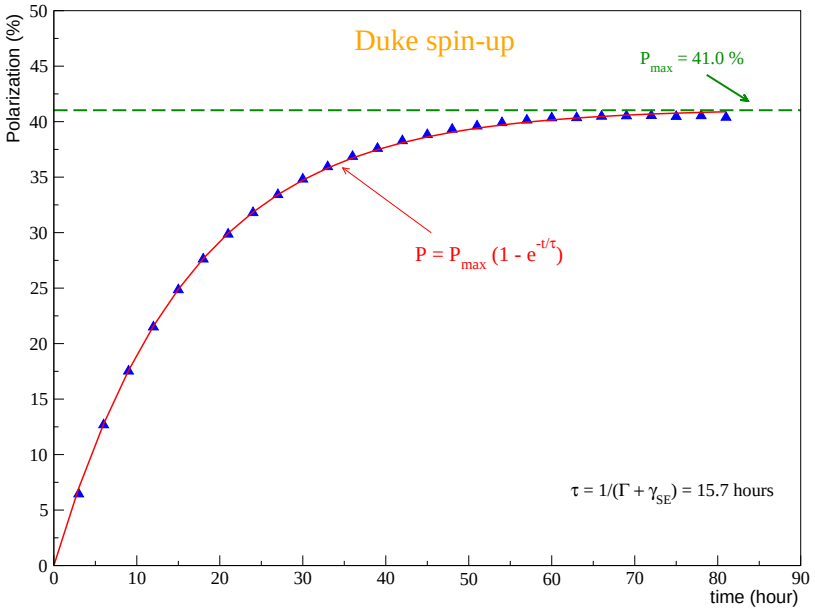


**Figure 5.3:** Spin up curve. Measurement performed on the cell *Duke*.

- The inhomogeneity of holding field $B_z$ which induces perpendicular field gradients $\nabla B_x$ and $\nabla B_y$:

$$\Gamma_{\nabla B} = 2D\frac{|\nabla B_x|^2 + |\nabla B_y|^2}{B_z^2} \tag{5.9}$$

  Here $D \simeq 0.28$ cm$^2$/s is $^3$He self-diffusion coefficient. The gradient was measured [Sulkosky, 2006] before the experiment and was found to be small ($= 8$ mG/cm), therefore $\Gamma_{\Delta B} \simeq 1/4800$ h$^{-1}$ and is negligible.

- The collision with the walls containing paramagnetic impurities and/or micro-fissures, creating a spin relaxation $\Gamma_{wall}$. It can be determined by looking at the decay of the target polarization at room temperature. This is called a *spindown* and allows the determination of the lifetime

$\tau$ of the polarization in the cell:

$$\frac{1}{\tau} = \Gamma_{dipole} + \Gamma_{wall} + \Gamma_{\nabla B} \tag{5.10}$$

It is an exponential decay, as can be seen in Fig. 5.4, and the lifetime $\tau$ of the target is extracted from the fit. The lifetime is one of the parameters used to determine the quality of a cell. For Duke, $\Gamma_{wall}$ is about $1/153$ h$^{-1}$.

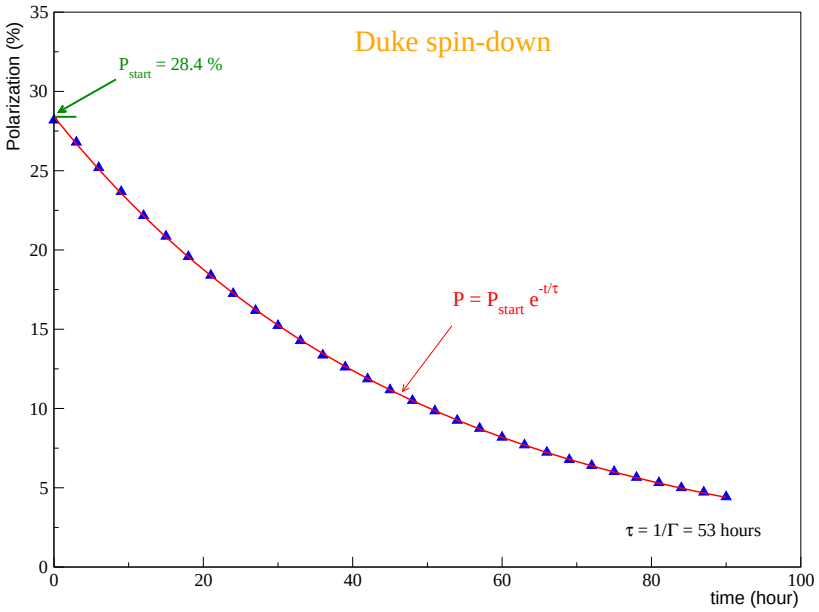


**Figure 5.4:** Spin down curve corrected for AFP loss [Solvignon, 2002]. Measurement performed on the cell Duke in the target test lab.

- Finally, the electron beam passing through the target cell induces depolarization by ionizing the $^3$He atoms. From [Bonin, 1988], the ionization

rate per $^3$He atoms is expressed as:

$$\Gamma_{ion} = \frac{[^3\mathrm{He}]\mathrm{M}_{^3\mathrm{He}}\mathrm{L}_{\mathrm{tc}}}{N_{^3\mathrm{He}}} \frac{1}{\Delta E} \frac{dE}{dx} I \tag{5.11}$$

$\Delta E$ is the mean energy expended by electrons in the creation of a $^3$He$^+$ ion and is approximatively 32 eV. $dE/dx$ is the energy loss per unit length for electrons passing through $^3$He gas. Considering that only the target chamber $^3$He atoms are subject to the ionization of the beam, the number of $^3$He atoms $N_{^3\mathrm{He}}$ equal to $V_{tc}[^3\mathrm{He}] = \mathrm{L}_{\mathrm{tc}}\pi\mathrm{r}_{\mathrm{tc}}^2[^3\mathrm{He}]$. The typical target chamber radius is $r_{tc} = 0.9$cm and the target chamber length was 40 cm for cells used during E01-012. Thus, the ionization rate is found to be $I/362$ h$^{-1}$. The depolarization effect is proportional to the ionization rate:

$$\Gamma_{beam} = n_d \Gamma_{ion} \tag{5.12}$$

where $n_d$ is the mean number of nuclei depolarized for each $^3$He$^+$ ion created. $n_d = n_a + n_m$ with $n_m$ and $n_a$ the number of $^3\mathrm{He}_2^+$ molecular ions and $^3$He$^+$ atomic ions formed, respectively. $n_m$ is suppressed by the presence of $\mathrm{N}_2$ in the cell and $n_a$ is constrained by the fact that an atomic ion depolarizes no more than one nucleus. Therefore, $n_a \leq 1$ and:

$$\Gamma_{beam} \leq \frac{I(\mu\mathrm{A})}{362}\mathrm{h}^{-1} \tag{5.13}$$

During the experiment, four beam currents (5, 10, 12 and 15$\mu$A) were

used, depending on the trigger rates and the target depolarization effect.

## 5.3 Target density and temperatures

It is important for the extraction of the target polarization and of the cross sections to be able to predict the internal target temperature and density at each instant. For this purpose, Resistance Temperature Detectors (RTDs) are placed on the cell as illustrated in Fig. 5.5 and their outputs are read-out and recorded by EPICS every 10 seconds.

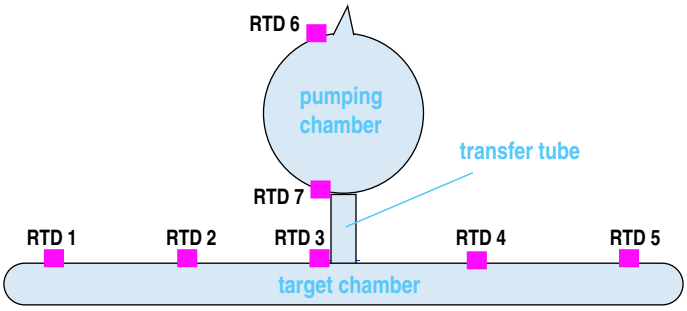


**Figure 5.5:** RTD position on the target chamber.

### 5.3.1 Target density and temperature extraction

To determine the temperature and the density inside the target under running conditions, dedicated tests were performed when experimental conditions, such as realignment of the lasers, were changed. The temperature test consists of taking several NMR measurements with lasers on ($S^{on}$) and off

($S^{off}$). Assuming $^3$He is an ideal gas, the temperature inside the pumping chamber can be predicted [Jensen, 2000] by the following equation:

$$T_{pred} = \frac{V_p\ T_t^{on}}{\frac{S^{off}}{S^{on}}\frac{T_t^{on}}{T_t^{off}}\frac{T_c^{off}}{T_c^{on}}\left[V_{tot} + V_p\left(\frac{T_t^{on}}{T_p^{off}} - 1\right)\right] - V_{tot} + V_p} \tag{5.14}$$

and the densities of the pumping and target chamber can be written as:

$$n_P = \frac{n_0}{1 + \frac{V_T}{V_{tot}}\left(\frac{T_{pred}}{T_t^{on}} - 1\right)} \qquad n_T = \frac{n_0}{1 + \frac{V_P}{V_{tot}}\left(\frac{T_t^{on}}{T_{pred}} - 1\right)} \tag{5.15}$$

$T_t$, $T_c$ and $T_p$ corresponds to the average surface temperature of the target chamber, of the target chamber portion between the pick-up coils and of the pumping chamber respectively. $V_{tot}$ is the total internal volume of the cell: $V_{tot} = V_T + V_{tr} + V_P$ where $V_T$ and $V_P$ are the volumes of the target chamber and the pumping chamber, and $V_{tr}$ is the volume of the transfer tube connecting them (Fig. 5.5). The characteristics of the two cells, *Duke* and *Exodus*, used during the experiment are summarized in Ref. [Singh, 2003].

The surface temperature of the pumping chamber is given by the average of RTD 6 and 7 (Fig. 5.5). In order to extract the temperature distribution along the target chamber, a polynomial function is used to fit the RTD data (Fig. 5.6). The fit is then integrated and averaged over the target chamber length [Solvignon, 2005b]. Table 5.1 summarizes the results of the different temperature tests performed during the experiment.

Since $T_{pred}$ is equal to $T_p$ when the lasers are off, an interpolation can be done for any $T_p$ [Kramer, 2003] as illustrated in Fig. 5.7. For the cell *Duke*,

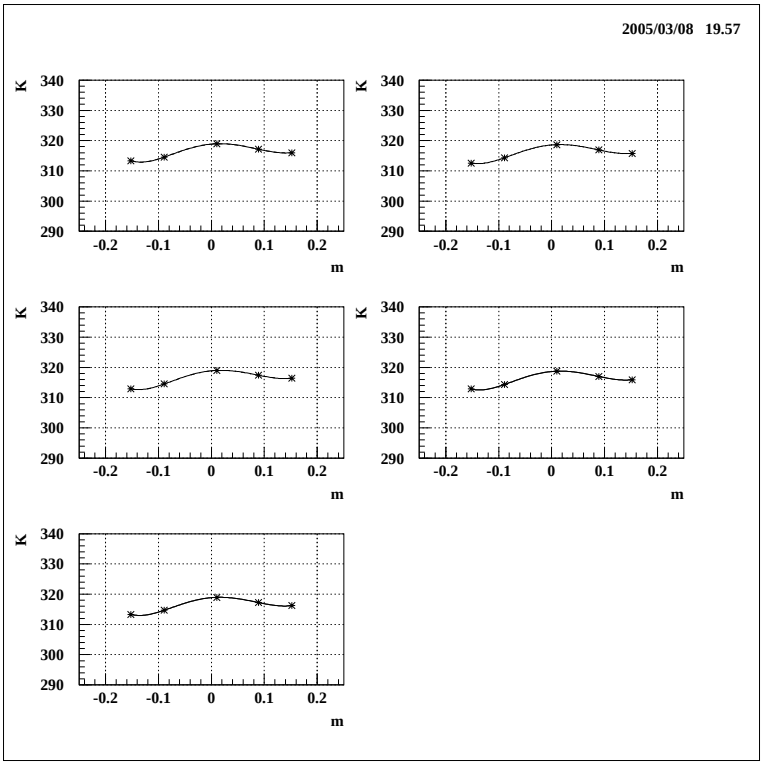


**Figure 5.6:** Fit of the target chamber RTD readings for 5 NMR measurements. The first measurement was done with lasers on, the second one with lasers off, then the next one will lasers on and etc.

| Cell | Date | $T_p$ (K) | $T_{pred}$ (K) | $n_t$ (amg) | $n_p$ (amg) |
|---|---|---|---|---|---|
| Duke | 01/06/03 | 455 | 503 | 11.6 | 7.4 |
| | 01/07/03 | 454 | 501 | 11.6 | 7.4 |
| | 01/16/03 | 456 | 501 | 11.6 | 7.4 |
| Exodus | 02/13/03 | 457 | 510 | 12.0 | 7.6 |

**Table 5.1:** Results of temperature tests performed during the experiment.

two equations are used for periods prior (Eq. 5.16) and after (Eq. 5.17) laser

realignement*. The last equation (E.5.18) is for the cell *Exodus*. The fit gives:

$$T_{pred} = 3.12\ T_p - 916.04 \tag{5.16}$$

$$T_{pred} = 2.79\ T_p - 774.38 \tag{5.17}$$

$$T_{pred} = 4.17\ T_p - 1398.44 \tag{5.18}$$

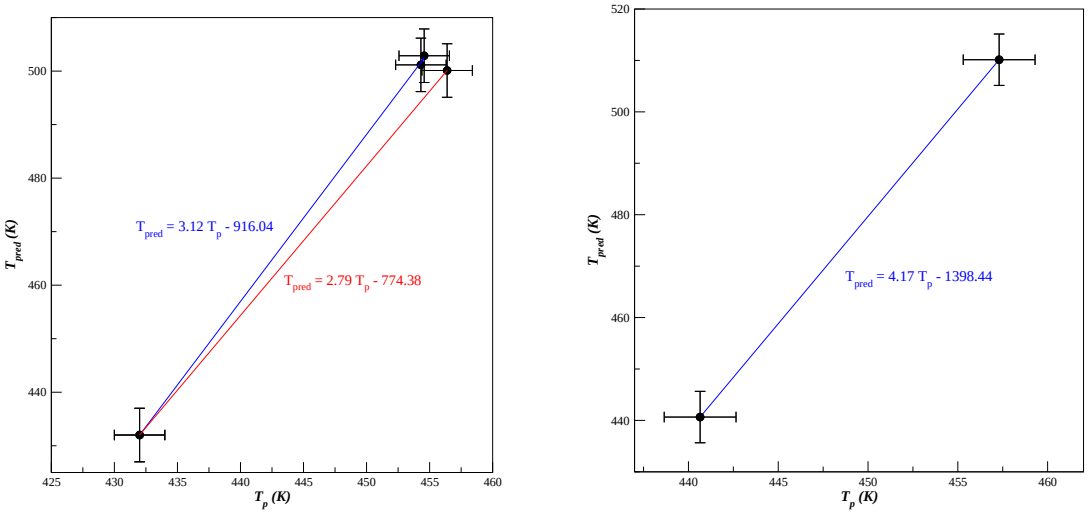


**Figure 5.7:** Estimate of the temperature inside the pumping chamber of as a function of the surface temperature for *Duke* (left) and for *Exodus* (right).

*For data analysis concern, the realignment happened between run numbers 244 and 245

### 5.3.2 Cell density for polarized $^3$He runs

The density of the target chamber for each run is determined by using Eq. (5.15) along with Eqs. (5.16), (5.17) or (5.18). The RTD readouts are extracted 8 minutes after the beginning of each run, so the temperature has had time to stabilize in case there is a change of configuration before the run started. Fig. 5.8 shows the temperature and the density of the cell for each run. A jump is observed in the target chamber temperature for run numbers between 400 and 500 approximately. This is due to a decrease of the cooling jet flow at this period (see [Solvignon, 2005b]).

In order to evaluate the density uncertainty due to the uncertainties of the internal temperatures of the cell, a mathematical variation of 5K was applied to the RTD read-out and the effect was propagated to the final quantities. Finally, the average temperatures and densities of each cell during their running time are:

$$T_{pred} = (501 \pm 6)\ \mathrm{K} \tag{5.19}$$

$$n_P = (7.4 \pm 0.1)\ \mathrm{amg} \quad \text{and} \quad n_T = (11.6 \pm 0.1)\ \mathrm{amg} \tag{5.20}$$

for *Duke* and:

$$T_{pred} = (510 \pm 6)\mathrm{K} \tag{5.21}$$

$$n_P = (7.6 \pm 0.1)\ \mathrm{amg} \quad \text{and} \quad n_T = (12.0 \pm 0.1)\ \mathrm{amg} \tag{5.22}$$

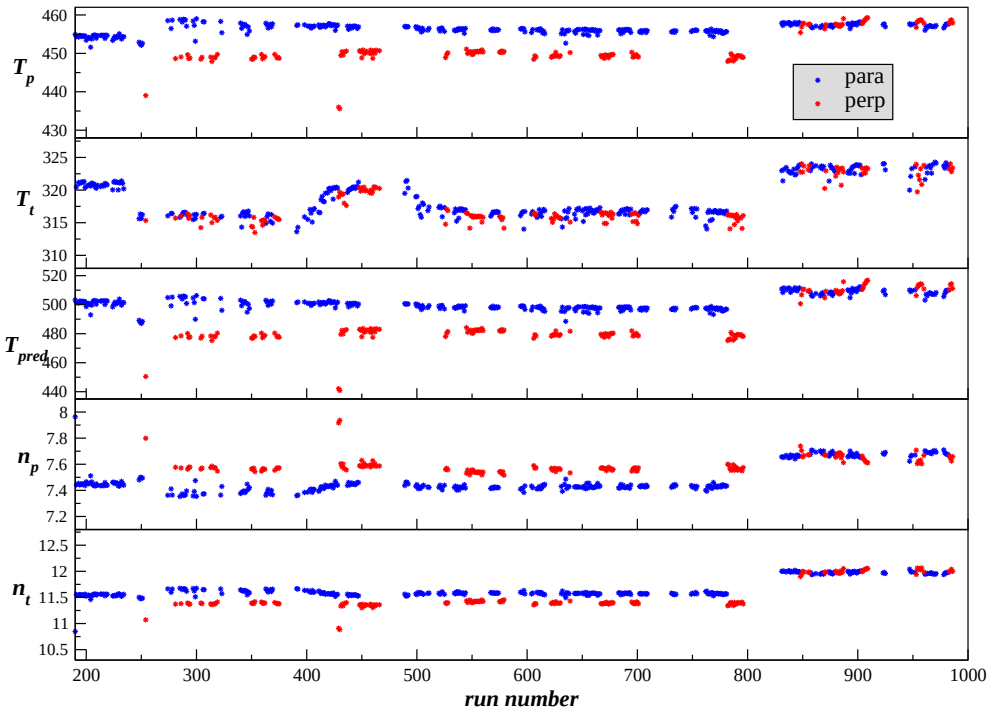


**Figure 5.8:** Results from temperature test interpolation to each $^3$He run. From the top to the bottom: surface temperature of the pumping chamber $T_p$ and of the target chamber $T_t$, temperature predicted inside the pumping chamber $T_{pred}$, pumping and target chamber densities ($n_P$ and $n_T$ in amagats)

for *Exodus*. The density systematic errors from the temperature uncertainties are about 1% relative. Adding the volume and the nominal density uncertainties, the total systematic error is 2.65% relative.

## 5.4 Target polarimetries

### 5.4.1 Adiabatic Fast Passage

The Adiabatic Fast Passage (AFP) allows the reversal of the $^3$He spins while minimizing the polarization loss [Abragam, 1996]. In the presence of an external field $\vec{H}_0$ ($= -\omega_o/\gamma\vec{k}$, where the gyromagnetic ratio $\gamma = 2\pi \times 3243$ Hz/G for $^3$He), the magnetic moment of the spin ($M = \gamma\hbar I$) is subjected to a torque equal to the rate of change of its angular momentum:

$$\hbar\frac{d\vec{I}}{dt} = \vec{M} \times \vec{H}_0 \quad \Rightarrow \quad \frac{d\vec{M}}{dt} = \gamma\vec{M} \times \vec{H}_0 \tag{5.23}$$

Now considering this system in a frame rotating at an angular velocity $\omega$ with respect to the reference frame, the evolution of the magnetic moment becomes:

$$\frac{\partial\vec{M}}{\partial t} = -\gamma\vec{M} \times \vec{H}_0 + \vec{\omega} \times \vec{M} \tag{5.24}$$

Moreover, if an oscillating field $\vec{H}_1$ ($= -\omega_1/\gamma\vec{i}'$) perpendicular to the main field is applied, Eq. (5.25) contains a new term:

$$\frac{\partial\vec{M}}{\partial t} = -\gamma\vec{M} \times (\vec{H}_0 + \vec{H}_1) + \vec{\omega} \times \vec{M} \tag{5.25}$$

Thus, in the rotating frame, the magnetic moment experiences a torque with the effective field $\vec{H}_{eff} = (\omega_0 - \omega)\vec{k} + \omega_1\vec{i}'$ and precesses around it with a Larmor frequency $\omega_{eff} = -\gamma H_{eff}$. Finally the holding field amplitude is swept through the resonance and the spins follow the effective field from aligned to anti-aligned with respect to the main field.

The reversal of the magnetization is done under adiabatic conditions. The sweep of the main field should be slow enough to perform a complete reversal of the spins orientation, but fast enough so that relaxation of the spins does not occur. The AFP conditions can be expressed as follows:

$$\frac{1}{T_2} \ll \frac{1}{H_1}\left|\frac{dH_0}{dt}\right| \ll |\gamma H_1| \tag{5.26}$$

where $T_2$ is the transverse relaxation time.

### 5.4.2 Nuclear Magnetic Resonance

The motion of the spins creates an electromotive force (EMF) which can detected in a pair of pick-up coils through a lock-in amplifier referenced to the RF frequency. The Nuclear Magnetic Resonance (NMR) signal is proportional to the transverse component of the magnetization:

$$S(t) = \frac{MH_1}{\sqrt{H_1^2 + (H_0(t) - H_0^{res})^2}} \tag{5.27}$$

where $H_0^{res}$ is the value of the holding field at the resonance. Fig. 5.9 shows the NMR response after sweeping the holding field through the resonance from above and below. The functional form of the fit is a square root of a Lorentzian. Five parameters are extracted from the fit: the height, the width and the centroid of the peak, as well as a linear fit to the background. More details on the NMR system can be found in [Incerti, 1998b].

The $^3$He NMR signal is calibrated against the thermal polarization of the protons in water. To this end, a cell with almost identical geometric

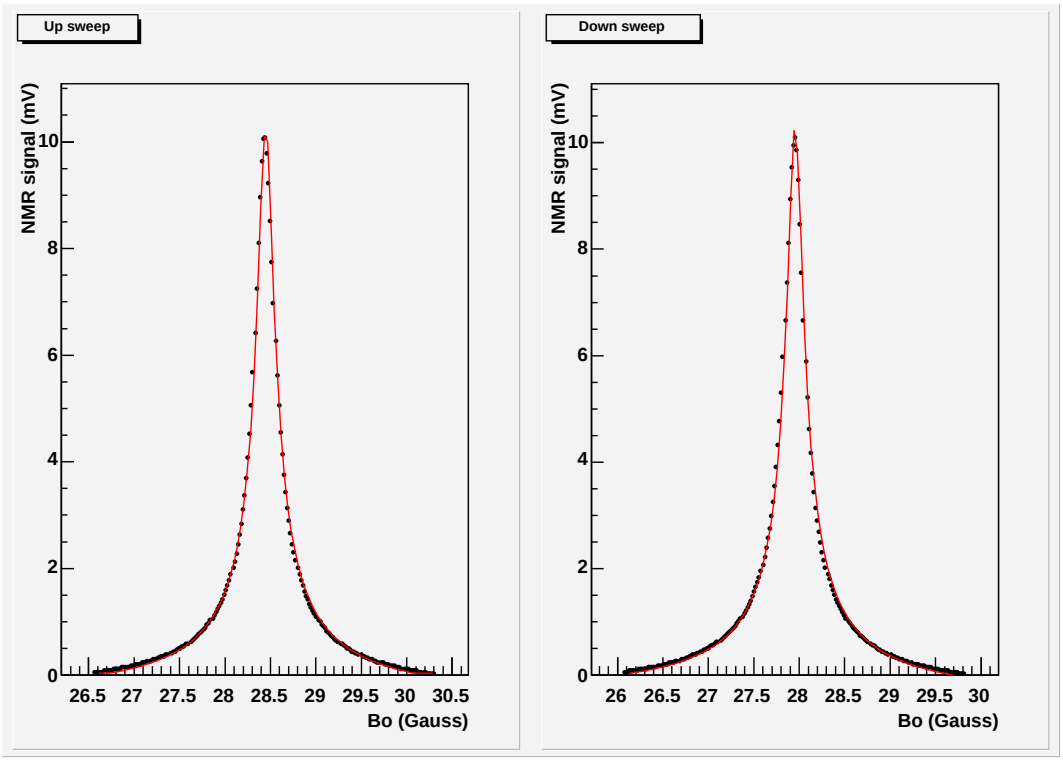


**Figure 5.9:** $^3$He NMR signal for the holding field ramping up (left plot) and ramping down (right plot). The black points are read from the lockin amplifier output. The fit of the data (red curve) corresponds to Eq. (5.27).

characteristics filled with water is placed in the polarized $^3$He system. The polarization of the protons in water obeys the Boltzman distribution:

$$P = \tanh \frac{\mu_p B}{kT} \tag{5.28}$$

with $\mu_p$ the magnetic moment of the proton and $k$ the Boltzman constant. At room temperature and in a field of 25 G, the polarization of the protons is $P \approx 8.57 \times 10^{-9}$. Because of the difficulty in detecting of the NMR signal from water, hundreds of consecutive measurements are averaged in

order to improve the signal to noise ratio. With an RF frequency of 91 kHz, the NMR resonance from protons ($\gamma_p = 2\pi \times 4.257$ kHz/Gauss) happens at $H_{res} = 21.38$ G. Fig. 5.10 shows the average of the NMR down sweeps of a water calibration done for the experiment E01-012. The heights of the NMR signals are extracted from a fit based on the Bloch equations [Incerti, 1998c]. There were six water calibrations performed before and after the experiment. The detail of the water analysis can be found in Ref. [Sulkosky, 2006].

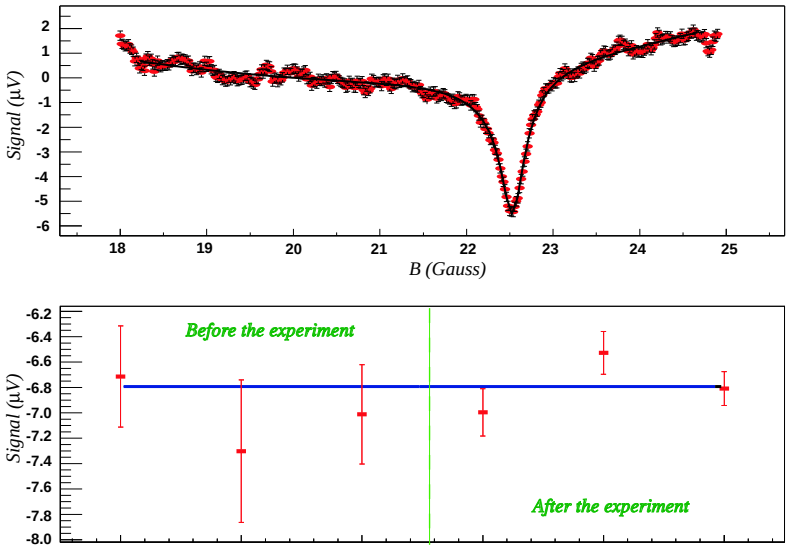


**Figure 5.10:** Results from water calibrations. The top plot shows the down sweep of a water signal. In the bottom plot are the calibration constants determined from the water calibrations performed before and after the experiment.

### 5.4.3 Electron Paramagnetic Resonance

Inside the pumping chamber, polarized $^3$He nuclei create a shift of the electron paramagnetic resonance (EPR) [Romalis, 1998]: $\nu_{EPR} = \nu_o \pm \Delta\nu_{EPR}$ where $\nu_o$ is the EPR baseline frequency in a static field and is equal to $k_z B_0$ with $k_z = 0.466$ MHz/G. This shift comes from two sources: a small effective magnetic field created by Rb-$^3$He spin exchange interactions:

$$B_{SE} = \frac{2\hbar K_{SE}[^3\mathrm{He}]\Gamma_{\mathrm{SE}}}{g_e \mu_B} P \tag{5.29}$$

and the extra magnetic field created by polarized $^3$He:

$$B_M = C\mu_{^3\mathrm{He}}[^3\mathrm{He}]\mathrm{P} \tag{5.30}$$

$K_{SE}$ is the ratio of the imaginary part of the spin-exchange cross section to its real part. $\Gamma_{SE}$ is the Rb-$^3$He spin-exchange rate per Rb atom. $g_e$ and $\mu_B$ are the gyromagnetic ratio and the Bohr magneton respectively. $\mu_{^3\mathrm{He}}$ is the $^3$He nuclear magnetic moment. The constant $C$ depends of the shape of the cell.

Using an RF field to initiate the transition $M_F = -3 \rightarrow M_F = -2$, the resonance frequency is found when the D1 light absorption is maximum. D1 is also the wavelength of the laser light which make difficult the detection of the small increase of light due to the RF field. Instead, the D2 transition is selected using a D2-filter in front of the photodiode. The energy gap between the D1 and D2 line is only 0.0294 eV. Thus, under the running condition, the electrons can acquire enough kinetic energy to make the jump. Finally, by

flipping the $^3$He spin direction, the extra field $\delta B_{^3\mathrm{He}} (= B_{SE} + B_M)$ subtracts to the holding field inducing a decrease of the EPR frequency. The change of the EPR frequency due to these extra fields can be expressed by taking the derivative of the EPR frequency with respect to the magnetic field:

$$\Delta\nu_{EPR} = \frac{d\nu_{EPR}(F,M)}{dB}(B_{SE} + B_M) \tag{5.31}$$

$$= \frac{8\pi}{3}\frac{\mu_0}{4\pi}\frac{d\nu_{EPR}(F,M)}{dB}\kappa_0\mu_{^3\mathrm{He}}[^3\mathrm{He}]\ \mathrm{P} \tag{5.32}$$

Here, $\kappa_0$ is a dimensionless constant depending on the temperature and has been measured for spherical cells [Romalis, 1998][†]:

$$\kappa_0 = 4.52 + 0.00934\ T(^\circ\mathrm{C}) \tag{5.34}$$

A typical EPR measurement during the experiment E01-012 is shown in Fig. 5.11.

### Holding field amplitude

For a holding field of about 25 G, the Zeeman splitting is smaller than the hyperfine splitting $\nu_{hf}$ (see Fig. 5.12). The energy of the sublevels can be determined for $^{85}$Rb (I=5/2,S=1/2) from the Breit-Rabi formula [Romalis, 1997]:

$$E_{F,m_F} = -\frac{h\nu_{hf}}{2(2I+1)} - g_I\mu_N B_0 m_F \pm \frac{h\nu_{hf}}{2}\sqrt{1 + \frac{4m_F}{2I+1}x + x^2} \tag{5.35}$$

corresponding to the total spin $F = \mathrm{I} \pm \mathrm{S}$.

[†]Another measurement has been performed recently [Babcock, 2005] which is consistent with Eq. (5.34) for temperatures up to 350°C:

$$\kappa_0 = 6.39 + 0.00914[T(^\circ\mathrm{C}) - 200] \tag{5.33}$$

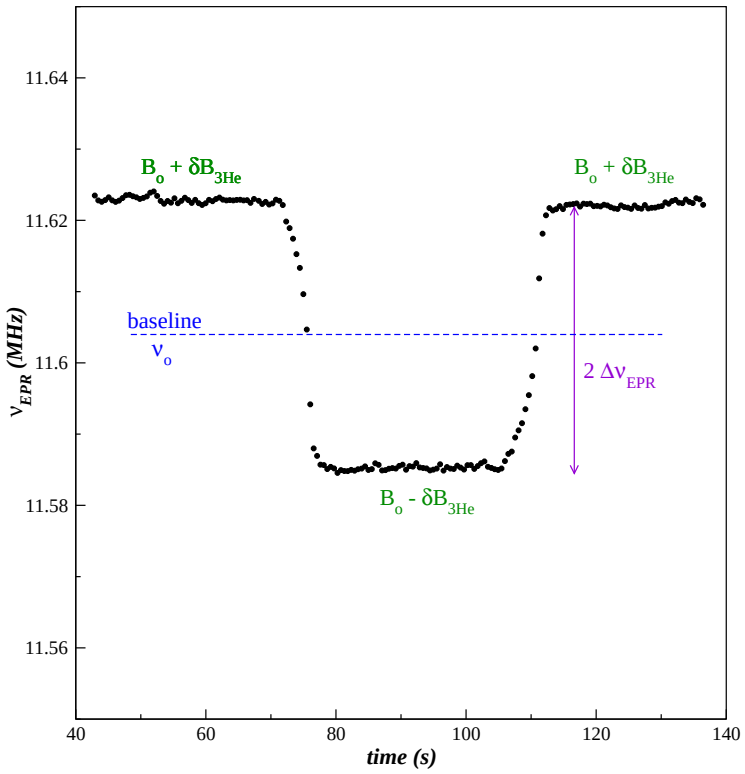


**Figure 5.11:** EPR measurement spectrum.

During E01-012, the polarized light wavelength and the holding field were chosen in order to populate the level $m_F = -3$. The magnitude of the static field can be extracted from the EPR baseline frequency $\nu_{res} = \nu_0$ [Zheng, 2002]:

$$\begin{aligned} h\nu_{res.} &= E_{3,-2} - E_{3,-3} \\ &= -g_I \mu_N B_0 + \frac{h\nu_{hf}}{2}\left[\sqrt{1 - \frac{4}{3}x + x^2} - \sqrt{1 - 2x + x^2}\right] \end{aligned} \quad (5.36)$$

with $x = \frac{g_J\mu_B + g_I\mu_N}{h\nu_{hf}}\ \mathrm{B}_0 \simeq \frac{g_J\mu_B}{h\nu_{hf}}\ \mathrm{B}_0$ since $\frac{g_I\mu_N}{g_J\mu_B} \simeq \frac{1}{1800}$.

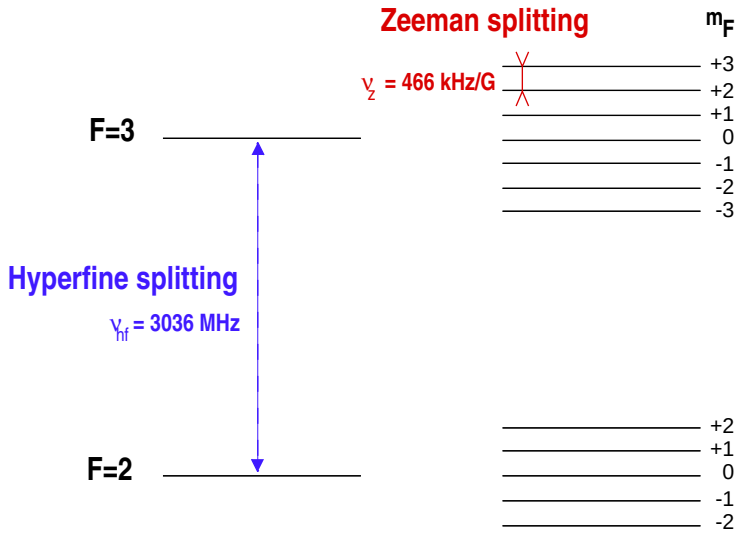


**Figure 5.12:** Energy levels of $^{85}$Rb.

$B_0$ can be found by solving Eq. (5.37) with $x = 9.2297 \cdot B_0(\text{Gauss})$.

$$\frac{\nu_{res.}}{\nu_{hf}} = \frac{1}{6}x + \frac{5}{36}x^2 + \frac{1}{6}x^3 - \frac{1}{16}x^4 + O(x^5) \tag{5.37}$$

### Determination of the EPR constants

The EPR constant is defined from Eq. (5.32) by:

$$\kappa_{\text{EPR}} = \frac{2}{3}\mu_0 \frac{\mathrm{d}\nu_{\text{EPR}}(\mathrm{F}, \Delta \mathrm{m_f})}{\mathrm{dB}} \kappa_0 \mu_{^3\text{He}}[^3\text{He}] \tag{5.38}$$

with [Korsch, 1998]:

$$\frac{\mathrm{d}\nu_{\text{EPR}}(3, -2 \leftrightarrow -3)}{dB} = 0.4671 + 0.0007B \tag{5.39}$$

For each EPR measurement, the pumping chamber temperature and density are calculated as in section 5.3. The holding field magnitude, the pumping

chamber temperature and density, as well as the EPR constant $\kappa_{\mathrm{EPR}}$ for each EPR measurement, are shown in Fig. 5.13.

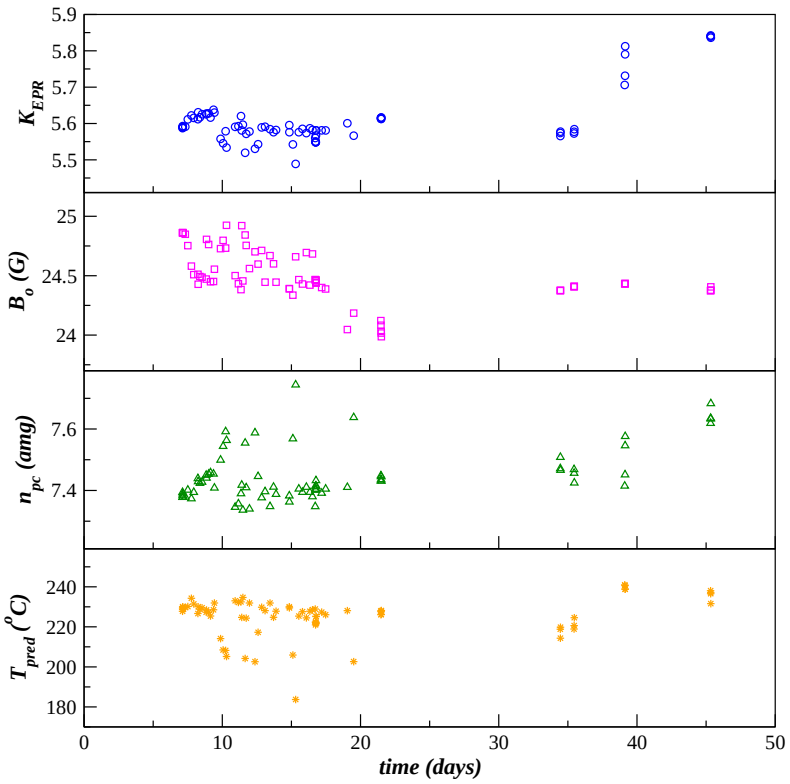


**Figure 5.13:** EPR constants $\kappa_{EPR}$ for each EPR measurement (top plot). Also plotted are the holding field $B_0$, the density $n_{pc}$ and the temperature predicted $T_{pred}$ inside the pumping chamber.

### Polarization gradient

EPR polarimetry measures the polarization in the pumping chamber. In order to obtain the polarization in the target chamber, a model [Romalis, 1997]

was created to evaluate the polarization gradient between the two chambers.

Assuming that the flux in the presence of a temperature gradient is constant and that the temperature varies linearly along the transfer tube, the polarization gradient can be expressed from the following diffusion rates:

$$\frac{dP_T}{dt} = d_P(P_T - P_P) + \gamma_{SE}(P_{Rb} - P_P) - \Gamma_P P_P \tag{5.40}$$

$$\frac{dP_P}{dt} = d_T(P_P - P_T) - \Gamma_T P_T \tag{5.41}$$

$P_T$ and $P_P$ are the target and pumping chamber polarizations. $\Gamma_T$ is the total relaxation rate under running conditions. The reduced diffusion constants $d_P$ and $d_T$ are expressed as follows:

$$d_P = \frac{A_{tr} D_T}{V_T L_{tr}} K \tag{5.42}$$

$$d_T = \frac{A_{tr} D_T n_T}{V_P L_{tr} n_P} K \tag{5.43}$$

with $A_{tr}$ anf $L_{tr}$ the cross sectional area and the length of the transfer tube. $D_T$ is the diffusion coefficient of $^3$He along the transfer tube:

$$D_T = D(T_0)\frac{n_0}{n_T}(\frac{T_T}{T_0})^{m-1} \tag{5.44}$$

$D(T_0) = 2.76$ cm$^2$/s at 80°C and $n_0 = 0.773$ amg, $m = 1.7$. The dimensionless constant K is given by:

$$K = \frac{(m-2)(T_T - T_P)T_T}{(T_T/T_P)^m T_P^2 - T_T^2} \tag{5.45}$$

There are two methods to calculate the change of polarization between the pumping and the target chambers: the static solution assumes that the diffusion between the two chambers is at equilibrium during the EPR measurement, contrary to the dynamic solution. It has been shown [Zheng, 2002] that

the results from these two methods differ by about half a percent. Therefore, the first scenario will be used in the analysis. The equilibrium solution ($dP_T/dt = 0$) can be derived from Eq. (5.14):

$$P_T = \frac{1}{1 + \frac{\Gamma_T}{d_T}} P_P \tag{5.46}$$

The spin relaxation rate in the target chamber $\Gamma_T$ under running conditions can be extracted from the spindown equation Eq. (5.10), the $^3$He-$^3$He magnetic dipolar relaxation rate evaluated at the running density, the beam ionization and with the assumption that the wall relaxation is the same at room temperature and under operation conditions. Thus:

$$\Gamma_T^{running} = \frac{1}{\tau} + \Gamma_{dip}^{running} + \frac{I}{362} \tag{5.47}$$

Using the cell characteristics of Table 5.2, the gradient of polarization be-

| Quantities | Duke | Exodus |
|---|---|---|
| $\tau$ (h) | 52.6 | 49.5 |
| $n_0$ (amg) | 9.18 | 9.62 |
| $V_P$ ($cm^3$) | 113.8 | 103.9 |
| $V_T$ ($cm^3$) | 82.6 | 84.7 |
| $dB_z/dz$ (mG/cm) | 7.6 | 7.8 |

**Table 5.2:** Cell characteristics needed in the polarization gradient calculation.

tween the pumping chamber and the target chamber is calculated for each EPR measurements (Fig. 5.14). The average pumping and target chambers polarizations are given in Table 5.3 with respect to the three beam currents

at which the experiment was running at the time of the EPR measurements.

| Average polarization | I=5$\mu$A | I=10$\mu$A | I=12$\mu$A |
|---|---|---|---|
| $\langle P_P \rangle$ (%) | 35.10 | 36.00 | 35.61 |
| $\langle P_T \rangle$ (%) | 34.14 | 34.64 | 34.14 |
| diff (% rel.) | 2.8 | 3.8 | 4.2 |

**Table 5.3:** Average pumping chamber polarizations from EPR measurements with respect to the beam current. The target chamber polarizations are evaluated from the polarization gradient model.

The polarization gradient makes a significant correction of 3.6% on average.

## 5.5 Target polarization performance

### 5.5.1 Target polarization from NMR measurements

The polarization of the $^3$He target can be determined from the water calibration and Eq. 5.27 as follows:

$$P(t) = C_W S(t) \tag{5.48}$$

The water calibration constant $C_W$ is determined by:

$$C_W = \frac{1}{c'_W \Phi_{^3\mathrm{He}} n_T} \tag{5.49}$$

where $c'_w$ is a constant proportional to the NMR signal height of water and to the characteristics of the water cell [Sulkosky, 2006]. Here, $\Phi_{^3\mathrm{He}}$ is the flux

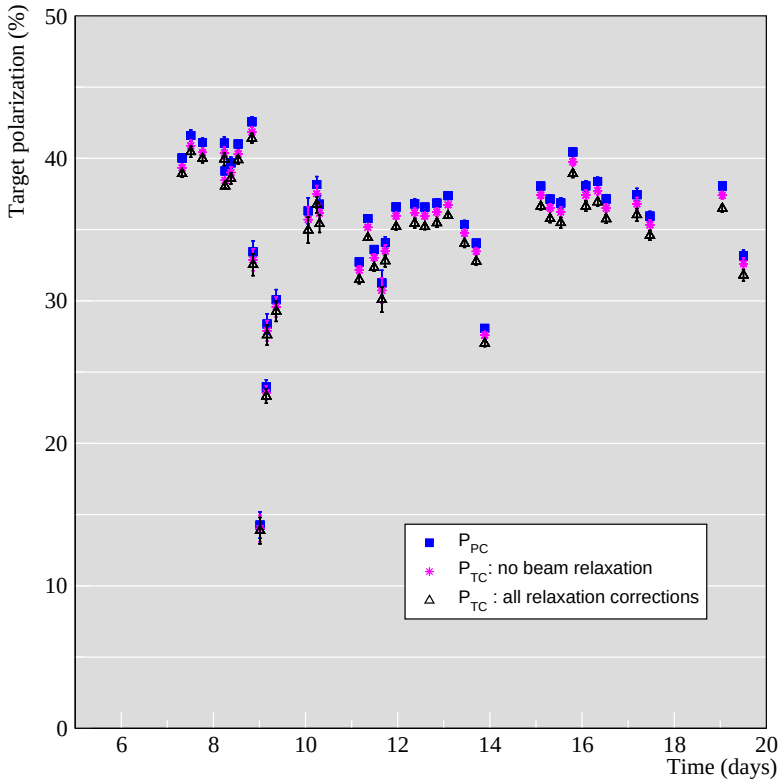


**Figure 5.14:** Target chamber polarization from EPR. The blue squares are the pumping chamber polarizations. The magenta stars correspond to effect of the polarization gradient assuming no beam. The beam depolarization effect is included for the black triangles.

of the polarized $^3$He target felt by the pick-up coils, and $n_T$ is the density in the target chamber.

The results for $c'_W$ and $\Phi_{tot}$ are given in Table 5.4

For the cell *Exodus*, the pick-up coils were slightly displaced. Since $c'_W$ is proportional to the water flux, it needs to be corrected as well as $\Phi_{^3\mathrm{He}}$. So two different sets of parameters are used for *Exodus* in the NMR analysis.

| Period | Cell | $c'_W$ (mV cm$^{-2}$ amg$^{-1}$) | $\Phi_{^3\mathrm{He}}$ (cm$^2$) |
|---|---|---|---|
| 01/04 - 02/06 | Duke | 0.07265 $\pm$ 0.00072(stat.) $\pm$ 0.00168(syst.) | 38.67 $\pm$ 0.65 |
| 02/07 - 02/10 | Exodus | 0.07258 $\pm$ 0.00072(stat.) $\pm$ 0.00191(syst.) | 40.39 $\pm$ 0.78 |
| 02/10 - 02/14 | Exodus | 0.07279 $\pm$ 0.00072(stat.) $\pm$ 0.00160(syst.) | 37.92 $\pm$ 0.70 |

**Table 5.4:** Water calibration constants and polarized $^3$He fluxes.

The target chamber density $n_T$ was extracted as described in Section 5.3 at the time of a NMR measurement. The total uncertainty of the target density is 2.65% under running conditions. Considering all these parameters, the average target polarization for each period can be calculated, and the results are listed in Table 5.5.

| Period | Cell | $P_T \pm stat. \pm syst.$ |
|---|---|---|
| 01/04 - 02/06 | Duke | 37.61 $\pm$ 0.09 $\pm$ 1.53 |
| 02/07 - 02/10 | Exodus | 39.76 $\pm$ 0.09 $\pm$ 1.71 |
| 02/10 - 02/14 | Exodus | 41.25 $\pm$ 0.10 $\pm$ 1.67 |

**Table 5.5:** Average over the NMR measurements of the target polarization (the uncertainties are absolute).

### 5.5.2 Target polarization from EPR measurements

The dominant systematic uncertainty of the EPR polarimetry comes from the EPR constant in Eq. (5.38). The density uncertainties are the same as for the NMR measurement in the previous section. The measurement of $\kappa_0$ [Romalis, 1998] has an accuracy of 1.5%. The uncertainty of $d\nu_{\mathrm{EPR}}/dB$ comes from the external field which enters in Eq. (5.39) as a correction which

is three orders of magnitude smaller than the nominal quantity. Therefore it can be safely neglected. The polarization gradient is also a small correction compared to the total polarization, so its uncertainty is also neglected. The average polarizations from EPR in the pumping chamber and in the target chamber are given in Table 5.5.

| Period | Cell | $P_P \pm stat. \pm syst.$ | $P_T \pm stat. \pm syst.$ |
|---|---|---|---|
| 01/04 - 01/19 | Duke | 35.69 ± 0.39 ± 1.09 | 34.46 ± 0.38 ± 1.05 |

**Table 5.6:** Average over the EPR measurements of the target polarizations (the uncertainties are absolute).

After the first two weeks of the experiment, large depolarizations were triggered by EPR measurements. This phenomenon is called masing and can be cancelled by creating field gradients around the pumping chamber [Romalis, 1997]. An EPR measurement featuring strong masing is shown in Fig. 5.15. In consequence, the target chamber polarization $P_T$ from Table 5.6 should be compared to the average polarization from NMR measurements taken during the same period which is: $P_T$= 36.25 ± 0.09 ± 1.53 %. The two polarimetries agree within the error bars. The final results for EPR and NMR measurements are plotted in Fig. 5.16.

### 5.5.3 Interpolation of the polarization

Small polarization losses occur during polarimetry, and whenever the target field direction is changed. Corrections for these effects are applied to each

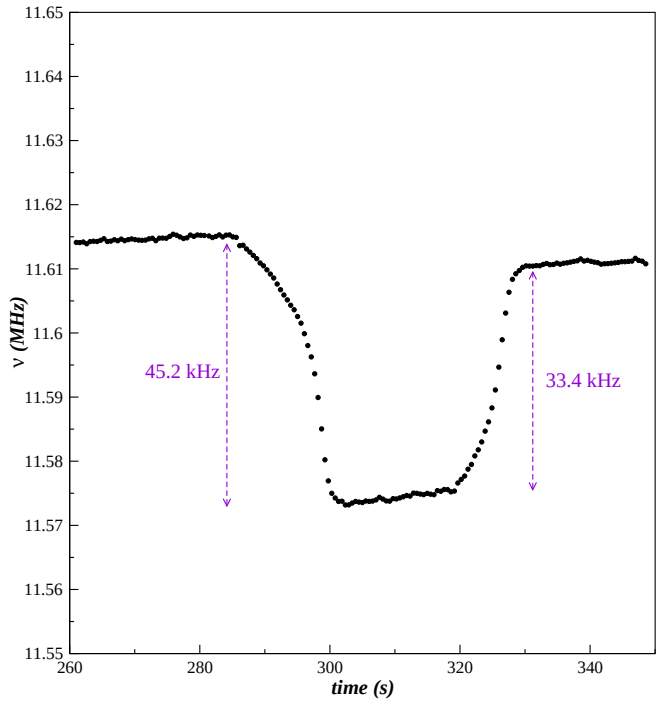


**Figure 5.15:** EPR measurement spectrum showing strong masing

EPR and NMR measurement before interpolating the target polarization between polarimetry measurements. The AFP and rotational losses (Table 5.7) were estimated by a series of tests done before and after the experiment.

| | NMR | EPR |
|---|---|---|
| AFP loss | 0.047 mV | 0.52 kHz |
| Rot. loss | 0.026 mV | 0.15 kHz |

**Table 5.7:** AFP and rotational losses from EPR and NMR measurements. The AFP losses are given per measurement. The rotational loss is per rotation of 90°

Finally, the polarization evolution during the experiment is extracted

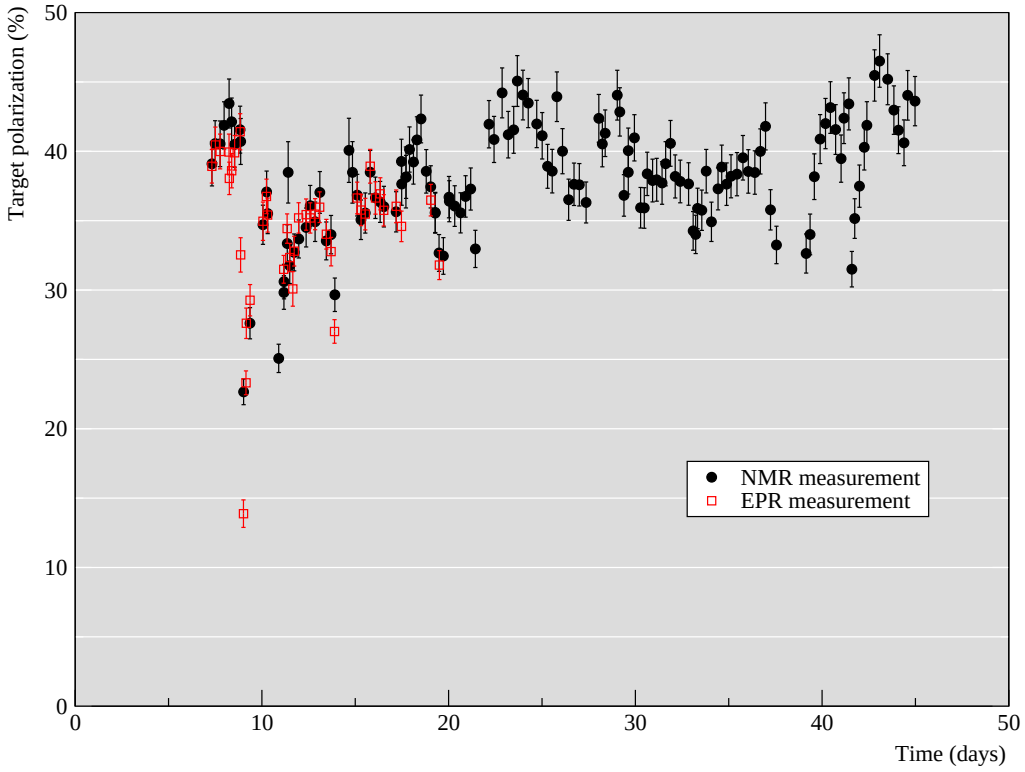


**Figure 5.16:** Target polarization from EPR and NMR during the experiment E01-012.

from the average of corrected EPR and NMR measurements (when both are available at the same time) by performing a linear interpolation between measurements. Fig. 5.17 shows the resulting target polarizations used in the physics analysis.

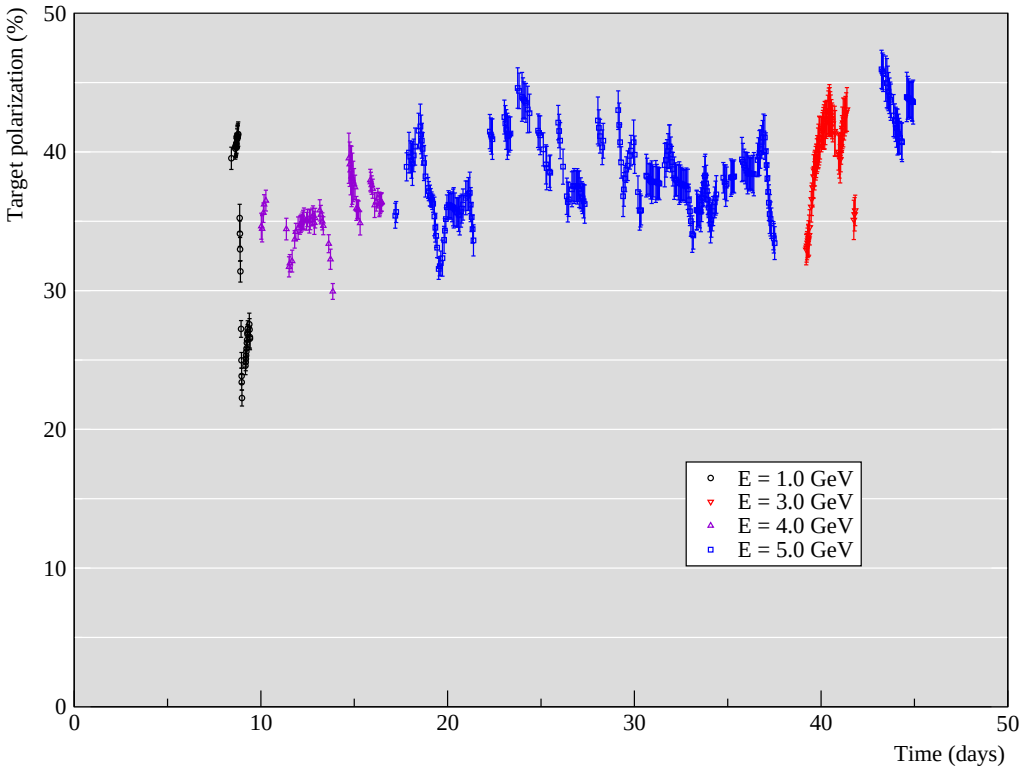


**Figure 5.17:** Interpolation of the target polarization to each period of data taking.

# CHAPTER 6

# DATA ANALYSIS

In order to extract the relevant physical quantities, many analysis steps are necessary to discriminate between good electron events and unwanted background. This background is mostly composed of negative charged pions, low energy electrons and high energy cosmic rays. To qualify as a good event, the scattered particle has to pass several selection criteria. This chapter will review in detail the selection of good events and the different data quality checks.

## 6.1 From raw data to physics asymmetries and cross sections

The raw asymmetries are calculated as follows:

$$A_{\|,\perp}^{raw} = \frac{\frac{d^2\sigma^{\downarrow\Uparrow}}{d\Omega dE'} - \frac{d^2\sigma^{\uparrow\Downarrow}}{d\Omega dE'}}{\frac{d^2\sigma^{\downarrow\Uparrow}}{d\Omega dE'} + \frac{d^2\sigma^{\uparrow\Downarrow}}{d\Omega dE'}} = \frac{\frac{N^+}{Q^+LT^+} - \frac{N^-}{Q^-LT^-}}{\frac{N^+}{Q^+LT^+} + \frac{N^-}{Q^-LT^-}} \tag{6.1}$$

where $N^{+(-)}$ are the number of good events within the acceptance and the detector cuts for which the incident electron helicities were +1(-1). $Q^{+(-)}$ is the total charge of helicity +1(-1) and $LT^{+(-)} = 1 - DT^{+(-)}$, with $DT^{+(-)}$ the helicity dependent data acquisition deadtime for incident electrons.

The experimental asymmetries are generated by correcting the raw asymmetries for the nitrogen dilution and for the target and beam polarizations:

$$A_{\parallel,\perp}^{exp} = \frac{1}{f\ P_t\ P_b} A_{\parallel,\perp}^{raw} \tag{6.2}$$

with

$$f = 1 - \frac{\rho_{\mathrm{N}_2}}{\rho_{\mathrm{N}_2} + \rho_{^3\mathrm{He}}}\ \sigma_{\mathrm{N}_2} \tag{6.3}$$

After applying internal and external radiative corrections, the Born asymmetries are:

$$A_{\parallel,\perp}^{Born} = A_{\parallel,\perp}^{exp} + \Delta A_{RC}^{int} + \Delta A_{RC}^{ext} \tag{6.4}$$

The unpolarized raw cross sections can be written as follows:

$$\sigma^{raw} \equiv \frac{d\sigma^{raw}}{d\Omega dE'} = \frac{N}{(Q/e)\rho LT\epsilon_{det}}\ \sigma_{MC} \tag{6.5}$$

where $N$ is the number of scattered particles which passes the acceptance and detector cuts. $Q/e$ corresponds to the number of incident electrons of any helicity states. $\rho$ is the density of the target. $LT = 1 - DT$ with $DT$ the data acquisition deadtime. $\epsilon_{det}$ is the product of all the detector efficiencies, which corrects for the missing detections and for the (unwanted) removal of good electrons by the analysis cuts. The cross section must also be normalized by the spectrometer acceptance:

$$\sigma_{MC} = \frac{N_{MC}^{trial}}{N_{MC}^{acc} dE'_{MC} d\Omega_{MC}} \tag{6.6}$$

The non-uniformity of the field created by the spectrometer magnet induces a different angular and momentum acceptance from the one defined by the physical aperture. Therefore, a Monte Carlo simulation was used to produce random rays, and then check if the deflected rays pass to the spectrometer focal plane. This was done with knowledge of the magnetic transfer functions of each spectrometer and the physical placement of all apertures [Deur, 2000b]. The phase space obtained is then weighted by the Mott cross section. $N_{MC}^{trial}$ is the number of trial events of the simulation, $N_{MC}^{acc}$ is the number of events within the phase space and the acceptance cuts. $dE'_{MC}$ and $d\Omega_{MC}$ are the illuminated momentum and solid angle ranges, which are chosen to be larger than the actual ones.

The experimental cross section is obtained after subtracting the nitrogen contribution as follows:

$$\sigma^{exp} = \sigma^{raw} - \frac{\rho_{\rm N}}{\rho_{\rm N} + \rho_{^3{\rm He}}} \sigma_{\rm N} \tag{6.7}$$

with $\rho_{\rm N}$ and $\rho_{^3{\rm He}}$ the atomic density of nitrogen and $^3$He respectively, and $\sigma_{\rm N}$ the nitrogen cross section.

The unpolarized Born cross section is generated after internal and external radiative corrections:

$$\sigma^{Born} = \sigma^{exp} + \Delta\sigma^{int} + \Delta\sigma^{ext} \tag{6.8}$$

The experimental polarized cross section differences can be expressed from Eq. (6.1), and from the experimental asymmetries and cross sections as

follows:

$$\Delta\sigma^{exp}_{\parallel,\perp} = 2A^{exp}_{\parallel,\perp}\ \sigma^{exp} \tag{6.9}$$

and after radiative corrections, the polarized cross section differences become:

$$\Delta\sigma^{Born}_{\parallel,\perp} = \Delta\sigma^{exp}_{\parallel,\perp} + \delta(\Delta\sigma_{\parallel,\perp})^{int} + \delta(\Delta\sigma_{\parallel,\perp})^{ext} \tag{6.10}$$

The radiative correction procedure is explained in detail in Appendix A.

## 6.2 Spectrometer optics

The position and momentum reconstruction of an event from the spectrometer focal plane to the vertex is done by using the Transport tensor. Using the optical properties of the spectrometer magnets, the quantities in the focal plane coordinate system can be related to quantities in the target coordinate system. In the first order approximation and because of the mid-plane symmetry of the spectrometer, the optics matrix can be written as [Liyanage, 2002]:

$$\begin{bmatrix} \delta_{tg} \\ \theta_{tg} \\ y_{tg} \\ \phi_{tg} \end{bmatrix} = \begin{bmatrix} \langle\delta|x\rangle & \langle\delta|\theta\rangle & 0 & 0 \\ \langle\theta|x\rangle & \langle\theta|\theta\rangle & 0 & 0 \\ 0 & 0 & \langle y|y\rangle & \langle y|\phi\rangle \\ 0 & 0 & \langle\phi|y\rangle & \langle\phi|\phi\rangle \end{bmatrix} \begin{bmatrix} x_{fp} \\ \theta_{fp} \\ y_{fp} \\ \phi_{fp} \end{bmatrix} \tag{6.11}$$

The optics matrix elements were determined using elastic data taken on seven carbon foils aligned under the polarized $^3$He target and a sieve slit

inserted as a collimator at the spectrometer entrance. The sieve slit hole positions and the carbon foil positions were surveyed before the experiment. The seven carbon foils allow the determination of the variable $y_{tg}$, the sieve slit pattern maps the $\theta_{tg}$-$\phi_{tg}$ plane, and the elastic peak gives the momentum resolution $\delta_{tg}$.

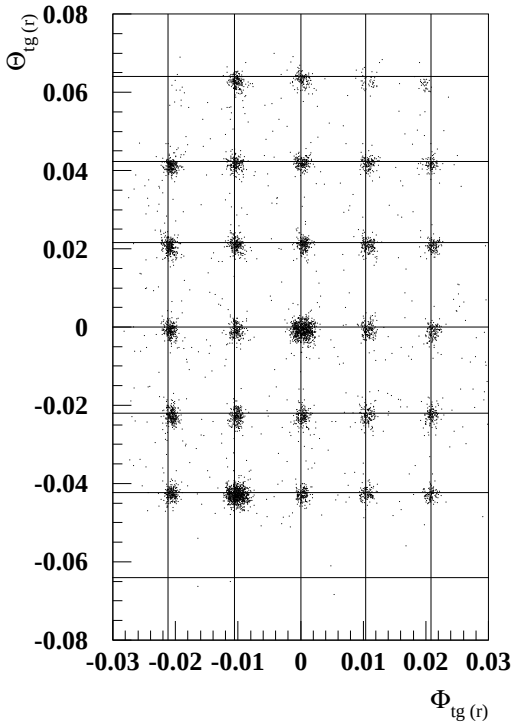


**Figure 6.1:** Sieve slit hit pattern in the plane defined by the variables $\phi_{tg}$ and $\theta_{tg}$.

The sieve slit pattern can be seen in Fig. 6.1 with the crossing lines indicating the expected hole positions from the survey. The reconstructed carbon foil positions are shown in Fig. 6.2 with the lines indicating their

surveyed positions. The data from the carbon foil at 13.4 cm has not been included in the optimization due to lack of statistics, but it is also outside the acceptance cuts. The optimization is discussed in [Liyanage, 2005].

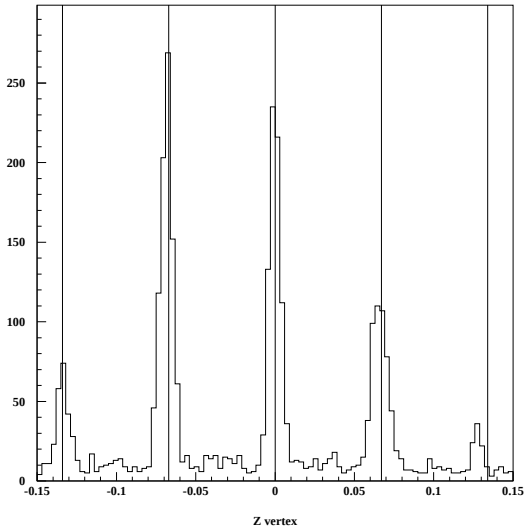


**Figure 6.2:** Reconstructed carbon foil positions.

## 6.3 Detectors

In the process of generating cross sections, the performance of the detectors has to be evaluated. As such, hardware and software efficiencies are studied in detail.

### 6.3.1 VDC analysis: one-track efficiency

The hardware efficiency of the VDCs is close to 100% [Alcorn, 2004]. However, inefficiency arises from no-track and multi-tracks events, which are generated by the software misreconstruction of particle tracks or the possibility of several particles crossing the wire chambers simultaneously. In the latter case, several trajectories become possible and it is difficult to discriminate between a good and a bad event. In the analysis only one-track events are kept, so the cross sections must be corrected for the missing events. This is called the one-track efficiency and can be calculated as follows:

$$\epsilon_1 = \frac{N_1}{\sum_i N_i} \tag{6.12}$$

where $i = 0, 1, 2, 3, 4$ is the number of tracks*.

In order to determine the one-track efficiency for good electrons, it is important to use the same cuts as for generating the cross sections. Therefore, only the main trigger events are kept. Cosmic rays are mostly removed by applying a cut on the speed of the particles called $\beta$-cut (see Section 6.3.2). Particle identification detector (PID) cuts† are set to reject more than 99% of background as explained in Section 6.3.3.

During the experiment, the one-track efficiency was better than 99% for both HRS VDCs (see Table 6.1 and Fig. 6.3). The uncertainty is taken to be

*The software reconstructs a maximum of 4 tracks.

†The shower variables used in this case are not the ones of the shower calibration. The variables of the shower calibration contain the tracking specifications which reject zero-track events.

equal to the multiple-track efficiencies (1%) since it is very likely that one of the multi-tracks is from a good electron.

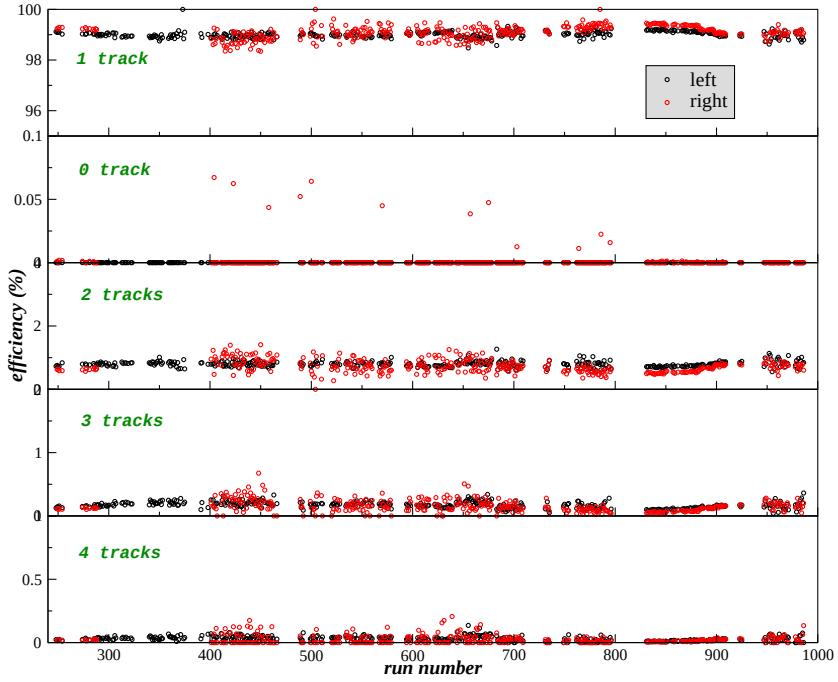


**Figure 6.3:** All track efficiencies for left and right HRS and for each run.

| # of tracks | $\epsilon$ (left HRS) | $\epsilon$ (right HRS) |
|---|---|---|
| 0 | $1.2 \times 10^{-6}$ | $1.4 \times 10^{-3}$ |
| 1 | 99.01 | 99.10 |
| 2 | 0.79 | 0.72 |
| 3 | 0.17 | 0.15 |
| 4 | 0.03 | 0.02 |

**Table 6.1:** Average tracking efficiency for the left and right HRS VDCs. The efficiency are in percent.

In the cross section analysis, the VDC efficiency for each run (= data

taking period) was evaluated: this is a good check of the VDC performance during the experiment, and runs with problems can be identified and excluded from the analysis.

### 6.3.2 Scintillator efficiency

Photo-multiplier tube inefficiency or inhomogeneity of the paddle plastic are the origin of the scintillator inefficiency. As explained in Section 6.3.2, there are two trigger types considered as good events. Only main triggers are kept in the analysis and secondary triggers are used to determine hardware inefficiency. The scintillator efficiency is:

$$\epsilon_{R,L} = \frac{T_i}{T_i + T_{i+1}} \tag{6.13}$$

where R(L) stands for right(left) HRS and $i = 1, 3$. The trigger type 1(3) and 2(4) are the main and secondary triggers for right(left) HRS

As in previous section, the efficiency is estimated for good electrons by considering only one-track events, removing the cosmic events with a $\beta$-cut and applying PID cuts defined in Section 6.3.3. Fig. 6.4 shows the scintillator efficiency for all runs. The efficiency is better than 99.8%. Therefore the number of events $T_2(T_4)$ inside the cuts are very small and excluding them has a negligible effect.

The speed of the electrons serve as a time basis to calibrate all the TDCs of the scintillators. Their speed is close to the speed of light so when generating the time-of-flight of the particles, a large peak at $\beta \simeq 1$ appears as in Fig 6.5.

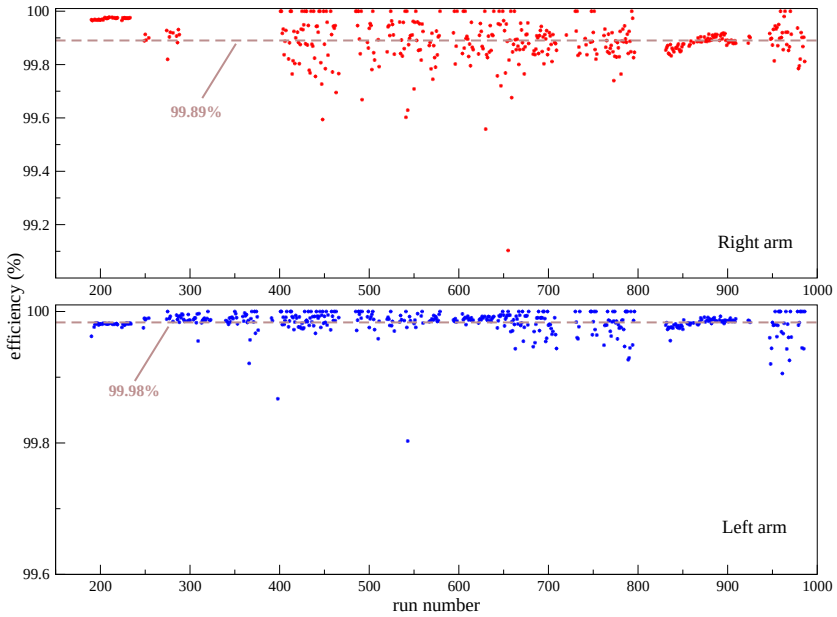


**Figure 6.4:** Scintillator efficiency for the right (top plot) and left (bottom plot) HRS. Only good electrons were selected.

The peak at $\beta \simeq -1$ represents mostly cosmic particles which travel at the speed of incident particles but in opposite direction. Therefore, a cut on positive $\beta$ allows to remove most of the comics.

### 6.3.3 Čerenkov efficiency

The $CO_2$ gas Čerenkov detector is a very powerful device to discriminate between electrons and pions. Due to its threshold, pions cannot trigger the detector. The first step in the Čerenkov analysis is the calibration of the ten ADCs linked to the ten PMTs. This consists of subtracting the pedestals

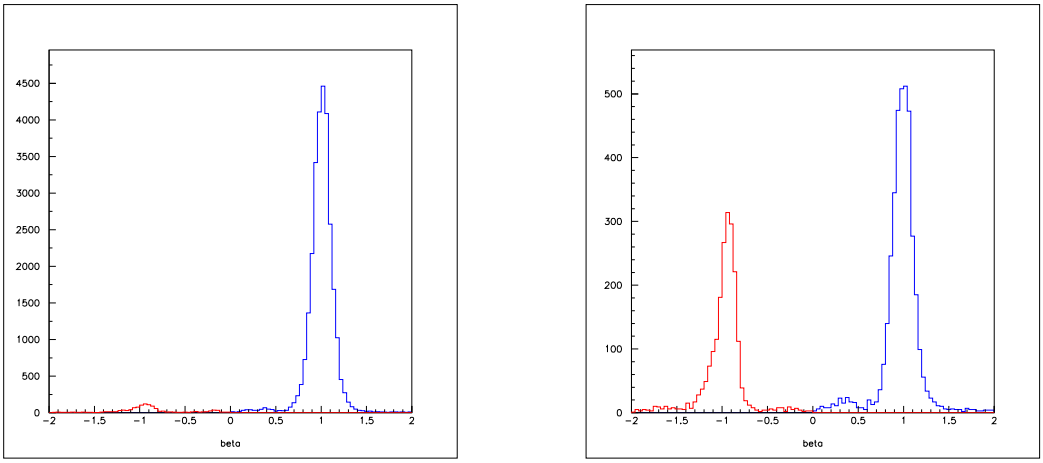


**Figure 6.5:** Particle velocity ($\beta$) for different kinematics: left and right plot kinematics have a rate of about 100 Hz and 20 Hz respectively. The cosmic contamination is shown in red. It can be seen that cosmic ray events are in proportion higher for low rate kinematics.

and then adjusting the gains in order to align the one-photo-electron peaks. We choose to align them at channel 200 as illustrated in Fig. 6.6. Once the calibration is done, all ADC spectra are added together and the detection and cut efficiencies are evaluated on the sum. More details about the Čerenkov calibration can be found in [Solvignon, 2004a].

To determine the detection efficiency of the Čerenkov detectors, a low pion run is selected: E = 3.028 GeV, $P_0$ = 2.150 GeV/c, $\theta = 25^\circ \Rightarrow$ W = 1.142 GeV (threshold for production of pions is at W = 1.08 GeV). With the help of the already calibrated shower counters, an electron sample is selected (as in Fig. 6.7, but with an even tighter cut). The number of events selected in this cut is called $n_{sh}$ and the number of these events that triggered the

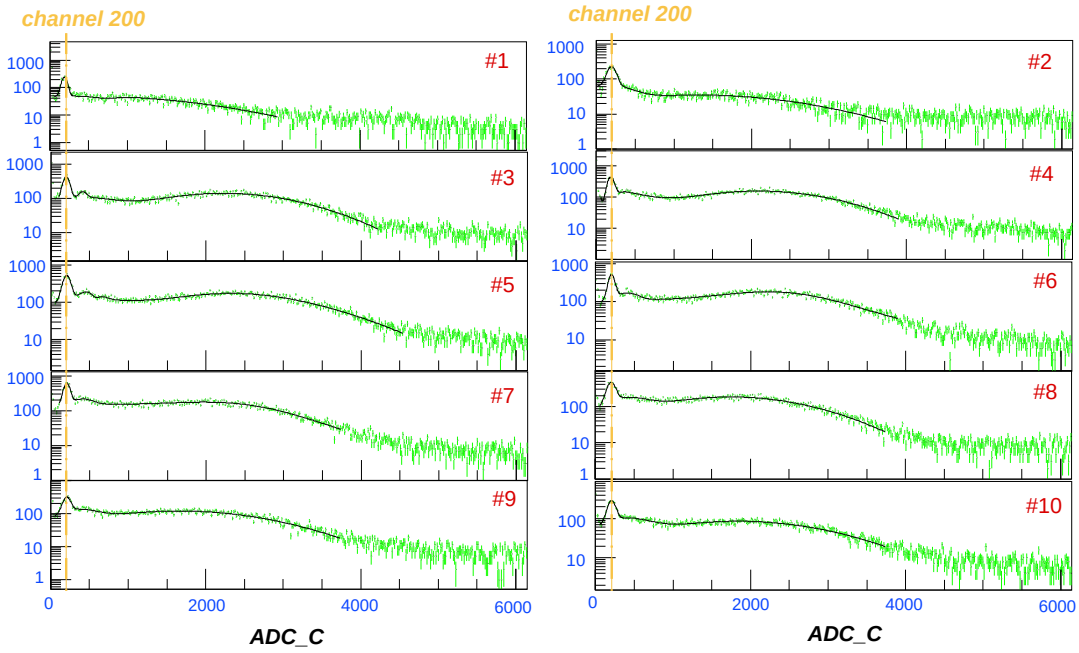


**Figure 6.6:** Single photo-electron peaks aligned at channel 200 (left arm).

Čerenkov detector is $n_{cer}$. Then the detection efficiency can be written as:

$$\epsilon_{det} = \frac{n_{cer}}{n_{sh}} \tag{6.14}$$

The detection efficiency is found to be 99.99% for the right HRS Čerenkov detector and 99.98% for the left.

The goal of the PID analysis is to reject as much of the background particles as possible while keeping a high electron efficiency. To estimate the loss of electrons due to the cut, pions and electrons are selected in the two-dimensional shower plot and then their distributions are observed in the Čerenkov spectrum as in Fig. 6.7.

The single photo-electron peak comes mostly from knock-on electrons,

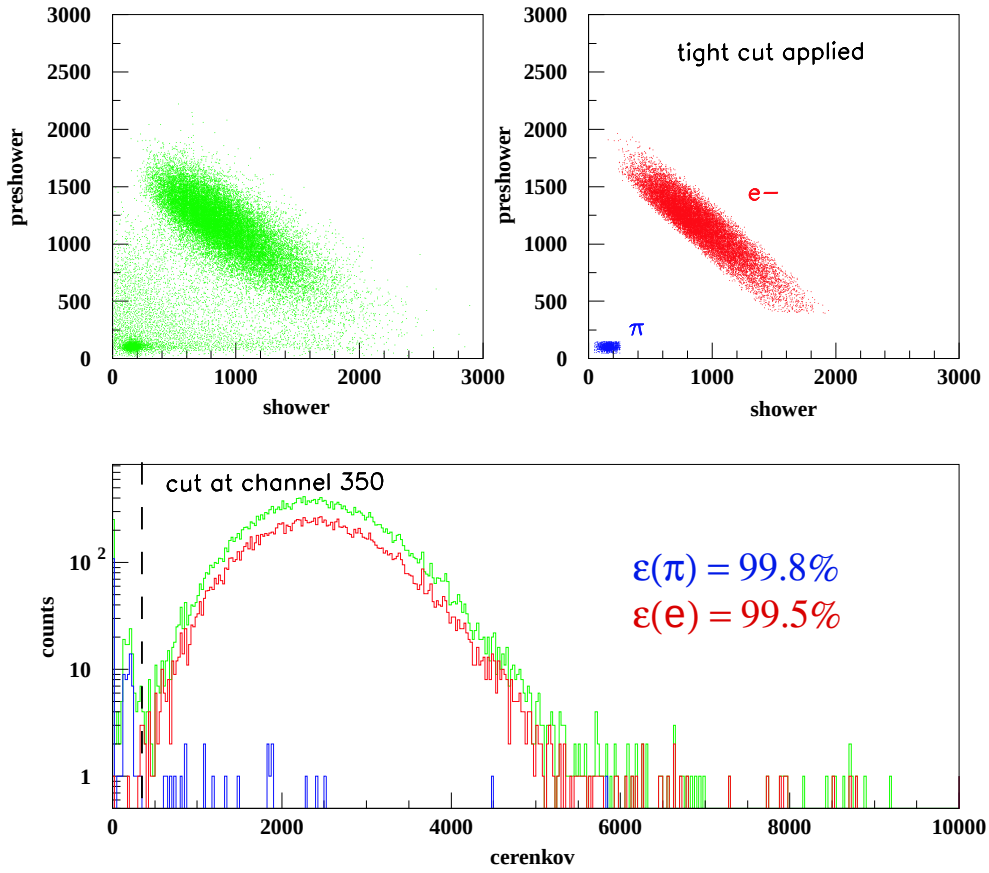


**Figure 6.7:** Left HRS Čerenkov cut efficiency study. The top left plot represents all the events in the two-dimensional shower plan. On the top right plot, pion and electron samples are selected. Their distributions in the Čerenkov spectrum are observed (bottom plot). Here a cut at channel 350 is applied.

which are low energy electrons produced by pions interacting with the medium [Deur, 1998]. Therefore it needs to be cut out in the analysis. Fig. 6.8 shows the evolution of the electron cut efficiency and pion rejection efficiency as a function of the cut applied on the Čerenkov. The electron detection efficiency

was found to better than 99.5% for a cut position at channel 350.

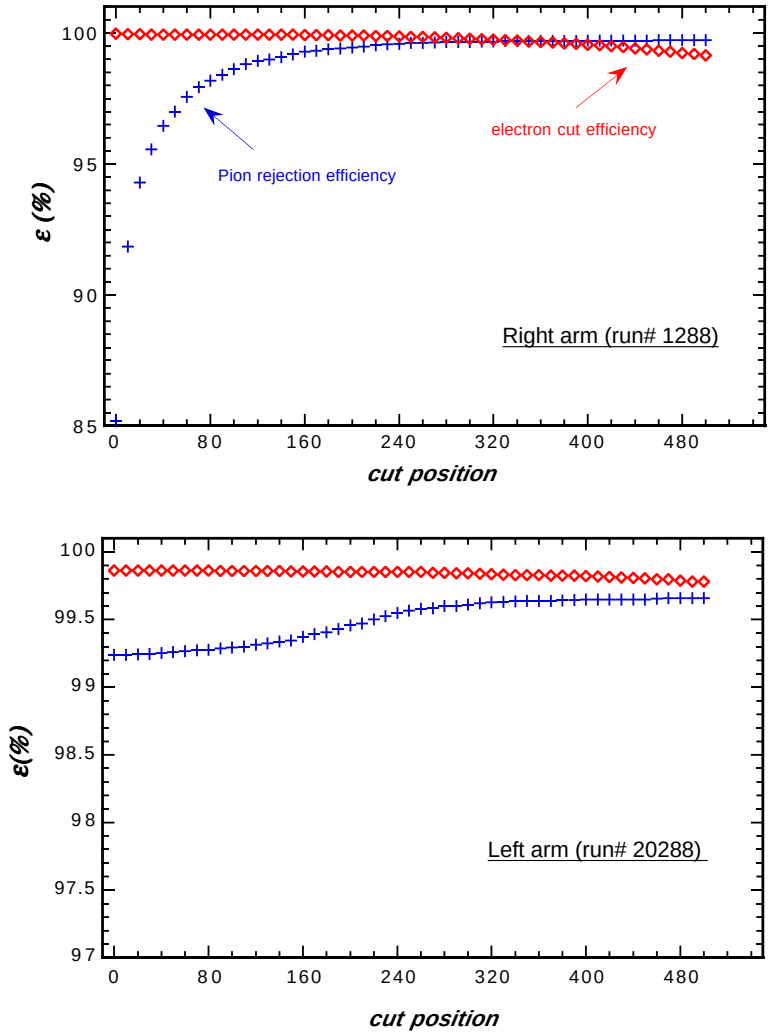


**Figure 6.8:** Čerenkov electron efficiency as a function of the cut position for a typical run. Also plotted is the pion rejection efficiency.

### 6.3.4 Electromagnetic calorimeter efficiency

A plot of the ratio of the energy as measured in the calorimeter divided by the momentum as measured in the spectrometer (E/P) can be used as a measurement of the resolution of the calorimeter. New shower calibrations were generated when the $E/P$ peak positions and widths deviated too much from the expected value. $E$ represents the total energy deposit by the incident particle in the layer of the calorimeter with $P$ its momentum. Due to multiple hardware problems, several calibrations were needed.

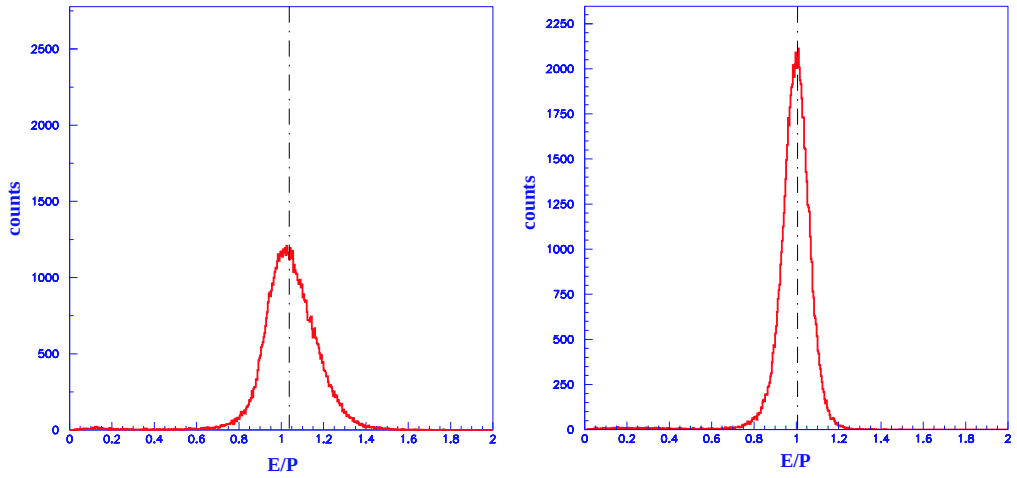


**Figure 6.9:** E/P peaks for right (total shower) and left (pion rejector) HRS after a cut on the Čerenkov to remove most of the pions.

Fig. 6.9 shows the $E/P$ peaks for electrons (a cut on the Čerenkov has been applied to separate electrons from pions). Data from both spectra are from the same run indicating clearly the lower resolution of the pion rejector. When looking at all kinematic settings, the resolution of the calorimeter can

be extracted by fitting the widths of each electron peak. During E01-012, the total shower had a resolution of 6.7% (see Fig. 6.11) and the pion rejector 10% (see Fig. 6.10).

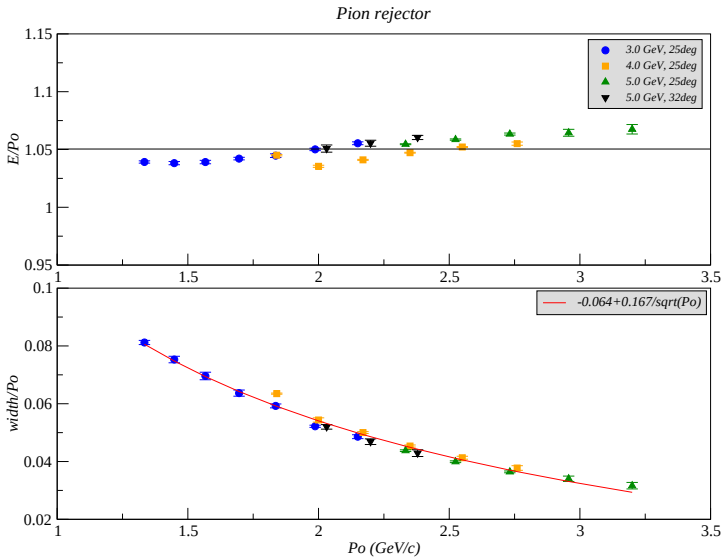


**Figure 6.10:** Pion rejector calibration: peak position and width from the gaussian fit of the E/P plot for each kinematic setting.

In order to determine the detection efficiency of the calorimeters, a tight cut is applied on the main peak of the Čerenkov spectrum. The number of events in this cut is called $\eta_{cer}$. Then the number of these events that triggered both layers of the EM calorimeter is counted ($\eta_{sh}$) and the detection efficiency can be determined by:

$$\epsilon_{det} = \frac{\eta_{sh}}{\eta_{cer}} \tag{6.15}$$

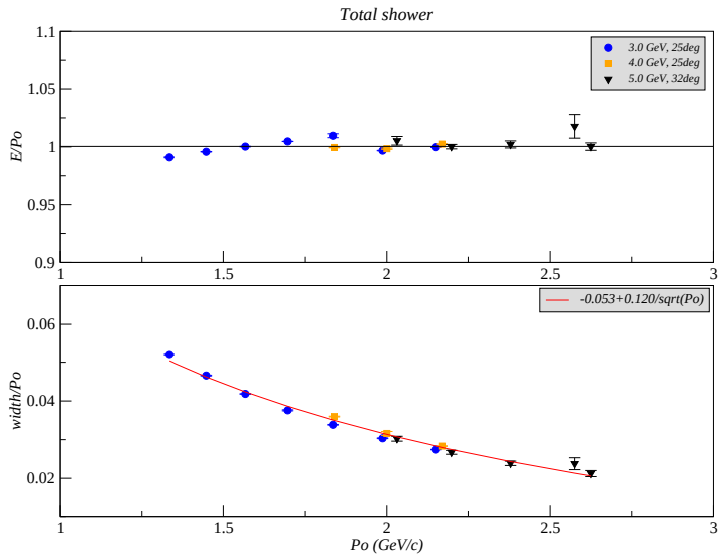


**Figure 6.11:** Total shower calibration: peak position and width from the gaussian fit of the E/P plot for each kinematic setting.

It was found that $\epsilon_{det} = 99.67\%$ for the pion rejector and $\epsilon_{det} = 99.76\%$ for the total shower. Because of some hardware problems, the right HRS preshower has to be excluded from the cross section analysis for most of the kinematics. The shower alone has a detection efficiency of 99.89%.

To complement the Čerenkov cut, the PID analysis can be improved by applying cuts on the electromagnetic calorimeters. To discriminate between electrons and pions, a Čerenkov or anti-Čerenkov cut is applied. Then a two-step method is used as in [Slifer, 2000]: cuts on E/P spectrum and on the two-dimensional shower plot (or the two-dimensional pion rejector plot) are optimized in order to get a total efficiency greater than 99% as illustrated in Fig. 6.12.

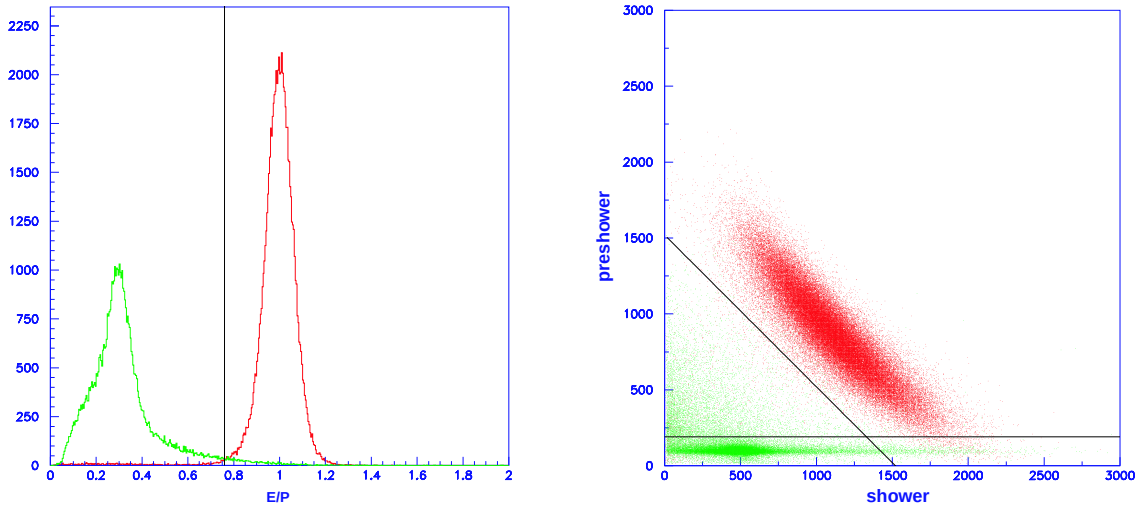


**Figure 6.12:** Cuts on the right HRS calorimeter: electrons (in red) and pions (in green).

By combining the Čerenkov detector with the electromagnetic calorimeter, the $\pi/e^-$ ratio can be reduced by a factor of about $10^4$ [Solvignon, 2004b] while keeping the electron efficiency better than 99% when no hardware problems occurred. Otherwise, the pion contamination is at a $10^{-3}$ level and affects only the cross section analysis. But removing the preshower from the asymmetry analysis would have induced an increase of pion contamination at a level of 1 pion for 100 electrons. The pion asymmetries being a lot larger than the electron asymmetries (see Fig. 6.23), it is crucial to have good pion rejection. However the two high inefficient preshower blocks creates holes in the acceptance and therefore glitches can be observed in the yield as in Fig. 6.13. Therefore PID cuts are different for asymmetry and cross section analyses.

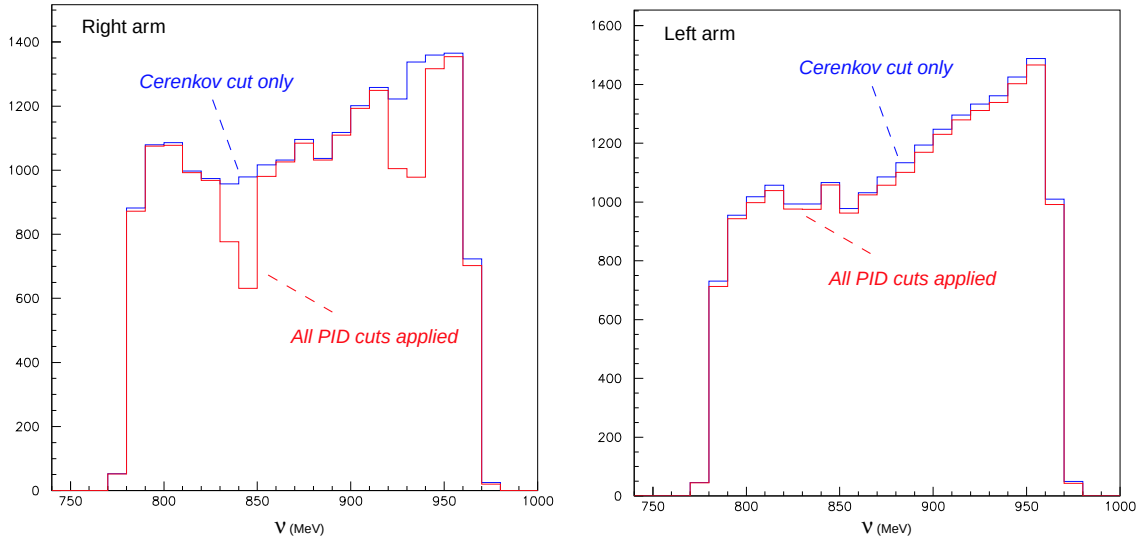


**Figure 6.13:** Yield versus energy transfer ($\nu$). The left plot shows inefficiency caused by the preshower cut. The blue histogram has only Čerenkov cut applied and the red histogram has all PID cuts applied. The left HRS yields are shown as a reference.

## 6.4 $^3$He elastic scattering

The unpolarized elastic scattering cross section can be written as a function of the charge and magnetic form factors as follows [Amroun, 1994]:

$$\sigma_0^{el} \equiv \frac{d\sigma}{d\Omega} = \sigma_{Mott}\ \frac{1}{\eta}\left[\frac{q^2}{|\vec{q}|^2}F_c^2(q) + \frac{\mu q^2}{2M^2}\left(\frac{1}{2}\frac{q^2}{|\vec{q}|^2} + \tan^2\frac{\theta}{2}\right)F_m^2(q)\right] \qquad (6.16)$$

$\mu$ is the $^3$He magnetic moment and $\eta$ is given by $1+q^2/4M^2$. $M$ is the mass of the target ($M_{^3\mathrm{He}} = 2809.4$ MeV). The $^3$He charge and magnetic form factors are known accurately from Ref. [Amroun, 1994]. The formalism used in unpolarized elastic scattering has already been introduced in Section 2.4.1.

In the case of polarized elastic scattering, the polarized cross section difference can be expressed from the formalism of Ref. [Donnelly, 1986] as follows:

$$\sigma_{el}^{\downarrow\Uparrow} - \sigma_{el}^{\uparrow\Uparrow} = -\sigma_{Mott}[V_{T'}R_{T'}(Q^2)\cos\theta^* + V_{TL'}R_{TL'}(Q^2)\sin\theta^*\cos\phi^*] \quad (6.17)$$

where $\theta^*$ and $\phi^*$ are the polar and azimuthal angle of the target spin with respect to $\vec{q}$. The response functions for a nucleus (A,Z) are functions of $F_c$ and $F_m$:

$$R_{T'}(Q^2) = \frac{2\tau E'}{E}(\mu F_m)^2 \quad (6.18)$$

$$R_{TL'}(Q^2) = -\frac{2\sqrt{2\tau(1+\tau)}E'}{E}(ZF_c)(\mu F_m) \quad (6.19)$$

and $V_{T'}$ and $V_{TL'}$ are kinematic factors:

$$V_{T'} = \tan\frac{\theta}{2}\sqrt{\frac{Q^2}{|\vec{q}^2|} + \tan^2\frac{\theta}{2}} \quad (6.20)$$

$$V_{TL'} = -\frac{Q^2}{\sqrt{2}|\vec{q}^2|} + \tan^2\frac{\theta}{2} \quad (6.21)$$

From Eq. (6.16) and Eq. (6.17), the elastic asymmetry can be written as:

$$A_{\|} = -\eta\frac{V_{T'}R_{T'}(Q^2)\cos\theta^* + V_{TL'}R_{TL'}(Q^2)\sin\theta^*\cos\phi^*}{\frac{q^2}{|\vec{q}|^2}F_c^2(q) + \frac{\mu q^2}{2M^2}(\frac{1}{2}\frac{q^2}{|\vec{q}|^2} + \tan^2\frac{\theta}{2})F_m^2(q)} \quad (6.22)$$

Therefore, by knowing the charge and magnetic form factors of $^3$He, the parallel asymmetry can be calculated theoretically and compared to the data.

This is a powerful tool to check the corrections applied to the physics asymmetries, such as the target and beam polarizations, and the nitrogen dilution.

The theoretical asymmetry of Eq. (6.22) is implemented in the Monte Carlo calculations, and the conditions of the experiment are simulated and applied to the theoretical asymmetry. This asymmetry is radiated by correcting for internal and external Bremsstrahlung and also ionization loss using the material thicknesses and conditions of the experiment. The result is a prediction of the experimental elastic asymmetry and cross section which can be directly compared to the data.

### 6.4.1 Elastic asymmetry

Data and simulation are generated with the same acceptance cuts. The cuts applied for the asymmetry analysis are listed in Table 6.2, where care was taken in removing the cell windows.

| variables | left arm | right arm |
|---|---|---|
| $y_{tg}$ (cm) | [-4;+3] | [-4;+3] |
| $\theta_{tg}$ (mrad) | [-60;+30] | [-30;+60] |
| $\phi_{tg}$ (mrad) | [-25;+25] | [-20;+30] |
| $dp$ (%) | [-4.5;+4.5] | [-4.5;+4.5] |
| $W - M$ (MeV) | [0;4.0] | [0;4.0] |

**Table 6.2:** Acceptance cuts used for the elastic asymmetry analysis.

The agreement between simulated quantities and the data is very good for both arms as can be seen in Fig. 6.14 and Fig. 6.15.

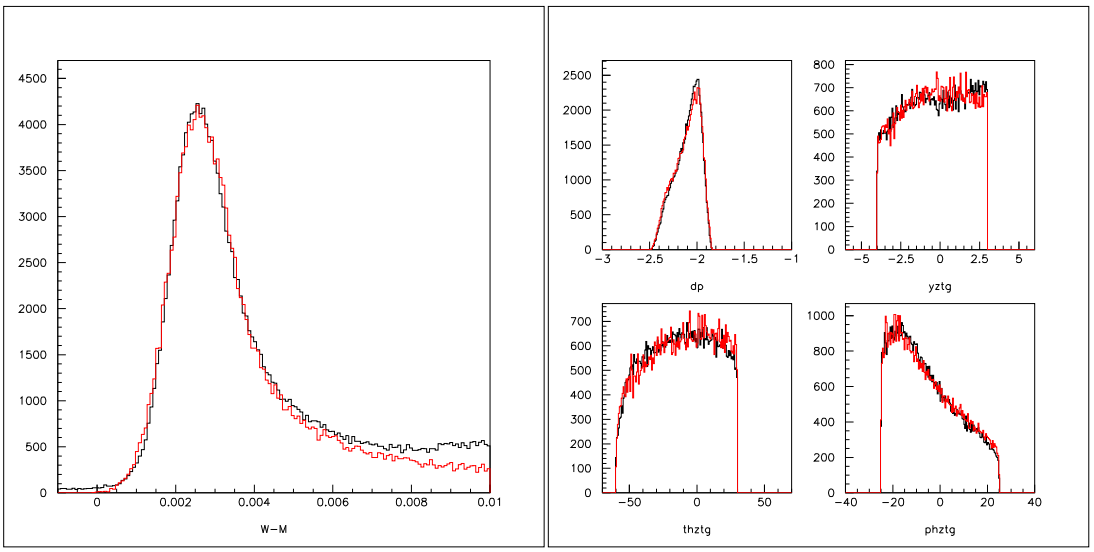


**Figure 6.14:** Comparison of the simulation (red) and the data (black) within the cuts defined in Table 6.2 for the left HRS. The left plot represents the elastic peak plotted as a function of $W_{^3\mathrm{He}} - M_{^3\mathrm{He}}$. The yield excess of the data at large $W_{^3\mathrm{He}} - M_{^3\mathrm{He}}$ is due to the quasi-elastic scattering contamination. The four plots on the right are spectra of $dp$ (top left corner), $y_{tg}$ (top right), $\theta_{tg}$ (bottom left) and $\phi_{tg}$ (bottom right).

In order to compare the simulated asymmetry to the data, detector cuts must be applied in order to remove the background which could contaminate the asymmetry. Moreover, the nitrogen contribution must be removed as indicated in Eq. (6.2). The nitrogen dilution is evaluated from data taken at the same kinematic but with a reference cell filled with nitrogen. The reference cell has physical properties very close to the polarized cell. From the nitrogen density and the yield of each cell, the dilution factor can be calculated as follows:

$$f_{\mathrm{N}_2} = 1 - \frac{n^{pol}_{\mathrm{N}_2}}{n^{pol}_{\mathrm{N}_2} + n^{pol}_{^3\mathrm{He}}} \frac{Y^{ref}_{\mathrm{N}_2}}{Y^{pol}} \tag{6.23}$$

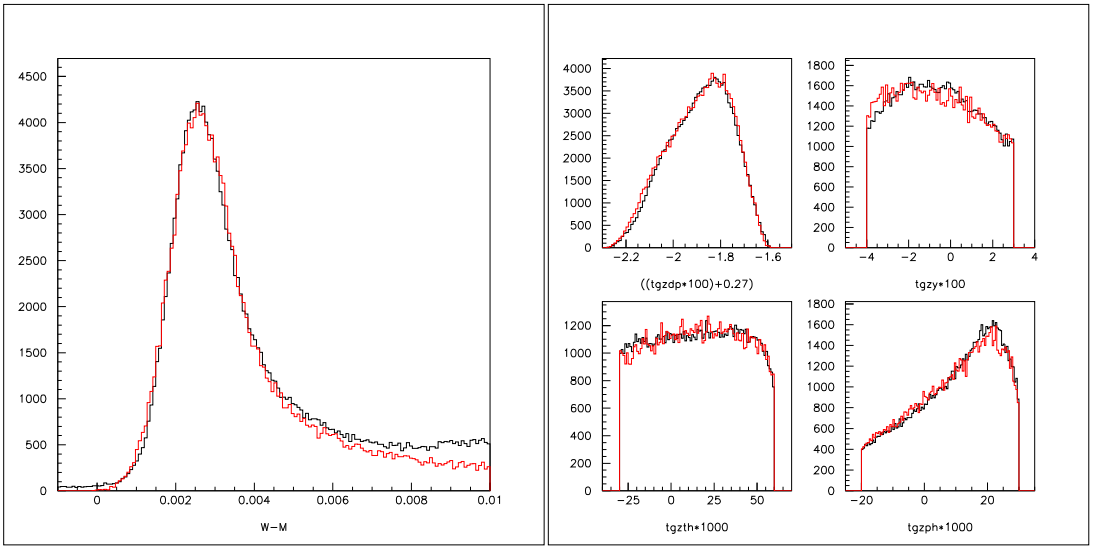


**Figure 6.15:** Same legend as for Fig. 6.14 for the right arm.

where $\sigma_0^{pol}$ is the $^3$He unpolarized cross section before nitrogen subtraction from the polarized $^3$He cell. $\sigma_{\mathrm{N}_2}^{ref}$ is the nitrogen unpolarized cross section from the reference cell. The nitrogen and $^3$He densities of the polarized cell, $n_{\mathrm{N}_2}^{pol}$ and $n_{^3\mathrm{He}}^{pol}$, are the filling densities since both densities are expected to be affected the same way under running conditions. The dilution factor is 0.976 for the left arm and 0.975 for the right arm.

The target and beam polarization corrections are applied to the data and the elastic asymmetry can be extracted. The dominant systematic uncertainties of the experimental elastic asymmetry come from the beam ($\pm$3.4%, see Table 4.2) and target polarization ($\pm$2.8%, see Fig. 5.17) and the nitrogen dilution has a maximum uncertainty of 0.6% [Solvignon, 2006a].

For the simulation, the uncertainties on the form factors for $Q^2 = 0.085$ (GeV/c)$^2$ are $\Delta f_m = \pm 0.002$ and $\Delta f_c = \pm 0.001$ [Amroun, 1994]. These

result in a $\pm 1.1\%$ uncertainty in the simulated parallel asymmetry. Then, after propagating the uncertainties from the beam energy ($\pm 0.5$ MeV, see Table 4.1), the spectrometer central angle ($\pm 0.06^{\circ}$, [Ibrahim, 2002]), the spectrometer central momentum ($\pm 0.5 \times 10^{-4}$, [Liyanage, 2001]), and the target spin angle ($\pm 0.1^{\circ}$, [JLab Alignment Group, 2003]), an additional $\pm 0.7\%$ contribution to the systematic errors is found. The radiative correction corresponds to a difference of $\pm 0.8\%$ between the radiated and the Born asymmetry. To be conservative, this value will also be taken as the radiative correction uncertainty. The uncertainties (see Table B.4) of the material thicknesses in the electron path has a negligible contribution to the systematic errors.

The final systematic errors on the simulated and experimental elastic asymmetries are 1.5% and 4.4%, respectively.

The results are listed in Table 6.3 and are plotted in Fig. 6.16. Data and simulation agree pretty well for the right HRS and even better for the left HRS..

| HRS | $A_{\parallel}^{data} \pm$ stat. $\pm$ syst. | $A_{\parallel}^{MC} \pm$ syst. |
|---|---|---|
| Left | $4.16 \pm 0.21 \pm 0.18$ | $4.16 \pm 0.06$ |
| Right | $3.92 \pm 0.19 \pm 0.17$ | $4.12 \pm 0.06$ |

**Table 6.3:** Elastic asymmetry results (in %).

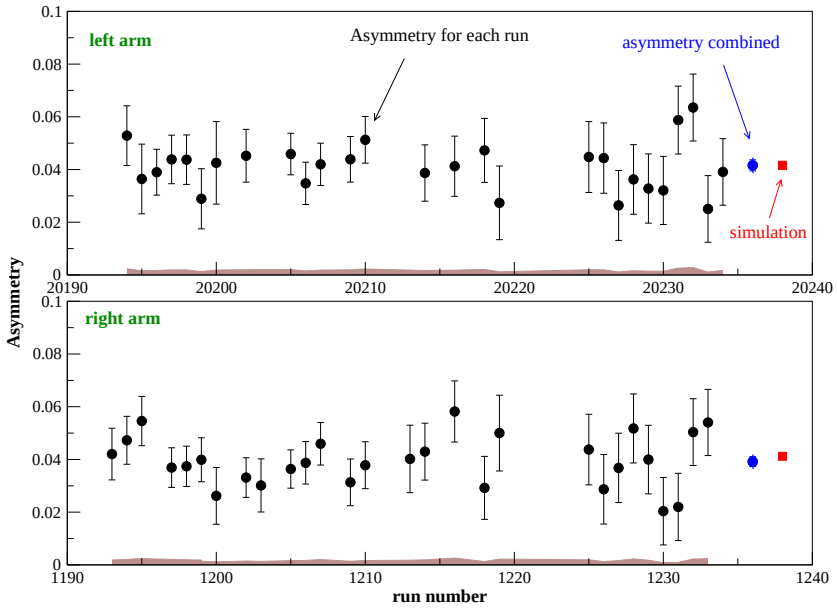


**Figure 6.16:** Elastic asymmetry results: the elastic asymmetries are shown for each run (black circles) and then combined (blue circle) to be compared the simulation (red square). The top plot is for the left arm and the bottom plot for the right arm. The systematic uncertainty for each run is represented by the brown band and by the outer error bar for the combined asymmetry. The error on the simulation is smaller than the size of the symbol.

### 6.4.2 Elastic unpolarized cross section

For the unpolarized cross section, the edges of the acceptance are excluded:

$$|\theta_{tg}| < 30.0 \text{ mrad}, \qquad |\phi_{tg}| < 15.0 \text{ mrad} \tag{6.24}$$

The detector efficiencies, the target density (from Section 5.3), the nitrogen dilution (same as for asymmetry) and the DAQ deadtime corrections are evaluated and applied for each run. The acceptance is generated by the same Monte Carlo code used to predict elastic asymmetry and cross section.

The uncertainty on the acceptance was determined to be of the order of 5% [Deur, 2000a]. In elastic scattering, pions are absent and the detector efficiency uncertainties come from the 2.5% inefficiency of the VDCs. The target density carries an uncertainty of 2.6% and the error on the nitrogen dilution is at maximum 0.6%. Other quantity uncertainties can be neglected. Thus, the total systematic error on the experimental cross section is found to be 6.2% and the statistical error is negligible.

In order to evaluate the systematic error of the simulated unpolarized cross section, quantity uncertainties were propagated inside the Monte Carlo. The form factor uncertainties at $Q^2 = 0.085$ are $\Delta f_m = \pm 0.002$ and $\Delta f_c = \pm 0.001$ [Amroun, 1994] and result in 0.9% error on the cross section. The uncertainties from the beam energy ($\pm 0.5$ MeV, see Table 4.1), the spectrometer central angle ($\pm 0.06^\circ$, [Ibrahim, 2002]) and the spectrometer central momentum ($\pm 0.5 \times 10^{-4}$, [Liyanage, 2001]) bring a 3.5% additional error. The same code is used to determine the spectrometer acceptance for the experimental data and the acceptance uncertainty is 5%. The radiative correction uncertainty due to the radiation length of the material on the electron path is 0.8%. The simulation total systematic error is 6.2%.

After implementing all these quantities in Eq. (6.7), the results for the elastic unpolarized cross section are listed in Table 6.4 and are shown in Fig. 6.17 where good agreement between data and simulation can be observed.

| HRS | $\sigma_0^{data} \pm$ syst. | $\sigma_0^{MC} \pm$ syst. |
|---|---|---|
| Left | $1.569 \pm 0.097$ | $1.553 \pm 0.096$ |
| Right | $1.571 \pm 0.097$ | $1.519 \pm 0.094$ |

**Table 6.4:** Elastic unpolarized cross section results (in $\mu$b/MeV/sr).

## 6.5 Target density from pressure curves

The density of the polarized $^3$He target under running conditions can be determined from the pressure curves. This consists of taking data with a reference cell filled with $^3$He gas at known pressures. The yield obtained from the polarized $^3$He data is projected on the curve defined by the yields of the reference cell data. The yield is calculating as followed:

$$\mathrm{Y(nb)} = \frac{\mathrm{N_{acc}}}{\mathrm{Q/e\ LT\ \epsilon_{det}\ L_{tg}}} \tag{6.25}$$

where PS is the prescale factor, Q/e is the number of incident electrons, LT is the data acquisition livetime, $\epsilon_{det}$ is the product of all detector efficiencies for the cuts chosen, $L_{tg}$ is the target chamber length and $N_{acc}$ is the number of good events passing all the cuts.

Since the reference cell and the polarized target cell are practically identical and the same cuts are used, the acceptance effects are assumed to be negligible. Depending on gas thicknesses, the collisional loss creates a shift of the elastic peak. It is corrected before applying the cuts.

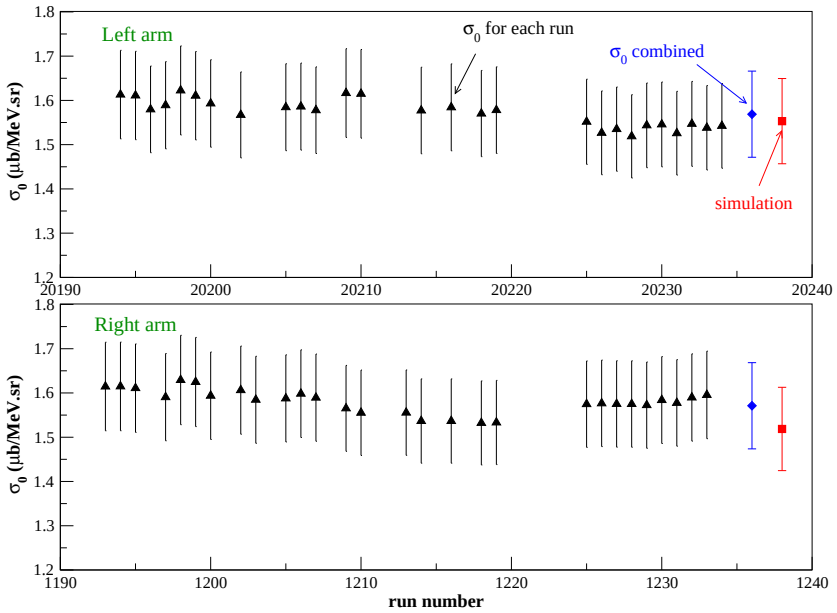


**Figure 6.17:** Elastic cross section results: the elastic cross sections are shown for each run (black triangles) and then combined (blue diamond) to be compared the simulation (red square). The error bars are from the systematic uncertainties only since the statistical error are negligible. The top plot is for the left arm and the bottom plot for the right arm.

### 6.5.1 Pressure curve for *Duke*

For *Duke*, the pressure curve was done in the elastic kinematic. The reference cell was filled with $^3$He gas at 36, 74, 110 and 147 psig. Due to collisional loss, the elastic peaks of each filling pressure shift by a small amount. Before extracting the yields, radiative corrections are applied to the yield by using the elastic simulation described in Section 6.4. The elastic peak is then selected from the corrected yield as shown in Fig. 6.18. A linear fit is performed on the yields as in Fig. 6.19.

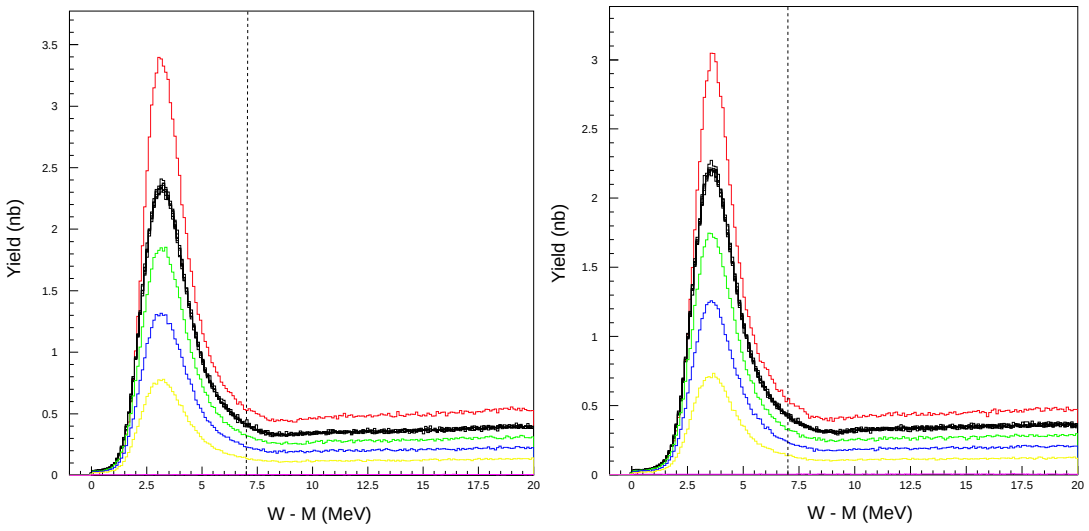


**Figure 6.18:** Cut on $^3$He elastic peak for left and right HRS: $0.0 < W_{^3He}$ - $M_{^3He} < 7.0$ MeV. The reference cell yields are: magenta for empty, yellow for 36 psig, blue for 74 psig, green for 110 psig and black for 147 psig. The polarized $^3$He yield is in red.

The projection of the polarized $^3$He yield on the fit gives:

$$\text{Yield(nb)} = 0.230(\pm 0.005) + 6.432(\pm 0.003)\ \text{P(atm)} \tag{6.26}$$

for the left arm, and:

$$\text{Yield(nb)} = 0.167(\pm 0.004) + 5.542(\pm 0.003)\ \text{P(atm)} \tag{6.27}$$

for the right arm. The systematic error has been evaluated in Section 6.4.2. Since only yields are considered in the pressure curve analysis, the spectrometer acceptances are not taking into account here. Therefore, the systematic error on the yield is 3.7%. After averaging both HRS' pressure, the density $n_T$ in the target chamber is found to be:

$$P = (13.28 \pm 0.01 \pm 0.49)\ \text{atm} \Rightarrow n_T = (11.33 \pm 0.01 \pm 0.42)\ \text{amg} \tag{6.28}$$

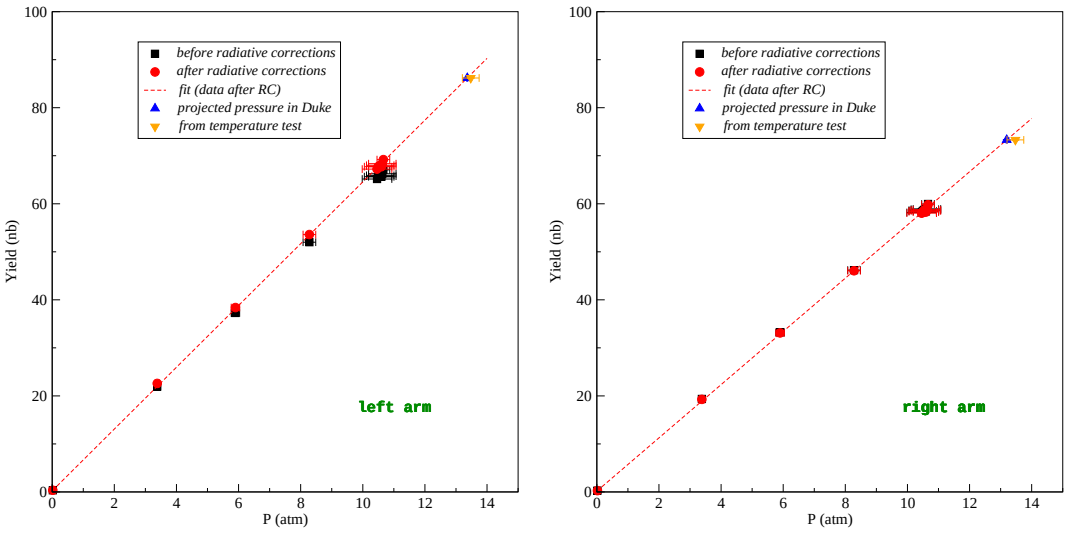


**Figure 6.19:** $^3$He pressure curve for *Duke*.

This value agrees well with the temperature test result [Solvignon, 2005b]: $(11.5 \pm 0.2 \pm 0.3)$ amg. This gives confidence in the density extraction from the temperature test and since it can predict the cell density at any time during the experiment (the RTDs are read every 10 seconds), it will be the method used in the data analysis.

### 6.5.2 Pressure curve for *Exodus*

For *Exodus*, the pressure curve data were taken in the deep inelastic region (Fig. 6.20) and only with the left HRS. The reference cell was filled with $^3$He at 26, 66 and 146 psig. In order to take into account the thickness differences, radiated cross sections are generated with the modified QFS model [Slifer, 2003] at $W_N = 2420.0$ MeV. Here no cuts are applied on $W$.

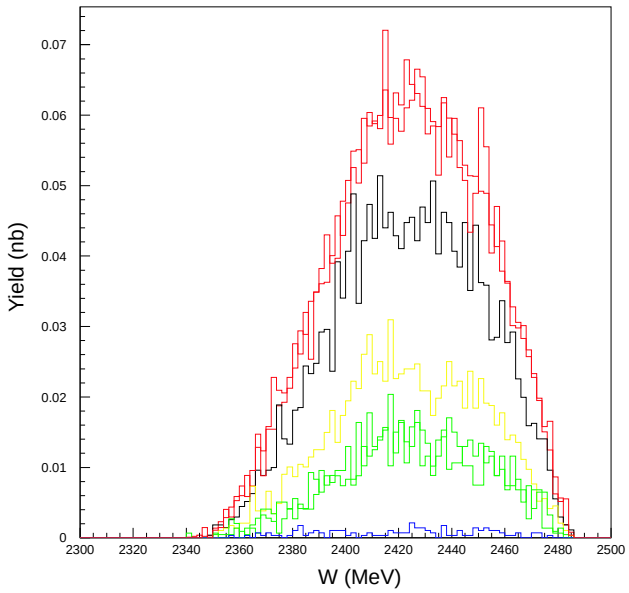


**Figure 6.20:** Deep inelastic scattering yield for $^3$He pressure curve for *Exodus*. The reference cell yields are: blue for empty, green for 26 psig, yellow for 66 psig and black for 146 psig. The yield of the polarized $^3$He is in red.

The linear fit performed of the DIS yields is shown in Fig. 6.21. The fit gives:

$$\text{Yield(nb)} = 0.039(\pm 0.004) + 0.165(\pm 0.002)\ \text{P(atm)} \tag{6.29}$$

Elastic and deep inelastic scattering data are have slightly different systematic uncertainties. The VDC inefficiency becomes about 1% but with increasing pion contamination the PID efficiencies are determined with a higher uncertainties. The uncertainties from the detector analysis in inelastic kinematics and other relevant quantities in the calculation of the yield are summarized in Table 7.1. The total systematic error on the yield is found to be 3.3%.

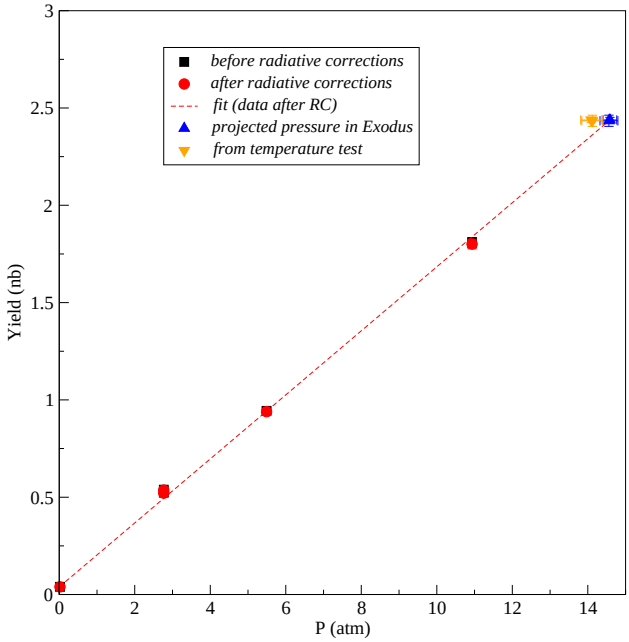


**Figure 6.21:** Result of the $^3$He pressure curve for *Exodus*.

Under running conditions, the temperature test gives $(12.0 \pm 0.2 \pm 0.3)$ amg [Solvignon, 2005b] and is in good agreement with the pressure curve result $(12.4 \pm 0.1 \pm 0.4)$ amg.

### 6.5.3 Nitrogen pressure curve

The nitrogen density can, in principle, be extracted from the analysis of the nitrogen pressure curve. Because of the small amount of nitrogen contained in the polarized $^3$He cell and the large background coming from $^3$He elastic events, it is difficult to isolate only nitrogen elastic events. Moreover, the reference cell used at the time was leaking, and a pressure loss of up to 15% was

recorded. As a result, a 20% discrepancy was found between filling density and the pressure curve projected value [Solvignon, 2006b]. Therefore, the nitrogen filling density will be used in the data analysis with an uncertainty of 5% [Singh, 2005].

## 6.6 Dilution and contamination

The observed asymmetry can be affected by the asymmetry of the beam itself, the pion contamination and dilution from unpolarized materials in the polarized target cell. All these effects have to be evaluated and, when they are significant, they must be corrected for.

### 6.6.1 False asymmetries

Because the electron beam can possess a false asymmetry itself, a check is made by using all unpolarized data (reference cell and carbon runs). PID cuts are applied in order to select only electrons, but very loose cuts are applied on the acceptance in order to improve the statistical errors. Fig. 6.22 shows the false asymmetries for each $W$-bin of the inelastic kinematics and the average of all $W$-bins with the $\chi^2$. The averages are consistent with zero (see Table 6.5 for the values) and the reduced-$\chi^2$ is close to 1 for each case. Therefore, the correction from false asymmetry is small and the total false asymmetry will be used as part of the systematic uncertainty of the final results.

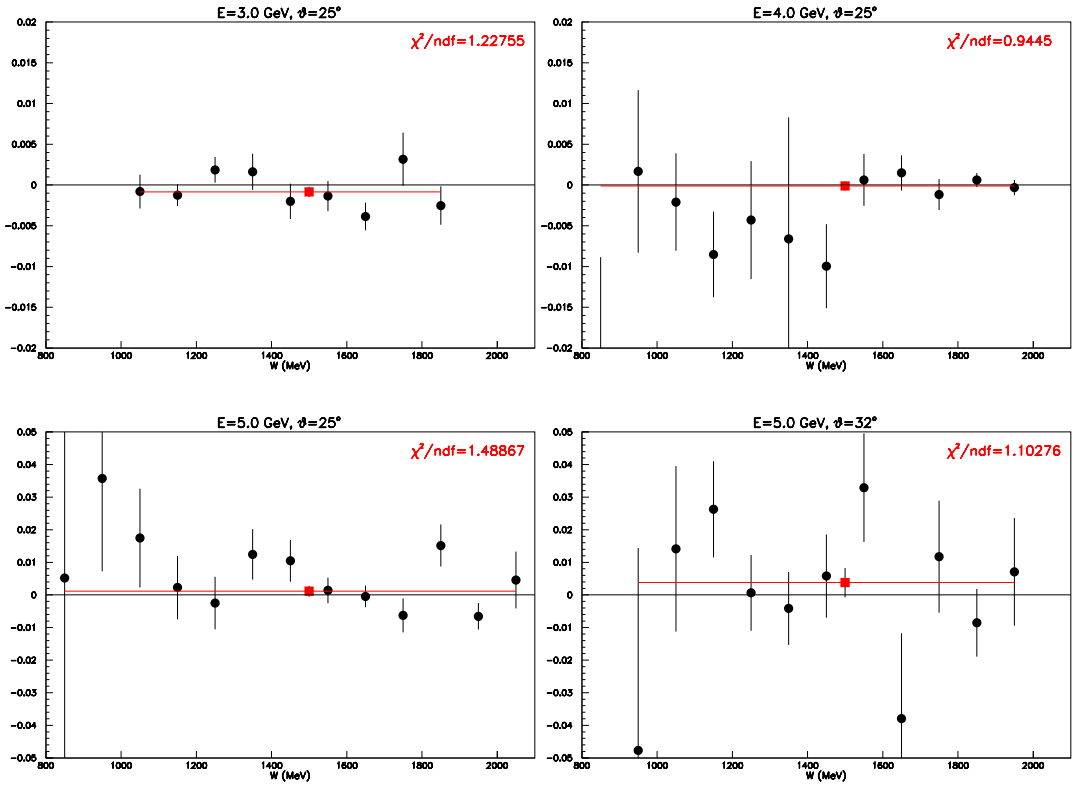


**Figure 6.22:** False asymmetry for our four kinematic settings. The black circle are the false asymmetry per $W$-bin. The red square is the average. Also shown are the reduced-$\chi^2$.

| kinematics | average (in ppm) | $\chi^2$/ndf |
|---|---|---|
| 1.0 GeV, 16° | 160 ± 183 | - |
| 3.0 GeV, 25° | -835 ± 629 | 1.2 |
| 4.0 GeV, 25° | -113 ± 555 | 0.9 |
| 5.0 GeV, 25° | 1141 ± 1658 | 1.5 |
| 5.0 GeV, 32° | 3787 ± 4499 | 1.1 |
| **total** | **81 ± 167** | - |

**Table 6.5:** False asymmetry averaged.

### 6.6.2 Pion asymmetry

Even with good PID detectors, a small number of pions can make it through the cuts. In order to evaluate the pion contamination to the electron asymmetries, the pion asymmetries are extracted for all kinematics using Eq. (6.2). The only difference here is the selection of pions through a cut on events not detected by the Čerenkov counter. Fig 6.23 shows the parallel and perpendicular asymmetries for all the kinematics except elastic. The asymmetries have been corrected for nitrogen dilution and target and beam polarization. Radiative corrections have not been applied. The pion asymmetries can go as high as 15%, which requires a high pion rejection factor in the electron asymmetry analysis.

The PID cuts reduce the ratio of the number of pions over the number of electrons by a factor of $10^4$. The contamination of the remaining pions can be evaluated as follows:

$$A^e_{cont} = \frac{1}{f_{\mathrm{N}_2} P_b P_t} \frac{\Delta N}{N_{tot}} \tag{6.30}$$

$$= \frac{1}{f_{\mathrm{N}_2} P_b P_t} \frac{\Delta N^e + \Delta N^\pi}{N^e_{tot} + N^\pi_t ot} \tag{6.31}$$

where $A^e_{cont}$ is the electron asymmetry (parallel or perpendicular) contaminated by the pions. Here $\Delta N = N_+ - N_-$ and $N_{tot} = N_+ + N_-$ with $N^{e(\pi)}_{+(-)}$ is the number of electrons (pions) with incident helicity $+1(-1)$.

With $N^\pi_{tot} = 10^{-4} N^e_{tot}$ and $\Delta N^\pi = f_{\mathrm{N}_2} P_b P_t N^\pi_{tot} A^\pi$, Eq. (6.31) becomes:

$$A^e_{cont} = \frac{1}{f_{\mathrm{N}_2} P_b P_t} \frac{\Delta N^e (1 + 10^{-4} f_{\mathrm{N}_2} P_b P_t A^\pi)}{N^e_{tot} + 10^{-4} N^e_{tot}} \tag{6.32}$$

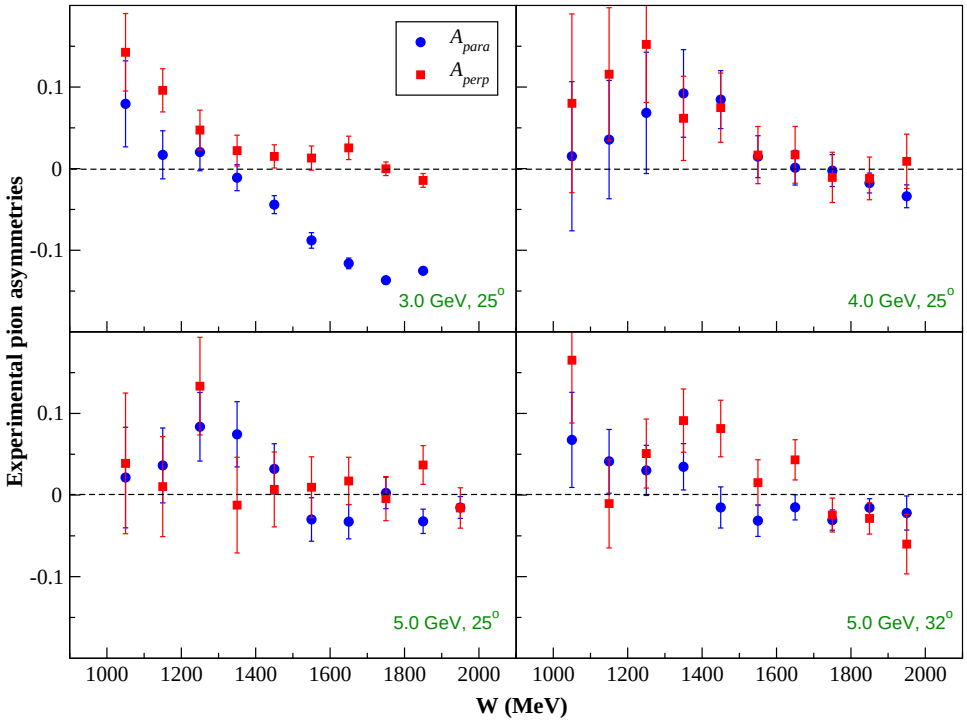


**Figure 6.23:** Experimental pion asymmetries (radiative corrections have not been applied).

$$\approx \quad \frac{1}{f_{\mathrm{N}_2} P_b P_t} \frac{\Delta N^e}{N^e_{tot}} + 10^{-4} A^\pi \tag{6.33}$$

where $A^\pi$ is the pion asymmetry (parallel or perpendicular). Defining $A^e$ as the "clean" electron asymmetry, the variation of the electron asymmetry due to the pion contamination can be written as:

$$\Delta A^e = A^e_{cont} - A^e \tag{6.34}$$

$$= 10^{-4} A^\pi \tag{6.35}$$

The contamination is maximum for the pion asymmetry at 15%, which gives:

$$\Delta A^e_{max} = 10^{-4} A^\pi_{max} \quad (6.36)$$

$$= 15 \text{ ppm} \quad (6.37)$$

Therefore, due to the good discrimination of the PID detectors, the pion contamination even with large pion asymmetry is negligible for all the kinematics.

### 6.6.3 Nitrogen unpolarized cross section

The polarized $^3$He cell contains a small amount of nitrogen (about 1% of the $^3$He density). Therefore, data were taken with the reference cell filled with nitrogen for most of the spectrometer momentum settings. First, the experimental nitrogen cross section is evaluated as follows:

$$\sigma_{\rm N} = \frac{N}{(Q/e)\rho_{\rm N} LT\epsilon_{det}} \sigma_{accep} \quad (6.38)$$

where $\sigma_{accep}$ is the correction for the acceptance and is the same as in the case of the polarized $^3$He cell (see Eq. 6.5). Here $\rho_{\rm N}$ is the number of nitrogen atoms per cm$^3$.

Because of time constraints, it was not possible to take nitrogen data at each spectrometer momentum settings. Therefore the nitrogen cross section is predicted for the missing coverage from a calculation based on the Quasi-Free Scattering model (QFS model) [Lightbody Jr., 1988]. More details on the model used for nitrogen cross sections and also the nitrogen Born cross sections can be found in [Solvignon, 2006a].

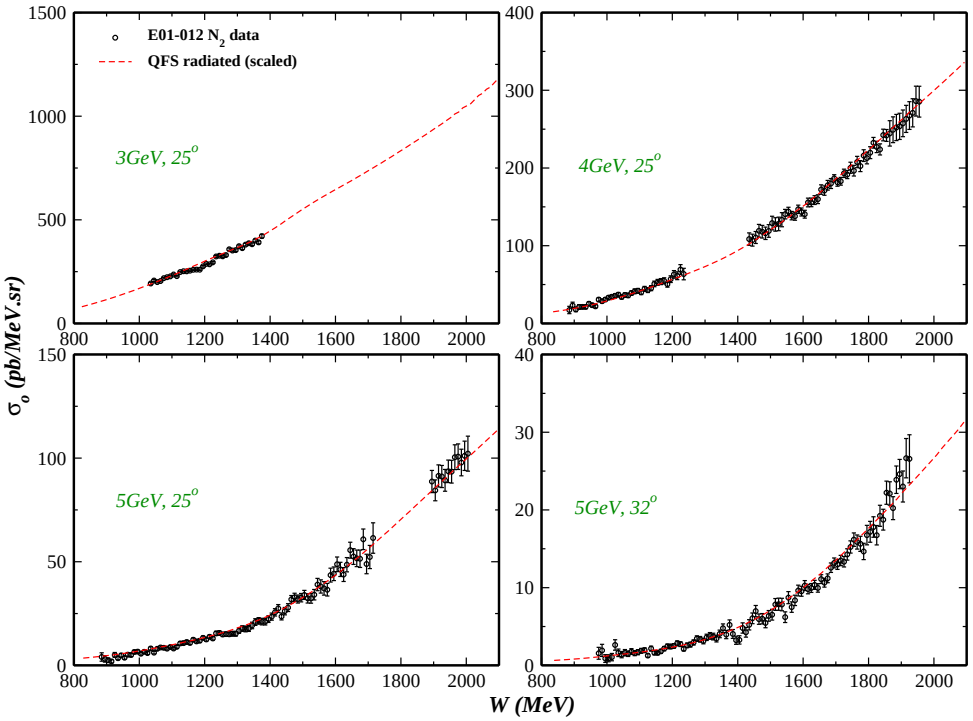


**Figure 6.24:** Experimental nitrogen cross sections (radiative corrections have not been applied). The red dashed curve is from the QFS model [Lightbody Jr., 1988] scaled to predict our data.

The experimental nitrogen cross sections and models are shown in Fig.6.24. They can be used directly to correct the $^3$He unpolarized cross sections after correcting for the density ratio:

$$\sigma_{\rm N}^{dil} = \frac{n_{\rm N}}{n_{\rm N} + n_{^3{\rm He}}}\sigma_{\rm N} \tag{6.39}$$

It is found to be a 5-9% correction to the $^3$He unpolarized cross sections depending on the kinematics with a systematic uncertainty from the dilution between 0.2-0.6% [Solvignon, 2006a].

# CHAPTER 7

# RESULTS

In this chapter, the $^3$He spin structure functions and virtual photon asymmetries are presented. In addition, quark-hadron duality is tested on the $^3$He and neutron spin structure functions.

## 7.1 Unpolarized cross sections

The unpolarized cross sections were measured from both HRS in symmetric configurations for most of our kinematics. We followed the analysis steps detailed in Section 6.1 to generate the unpolarized cross sections from the raw data.

### 7.1.1 Comparison of both HRS cross sections

The HRS provide two independent measurements of the cross sections. This gives an advantage in controlling the systematic uncertainties. For both spectrometers running simultaneously at the same configuration, the raw cross sections (Eq. 6.5) agree at the 2% level (see Fig. 7.1). This gives confidence for the single arm data, such as 5.0 GeV ($\theta$=25°) , since the same analysis scheme is used.

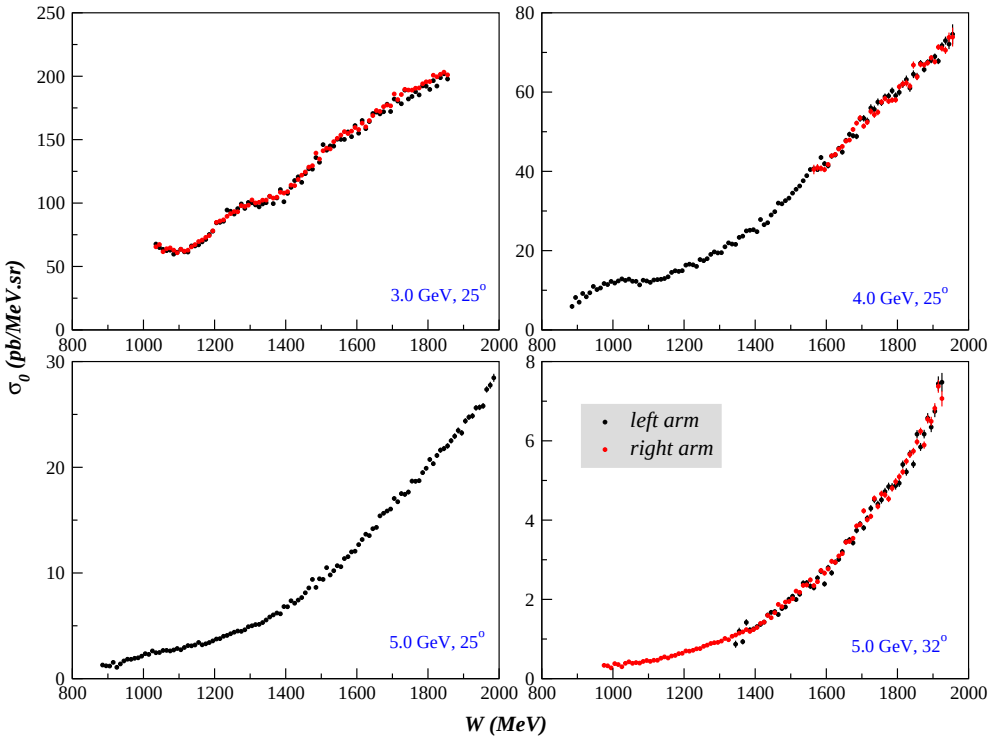


**Figure 7.1:** Comparison of the raw cross sections from the two HRS. Statistical errors only.

### 7.1.2 Experimental unpolarized cross sections

Both HRS raw cross sections are combined and, as defined by Eq. (6.7), the experimental cross sections are extracted by applying the nitrogen correction factor. The nitrogen dilution is found to have an effect of 5-9% depending of the kinematics as shown in Figs. 7.2 and 7.3.

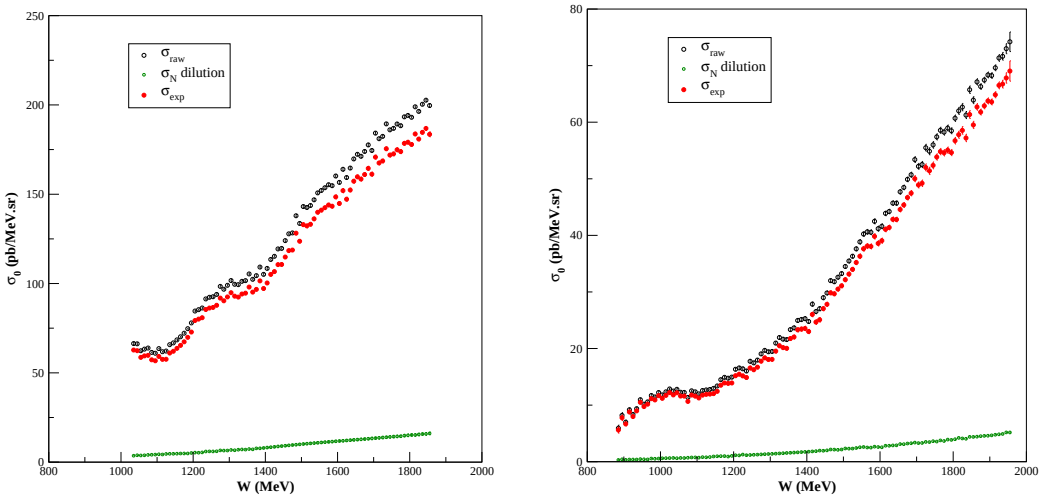


**Figure 7.2:** Experimental $^3$He cross sections. The incident energies are 3.028 GeV (left) and 4.018 GeV (right). The scattering angle is 25°. Only statistical errors are plotted.

### 7.1.3 Unpolarized Born cross section

Because of materials in their paths, incident and scattered electrons lose energy by bremsstrahlung, ionization and straggling. In addition, internal bremsstrahlung and other internal processes have to be taken into account. In order to extract the real reaction conditions, radiative corrections are applied (see Appendix A) to the experimental cross sections following the formalism of Mo and Tsai [Mo, 1969].

After the nitrogen dilution has been applied, the statistical errors of the experimental cross section is adjusted to account for the removal of nitrogen

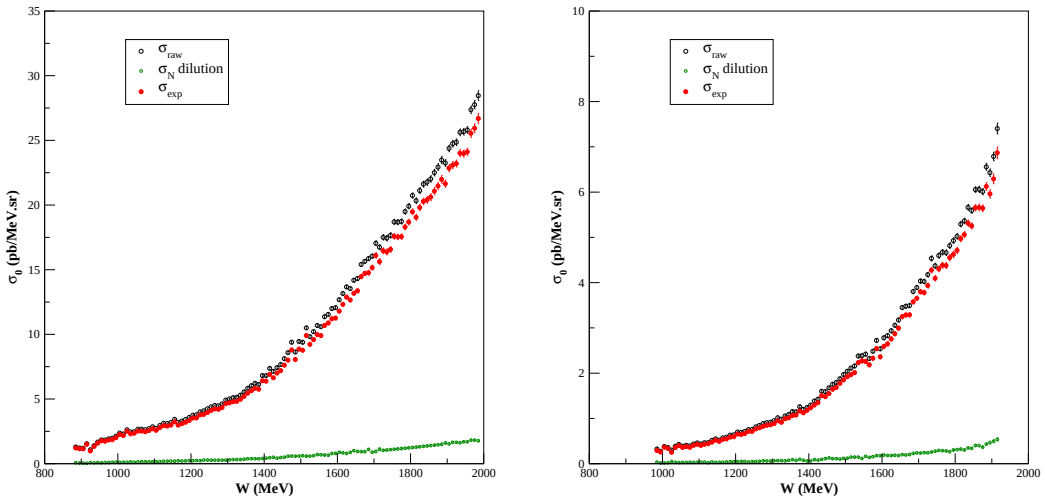


**Figure 7.3:** Experimental $^3$He cross section. The incident energy is 5.009 GeV and the scattering angles are 25° (left) and 32° (right). Only statistical errors are plotted.

events. The correction goes as follows:

$$\delta\sigma_{exp} = \delta\sigma_{raw}\sqrt{\frac{\sigma_{raw}}{\sigma_{exp}}} \tag{7.1}$$

The relative systematic uncertainty is calculated from Table 7.1 and from:

$$(\delta\sigma_{exp})^2 = (\delta\sigma_{raw})^2 + R_\rho^2(\delta\sigma_{\rm N})^2 \tag{7.2}$$

with $R_\rho = \rho_{\rm N}/(\rho_{\rm N} + \rho_{^3{\rm He}})$ and $\delta\sigma_{\rm N}$ being the systematic uncertainty on the nitrogen dilution which was found to have an effect of less than a percent on the $^3$He Born cross sections (see Section 6.6.3).

The systematic uncertainty from the radiative corrections comes principally from the model or the data used for the lower energy cross sections needed in the radiative correction process. In this work, the model is extracted from previous experimental data [Slifer, 2004]. These data have a

maximum total uncertainty of 9%. When varying this model by 10%, our Born cross sections fluctuate by less than 4%.

Another origin of uncertainty from the radiative corrections could be from knowledge of the material thicknesses (see Appendix B). Changing the total radiation lengths before and after scattering by ±10% is found to have a maximum effect on the Born cross sections of 4.8% in the quasi-elastic region.

The final systematic uncertainties have been calculated with:

$$(\delta\sigma_{born})^2 = (\delta\sigma_{exp})^2 + \left(\delta RC \frac{\sigma_{born} - \sigma_{exp}}{\sigma_{born}}\right)^2 \tag{7.3}$$

and reported in Table 7.1.

| Kinematics: E (GeV), $\theta$ (°) | 3.0, 25 | 4.0, 25 | 5.0, 25 | 5.0, 32 |
|---|---|---|---|---|
| Charge | 0.5 % | | | |
| Energy | 0.05 % | | | |
| Target density | 2.6 % | | | |
| Acceptance‡ | 1.7 % | 2.0 % | 2.0 % | 3.0 % |
| VDC efficiency | 1.0% | | | |
| Scintillator eff. | 0.5 % | | | |
| Cerenkov detection eff. | 0.0 % | | | |
| Cerenkov cut eff. | 1.0 % | | | |
| Calorimeter detection eff. | 0.5 % | | | |
| Calorimeter cut eff. | 1.0 % | | | |
| $\delta\sigma_{raw}$ | 3.7 % | 3.8 % | 3.8 % | 4.4 % |
| Nitrogen dilution | 0.2-0.6 % | | | |
| $\delta\sigma_{exp}$ | 4.0 % | 4.1 % | 4.1 % | 4.9 % |
| Radiative corrections | 1.3-2.8 % | 1.7-4.4 % | 1.8-3.9 % | 1.9-4.4 % |
| $\delta\sigma_{Born}$ | 4.0-5.7 % | 3.9-5.0 % | 3.9-4.4 % | 4.6-6.7 % |

**Table 7.1:** Systematic uncertainties for unpolarized cross sections.

The unpolarized $^3$He cross sections are plotted in Figs. 7.4 and 7.5, and tabulated in Appendix C. At the lowest energy, the $\Delta(1232)$ can be clearly seen. At 4 GeV and 5 GeV, our data cover also the quasi-elastic scattering region. At all our kinematics, the unpolarized cross sections show a large non-resonant background.

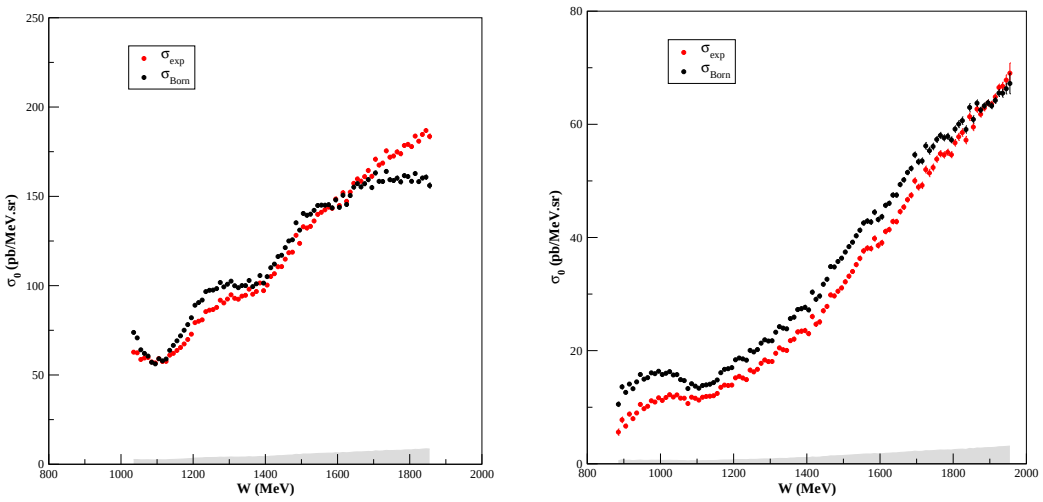


**Figure 7.4:** $^3$He experimental (red) and Born (black) cross sections for incident energies of 3.028 GeV (left) and 4.018 GeV (right), and a scattering angle of 25°. The grey band is the systematic uncertainty.

## 7.2 Polarized cross section differences

The polarized cross section differences are generated from the experimental parallel and perpendicular asymmetries and the experimental unpolarized cross sections using Eq. (6.9).

*The uncertainty from the acceptance was studied in [Solvignon, 2004c].

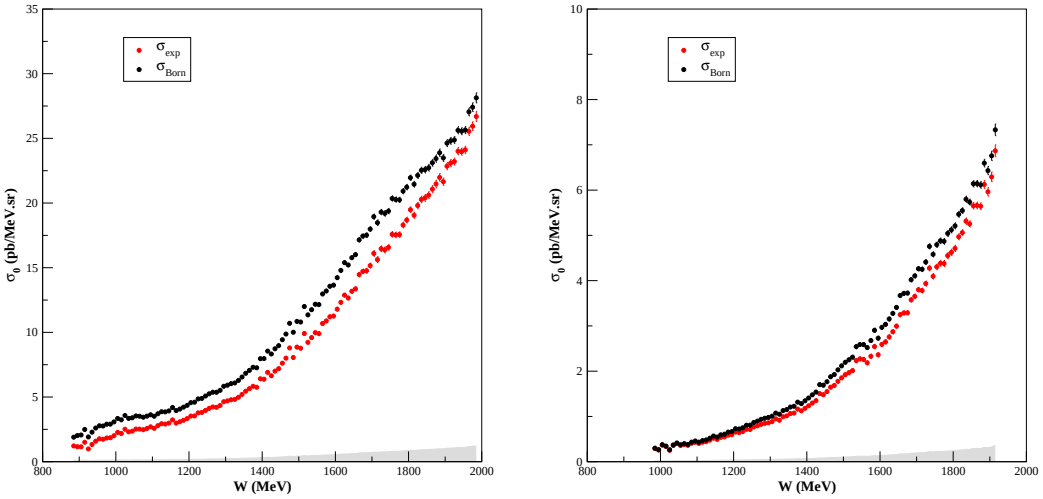


**Figure 7.5:** $^3$He experimental (red) and Born (black) cross sections for incident energy of 5.009 GeV and scattering angles of 25° (left) and 32° (right). The grey band is the systematic uncertainty.

The experimental systematic uncertainty comes from the target polarization (3-4%), the beam polarization (3.4%, see Table 4.2) and the unpolarized raw cross sections (see Table 7.1). Radiative corrections are applied following the method of Ref. [Mo, 1969] and Ref. [Akushevich, 1994] detailed in Appendix A. Figs. 7.6 and 7.7 show the polarized Borncross section differences for all the kinematics of the experiment. The radiative corrections are also plotted (dashed curves). The dominant uncertainty comes from the fit of our data and the spin structure function models which are used by the radiative correction codes. By varying the fit of our data over a reasonable range and the model by ±10%, the resulting polarized cross section differences were found to fluctuate within 6%. All systematic errors are added in quadrature and we find a total systematic uncertainty of 8-9%. The results

for the polarized $^3$He cross section differences are tabulated in Appendix D.

The dominant resonance, $\Delta(1232)$, can be seen at the lowest energy in Fig. 7.6. As the incident energy increases and also the scattering angle (Figs. 7.6 and 7.7), the resonances smear out, and the remaining strength is due to the increasing non-resonant background.

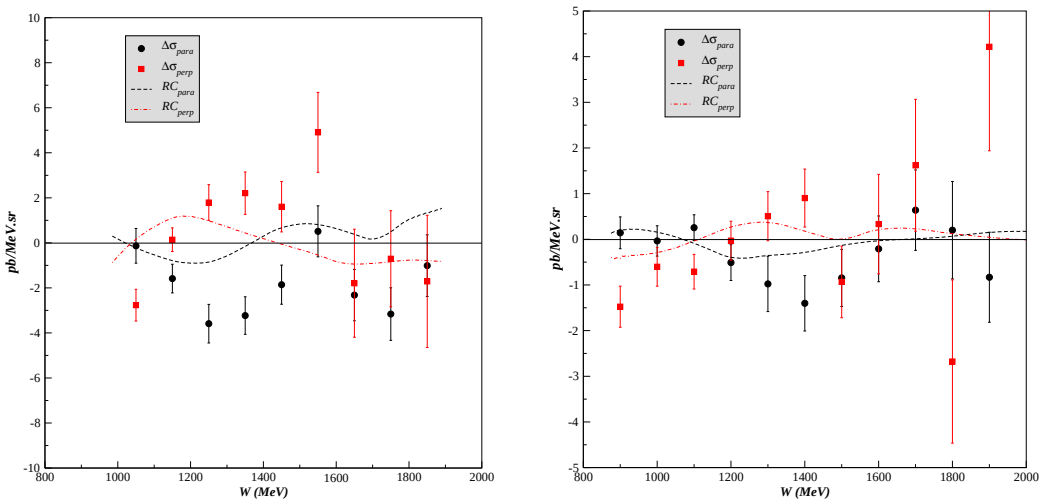


**Figure 7.6:** $^3$He Born polarized cross section differences. The incident energies are 3.028 GeV (left) and 4.018 GeV (right), and the scattering angle is 25°. Also shown is the size of the radiative corrections. The error bars represent statistical and systematic uncertainties added in quadrature.

## 7.3 Born asymmetries

The Born asymmetries can be extracted from the unpolarized Born cross sections and the polarized Born cross section differences:

$$A_{\parallel,\perp}^{Born} = \frac{\Delta\sigma_{\parallel,\perp}^{Born}}{2\ \sigma_0^{Born}} \tag{7.4}$$

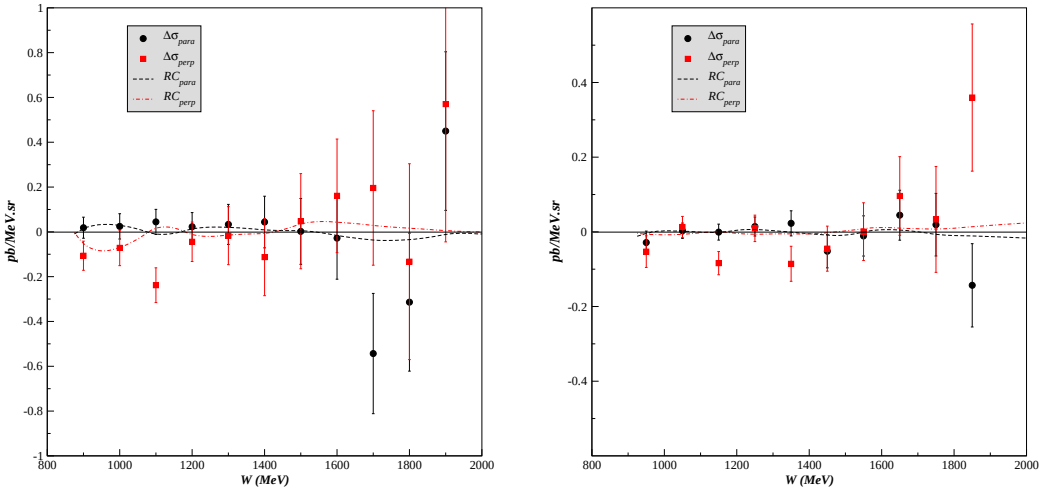


**Figure 7.7:** $^3$He Born polarized cross section differences. The incident energy is 5.009 and the scattering angles are 25° (left) and 32° (right) . Also shown is the size of the radiative corrections. The error bars represent statistical and systematic uncertainties added in quadrature.

The systematic uncertainty comes from target polarization (3-4%), the beam polarization (3.4%, see Table 4.2), the nitrogen dilution (0.2-0.6%) and the internal radiative correction uncertainties ($< 3\%$). Adding in quadrature, we obtain 5-6% systematic uncertainties on the parallel and perpendicular asymmetries. The polarized $^3$He asymmetries are tabulated in Appendix E.

The same features as in the polarized cross section differences are present in the asymmetries. The $\Delta(1232)$ transition is clearly observed at the lowest energy with an apparent change of sign with respect to the parallel and perpendicular configurations. Some strength of the $\Delta(1232)$ can still be seen at the next energy. At higher energy, the asymmetries in the $\Delta(1232)$ region are brought down to zero due to the falling of the $\Delta(1232)$ form factors with

increasing $Q^2$ and the rising of the non-resonant background.

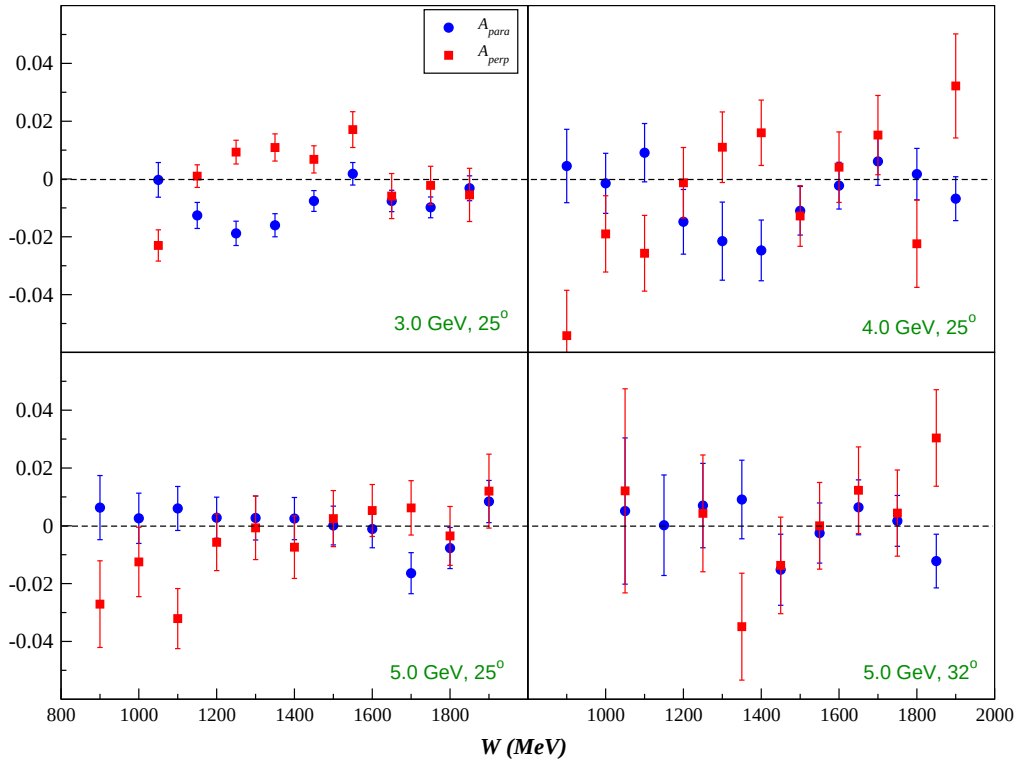


**Figure 7.8:** $^3$He Born asymmetries.

## 7.4 Photon-nucleon asymmetries

Existing DIS $A_1$ data for $^3$He are shown in Fig 7.9. As can be seen, the high $x$ region is lacking measurements due to the experimental difficulty to access it from deep inelastic scattering.

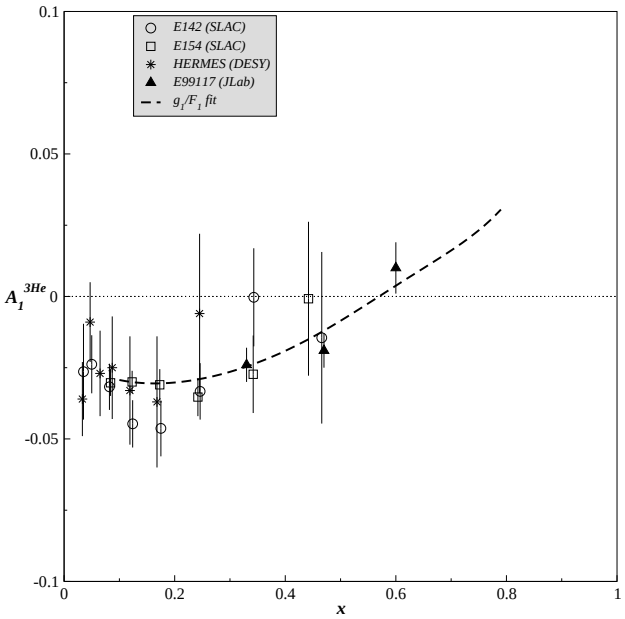


**Figure 7.9:** $A_1$ for $^3$He in the deep inelastic scattering region. Data are from E142 [Anthony, 1996], E154 [Incerti, 1998a], HERMES [Ackerstaff, 1999] and E99-117 [Zheng, 2004].

From our resonance parallel and perpendicular asymmetries, the virtual photon asymmetries $A_1$ and $A_2$ are extracted by using Eq. (2.31) and Eq. (2.32). However, the longitudinal to transverse cross sections ratio $R(x, Q^2)$ has never been measured on $^3$He in the resonance region. Therefore it will be one of the major contributions to the systematic uncertainties. The variation of $A_1$ and $A_2$ with different assumptions for $R(x, Q^2)$ were studied. First, the proton data for $R(x, Q^2)$ in the resonance region [Liang, 2004] are scaled assuming:

$$\left(\frac{R_d}{R_p}\right)_{res.} \approx \left(\frac{R_d}{R_p}\right)_{DIS} \tag{7.5}$$

The approximation made in Eq. (7.5) assumes quark-hadron duality for $R(x, Q^2)$, which has been shown [Melnitchouk, 2005] to hold in the $Q^2$-range of our data. The ratio $R_d/R_p$ in the DIS has been measured and was found to be about 0.7 [Tvaskis, 2004]. In order to take into account the different structures and behaviors between the deuteron and $^3$He, the ratio $R_{^3\mathrm{He}}/R_p$ was chosen to be 0.5.

To reflect the arbitrary choice of $R$, we investigated the effects of using other values of $R$. Extractions of $A_1$ and $A_2$ were done with constant values of $R_{^3\mathrm{He}}$ equal to 0.10, 0.20 and 0.25 (which are close to the average of the DIS data) and also with $R_{^3\mathrm{He}} = 0.7\ R_p$. The variations of $A_1$ and $A_2$ from these five extractions was found to be less than 15% (relative). This value is small compared to the 20-30% relative statistical uncertainties, and is added to the systematic errors.

The spin asymmetry $A_1^{^3\mathrm{He}}$ in the resonance region is presented in Figs. 7.10 and 7.11, and reported in Table 7.2. Also plotted are the DIS data for $^3$He in order to provide a direct comparison between the deep inelastic scattering behavior and the resonance data trend. The $g_1/F_1$ fit for $^3$He is formed from fits [Zheng, 2002] for the proton and the neutron using the effective polarization equation method of Eq. (7.10).

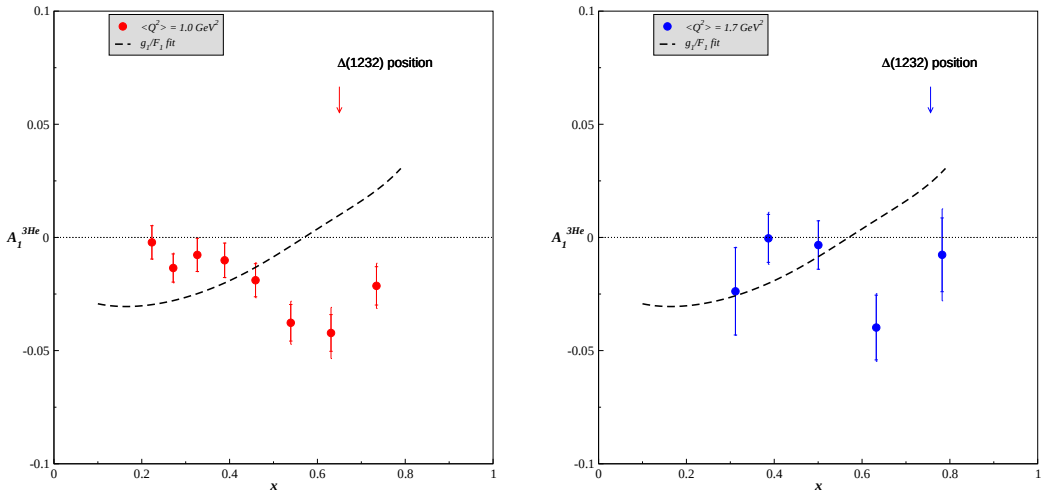


**Figure 7.10:** $A_1^{^3\mathrm{He}}$ in the resonance region for average $Q^2$ of 1.0 and 1.7 $(\mathrm{GeV/c})^2$

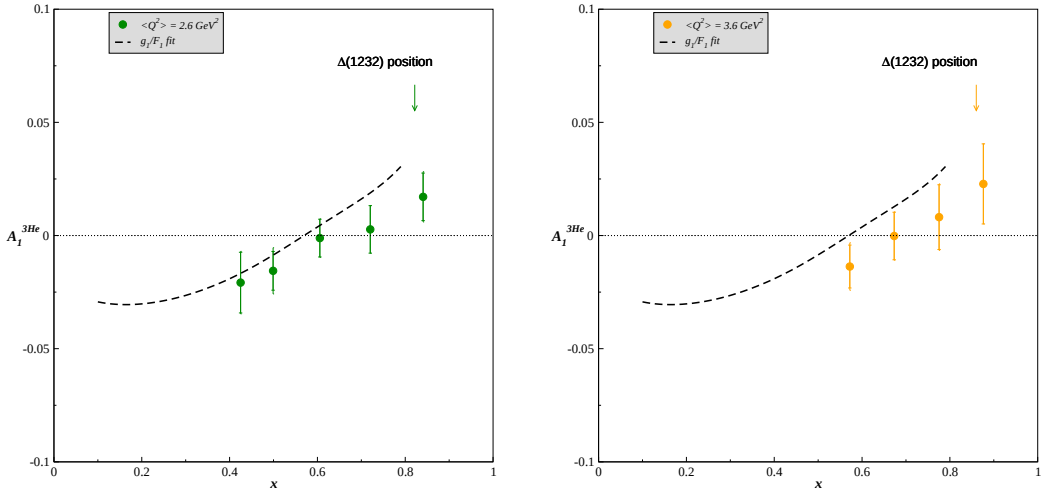


**Figure 7.11:** $A_1^{^3\mathrm{He}}$ in the resonance region for average $Q^2$ of 2.6 and 3.6 $(\mathrm{GeV/c})^2$

When we form $A_1^{^3\mathrm{He}}$ and $A_2^{^3\mathrm{He}}$, a large $x$ (or $W$) binning of our data is used in order to improve the statistics. This also implies that $A_1$ from our data has been averaged locally and therefore, a qualitative test of local duality can be performed. For our two lowest average $Q^2$, it can be seen that $A_1^{^3\mathrm{He}}$ in the vicinity of the $\Delta(1232)$ peak is large and negative unlike the DIS behavior. But as $Q^2$ increases, $A_1^{^3\mathrm{He}}$ in the resonance region crosses zero and becomes positive even in the $\Delta(1232)$ region. This is due to the increasing importance of the non-resonant background with respect to the resonance strength. Moreover, the fall off of the $\Delta(1232)$ form factors reduces the strength of the $\Delta(1232)$ as $Q^2$ increases.

In addition, our two highest averaged $Q^2$ sets agree very well following the same trend (see Fig 7.12). This is an indication that the $Q^2$-dependence of $A_1$ has weakened, as expected from the pQCD predictions. However, the slope of the resonance data is different from the one seen in DIS. That might be a sign that local duality does not work well for the spin structure functions.

The spin asymmetry $A_2^{^3\mathrm{He}}$ in the resonance region is presented in Fig. 7.13 and reported in Table 7.2. Also plotted are the DIS data for $^3$He in order to provide a direct comparison between deep inelastic scattering behavior and the resonance data trend.

The large $\Delta(1232)$ contribution observed in $A_1$ for $Q^2 < 2.0$ GeV$^2$ is not seen in $A_2$. This may be due to the fact that $A_2$ is proportional to $g_1 + g_2$, which are approximately equal and opposite in the $\Delta(1232)$ region.

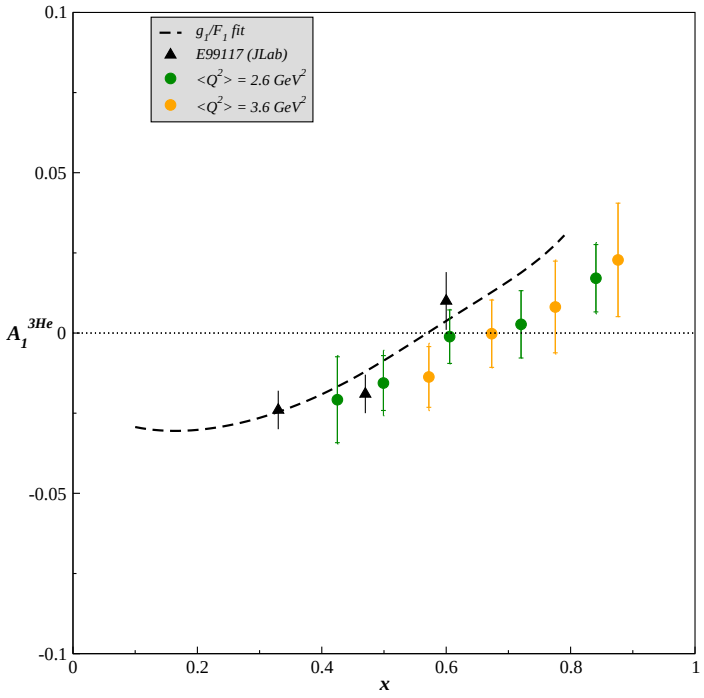


**Figure 7.12:** $A_1^{^3\mathrm{He}}$ in the resonance region. Deep inelastic data from E99-117 [Zheng, 2004].

For all $Q^2$, the resonance region data seem to follow the same trend, going negative at high $x$. This behavior also agrees with the hinted high $x$ trend of the DIS data.

## 7.5 Spin structure functions

The spin structure functions $g_1$ and $g_2$ can be extracted directly from the polarized cross section differences $\Delta\sigma_{||}$ and $\Delta\sigma_{\perp}$. However, these quantities were measured at constant energy and scattering angle. Interpolations

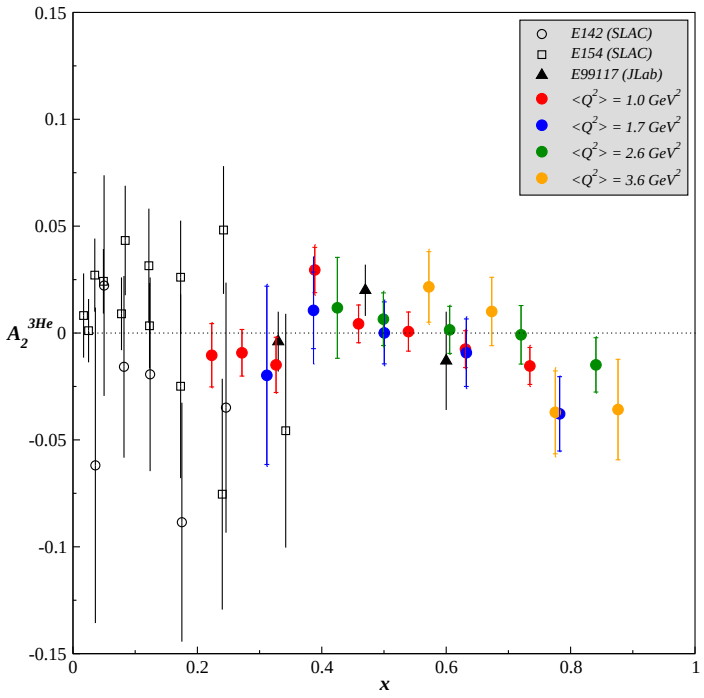


**Figure 7.13:** $A_2^{^3\mathrm{He}}$ in the resonance region. Deep inelastic data from E142 [Anthony, 1996], E154 [Incerti, 1998a] and from E99-117 [Zheng, 2004].

to constant $Q^2$ are performed in order to study the structure function moments. To do so, $g_1$ and $g_2$ are determined at constant energy and scattering angle, and then interpolated to constant $Q^2$ (1.2, 1.9, 2.6 and 3.3 GeV/c$^2$) as illustrated in Fig. 7.14.

In the extraction of $g_{1,2}^{^3\mathrm{He}}$ from Eqs. (2.21-2.22), the mass of the nucleon was used instead of the mass of $^3$He nucleus. The results for $g_1^{^3\mathrm{He}}$ are presented in Fig. 7.15 and in Appendix F. At low $Q^2$ (1.2 and 1.9 GeV$^2$), the resonance data seems to oscillate around the DIS parametrization [Gluck, 2001]. As to the two highest $Q^2$, our resonance data coincide with the DIS curve.

| kin | $W$ | $x$ | $Q^2$ | $A_1 \pm$ stat. $\pm$ syst. | $A_2 \pm$ stat. $\pm$ syst. |
|---|---|---|---|---|---|
| 3 | 1.15 | 0.735 | 1.22 | -0.0214 $\pm$ 0.0085 $\pm$ 0.0053 | -0.0154 $\pm$ 0.0087 $\pm$ 0.0042 |
| 3 | 1.25 | 0.631 | 1.16 | -0.0422 $\pm$ 0.0081 $\pm$ 0.0078 | -0.0075 $\pm$ 0.0086 $\pm$ 0.0033 |
| 3 | 1.35 | 0.539 | 1.10 | -0.0377 $\pm$ 0.0081 $\pm$ 0.0050 | 0.0007 $\pm$ 0.0091 $\pm$ 0.0016 |
| 3 | 1.45 | 0.459 | 1.04 | -0.0189 $\pm$ 0.0073 $\pm$ 0.0026 | 0.0043 $\pm$ 0.0088 $\pm$ 0.0019 |
| 3 | 1.55 | 0.389 | 0.97 | -0.0101 $\pm$ 0.0076 $\pm$ 0.0011 | 0.0295 $\pm$ 0.0106 $\pm$ 0.0052 |
| 3 | 1.65 | 0.327 | 0.89 | -0.0077 $\pm$ 0.0073 $\pm$ 0.0012 | -0.0149 $\pm$ 0.0129 $\pm$ 0.0031 |
| 3 | 1.75 | 0.272 | 0.81 | -0.0135 $\pm$ 0.0062 $\pm$ 0.0022 | -0.0092 $\pm$ 0.0109 $\pm$ 0.0005 |
| 3 | 1.85 | 0.223 | 0.73 | -0.0022 $\pm$ 0.0074 $\pm$ 0.0015 | -0.0104 $\pm$ 0.0148 $\pm$ 0.0036 |
| 4 | 1.20 | 0.782 | 2.00 | -0.0077 $\pm$ 0.0163 $\pm$ 0.0121 | -0.0378 $\pm$ 0.0174 $\pm$ 0.0035 |
| 4 | 1.40 | 0.632 | 1.85 | -0.0398 $\pm$ 0.0143 $\pm$ 0.0045 | -0.0092 $\pm$ 0.0158 $\pm$ 0.0058 |
| 4 | 1.60 | 0.501 | 1.68 | -0.0033 $\pm$ 0.0107 $\pm$ 0.0013 | 0.0001 $\pm$ 0.0145 $\pm$ 0.0051 |
| 4 | 1.80 | 0.387 | 1.48 | -0.0004 $\pm$ 0.0106 $\pm$ 0.0044 | 0.0106 $\pm$ 0.0179 $\pm$ 0.0176 |
| 4 | 1.95 | 0.312 | 1.32 | -0.0238 $\pm$ 0.0193 $\pm$ 0.0021 | -0.0198 $\pm$ 0.0417 $\pm$ 0.0086 |
| 5 | 1.20 | 0.841 | 2.95 | 0.0171 $\pm$ 0.0105 $\pm$ 0.0035 | -0.0149 $\pm$ 0.0127 $\pm$ 0.0035 |
| 5 | 1.40 | 0.720 | 2.77 | 0.0027 $\pm$ 0.0105 $\pm$ 0.0003 | -0.0008 $\pm$ 0.0137 $\pm$ 0.0010 |
| 5 | 1.60 | 0.606 | 2.57 | -0.0011 $\pm$ 0.0084 $\pm$ 0.0016 | 0.0015 $\pm$ 0.0110 $\pm$ 0.0033 |
| 5 | 1.80 | 0.499 | 2.35 | -0.0156 $\pm$ 0.0086 $\pm$ 0.0055 | 0.0065 $\pm$ 0.0123 $\pm$ 0.0043 |
| 5 | 1.95 | 0.425 | 2.16 | -0.0208 $\pm$ 0.0134 $\pm$ 0.0035 | 0.0118 $\pm$ 0.0236 $\pm$ 0.0008 |
| 6 | 1.20 | 0.876 | 3.96 | 0.0228 $\pm$ 0.0177 $\pm$ 0.0004 | -0.0358 $\pm$ 0.0235 $\pm$ 0.0015 |
| 6 | 1.40 | 0.775 | 3.72 | 0.0081 $\pm$ 0.0143 $\pm$ 0.0034 | -0.0371 $\pm$ 0.0194 $\pm$ 0.0078 |
| 6 | 1.60 | 0.673 | 3.46 | -0.0002 $\pm$ 0.0105 $\pm$ 0.0016 | 0.0101 $\pm$ 0.0160 $\pm$ 0.0004 |
| 6 | 1.80 | 0.572 | 3.15 | -0.0137 $\pm$ 0.0095 $\pm$ 0.0046 | 0.0216 $\pm$ 0.0165 $\pm$ 0.0063 |

**Table 7.2:** $A_1^{^3\mathrm{He}}$ and $A_2^{^3\mathrm{He}}$. $W$ and $Q^2$ are in GeV and (GeV/c)$^2$, respectively. The first column is defined in Appendix C.

This indicates a qualitative confirmation of global quark-hadron duality for the $^3$He spin structure function $g_1$. A quantitative study to confirm this observation is presented in Section 7.6.

The spin structure function $g_2$ was also extracted from our data. From the Operator Product Expansion, the structure function $g_2$ can be split into

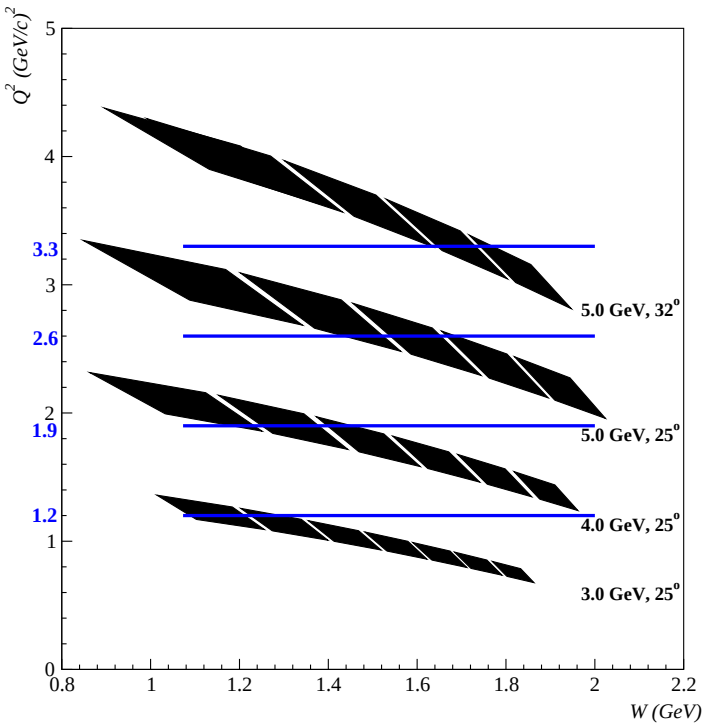


**Figure 7.14:** Constant $Q^2$ interpolation.

a leading-twist term and a higher-twist term:

$$g_2(x, Q^2) = g_2^{WW}(x, Q^2) + \bar{g}_2(x, Q^2) \tag{7.6}$$

Wandzura and Wilczek [Wandzura, 1977] derived the expression for the leading twist part of $g_2$ as a function of $g_1$:

$$g_2^{WW}(x) = -g_1(x) + \int_x^1 dx' \frac{g_1(x')}{x'} \tag{7.7}$$

Consequently, $g_2^{WW}$ can be expressed as a function of parton distributions within the parton model. Unlike in $g_1$, the higher twist contributions to $g_2$ are not suppressed by a factor $1/Q^2$, so the $g_2$ structure function is a

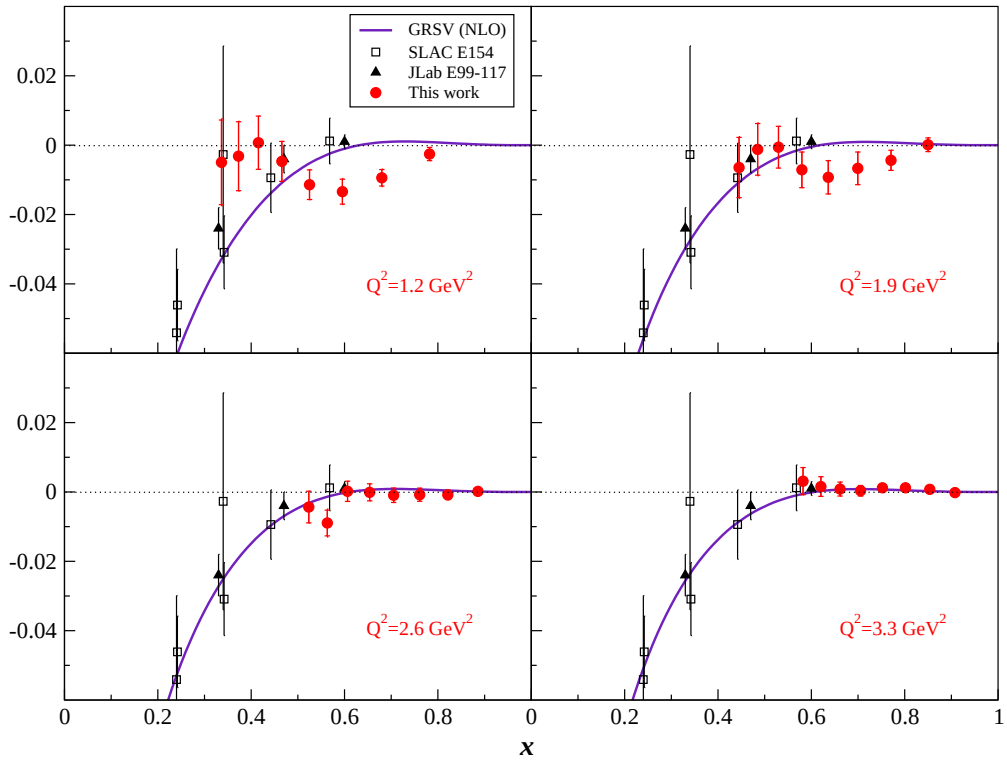


**Figure 7.15:** The spin structure function $g_1^{^3\mathrm{He}}$ in the resonance region at $Q^2$ of 1.2 (top left), 1.9 (top right), 2.6 (bottom left) and 3.3 (bottom right) (GeV$^2$). The curve was generated from the GRSV NLO parton distribution functions [Gluck, 2001].

useful quantity to study quark-hadron duality in terms of higher twist effect suppression or cancellation.

The spin structure function $g_2^{^3\mathrm{He}}$ is presented in Fig. 7.16 and in Appendix F. The resonance data seems fairly close to the $g_2^{WW}$ models. This would suggest that the higher twist contributions to $g_2$ in the resonance region at our $Q^2$ are small or cancel.

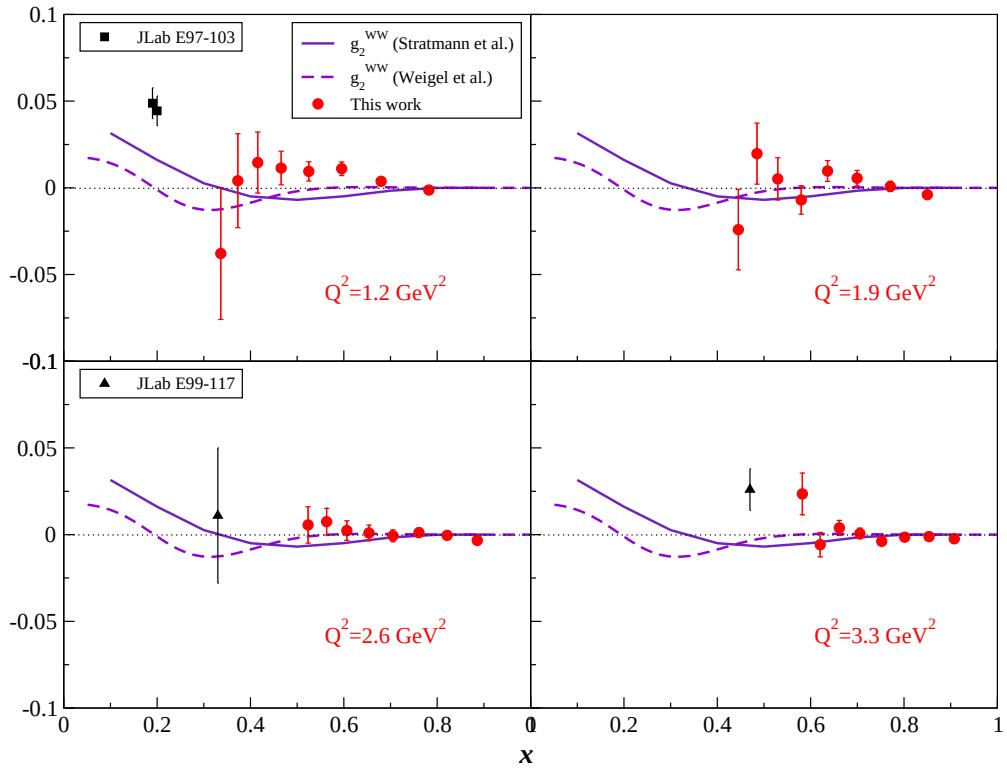


**Figure 7.16:** The spin structure function $g_2^{^3\mathrm{He}}$ in the resonance region at $Q^2$ of 1.2, 1.9, 2.6 and 3.3 (GeV/c)$^2$. DIS data are from E99-117 [Zheng, 2004] and E97-103 [Kramer, 2005]. The curves are from calculations of $g_2^{WW}$ at $Q^2 =$ 3.0 GeV$^2$ from Weigel *et al.* [Weigel, 1997] and Stratmann [Stratmann, 1993].

## 7.6 Test of quark-hadron duality

To test quark-hadron duality, the moments of the structure functions are calculated over the same $x$-range and at the same $Q^2$ in the DIS and resonance regions as discussed in [Bianchi, 2004]. We present the results in the following sections.

The first moment of $g_1$ is calculated only over the resonance region:

$$\tilde{\Gamma}_1^{res}(Q^2) = \int_{x_{min}}^{x_{max}} g_1^{res}(x, Q^2)\ dx \tag{7.8}$$

where $x_{min}$ corresponds to $W = 2$ GeV and $x_{max}$ to the pion production threshold.

Following the same steps as [Bianchi, 2004], the first moment of $g_1$ in the resonance region can be compared to the DIS one. To do so, both regions should be integrated over the same x-range and at the same $Q^2$, as in Eq. (7.8) for the resonance data and:

$$\tilde{\Gamma}_1^{DIS}(Q^2) = \int_{x_{min}}^{x_{max}} g_1^{DIS}(x, Q^2)\ dx \tag{7.9}$$

for the DIS region. If the two integrals are found equal then quark-hadron duality would be verified for the spin structure function $g_1$.

### 7.6.1 Integral of $g_1$

Fig 7.17 shows $\tilde{\Gamma}_1$ evaluated for all $Q^2$. Our results combined with data from JLab experiment E94-010 [Slifer, 2006] indicates a smooth transition from the strongly non-perturbative regime at low $Q^2$ to the high $Q^2$ perturbative regime.

In the resonance region, large nuclear effects prevent us to extract $g_{1,2}^n$ from $g_{1,2}^{^3\mathrm{He}}$ using the effective polarization equation defined as follows:

$$g_{1,2}^{^3\mathrm{He}} = p_n\ g_{1,2}^n\ +\ 2\ p_p\ g_{1,2}^p \tag{7.10}$$

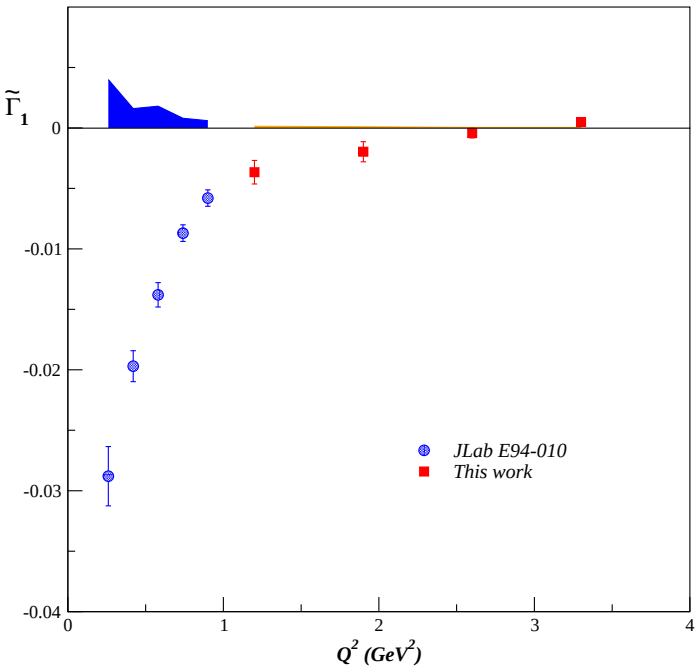


**Figure 7.17:** First moment of $g_1$ for $^3$He. Also plotted are data for the same quantity from E94-010 [Slifer, 2006]. The orange and blue bands represent the systematic uncertainties of each each data sets.

where $p_n$ and $p_p$ are the effective nucleon polarization in polarized $^3$He and are equal to [Friar, 1990]:

$$p_n = 0.86 \pm 0.02 \tag{7.11}$$

$$p_p = -0.028 \pm 0.004 \tag{7.12}$$

In fact, a full convolution approach [Bissey, 2002] should be performed using the $^3$He spectral functions $\Delta f_{n/^3\mathrm{He}}$ and $\Delta f_{p/^3\mathrm{He}}$:

$$g_{1,2}^{^3\mathrm{He}}(x, Q^2) = \int_x^3 \frac{dy}{y} \Delta f_{n/^3\mathrm{He}}(y) g_{1,2}^n(\frac{x}{y}, Q^2) \tag{7.13}$$

$$+\int_x^3 \frac{dy}{y}\Delta f_{p/^3\mathrm{He}}(y) g_{1,2}^p(\frac{x}{y}, Q^2) \qquad (7.14)$$

However, this approach was developed in the Bjorken limit with $Q^2$-independent spectral functions. In the resonance region, the structure functions show a strong $Q^2$-dependence due to large nuclear effects. Therefore, new $^3$He spectral functions are being calculated [Melnitchouk, 2006] in order to reflect these effects by adding a $Q^2$-dependence:

$$\begin{aligned} \Delta f_{n/^3\mathrm{He}}(x) &\longrightarrow \Delta f_{n/^3\mathrm{He}}(x, Q^2) \\ \Delta f_{p/^3\mathrm{He}}(x) &\longrightarrow \Delta f_{p/^3\mathrm{He}}(x, Q^2) \end{aligned}$$

These calculations were not complete at the time of this thesis, so the following method was used.

To perform a test of quark-hadron duality on the neutron, as for $^3$He, partial moments of structure functions need to be evaluated. In their analysis, Ciofi degli Atti and Scopetta [Ciofi degli Atti, 1997] integrated Eq. (7.10) and found:

$$\tilde{\Gamma}_1^{^3\mathrm{He}} = p_n\ \tilde{\Gamma}_1^n + 2\ p_p\ \tilde{\Gamma}_1^p \qquad (7.15)$$

which is applicable to both the resonance and DIS regions. They compared this method with the full convolution approach and found very good agreement in DIS, and a discrepancy smaller than 5% in the resonance region for $Q^2 > 1$ (GeV/c)$^2$. This will be added to the systematic uncertainties of $\tilde{\Gamma}_1^n$.

Eq. (7.15) was used to extract the partial moment of $g_1$ for the neutron over the resonance region. The results for $\tilde{\Gamma}_1$ on the neutron are presented

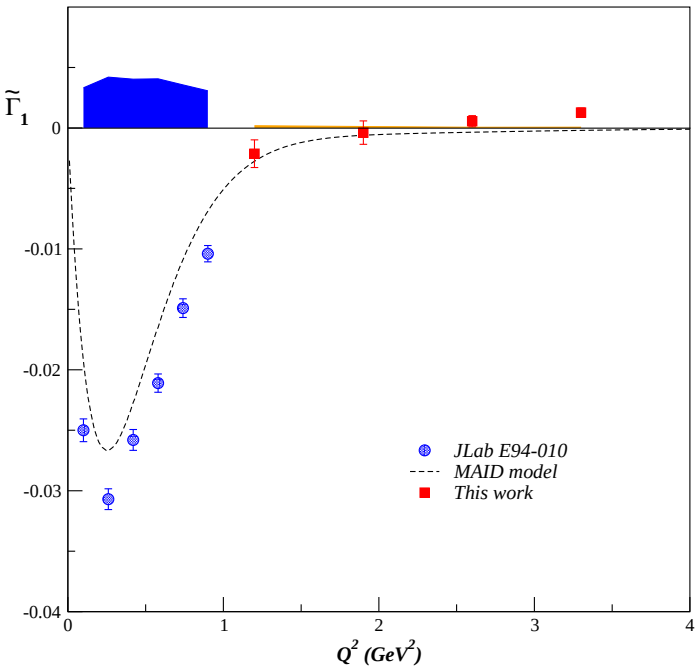


**Figure 7.18:** First moment of $g_1$ for the neutron. Also plotted are data for the same quantity from E94-010 [Amarian, 2004]. The curve is from the MAID model [Drechsel, 2001]. The orange and blue bands represent the systematic uncertainties of each each data sets.

in Fig. 7.18 and in Table 7.3. The proton contribution is evaluated from the data of JLab experiment EG1b [Prok, 2004]. As for $^3$He, the neutron data show a smooth transition between the low and high $Q^2$ regions.

| $Q^2$ | $\tilde{\Gamma}_1^{^3\mathrm{He}}$ | stat. | syst | $\tilde{\Gamma}_1^n$ | stat. | syst |
|---|---|---|---|---|---|---|
| 1.2 | -3.660E-03 | 0.976E-03 | 0.141E-03 | -2.132E-03 | 1.144E-03 | 0.183E-03 |
| 1.9 | -1.967E-03 | 0.831E-03 | 0.096E-03 | -0.386E-03 | 0.967E-03 | 0.113E-03 |
| 2.6 | -0.429E-03 | 0.396E-03 | 0.041E-03 | 0.554E-03 | 0.462E-03 | 0.056E-03 |
| 3.3 | 0.049E-03 | 0.313E-03 | 0.038E-03 | 1.276E-03 | 0.370E-03 | 0.063E-03 |

**Table 7.3:** $\tilde{\Gamma}_1^{^3\mathrm{He}}$ and $\tilde{\Gamma}_1^n$ for $Q^2$ of 1.2, 1.9, 2.6 and 3.3 (GeV/c)$^2$

### 7.6.2 Test of global duality

Since the DIS behavior is predicted by Parton Distribution Functions which assume a target mass of zero, a correction to take into account the non-zero mass dependence of our data must be applied. These target mass corrections (TMC) are done following the formalism of [Sidorov, 2006]:

$$\begin{aligned} g_1^{\mathrm{TMC}}(x,Q^2) &= \frac{x}{\xi(1+4M^2x^2/Q^2)^{3/2}} g_1(\xi,Q^2;M=0) \\ &+ \frac{4M^2x^2}{Q^2}\frac{x+\xi}{\xi(1+4M^2x^2/Q^2)^2}\int_\xi^1 \frac{d\xi'}{\xi'} g_1(\xi',Q^2;M=0) \\ &- \frac{4M^2x^2}{Q^2}\frac{2-4M^2x^2/Q^2}{2(1+4M^2x^2/Q^2)^{5/2}}\int_\xi^1 \frac{d\xi'}{\xi'}\int_{\xi'}^1 \frac{d\xi''}{\xi''} g_1(\xi'',Q^2;M=0) \end{aligned} \tag{7.16}$$

where $g_1(x,Q^2;M=0)$ is the pQCD parametrization of $g_1$ obtained at Leading or Next-to-Leading Order when target mass corrections are neglected.

Figs. 7.19 through 7.22 present the comparison of the integral of $g_1$ over the resonance region to DIS parametrizations [Blumlein, 2002, Gluck, 2001] abbreviated "BB" and "GRSV" respectively. Both parametrizations were taken at Next-to-Leading Order. The data plotted are the same as in Figs. 7.17 and 7.18. Target mass corrections have been applied to the DIS parametrizations. Our data are about $2\sigma$ away from the BB parametrization for our lowest and highest $Q^2$. However all our data agree within uncertainties with the GRSV parametrization, considering that the parametrization should also have an error band (the uncertainties on $g_1$ was not given). Therefore, it appears that quark-hadron duality holds globally even down to $Q^2 = 1.2$ GeV$^2$.

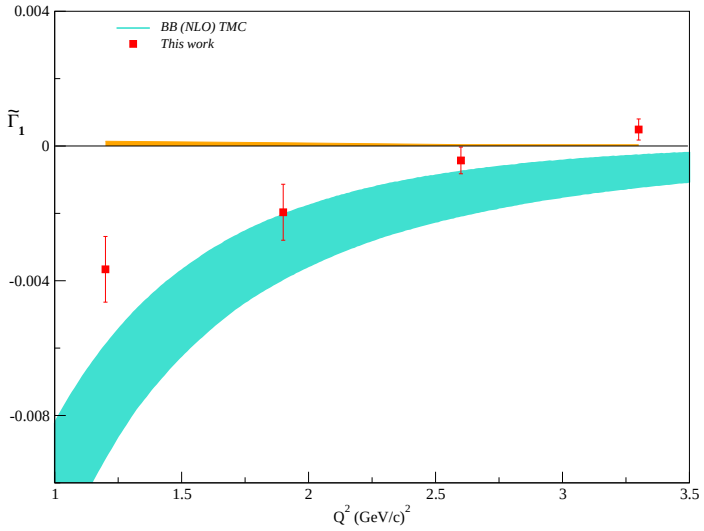


**Figure 7.19:** Test of spin duality on $^3$He. The blue band is from the DIS parametrization of Blumlein and Bottcher [Blumlein, 2002] with target mass corrections applied. The orange band represents the systematic uncertainty of our data.

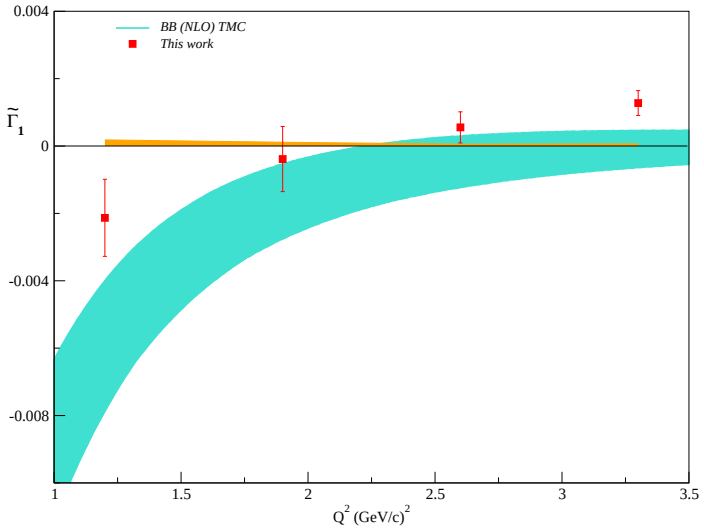


**Figure 7.20:** Same legend as in Fig. 7.19 for the neutron.

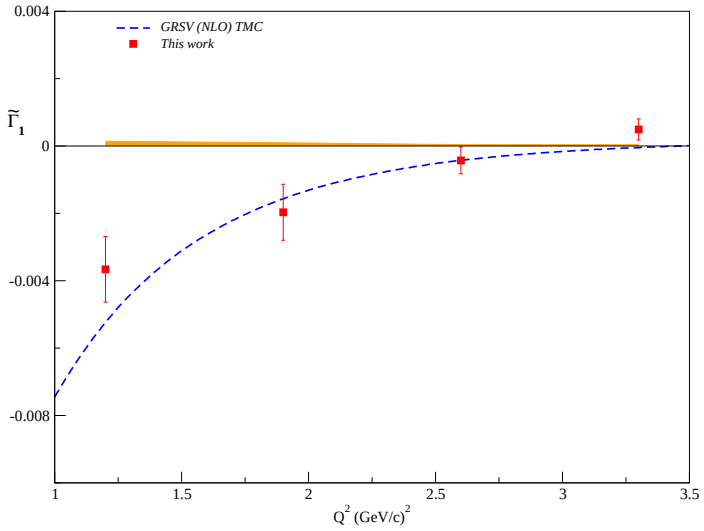


**Figure 7.21:** Test of spin duality on $^3$He. The dashed curve is from the GRSV DIS parametrization [Gluck, 2001] with target mass corrections applied. The orange band represents the systematic uncertainty of our data.

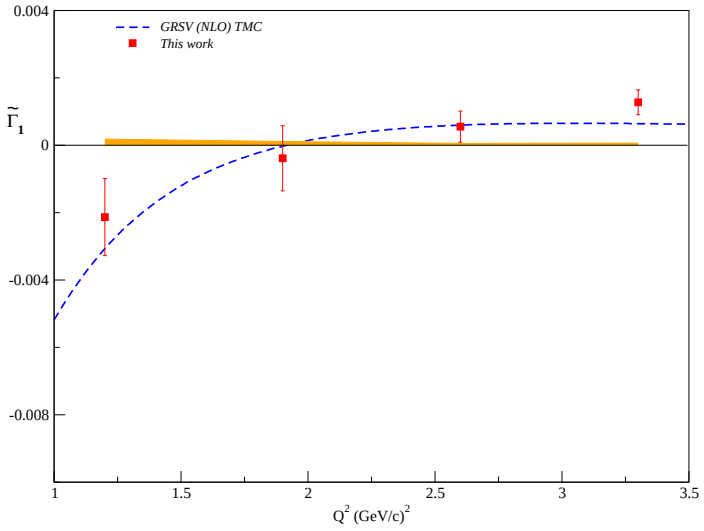


**Figure 7.22:** Same legend as in Fig. 7.21 for the neutron.

# CHAPTER 8

# CONCLUSION

Experiment E01-012 was dedicated to the study of the phenomenon of quark-hadron duality on the neutron ($^3$He) spin structure functions. The $Q^2$ coverage of the data was chosen to observe the onset of duality predicted from different theoretical approaches. For unpolarized structure functions, duality holds as low as $Q^2 \approx 0.5$ GeV$^2$. However preliminary data [Forest, 2006] for the proton spin structure function shows global duality breaking down below $Q^2 \approx 1.2$ GeV$^2$. From our data, global duality is observed at all $Q^2$ for both $^3$He and neutron structure functions $g_1$, after target mass corrections have been applied. Another interesting observation is the agreement of our $g_2^{^3\mathrm{He}}$ data with $g_2^{WW}$. This suggests that the quark-quark and quark-gluon correlations are weak or cancel, even down to $Q^2 = 1.2$ GeV$^2$.

Our data also provides a measurement of the virtual photon asymmetries $A_1$ and $A_2$ for $^3$He at large $x$ where no DIS data are yet available. Ultimately, the virtual photon-neutron asymmetries will be extracted when $^3$He spectral functions for the resonance region become available [Melnitchouk, 2006]. The $A_1^{^3\mathrm{He}}$ resonance data shows a weak $Q^2$-dependence for $Q^2 > 2.0$ GeV$^2$, as expected from DIS data. It is also interesting to note that the trend of our data deviates slightly from the DIS trend, going positive less rapidly and at

a higher $x$.

As for $A_2^{^3\mathrm{He}}$, we observed a weak $Q^2$-dependence. Also, our data suggests $A_2^{^3\mathrm{He}}$ becoming negative at large $x$, as was hinted by the recent DIS data.

Finally, our data will also be used in the near future to extract sum rules, as the extended GDH sum [Ji, 2001] and the Burkhardt-Cottingham sum rule [Burkhardt, 1970], and higher moments of structure functions which provide information on the transition from partonic to hadronic degrees of freedom.

# REFERENCES


[Abragam, 1996] Abragam, A. (1996). Principles of nuclear magnetism. New York, USA: Oxford University Press Inc.

[Ackerstaff, 1999] Ackerstaff, K. et al. (1999). Flavor decomposition of the polarized quark distributions in the nucleon from inclusive and semi-inclusive deep-inelastic scattering. *Phys. Lett.*, B464:123–134.

[Akushevich, 1994] Akushevich, I. V. and Shumeiko, N. M. (1994). Radiative effects in deep inelastic scattering of polarized leptons by polarized light nuclei. *J. Phys.*, G20:513–530.

[Alcorn, 2004] Alcorn, J. et al. (2004). Basic Instrumentation for Hall A at Jefferson Lab. *Nucl. Instrum. Meth.*, A522:294–346.

[Altarelli, 1977] Altarelli, G. and Parisi, G. (1977). Asymptotic freedom in parton language. *Nucl. Phys.*, B126:298.

[Amarian, 2004] Amarian, M. et al. (2004). $Q^2$-evolution of the neutron spin structure moments using a $^3$He target. *Phys. Rev. Lett.*, 92:022301.

[Amroun, 1994] Amroun, A. et al. (1994). $^3$H and $^3$He electromagnetic form-factors. *Nucl. Phys.*, A579:596–626.

[Anthony, 1996] Anthony, P. L. et al. (1996). Deep inelastic scattering of polarized electrons by polarized $^3$He and the study of the neutron spin structure. *Phys. Rev.*, D54:6620–6650.

[Armstrong, 2000] Armstrong, D. and Michaels, R. (2000). Jlab experiment E00-114. http://www.jlab.org/exp_prog/proposals/00/PR00-114.pdf.

[Babcock, 2005] Babcock, E., Nelson, I. A., Kadlecek, S., and Walker, T. G. (2005). $^3$He polarization-dependent EPR frequency shifts of alkali-metal-$^3$He pairs. *Physical Review A (Atomic, Molecular, and Optical Physics)*, 71(1):013414.

[Bianchi, 2004] Bianchi, N., Fantoni, A., and Liuti, S. (2004). Parton hadron duality in unpolarized and polarized structure functions. *Phys. Rev.*, D69:014505.

[Bissey, 2002] Bissey, F., Guzey, V., Strikman, M., and Thomas, A. W. (2002). Complete analysis of spin structure function $g_1$ of $^3$He. *Phys. Rev.*, C65:064317.

[Bjorken, 1969] Bjorken, J. D. and Paschos, E. A. (1969). Inelastic electron-proton and gamma-proton scattering, and the structure of the nucleon. *Phys. Rev.*, 185:1975–1982.

[Bloom, 1970] Bloom, E. D. and Gilman, F. J. (1970). Scaling, duality, and the behavior of resonances in inelastic electron-proton scattering. *Phys. Rev. Lett.*, 25:1140.

[Blumlein, 2002] Blumlein, J. and Bottcher, H. (2002). QCD analysis of polarized deep inelastic scattering data and parton distributions. *Nucl. Phys.*, B636:225–263.

[Bonin, 1988] Bonin, K. D., Walker, T. G., and Happer, W. (1988). Relaxation of gaseous spin-polarized $^3$He targets due to ionizing radiation. *Phys. Rev. A*, 37(9):3270–3282.

[Breidenbach, 1969] Breidenbach, M. et al. (1969). Observed behavior of highly inelastic electron-proton scattering. *Phys. Rev. Lett.*, 23:935–939.

[Brodsky, 1975] Brodsky, S. J. and Farrar, G. R. (1975). Scaling laws for large momentum transfer processes. *Phys. Rev.*, D11:1309.

[Burkhardt, 1970] Burkhardt, H. and Cottingham, W. N. (1970). Sum rules for forward virtual Compton scattering. *Annals Phys.*, 56:453–463.

[Callan, 1969] Callan, Curtis G., J. and Gross, D. J. (1969). High-energy electroproduction and the constitution of the electric current. *Phys. Rev. Lett.*, 22:156–159.

[Carlson, 1998] Carlson, C. E. and Mukhopadhyay, N. C. (1998). Bloom-Gilman duality in the resonance spin structure functions. *Phys. Rev.*, D58:094029.

[Cates, 1991] Cates, G. D. (1991). Polarization induced transport asymmetry of light pulses: the PITA effect. Technical report, MIT-BATES. Internal note.

[Cates, 1999] Cates, G. D., Kumar, K., and Lhuillier, D. (1999). Jlab experiment E99-115. http://www.jlab.org/exp_prog/proposals/99/PR99-115.pdf.

[Chann, 2002] Chann, B., Babcock, E., Anderson, L. W., and Walker, T. G. (2002). Measurements of $^3$He spin-exchange rates. *Phys. Rev. A*, 66(3):032703.

[Chen, 2005] Chen, J.-P., Deur, A., and Meziani, Z.-E. (2005). Sum rules and moments of the nucleon spin structure functions. *Mod. Phys. Lett.*, A20:2745–2766.

[Chen, 2001] Chen, J.-P. et al. (2001). Hall A polarized $^3$He target operation and safety procedure. Technical report, JLab. http://hallaweb.jlab.org/experiment/E01-012.

[Choi, 2003] Choi, S. (2003). Private communication.

[Chudakov, 2003] Chudakov, E. et al. (2003). Results 2003. http://www.jlab.org/~moller/2003_raw_results_archive.html.

[Ciofi degli Atti, 1997] Ciofi degli Atti, C. and Scopetta, S. (1997). On the extraction of the neutron spin structure functions and the Gerasimov-Drell-Hearn integral from $^3\vec{\mathrm{He}}(\vec{e},e')X$ data. *Phys. Lett.*, B404:223–229.

[Close, 1972] Close, F. E., Gilman, F. J., and Karliner, I. (1972). Electroproduction of nucleon resonances with polarized leptons. *Phys. Rev.*, D6:2533.

[Close, 2001] Close, F. E. and Isgur, N. (2001). The origins of quark hadron duality: How does the square of the sum become the sum of the squares? *Phys. Lett.*, B509:81–86.

[Close, 2003] Close, F. E. and Melnitchouk, W. (2003). Symmetry breaking and quark hadron duality in structure functions. *Phys. Rev.*, C68:035210.

[De Rujula, 1977] De Rujula, A., Georgi, H., and Politzer, H. D. (1977). Demythification of the electroproduction, local duality and precocious scaling. *Ann. Phys.*, 103:315.

[Deur, 1998] Deur, A. (1998). Knock-On of $\delta$-electrons in the Hall A electron arm. Effect of the aerogel Čerenkov. Technical report, JLab. JLab-TN-98-028.

[Deur, 2000a] Deur, A. (2000a). *Etude experimentale de la structure en spin du neutron ($^3$He) à bas $Q^2$: Une connexion entre les règles de somme de Bjorken and Gerasimov-Drell-Hearn.* PhD thesis, Université Blaise Pascal.

[Deur, 2000b] Deur, A. (2000b). Single arm Monte Carlo for polarized $^3$He experiments in Hall A. Technical report, E94010 Collaboration. http://www.jlab.org/e94010, TN-E94010-33.

[Dharmawardane, 2004] Dharmawardane, K. G. V. G. (2004). *Spin structure functions of the deuteron measured with CLAS in and above the resonance region.* PhD thesis, Old Dominion University.

[Dodge, 2005] Dodge, G. E. (2005). Spin structure functions: A window into the structure of hadrons. *J. Phys. Conf. Ser.*, 9:256–259.

[Dokshitzer, 1977] Dokshitzer, Y. L. (1977). Calculation of the structure functions for deep inelastic scattering and $e^+$-$e^-$ annihilation by perturbation theory in quantum chromodynamics. (In russian). *Sov. Phys. JETP*, 46:641–653.

[Donnelly, 1986] Donnelly, T. W. and Raskin, A. S. (1986). Considerations of polarization in inclusive electron scattering from nuclei. *Annals Phys.*, 169:247–351.

[Drechsel, 2001] Drechsel, D., Kamalov, S. S., and Tiator, L. (2001). The GDH sum rule and related integrals. *Phys. Rev.*, D63:114010.

[Edelmann, 2000] Edelmann, J., Piller, G., Kaiser, N., and Weise, W. (2000). Resonances and higher twist in polarized lepton nucleon scattering. *Nucl. Phys.*, A665:125–136.

[Farrar, 1975] Farrar, G. R. and Jackson, D. R. (1975). Pion and nucleon structure functions near x = 1. *Phys. Rev. Lett.*, 35:1416.

[Fatemi, 2003] Fatemi, R. et al. (2003). Measurement of the proton spin structure function $g_1(x, Q^2)$ for $Q^2$ from 0.15-GeV$^2$ to 1.6-GeV$^2$ with CLAS. *Phys. Rev. Lett.*, 91:222002.

[Feynman, 1969] Feynman, R. P. (1969). Very high-energy collisions of hadrons. *Phys. Rev. Lett.*, 23:1415–1417.

[Forest, 2006] Forest, T. et al. (2006). In preparation.

[Friar, 1990] Friar, J. L., Gibson, B. F., Payne, G. L., Bernstein, A. M., and Chupp, T. E. (1990). Neutron polarization in polarized $^3$He targets. *Phys. Rev.*, C42:2310–2314.

[Friedman, 1972] Friedman, J. I. and Kendall, H. W. (1972). Deep inelastic electron scattering. *Ann. Rev. Nucl. Part. Sci.*, 22:203–254.

[Gluck, 2001] Gluck, M., Reya, E., Stratmann, M., and Vogelsang, W. (2001). Models for the polarized parton distributions of the nucleon. *Phys. Rev.*, D63:094005.

[Grames, 2000] Grames, J. M. (2000). *Measurement of a weak polarization sensitivity to the beam orbit of the CEBAF accelerator.* PhD thesis, University of Illinois at Urbana-Champaign.

[Gribov, 1972] Gribov, V. N. and Lipatov, L. N. (1972). Deep inelastic e-p scattering in perturbation theory. *Sov. J. Nucl. Phys.*, 15:438–450.

[Hand, 1963] Hand, L. N. (1963). Experimental investigation of pion electroproduction. *Phys. Rev.*, 129:1834–1846.

[Happer, 1972] Happer, W. (1972). Optical pumping. *Rev. Mod. Phys.*, 44(2):169–249.

[Humensky, 2003] Humensky, T. B. (2003). *Probing the standard model and nucleon structure via parity-violating electron scattering.* PhD thesis, Princeton University.

[Ibrahim, 2002] Ibrahim, H., Ulmer, P., and Liyanage, N. (2002). Calibration of spectrometer central angles using Hall A HRS in $^1$H(e, e′p). Technical report, JLab. JLab-TN-02-032.

[Incerti, 1998a] Incerti, S. (1998a). *Mesure de la fonction de structure polarisée $g_1^n$ du neutron par l'experience E154 au SLAC.* PhD thesis, Université Blaise Pascal.

[Incerti, 1998b] Incerti, S. (1998b). The NMR system of the Hall A polarized $^3$He target. Technical report, JLab. JLab-TN-98-049.

[Incerti, 1998c] Incerti, S. and Lakuriqi, E. (1998c). Model of the water signal shape from the Bloch equations. Technical report, E94010 Collaboration. http://www.jlab.org/e94010, TN-E94010-10.

[Jensen, 2000] Jensen, J. S. (2000). *Measurement of the neutron ($^3$He) spin structure function at low $Q^2$: a connection between the Bjorken and Drell-Hearn-Gerasimov sum rules.* PhD thesis, California Institute of Technology.

[Ji, 1997] Ji, X.-D. and Melnitchouk, W. (1997). Spin-dependent twist-four matrix elements from g1 data in the resonance region. *Phys. Rev.*, D56:1–5.

[Ji, 2001] Ji, X.-D. and Osborne, J. (2001). Generalized sum rules for spin-dependent structure functions of the nucleon. *J. Phys.*, G27:127.

[JLab Alignment Group, 2003] JLab Alignment Group (2003). Survey Reports. Technical report, JLab. http://hallaweb.jlab.org/news/minutes/Survey_Reports.

[Jones, 2002] Jones, M. (2002). Report on BCM calibration for Nov 13 2002 run. Technical report, JLab.

[Justis, 2004] Justis, N. (2004). Measuring glass thickness of a reference cell used in a polarized $^3$He experiment. Technical report, Brigham Young University.

[Kendall, 1991] Kendall, H. W. (1991). Deep inelastic scattering: Experiments on the proton and the observation. *Rev. Mod. Phys.*, 63:597–614.

[Killian, 1926] Killian, T. J. (1926). Thermionic phenomena caused by vapors of Rubidium and Potassium. *Phys. Rev.*, 27(5):578–587.

[Korsch, 1998] Korsch, W. (1998). Technical note on EPR. Technical report, E94010 Collaboration. http://www.jlab.org/e94010, TN-E94010-11.

[Kramer, 2005] Kramer, K. et al. (2005). The $Q^2$-dependence of the neutron spin structure function g2(n) at low $Q^2$. *Phys. Rev. Lett.*, 95:142002.

[Kramer, 2003] Kramer, K. M. (2003). *A search for higher twist effects in the neutron spin structure function* $g_2^n(x, Q^2)$. PhD thesis, The College of William and Mary.

[Leo, 1987] Leo, W. R. (1987). Techniques for nuclear and particle physics experiments: A how to approach. Berlin, Germany: Springer.

[Lepage, 1979] Lepage, G. P. and Brodsky, S. J. (1979). Exclusive processes in quantum chromodynamics: the form-factors of baryons at large momentum transfer. *Phys. Rev. Lett.*, 43:545–549.

[Liang, 2004] Liang, Y. et al. (2004). Measurement of $R = \sigma_L/\sigma_T$ and the separated longitudinal and transverse structure functions in the nucleon resonance region.

[Lightbody Jr., 1988] Lightbody Jr., J. W. and O'Connell, J. S. (1988). Modeling single arm electron scattering and nucleon production from nuclei by GeV electrons. *Computers in Physics*, May/June:57.

[Liyanage, 2001] Liyanage, N. (2001). Spectrometer constant determination for the Hall A high resolution spectrometer pair. Technical report, JLab. JLab-TN-01-049.

[Liyanage, 2002] Liyanage, N. (2002). Optics calibration of the Hall A high resolution spectrometers using the new optimizer. Technical report, JLab. JLab-TN-02-012.

[Liyanage, 2005] Liyanage, N. (2005). Private communication.

[Manohar, 1992] Manohar, A. V. (1992). An introduction to spin dependent deep inelastic scattering.

[Matsui, 2005] Matsui, K., Sato, T., and Lee, T. S. H. (2005). Quark-hadron duality and parity violating asymmetry of electroweak reactions in the Delta region. *Phys. Rev.*, C72:025204.

[Mecking, 2003] Mecking, B. A. et al. (2003). The CEBAF Large Acceptance Spectrometer (CLAS). *Nucl. Instrum. Meth.*, A503:513–553.

[Melnitchouk, 2005] Melnitchouk, W., Ent, R., and Keppel, C. (2005). Quark-hadron duality in electron scattering. *Phys. Rept.*, 406:127–301.

[Melnitchouk, 2006] Melnitchouk, W. et al. (2006). In preparation.

[Meziani, 2005] Meziani, Z. E. et al. (2005). Higher twists and color polarizabilities in the neutron. *Phys. Lett.*, B613:148–153.

[Mo, 1969] Mo, L. W. and Tsai, Y.-S. (1969). Radiative corrections to elastic and inelastic e-p and $\mu$-p scattering. *Rev. Mod. Phys.*, 41:205–235.

[Newbury, 1993] Newbury, N. R., Barton, A. S., Cates, G. D., Happer, W., and Middleton, H. (1993). Gaseous $^3$He-$^3$He magnetic dipolar spin relaxation. *Phys. Rev. A*, 48(6):4411–4420.

[Niculescu, 2000] Niculescu, I. et al. (2000). Evidence for valencelike quark hadron duality. *Phys. Rev. Lett.*, 85:1182–1185.

[Pitt, 2001] Pitt, M. (2001). Helicity control requests from the $G^0$ experiment. Technical report, $G^0$ Collaboration. http://g0web.jlab.org/DocDB/0002/000236/001/g0_helicity.pdf.

[Prok, 2004] Prok, Y. A. (2004). *Measurement of the spin structure function $g_1(x, Q^2)$ of the proton in the resonance region.* PhD thesis, University of Virginia.

[Romalis, 1997] Romalis, M. V. (1997). *Laser polarized* $^3$He *target used for a precision measurement of the neutron spin structure.* PhD thesis, Princeton University.

[Romalis, 1998] Romalis, M. V. and Cates, G. D. (1998). Accurate $^3$He polarimetry using the Rb Zeeman frequency shift due to the $Rb - {}^3$He spin-exchange collisions. *Phys. Rev. A*, 58(4):3004–3011.

[Rosenbluth, 1950] Rosenbluth, M. N. (1950). High Energy Elastic Scattering of Electrons on Protons. *Phys. Rev.*, 79(4):615–619.

[Sato, 1996] Sato, T. and Lee, T.-S. H. (1996). Meson-exchange model for $\pi$-N scattering and $\gamma$-N $\rightarrow$ $\pi$-N reaction. *Phys. Rev. C*, 54(5):2660–2684.

[Sidorov, 2006] Sidorov, A. V. and Stamenov, D. B. (2006). Target mass effects in polarized deep inelastic scattering. *Mod. Phys. Lett.*, A21:1991.

[Singh, 2003] Singh, J. (2003). Cell data table. http://galileo.phys.virginia.edu/research/groups/spinphysics/celldata.htm.

[Singh, 2005] Singh, J. (2005). Private communication.

[Slifer, 2000] Slifer, K. (2000). Shower detector calibration and cut optimization for E94010. Technical report, E94010 Collaboration. http://www.jlab.org/e94010, TN-E94010-31.

[Slifer, 2003] Slifer, K. (2003). Modifications to the QFS and RADCOR codes. Technical report, E94010 Collaboration. http://www.jlab.org/e94010, TN-E94010-44.

[Slifer, 2004] Slifer, K. (2004). *Spin structure of* $^3$He *and the neutron at low* $Q^2$*; A measurement of the extended GDH integral and the Burkhardt-Cottingham sum rule.* PhD thesis, Temple University.

[Slifer, 2006] Slifer, K. et al. (2006). In preparation.

[Soffer, 2000] Soffer, J. and Teryaev, O. V. (2000). Positivity constraints and flavor dependence of higher twists. *Phys. Lett.*, B490:106–110.

[Solvignon, 2002] Solvignon, P. (2002). Lifetime and AFP loss study of 3He target cells. Technical report, Temple University. http://www.jlab.org/~solvigno/reports/note-lifetime.pdf.

[Solvignon, 2004a] Solvignon, P. (2004a). PID detector calibration for E01-012. Technical report, E01012 Collaboration. http://hallaweb.jlab.org/experiment/E01-012, E01-012 analysis report 01.

[Solvignon, 2004b] Solvignon, P. (2004b). PID efficiency for E01-012. Technical report, E01012 Collaboration. http://hallaweb.jlab.org/experiment/E01-012, E01-012 analysis report 02.

[Solvignon, 2004c] Solvignon, P. (2004c). Study of the acceptance cut effect on the cross section for E01-012. Technical report, E01012 Collaboration. http://hallaweb.jlab.org/experiment/E01-012, E01-012 analysis report 03.

[Solvignon, 2005a] Solvignon, P. (2005a). Estimate of the total radiation lengths during E01-012. Technical report, E01012 Collaboration. http://hallaweb.jlab.org/experiment/E01-012, E01-012 analysis report 07.

[Solvignon, 2005b] Solvignon, P. (2005b). Target density during E01-012. Technical report, E01012 Collaboration. http://hallaweb.jlab.org/experiment/E01-012, E01-012 analysis report 05.

[Solvignon, 2006a] Solvignon, P. (2006a). Nitrogen cross sections and dilution factor for $1.0 < Q^2 < 4.0$ (GeV/c)$^2$. Technical report, E01012 Collaboration. http://hallaweb.jlab.org/experiment/E01-012, E01-012 analysis report 08.

[Solvignon, 2006b] Solvignon, P. (2006b). Target density from pressure curves for E01-012. Technical report, E01012 Collaboration. http://halla web.jlab.org/experiment/E01-012, E01-012 analysis report 09.

[Stratmann, 1993] Stratmann, M. (1993). Bag model predictions for polarized structure functions and their $Q^2$ evolutions. *Z. Phys.*, C60:763–772.

[Sulkosky, 2003] Sulkosky, V. (2003). Cell wall thickness measurements. http://www.jlab.org/∼vasulk/cell_thickness.html.

[Sulkosky, 2006] Sulkosky, V. (2006). Cell characteristics and the NMR system and analysis for E01-012. Technical report, E01012 Collaboration. http://hallaweb.jlab.org/experiment/E01-012, (in preparation).

[The Controls Software Group, 2004] The Controls Software Group (2004). The EPICS control system at Jefferson Lab. http://www.jlab.org/accel/ documents/epics_doc.html.

[The JLab CODA Group , 1995] The JLab CODA Group (1995). CODA, CEBAF online data acquisition. Technical report, JLab. *User's manual*, http://coda.jlab.org/manuals.htm.

[The Jlab HallA Collaboration, 2002] The Jlab HallA Collaboration (2002). ESPACE manual: Event scanning program for Hall A collaboration experiments. Technical report, JLab. http://hallaweb.jlab.org/espace.

[Thomas, 2001] Thomas, A. W. and Weise, W. (2001). The structure of the nucleon. Berlin, Germany: Wiley-VCH.

[Tiefenback, 2006] Tiefenback, M. (2006). Private communication.

[Tvaskis, 2004] Tvaskis, V. (2004). *Longitudinal-transverse separation of deep-inelastic scattering at low $Q^2$ on nucleons and nuclei.* PhD thesis, Vrije Universiteit.

[Unser, 1981] Unser, K. (1981). A toroidal DC beam current transformer with high resolution. *IEEE Trans. Nucl. Sci.*, 28:2344–2346.

[Vacheret, 2004a] Vacheret, A. (2004a). Private communication.

[Vacheret, 2004b] Vacheret, A. (2004b). *Precision measurements of parity violation in electron scattering: experiments HAPPEX and E158.* PhD thesis, Université Louis Pasteur.

[Wagshul, 1994] Wagshul, M. E. and Chupp, T. E. (1994). Laser optical pumping of high-density Rb in polarized $^3$He targets. *Phys. Rev. A*, 49(5):3854–3869.

[Wandzura, 1977] Wandzura, S. and Wilczek, F. (1977). Sum rules for spin dependent electroproduction: test of relativistic constituent quarks. *Phys. Lett.*, B72:195.

[Weigel, 1997] Weigel, H., Gamberg, L. P., and Reinhardt, H. (1997). Polarized nucleon structure functions within a chiral soliton model. *Phys. Rev.*, D55:6910–6923.

[Wilson, 1969] Wilson, K. G. (1969). Non-lagrangian models of current algebra. *Phys. Rev.*, 179:1499–1512.

[Zheng, 2002] Zheng, X. (2002). *Precision measurement of neutron spin asymmetry $A_1^n$ at large $x_{Bj}$ using CEBAF at 5.7 GeV.* PhD thesis, Massachusetts Institut of Technology.

[Zheng, 2004] Zheng, X. et al. (2004). Precision measurement of the neutron spin asymmetries and spin-dependent structure functions in the valence quark region. *Phys. Rev.*, C70:065207.

# APPENDIX A

# RADIATIVE CORRECTIONS

Because of the different materials along its path, the incident electron loses energy by bremsstrahlung before scattering from the target. Consequently the incident energy at the reaction vertex is less than the one measured at the polarized electron source. Also, after scattering, the electron passes through other materials losing energy before arriving at the detector. So the energy of the scattered electron is higher at the vertex than what is measured. Therefore, external radiative corrections must be applied to evaluate the measured quantities (cross sections, asymmetries) at the true kinematics of the reaction. A schematic of the different materials in the path of the electrons is illustrated in Fig B.1 and the measured radiation lengths can be found in Appendix B.

In addition to the external radiative corrections, internal corrections are needed to account for internal bremsstrahlung, vertex corrections and other diagrams. These internal reactions can also trigger a spin flip in the target constituents which must be also considered.

Internal and external radiative corrections on the unpolarized cross sections are applied using the formalism of Mo and Tsai [Mo, 1969], through the modified FORTRAN code RADCOR.F [Slifer, 2003]. For the polarized cross

section differences, we used also Mo and Tsai [Mo, 1969] for the external part since the materials surrounding the target is unpolarized, and the formalism of [Akushevich, 1994] for the internal radiative corrections.

In the radiative correction, an iterative procedure is used to extract the Born cross section from the measured cross section. The program uses the experimental cross section as a first guess for the Born cross section. Using a cross section model or data at lower energies, the integral over all the energy spectra is performed and the input cross section is radiated. This radiated cross section is then compared to the initial experimental cross section. The difference is applied to the input cross section and the radiative corrections run for another iteration. After several cycles of this type, the procedure converges to the Born cross section.

Before all, the elastic radiative tail should be subtracted from the experimental cross section. At all our kinematics, this contribution was found to be three to four orders of magnitude smaller than the experimental cross section therefore negligible.

## A.1 Unpolarized cross section model

In order to perform the radiative corrections on our experimental cross sections, a cross section model is therefore needed. The kinematic range relevant to the unfolding is represented in Fig. A.1 by a "triangle" area for each of incident energy and scattering angle.

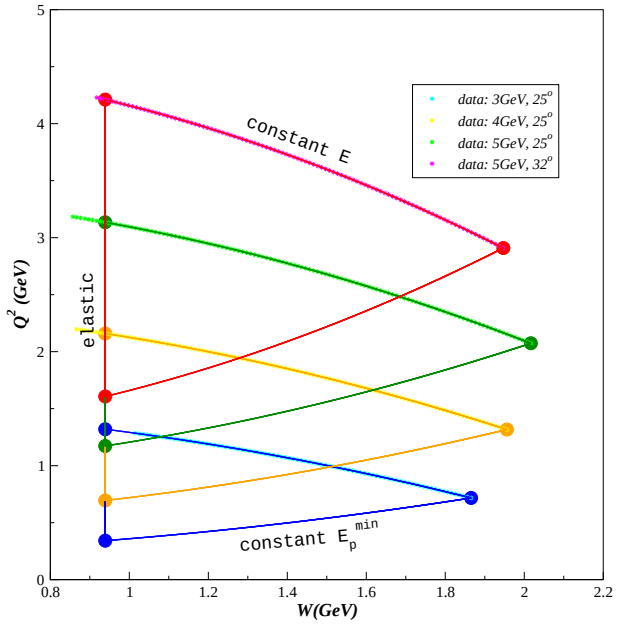


**Figure A.1:** Kinematic coverage needed in the unfolding procedure. Our data are on the upper side of the "triangle". $E_p^{min}$ corresponds to the pion threshold. The "triangle" area represents the kinematics needed in the radiative correction procedure for each of our energy and scattering angle setting.

For our three highest settings, our own data can be used. The unpolarized cross sections from JLab Hall A experiment E94-010 [Slifer, 2004] are in the range needed for our lowest point as shown in Fig. A.2.

Because E94-010 data were measured at a different scattering angle, a model $\sigma_o^m(x, Q^2, \theta_k)$ based on these data was created where $\theta_k$ represents our scattering angles. First, the needed $x$-$Q^2$ (or $W$-$Q^2$) coverage is calculated along constant energy and scattering angle $\theta_k$ lines. The E94-010 unpolarized cross sections $\sigma_0^d(E, E', \theta_d)$ are then interpolating to the defined values of $x$-$Q^2$, $\sigma_0^d(x, Q^2, \theta_d)$. The final step is to convert $\sigma_0^d(x, Q^2, \theta_d)$ to $\sigma_o^m(x, Q^2, \theta_k)$.

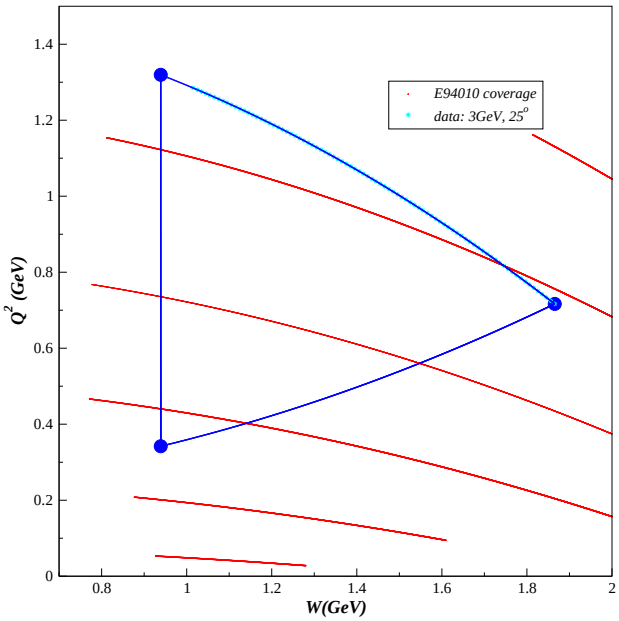


**Figure A.2:** Kinematic coverage needed for our data at incident energy of 3.0 GeV and scattering angle of 25°. Shown also on the plot, is the good kinematic coverage provided by experiment E94-010 data.

These three steps are realized by using the following relation:

$$\sigma_o^m(Q^2,x,\theta_k) = \frac{\sigma_{Mott}^k}{\sigma_{Mott}^d}\,\frac{\epsilon_d}{\epsilon_k}\,\frac{1+\epsilon_k\ R(x,Q^2)}{1+\epsilon_d\ R(x,Q^2)}\,\sigma_0^d(Q^2,x,\theta_d) \tag{A.1}$$

which is equivalent to forming the unpolarized structure function $F_2(x,Q^2)$ between $\sigma_o^m$ and $\sigma_0^d$. The quantity $\epsilon_{d,k}$ is defined by Eq. (2.16) for $\theta = \theta_{d,k}$. The expression of $\sigma_{Mott}^{d,k}$ is given in Eq (2.14) for $\theta = \theta_{d,k}$. The unpolarized cross section model at $\theta_k = 25°$ is shown in Fig. A.3.

After performing the radiative corrections for our 3.0 GeV energy data, the resulting Born cross section will become part of the model in the radiative corrections of our 4.0 GeV energy data, which Born cross section can then

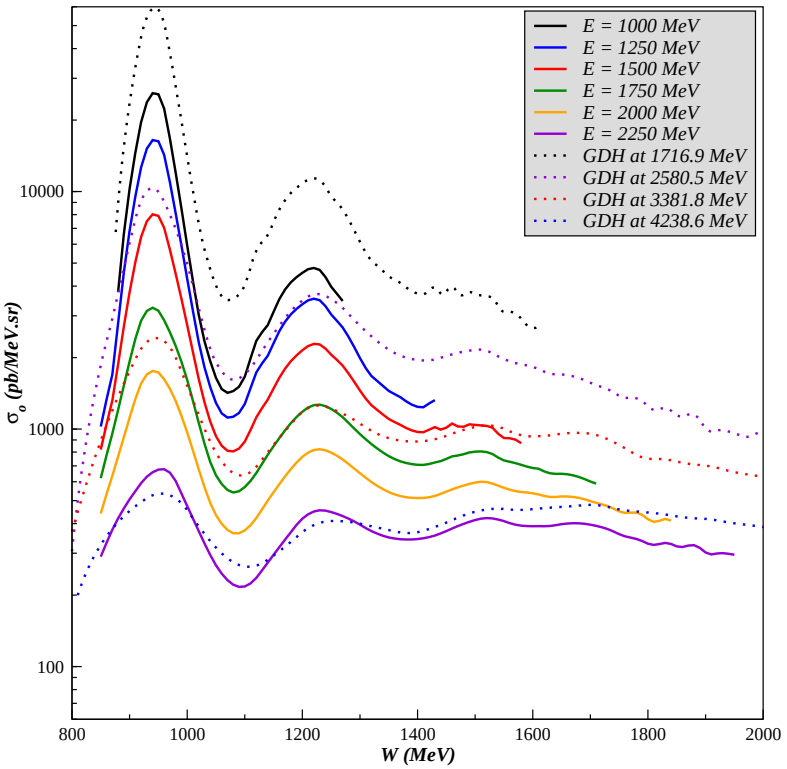


**Figure A.3:** Unpolarized cross section model at scattering angle of 25° (solid line). E94-010 cross sections are also plotted with the label "GDH".

be used for 5.0 GeV energy data. The same model can still be used as long as the scattering angle stays unchanged. For the highest kinematics, the scattering angle is 32°. So the same method, summarized in Eq. A.1, is used for $\theta_k = 32°$. But now, the interpolation is done with respect to our 25° data as shown in Fig. A.4.

The Quasi-Free Scattering model (QFS) [Lightbody Jr., 1988] was also used for the radiative corrections of our unpolarized cross sections in order to check the model dependence to the final cross section. The variation of

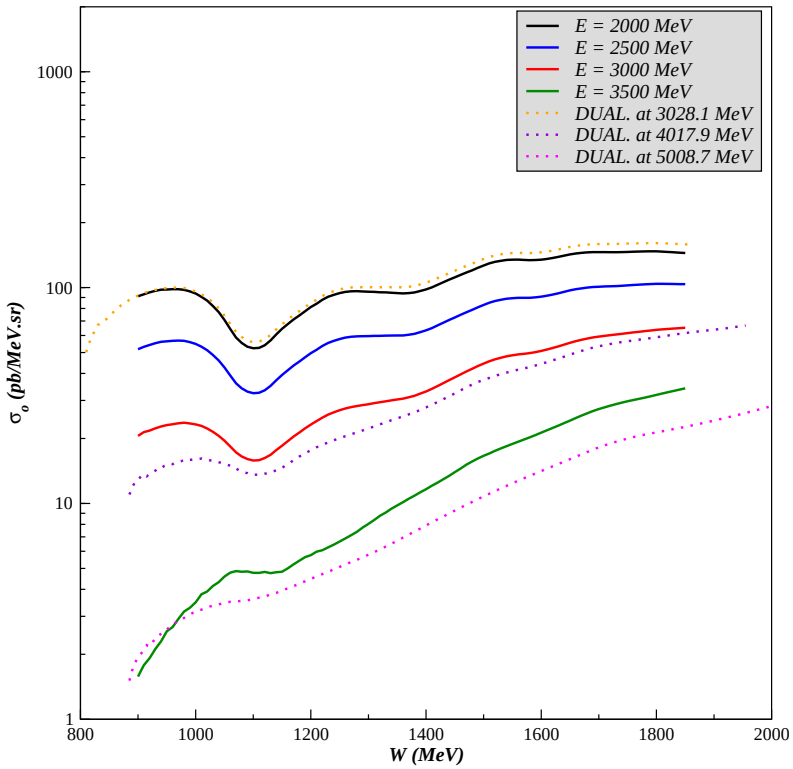


**Figure A.4:** Unpolarized cross section model at scattering angle of 32° (solid lines). Also plotted are our 25° data (dashed lines).

the resulting Born cross sections between the two models was found to be less than 5% and was taken into account in the final systematic errors.

## A.2 Polarized cross section model

Lower energy inputs are also necessary to perform radiative corrections on the polarized cross section differences. The procedure is very similar to that described in the previous section, except for the fact that here, the spin

structure functions $g_1(x, Q^2)$ and $g_2(x, Q^2)$ from E94-010 are interpolated to the needed $(Q^2, x)$ range. The polarized cross sections, $\Delta\sigma_{||}(x, Q^2, \theta_k)$ and $\Delta\sigma_{\perp}(x, Q^2, \theta_k)$, can then be determined from $g_1(x, Q^2)$ and $g_2(x, Q^2)$ using Eqs. (2.21) and (2.21) , at the desired scattering angle $\theta_k = 25^\circ$ and energies. For the $32^\circ$ data, the interpolated structure functions are extracted from our data on $g_{1,2}$ at $\theta = 25^\circ$.

# APPENDIX B

# RADIATION LENGTHS

In this appendix, we give the total radiation lengths before and after scattering used to applied the radiative corrections (see Appendix A).

The different materials that the incident and scattered electrons encounter on their paths is illustrated in Fig. B.1.

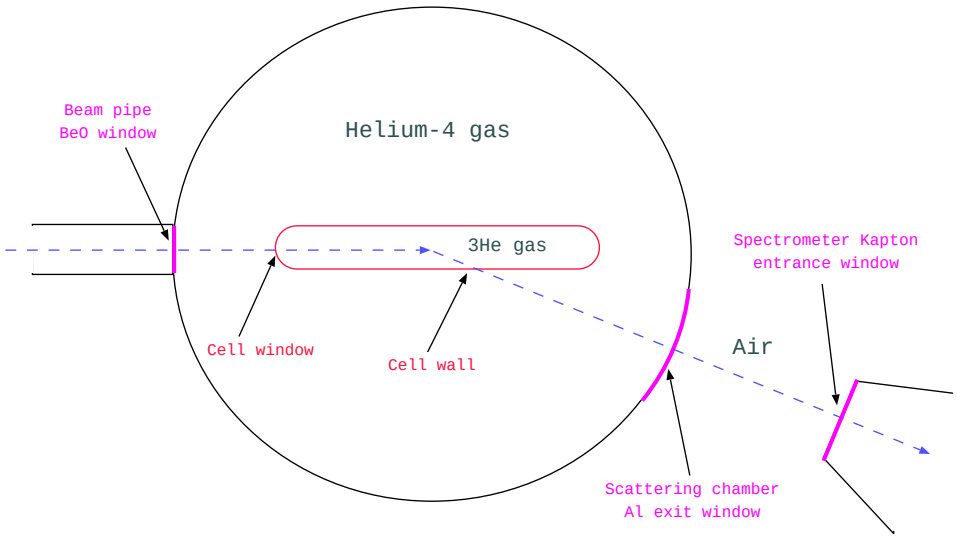


**Figure B.1:** Schematic of the different materials on the incident and scattered electron paths.

## B.1 Polarized $^3$He cells

All glass thickness measurements performed on cells used during experiment E01-012 are summarized in [Solvignon, 2005a] with details on the total radiation length calculations. The measurements are from [Singh, 2003], [Sulkosky, 2003] and [Justis, 2004].

### B.1.1 Radiation lengths before scattering

| Material | $X_0$ (cm) | | thickness (cm) | | # of $X_0$ | |
|---|---|---|---|---|---|---|
| | Duke | Exodus | Duke | Exodus | Duke | Exodus |
| Be | 35.28 | | 0.01778 | | $5.04\times10^{-4}$ | |
| $^4$He | 528107 | | 28.28 | | $5.35\times10^{-5}$ | |
| glass | 7.04 | | 0.0108 | 0.0101 | $1.53\times10^{-3}$ | $1.43\times10^{-3}$ |
| $^3$He | 43423 | 41975 | 19.7 | 19.8 | $4.54\times10^{-4}$ | $4.72\times10^{-4}$ |
| **Total** | | | | | $\mathbf{2.55\times10^{-3}}$ | $\mathbf{2.46\times10^{-3}}$ |

**Table B.1:** Radiation lengths of the material encountered before scattering.

### B.1.2 Radiation lengths after scattering

### B.1.3 Summary

The radiation lengths to be used for the radiative corrections are summarized in table B.3.

| Material | $X_0$ (cm) | | thickness (cm) | | # of $X_0$ | |
|---|---|---|---|---|---|---|
| | Duke | Exodus | Duke | Exodus | Duke | Exodus |
| $^3$He | 43423 | 41975 | $0.958/\sin\theta$ | $0.940/\sin\theta$ | $2.21\times10^{-5}/\sin\theta$ | $2.24\times10^{-5}/\sin\theta$ |
| glass (L) | 7.04 | | $0.141/\sin\theta$ | $0.118/\sin\theta$ | $0.0200/\sin\theta$ | $0.0168/\sin\theta$ |
| glass (R) | 7.04 | | $0.138/\sin\theta$ | $0.115/\sin\theta$ | $0.0196/\sin\theta$ | $0.0163/\sin\theta$ |
| $^4$He | 528107 | | 45.7 | | $8.65\times10^{-5}$ | |
| Al | 8.9 | | 0.04064 | | $4.57\times10^{-3}$ | |
| Air | 30423 | | 65.1 | | $2.14\times10^{-3}$ | |
| Kapton | 28.6 | | 0.01778 | | $6.22\times10^{-4}$ | |

**Table B.2:** Radiation lengths of the material encountered after scattering.

### Uncertainties

The total uncertainty on the wall and window measurements is about 0.6% and the errors arising with using the average value for the wall and window thicknesses are 3% and 1% respectively.

Before the experiment, the aluminum windows were measured with a caliper. The average is 17.06 mils* for the right side and 17.76 mils for the left arm. They were designed to be 15 mils thick, but were coated with a layer of black paint in order to avoid laser reflection. Moreover, they were not perfectly uniform therefore the caliper couldn't be positioned perfectly flat. The paint has a much lower radiation length than the aluminum, and the resulting uncertainty is reflected in the error of the thickness: (16.0±1.5) mils. The maximum relative errors on the radiation length before and after scattering are 3.5% and 3.6% respectively (see tables B.3-B.4).

*1 mil = 1/1000 of an inch = 0.0254 mm

| kinematics | | | total # of $X_0$ | |
|---|---|---|---|---|
| E (GeV) | arm | $\theta$ | before | after |
| 1.046 | l | 15.993 | $2.55\times10^{-3}$ | 0.0802 |
| 1.046 | r | 16.010 | " | 0.0786 |
| 4.018 | l | 24.998 | " | 0.0549 |
| 4.018 | r | 24.998 | " | 0.0539 |
| 5.009 | l | 24.998 | " | 0.0549 |
| 5.009 | l | 31.979 | " | 0.0453 |
| 5.009 | r | 32.001 | " | 0.0444 |
| 3.028 | l | 24.994 | $2.46\times10^{-3}$ | 0.0471 |
| 3.028 | r | 25.018 | " | 0.0461 |
| 5.009 | l | 31.977 | " | 0.0391 |
| 5.009 | r | 31.997 | " | 0.0383 |

**Table B.3:** Total radiation lengths before and after scattering.

| material | $X_0$ (cm) | $\sigma$ | $dX_0$ |
|---|---|---|---|
| Be | 35.28 | 0.5 mils | $3.60\times10^{-5}$ |
| $^4$He | 528107 | 2.5 cm | $4.73\times10^{-6}$ |
| glass (window) | 7.04 | 1.5 $\mu$m | $2.13\times10^{-5}$ |
| $^3$He | 41975 | 1.0 cm | $2.38\times10^{-5}$ |
| **Error total** | | | $\mathbf{8.58\times10^{-5}}$ |
| $^3$He | 41975 | 0.24 cm | $5.72\times10^{-6}$ |
| glass (wall) | 7.04 | 0.05 mm | $7.10\times10^{-4}$ |
| $^4$He | 528107 | 2.5 cm | $4.73\times10^{-6}$ |
| Al | 8.9 | 1.5 mils | $4.28\times10^{-4}$ |
| air | 30423 | 5.0 cm | $1.64\times10^{-4}$ |
| Kapton | 28.6 | 0.5 mils | $4.44\times10^{-5}$ |
| **Error total** | | | $\mathbf{1.36\times10^{-3}}$ |

**Table B.4:** Radiation length uncertainty summary.

## B.2 Reference cells

The reference cells were filled with $N_2$ or $^3$He at different pressures. We neglect here the thickness due to the gas itself, but it is accounted for in the nitrogen dilution [Solvignon, 2006a] and pressure curve analyses [Solvignon, 2006b].

| Material | $X_0$ (cm) | thickness (cm) | | # of $X_0$ | |
|---|---|---|---|---|---|
| | | Ref. Duke | Ref. Exodus | Ref. Duke | Ref. Exodus |
| Be | 35.28 | 0.01778 | | $5.04\times10^{-4}$ | |
| $^4$He | 528107 | 28.28 | | $5.35\times10^{-5}$ | |
| glass | 7.04 | 0.0118 | 0.0126 | $1.68\times10^{-3}$ | $1.79\times10^{-3}$ |
| **Total** | | | | $\mathbf{2.23\times10^{-3}}$ | $\mathbf{2.35\times10^{-3}}$ |

**Table B.5:** Radiation lengths of the material encountered before scattering.

| Material | $X_0$ (cm) | thickness (cm) | | # of $X_0$ | |
|---|---|---|---|---|---|
| | | Ref. Duke | Ref. Exodus | Ref. Duke | Ref. Exodus |
| glass (L) | 7.04 | $0.153/\sin\theta$ | $0.151/\sin\theta$ | $0.0217/\sin\theta$ | $0.0214/\sin\theta$ |
| glass (R) | 7.04 | $0.137/\sin\theta$ | $0.161/\sin\theta$ | $0.0195/\sin\theta$ | $0.0229/\sin\theta$ |
| $^4$He | 528107 | 45.7 | | $8.65\times10^{-5}$ | |
| Al | 8.9 | 0.04064 | | $4.57\times10^{-3}$ | |
| Air | 30423 | 65.1 | | $2.14\times10^{-3}$ | |
| Kapton | 28.6 | 0.01778 | | $6.22\times10^{-4}$ | |

**Table B.6:** Radiation lengths of the material encountered after scattering.

The radiation lengths to be used for the radiative corrections are summarized in table B.7. The cell filling gas thicknesses will be added to these numbers.

| kinematics | | | total # of $X_0$ | |
|---|---|---|---|---|
| E (GeV) | arm | $\theta$ | before | after |
| 1.046 | l | 15.993 | $2.23\times10^{-3}$ | 0.0863 |
| 1.046 | r | 16.010 | " | 0.0780 |
| 4.018 | l | 24.998 | " | 0.0588 |
| 4.018 | r | 24.998 | " | 0.0535 |
| 5.009 | l | 24.998 | " | 0.0588 |
| 5.009 | l | 31.979 | " | 0.0485 |
| 5.009 | r | 32.001 | " | 0.0441 |
| 3.028 | l | 24.994 | $2.35\times10^{-3}$ | 0.0582 |
| 3.028 | r | 25.018 | " | 0.0615 |
| 5.009 | l | 31.977 | " | 0.0479 |
| 5.009 | r | 31.997 | " | 0.0506 |

**Table B.7:** Total radiation lengths before and after scattering for empty reference cells.

# APPENDIX C

# UNPOLARIZED CROSS SECTIONS

In the following, the first column is defined as:

- kin=3 for data at (3.028 GeV, 25°)
- kin=4 for data at (4.018 GeV, 25°)
- kin=5 for data at (5.009 GeV, 25°)
- kin=6 for data at (5.009 GeV, 32°)

The other quantities are the invariant mass $W$ in MeV, the raw cross section formed from Eq. (6.5), the nitrogen dilution $\sigma_{\rm N}^{dil}$ evaluated in Section 6.6.3, the experimental cross section $\sigma_{exp}$ as defined in Eq. (6.7), the Born cross section $\sigma_{Born}$ generated from Eq. (6.8). The Born cross section statistical and systematic uncertainties are also tabulated. All the cross section values and the uncertainties are given in pb/MeV.sr.

Table C.1: Unpolarized cross sections.

| kin | $W$ | $\sigma_{raw}$ | $\sigma_{\rm N}^{dil}$ | $\sigma_{exp}$ | $\sigma_{Born}$ | stat | syst |
|---|---|---|---|---|---|---|---|
| 3 | 1035.0 | 66.383 | 3.607 | 62.776 | 73.807 | 0.762 | 2.674 |
| 3 | 1045.0 | 66.259 | 3.859 | 62.400 | 70.769 | 0.605 | 2.640 |
| 3 | 1055.0 | 62.383 | 3.734 | 58.649 | 64.082 | 0.491 | 2.459 |
| 3 | 1065.0 | 63.297 | 3.820 | 59.476 | 62.062 | 0.450 | 2.487 |
| 3 | 1075.0 | 63.869 | 4.062 | 59.808 | 60.562 | 0.411 | 2.506 |
| 3 | 1085.0 | 61.431 | 4.150 | 57.281 | 57.079 | 0.363 | 2.420 |
| 3 | 1095.0 | 60.978 | 4.233 | 56.745 | 56.216 | 0.334 | 2.407 |
| 3 | 1105.0 | 63.564 | 4.397 | 59.167 | 59.056 | 0.337 | 2.520 |
| 3 | 1115.0 | 61.819 | 4.266 | 57.553 | 57.894 | 0.324 | 2.470 |
| 3 | 1125.0 | 62.193 | 4.599 | 57.594 | 58.915 | 0.324 | 2.492 |
| 3 | 1135.0 | 65.762 | 4.667 | 61.095 | 63.785 | 0.331 | 2.653 |
| 3 | 1145.0 | 66.763 | 4.680 | 62.083 | 66.572 | 0.325 | 2.715 |

*continued on next page*

Table C.1: *continued*

| kin | $W$ | $\sigma_{raw}$ | $\sigma_{\mathrm{N}}^{dil}$ | $\sigma_{exp}$ | $\sigma_{Born}$ | stat | syst |
|---|---|---|---|---|---|---|---|
| 3 | 1155.0 | 68.455 | 4.735 | 63.720 | 69.107 | 0.324 | 2.798 |
| 3 | 1165.0 | 70.176 | 4.812 | 65.364 | 71.891 | 0.324 | 2.876 |
| 3 | 1175.0 | 72.190 | 4.838 | 67.352 | 75.029 | 0.324 | 2.970 |
| 3 | 1185.0 | 74.714 | 4.838 | 69.876 | 78.201 | 0.327 | 3.076 |
| 3 | 1195.0 | 77.958 | 5.126 | 72.832 | 82.031 | 0.347 | 3.210 |
| 3 | 1205.0 | 84.604 | 5.322 | 79.282 | 89.057 | 0.394 | 3.493 |
| 3 | 1215.0 | 85.366 | 5.292 | 80.074 | 90.521 | 0.410 | 3.520 |
| 3 | 1225.0 | 86.301 | 5.454 | 80.847 | 91.914 | 0.432 | 3.556 |
| 3 | 1235.0 | 91.389 | 5.950 | 85.439 | 96.674 | 0.488 | 3.759 |
| 3 | 1245.0 | 92.305 | 6.025 | 86.281 | 97.410 | 0.532 | 3.780 |
| 3 | 1255.0 | 92.614 | 5.983 | 86.631 | 97.527 | 0.537 | 3.787 |
| 3 | 1265.0 | 93.899 | 6.073 | 87.826 | 98.337 | 0.480 | 3.823 |
| 3 | 1275.0 | 98.402 | 6.565 | 91.837 | 101.784 | 0.482 | 3.994 |
| 3 | 1285.0 | 96.800 | 6.467 | 90.332 | 99.330 | 0.471 | 3.913 |
| 3 | 1295.0 | 99.003 | 6.508 | 92.495 | 100.804 | 0.481 | 3.989 |
| 3 | 1305.0 | 101.687 | 6.828 | 94.859 | 102.523 | 0.491 | 4.091 |
| 3 | 1315.0 | 99.577 | 6.660 | 92.917 | 99.939 | 0.478 | 3.993 |
| 3 | 1325.0 | 99.363 | 6.958 | 92.405 | 98.857 | 0.479 | 3.980 |
| 3 | 1335.0 | 101.234 | 7.097 | 94.137 | 100.062 | 0.485 | 4.054 |
| 3 | 1345.0 | 101.630 | 7.013 | 94.617 | 100.035 | 0.494 | 4.061 |
| 3 | 1355.0 | 105.363 | 7.328 | 98.035 | 102.906 | 0.557 | 4.209 |
| 3 | 1365.0 | 102.367 | 7.170 | 95.198 | 99.447 | 0.571 | 4.084 |
| 3 | 1375.0 | 104.415 | 7.702 | 96.713 | 101.039 | 0.607 | 4.168 |
| 3 | 1385.0 | 109.223 | 7.734 | 101.489 | 105.639 | 0.746 | 4.364 |
| 3 | 1395.0 | 105.143 | 7.939 | 97.204 | 101.441 | 0.738 | 4.205 |
| 3 | 1405.0 | 108.477 | 8.169 | 100.308 | 105.049 | 0.688 | 4.346 |
| 3 | 1415.0 | 113.459 | 8.361 | 105.098 | 110.046 | 0.682 | 4.549 |
| 3 | 1425.0 | 115.246 | 8.567 | 106.679 | 112.062 | 0.687 | 4.634 |
| 3 | 1435.0 | 119.373 | 8.778 | 110.595 | 116.294 | 0.703 | 4.804 |
| 3 | 1445.0 | 119.673 | 8.987 | 110.685 | 117.027 | 0.702 | 4.818 |
| 3 | 1455.0 | 124.014 | 9.184 | 114.830 | 121.281 | 0.715 | 4.997 |
| 3 | 1465.0 | 127.832 | 9.394 | 118.438 | 125.018 | 0.728 | 5.148 |
| 3 | 1475.0 | 128.328 | 9.584 | 118.743 | 125.670 | 0.747 | 5.172 |
| 3 | 1485.0 | 137.951 | 9.771 | 128.180 | 135.216 | 0.833 | 5.554 |

*continued on next page*

Table C.1: *continued*

| kin | $W$ | $\sigma_{raw}$ | $\sigma_{\mathrm{N}}^{dil}$ | $\sigma_{exp}$ | $\sigma_{Born}$ | stat | syst |
|---|---|---|---|---|---|---|---|
| 3 | 1495.0 | 133.637 | 9.966 | 123.672 | 131.090 | 0.860 | 5.379 |
| 3 | 1505.0 | 143.116 | 10.153 | 132.962 | 140.437 | 0.970 | 5.755 |
| 3 | 1515.0 | 142.583 | 10.315 | 132.268 | 139.414 | 1.035 | 5.727 |
| 3 | 1525.0 | 143.696 | 10.506 | 133.190 | 140.023 | 0.949 | 5.769 |
| 3 | 1535.0 | 146.876 | 10.678 | 136.199 | 142.172 | 0.930 | 5.891 |
| 3 | 1545.0 | 150.764 | 10.847 | 139.917 | 144.892 | 0.950 | 6.045 |
| 3 | 1555.0 | 152.106 | 11.014 | 141.093 | 145.089 | 0.959 | 6.100 |
| 3 | 1565.0 | 153.643 | 11.184 | 142.459 | 145.060 | 0.966 | 6.163 |
| 3 | 1575.0 | 155.326 | 11.345 | 143.981 | 145.333 | 0.976 | 6.237 |
| 3 | 1585.0 | 154.782 | 11.497 | 143.285 | 143.568 | 1.010 | 6.221 |
| 3 | 1595.0 | 160.190 | 11.671 | 148.519 | 148.024 | 1.109 | 6.438 |
| 3 | 1605.0 | 156.647 | 11.826 | 144.820 | 143.841 | 1.124 | 6.302 |
| 3 | 1615.0 | 163.981 | 11.967 | 152.014 | 150.617 | 1.192 | 6.602 |
| 3 | 1625.0 | 159.348 | 12.137 | 147.212 | 145.439 | 1.087 | 6.413 |
| 3 | 1635.0 | 164.654 | 12.290 | 152.364 | 150.446 | 1.042 | 6.630 |
| 3 | 1645.0 | 169.755 | 12.457 | 157.298 | 155.167 | 1.060 | 6.840 |
| 3 | 1655.0 | 172.346 | 12.614 | 159.733 | 157.115 | 1.069 | 6.945 |
| 3 | 1665.0 | 171.241 | 12.761 | 158.480 | 155.309 | 1.069 | 6.905 |
| 3 | 1675.0 | 173.961 | 12.923 | 161.038 | 157.055 | 1.086 | 7.022 |
| 3 | 1685.0 | 177.600 | 13.104 | 164.496 | 159.363 | 1.179 | 7.182 |
| 3 | 1695.0 | 174.501 | 13.268 | 161.232 | 154.929 | 1.173 | 7.074 |
| 3 | 1705.0 | 184.225 | 13.434 | 170.791 | 163.104 | 1.186 | 7.495 |
| 3 | 1715.0 | 181.100 | 13.601 | 167.500 | 158.407 | 1.084 | 7.385 |
| 3 | 1725.0 | 182.394 | 13.769 | 168.625 | 158.310 | 1.052 | 7.461 |
| 3 | 1735.0 | 189.384 | 13.915 | 175.469 | 163.973 | 1.076 | 7.769 |
| 3 | 1745.0 | 186.045 | 14.125 | 171.920 | 159.314 | 1.076 | 7.645 |
| 3 | 1755.0 | 186.882 | 14.289 | 172.593 | 158.869 | 1.086 | 7.690 |
| 3 | 1765.0 | 189.326 | 14.418 | 174.908 | 160.199 | 1.161 | 7.811 |
| 3 | 1775.0 | 188.377 | 14.495 | 173.883 | 158.128 | 1.205 | 7.784 |
| 3 | 1785.0 | 193.335 | 14.840 | 178.495 | 161.606 | 1.154 | 8.009 |
| 3 | 1795.0 | 194.136 | 15.017 | 179.120 | 161.079 | 1.051 | 8.069 |
| 3 | 1805.0 | 193.070 | 15.195 | 177.875 | 158.447 | 1.021 | 8.053 |
| 3 | 1815.0 | 198.961 | 15.213 | 183.748 | 162.767 | 1.040 | 8.348 |
| 3 | 1825.0 | 196.369 | 15.483 | 180.886 | 158.248 | 1.048 | 8.272 |

*continued on next page*

Table C.1: *continued*

| kin | $W$ | $\sigma_{raw}$ | $\sigma_{\mathrm{N}}^{dil}$ | $\sigma_{exp}$ | $\sigma_{Born}$ | stat | syst |
|---|---|---|---|---|---|---|---|
| 3 | 1835.0 | 200.383 | 15.716 | 184.667 | 160.256 | 1.074 | 8.504 |
| 3 | 1845.0 | 202.660 | 15.811 | 186.849 | 160.748 | 1.174 | 8.654 |
| 3 | 1855.0 | 199.649 | 16.098 | 183.551 | 156.053 | 1.531 | 8.549 |
| 4 | 885.0 | 5.917 | 0.312 | 5.605 | 10.527 | 0.415 | 0.542 |
| 4 | 895.0 | 8.185 | 0.419 | 7.766 | 13.603 | 0.374 | 0.720 |
| 4 | 905.0 | 6.998 | 0.326 | 6.671 | 12.629 | 0.251 | 0.621 |
| 4 | 915.0 | 9.175 | 0.384 | 8.791 | 14.100 | 0.281 | 0.636 |
| 4 | 925.0 | 8.362 | 0.385 | 7.977 | 13.272 | 0.218 | 0.564 |
| 4 | 935.0 | 9.371 | 0.384 | 8.987 | 14.476 | 0.218 | 0.617 |
| 4 | 945.0 | 10.959 | 0.459 | 10.500 | 15.784 | 0.235 | 0.656 |
| 4 | 955.0 | 10.168 | 0.424 | 9.744 | 14.961 | 0.196 | 0.603 |
| 4 | 965.0 | 10.574 | 0.398 | 10.175 | 15.229 | 0.183 | 0.598 |
| 4 | 975.0 | 11.694 | 0.555 | 11.139 | 16.078 | 0.192 | 0.636 |
| 4 | 985.0 | 11.436 | 0.519 | 10.917 | 15.935 | 0.175 | 0.627 |
| 4 | 995.0 | 12.225 | 0.557 | 11.669 | 16.365 | 0.176 | 0.636 |
| 4 | 1005.0 | 11.804 | 0.601 | 11.203 | 15.775 | 0.163 | 0.607 |
| 4 | 1015.0 | 12.347 | 0.620 | 11.727 | 16.007 | 0.162 | 0.615 |
| 4 | 1025.0 | 12.860 | 0.643 | 12.217 | 16.297 | 0.164 | 0.626 |
| 4 | 1035.0 | 12.480 | 0.670 | 11.809 | 15.707 | 0.157 | 0.605 |
| 4 | 1045.0 | 12.796 | 0.615 | 12.181 | 15.771 | 0.163 | 0.605 |
| 4 | 1055.0 | 12.266 | 0.662 | 11.604 | 14.878 | 0.159 | 0.573 |
| 4 | 1065.0 | 12.244 | 0.652 | 11.592 | 14.706 | 0.160 | 0.572 |
| 4 | 1075.0 | 11.360 | 0.707 | 10.652 | 13.298 | 0.151 | 0.518 |
| 4 | 1085.0 | 12.525 | 0.748 | 11.778 | 14.148 | 0.167 | 0.562 |
| 4 | 1095.0 | 12.344 | 0.759 | 11.585 | 13.728 | 0.165 | 0.550 |
| 4 | 1105.0 | 11.988 | 0.724 | 11.264 | 13.368 | 0.158 | 0.537 |
| 4 | 1115.0 | 12.578 | 0.805 | 11.773 | 13.839 | 0.166 | 0.564 |
| 4 | 1125.0 | 12.685 | 0.776 | 11.909 | 13.952 | 0.163 | 0.567 |
| 4 | 1135.0 | 12.768 | 0.821 | 11.947 | 14.068 | 0.166 | 0.574 |
| 4 | 1145.0 | 12.957 | 0.920 | 12.037 | 14.357 | 0.172 | 0.589 |
| 4 | 1155.0 | 13.388 | 0.957 | 12.431 | 14.822 | 0.181 | 0.606 |
| 4 | 1165.0 | 14.495 | 0.973 | 13.522 | 16.110 | 0.200 | 0.661 |
| 4 | 1175.0 | 14.906 | 0.991 | 13.915 | 16.701 | 0.204 | 0.679 |
| 4 | 1185.0 | 14.755 | 0.913 | 13.841 | 16.811 | 0.206 | 0.678 |

*continued on next page*

Table C.1: *continued*

| kin | $W$ | $\sigma_{raw}$ | $\sigma_{\mathrm{N}}^{dil}$ | $\sigma_{exp}$ | $\sigma_{Born}$ | stat | syst |
|---|---|---|---|---|---|---|---|
| 4 | 1195.0 | 14.942 | 1.031 | 13.911 | 17.003 | 0.213 | 0.682 |
| 4 | 1205.0 | 16.337 | 1.142 | 15.195 | 18.388 | 0.240 | 0.744 |
| 4 | 1215.0 | 16.573 | 1.111 | 15.462 | 18.700 | 0.256 | 0.752 |
| 4 | 1225.0 | 16.418 | 1.256 | 15.161 | 18.541 | 0.269 | 0.745 |
| 4 | 1235.0 | 16.029 | 1.150 | 14.879 | 18.325 | 0.290 | 0.731 |
| 4 | 1245.0 | 17.749 | 1.186 | 16.563 | 20.053 | 0.307 | 0.796 |
| 4 | 1255.0 | 17.468 | 1.219 | 16.249 | 19.771 | 0.280 | 0.784 |
| 4 | 1265.0 | 17.961 | 1.253 | 16.708 | 20.200 | 0.270 | 0.801 |
| 4 | 1275.0 | 19.051 | 1.286 | 17.764 | 21.330 | 0.274 | 0.847 |
| 4 | 1285.0 | 19.674 | 1.321 | 18.353 | 21.911 | 0.281 | 0.870 |
| 4 | 1295.0 | 19.425 | 1.356 | 18.069 | 21.698 | 0.274 | 0.860 |
| 4 | 1305.0 | 19.480 | 1.391 | 18.088 | 21.749 | 0.273 | 0.859 |
| 4 | 1315.0 | 20.963 | 1.427 | 19.535 | 23.261 | 0.288 | 0.923 |
| 4 | 1325.0 | 21.948 | 1.464 | 20.484 | 24.239 | 0.292 | 0.962 |
| 4 | 1335.0 | 21.661 | 1.501 | 20.160 | 23.981 | 0.286 | 0.950 |
| 4 | 1345.0 | 21.580 | 1.539 | 20.041 | 23.860 | 0.283 | 0.944 |
| 4 | 1355.0 | 23.342 | 1.577 | 21.766 | 25.661 | 0.305 | 1.019 |
| 4 | 1365.0 | 23.652 | 1.615 | 22.037 | 25.920 | 0.317 | 1.030 |
| 4 | 1375.0 | 24.965 | 1.654 | 23.311 | 27.263 | 0.352 | 1.087 |
| 4 | 1385.0 | 25.127 | 1.694 | 23.433 | 27.420 | 0.358 | 1.093 |
| 4 | 1395.0 | 25.281 | 1.734 | 23.547 | 27.659 | 0.361 | 1.102 |
| 4 | 1405.0 | 24.783 | 1.775 | 23.008 | 27.199 | 0.350 | 1.081 |
| 4 | 1415.0 | 27.844 | 1.816 | 26.028 | 30.339 | 0.387 | 1.214 |
| 4 | 1425.0 | 26.538 | 1.858 | 24.680 | 29.078 | 0.372 | 1.159 |
| 4 | 1435.0 | 27.040 | 1.964 | 25.076 | 29.650 | 0.369 | 1.189 |
| 4 | 1445.0 | 28.990 | 1.939 | 27.051 | 31.737 | 0.358 | 1.273 |
| 4 | 1455.0 | 29.821 | 2.001 | 27.819 | 32.620 | 0.331 | 1.308 |
| 4 | 1465.0 | 32.000 | 2.158 | 29.842 | 34.859 | 0.329 | 1.404 |
| 4 | 1475.0 | 31.811 | 2.136 | 29.675 | 34.793 | 0.325 | 1.396 |
| 4 | 1485.0 | 32.607 | 2.100 | 30.507 | 35.760 | 0.322 | 1.429 |
| 4 | 1495.0 | 33.242 | 2.153 | 31.089 | 36.347 | 0.327 | 1.454 |
| 4 | 1505.0 | 34.506 | 2.337 | 32.169 | 37.431 | 0.334 | 1.506 |
| 4 | 1515.0 | 35.467 | 2.306 | 33.162 | 38.386 | 0.337 | 1.544 |
| 4 | 1525.0 | 36.307 | 2.318 | 33.989 | 39.172 | 0.338 | 1.578 |

*continued on next page*

Table C.1: *continued*

| kin | $W$ | $\sigma_{raw}$ | $\sigma_{\mathrm{N}}^{dil}$ | $\sigma_{exp}$ | $\sigma_{Born}$ | stat | syst |
|---|---|---|---|---|---|---|---|
| 4 | 1535.0 | 37.619 | 2.415 | 35.204 | 40.297 | 0.354 | 1.629 |
| 4 | 1545.0 | 38.852 | 2.545 | 36.307 | 41.282 | 0.387 | 1.672 |
| 4 | 1555.0 | 40.240 | 2.604 | 37.636 | 42.566 | 0.409 | 1.727 |
| 4 | 1565.0 | 40.620 | 2.511 | 38.110 | 42.899 | 0.419 | 1.740 |
| 4 | 1575.0 | 40.545 | 2.496 | 38.048 | 42.734 | 0.419 | 1.734 |
| 4 | 1585.0 | 42.480 | 2.658 | 39.822 | 44.471 | 0.451 | 1.812 |
| 4 | 1595.0 | 41.182 | 2.595 | 38.586 | 43.179 | 0.445 | 1.756 |
| 4 | 1605.0 | 41.606 | 2.544 | 39.062 | 43.664 | 0.433 | 1.774 |
| 4 | 1615.0 | 43.884 | 2.817 | 41.067 | 45.685 | 0.412 | 1.866 |
| 4 | 1625.0 | 44.215 | 2.819 | 41.397 | 46.043 | 0.395 | 1.879 |
| 4 | 1635.0 | 45.698 | 2.872 | 42.826 | 47.491 | 0.402 | 1.940 |
| 4 | 1645.0 | 45.694 | 2.894 | 42.800 | 47.496 | 0.399 | 1.938 |
| 4 | 1655.0 | 47.694 | 3.118 | 44.576 | 49.363 | 0.409 | 2.019 |
| 4 | 1665.0 | 48.473 | 3.094 | 45.379 | 50.191 | 0.407 | 2.050 |
| 4 | 1675.0 | 49.898 | 3.217 | 46.681 | 51.492 | 0.419 | 2.108 |
| 4 | 1685.0 | 50.712 | 3.258 | 47.453 | 52.204 | 0.450 | 2.139 |
| 4 | 1695.0 | 53.394 | 3.378 | 50.015 | 54.612 | 0.504 | 2.246 |
| 4 | 1705.0 | 52.194 | 3.284 | 48.910 | 53.382 | 0.516 | 2.195 |
| 4 | 1715.0 | 52.521 | 3.311 | 49.210 | 53.519 | 0.541 | 2.205 |
| 4 | 1725.0 | 55.488 | 3.495 | 51.993 | 56.189 | 0.606 | 2.323 |
| 4 | 1735.0 | 54.865 | 3.468 | 51.398 | 55.338 | 0.629 | 2.296 |
| 4 | 1745.0 | 55.991 | 3.625 | 52.366 | 56.083 | 0.582 | 2.341 |
| 4 | 1755.0 | 57.411 | 3.558 | 53.853 | 57.326 | 0.539 | 2.398 |
| 4 | 1765.0 | 58.565 | 3.759 | 54.806 | 58.030 | 0.544 | 2.443 |
| 4 | 1775.0 | 58.253 | 3.665 | 54.588 | 57.609 | 0.537 | 2.428 |
| 4 | 1785.0 | 58.965 | 3.909 | 55.056 | 57.866 | 0.544 | 2.455 |
| 4 | 1795.0 | 58.485 | 3.851 | 54.634 | 57.254 | 0.535 | 2.434 |
| 4 | 1805.0 | 60.706 | 3.976 | 56.730 | 59.158 | 0.564 | 2.525 |
| 4 | 1815.0 | 62.005 | 4.208 | 57.797 | 60.040 | 0.631 | 2.576 |
| 4 | 1825.0 | 62.664 | 4.111 | 58.554 | 60.648 | 0.667 | 2.602 |
| 4 | 1835.0 | 61.265 | 4.053 | 57.212 | 59.086 | 0.641 | 2.545 |
| 4 | 1845.0 | 65.739 | 4.388 | 61.351 | 62.983 | 0.682 | 2.730 |
| 4 | 1855.0 | 63.897 | 4.378 | 59.519 | 60.874 | 0.632 | 2.656 |
| 4 | 1865.0 | 67.124 | 4.426 | 62.698 | 63.734 | 0.565 | 2.806 |

*continued on next page*

Table C.1: *continued*

| kin | $W$ | $\sigma_{raw}$ | $\sigma_{\mathrm{N}}^{dil}$ | $\sigma_{exp}$ | $\sigma_{Born}$ | stat | syst |
|---|---|---|---|---|---|---|---|
| 4 | 1875.0 | 66.305 | 4.510 | 61.794 | 62.538 | 0.518 | 2.775 |
| 4 | 1885.0 | 67.449 | 4.563 | 62.886 | 63.271 | 0.524 | 2.828 |
| 4 | 1895.0 | 68.349 | 4.590 | 63.759 | 63.788 | 0.524 | 2.871 |
| 4 | 1905.0 | 68.245 | 4.659 | 63.586 | 63.272 | 0.522 | 2.872 |
| 4 | 1915.0 | 69.618 | 4.764 | 64.854 | 64.222 | 0.544 | 2.934 |
| 4 | 1925.0 | 71.350 | 4.841 | 66.509 | 65.522 | 0.610 | 3.012 |
| 4 | 1935.0 | 71.645 | 4.905 | 66.741 | 65.496 | 0.711 | 3.027 |
| 4 | 1945.0 | 72.998 | 5.178 | 67.820 | 66.295 | 0.936 | 3.087 |
| 4 | 1955.0 | 74.211 | 5.165 | 69.046 | 67.221 | 1.820 | 3.142 |
| 5 | 885.0 | 1.291 | 0.073 | 1.218 | 1.897 | 0.101 | 0.107 |
| 5 | 895.0 | 1.213 | 0.057 | 1.157 | 2.019 | 0.071 | 0.112 |
| 5 | 905.0 | 1.195 | 0.045 | 1.150 | 2.066 | 0.054 | 0.106 |
| 5 | 915.0 | 1.542 | 0.035 | 1.507 | 2.492 | 0.058 | 0.127 |
| 5 | 925.0 | 1.077 | 0.091 | 0.986 | 1.915 | 0.040 | 0.085 |
| 5 | 935.0 | 1.392 | 0.063 | 1.329 | 2.286 | 0.042 | 0.099 |
| 5 | 945.0 | 1.675 | 0.087 | 1.588 | 2.604 | 0.047 | 0.114 |
| 5 | 955.0 | 1.837 | 0.067 | 1.771 | 2.775 | 0.046 | 0.116 |
| 5 | 965.0 | 1.829 | 0.093 | 1.736 | 2.762 | 0.043 | 0.114 |
| 5 | 975.0 | 1.926 | 0.091 | 1.835 | 2.899 | 0.041 | 0.119 |
| 5 | 985.0 | 1.972 | 0.117 | 1.855 | 2.903 | 0.039 | 0.117 |
| 5 | 995.0 | 2.129 | 0.120 | 2.009 | 3.075 | 0.039 | 0.123 |
| 5 | 1005.0 | 2.368 | 0.102 | 2.266 | 3.345 | 0.040 | 0.134 |
| 5 | 1015.0 | 2.297 | 0.118 | 2.179 | 3.241 | 0.037 | 0.127 |
| 5 | 1025.0 | 2.621 | 0.108 | 2.513 | 3.572 | 0.040 | 0.141 |
| 5 | 1035.0 | 2.456 | 0.148 | 2.308 | 3.347 | 0.037 | 0.130 |
| 5 | 1045.0 | 2.472 | 0.111 | 2.361 | 3.394 | 0.034 | 0.130 |
| 5 | 1055.0 | 2.669 | 0.145 | 2.524 | 3.540 | 0.036 | 0.138 |
| 5 | 1065.0 | 2.678 | 0.156 | 2.522 | 3.513 | 0.034 | 0.136 |
| 5 | 1075.0 | 2.625 | 0.153 | 2.472 | 3.440 | 0.033 | 0.132 |
| 5 | 1085.0 | 2.709 | 0.146 | 2.564 | 3.522 | 0.034 | 0.135 |
| 5 | 1095.0 | 2.857 | 0.160 | 2.696 | 3.626 | 0.035 | 0.140 |
| 5 | 1105.0 | 2.733 | 0.147 | 2.585 | 3.517 | 0.033 | 0.134 |
| 5 | 1115.0 | 2.952 | 0.162 | 2.790 | 3.707 | 0.036 | 0.143 |
| 5 | 1125.0 | 3.128 | 0.192 | 2.937 | 3.864 | 0.038 | 0.151 |

*continued on next page*

Table C.1: *continued*

| kin | $W$ | $\sigma_{raw}$ | $\sigma_{\mathrm{N}}^{dil}$ | $\sigma_{exp}$ | $\sigma_{Born}$ | stat | syst |
|---|---|---|---|---|---|---|---|
| 5 | 1135.0 | 3.106 | 0.195 | 2.912 | 3.849 | 0.036 | 0.150 |
| 5 | 1145.0 | 3.187 | 0.204 | 2.984 | 3.925 | 0.037 | 0.153 |
| 5 | 1155.0 | 3.427 | 0.196 | 3.230 | 4.190 | 0.039 | 0.164 |
| 5 | 1165.0 | 3.205 | 0.224 | 2.982 | 3.952 | 0.036 | 0.153 |
| 5 | 1175.0 | 3.296 | 0.209 | 3.087 | 4.070 | 0.036 | 0.158 |
| 5 | 1185.0 | 3.418 | 0.215 | 3.203 | 4.218 | 0.038 | 0.163 |
| 5 | 1195.0 | 3.576 | 0.240 | 3.336 | 4.360 | 0.040 | 0.170 |
| 5 | 1205.0 | 3.752 | 0.227 | 3.525 | 4.565 | 0.042 | 0.178 |
| 5 | 1215.0 | 3.789 | 0.249 | 3.540 | 4.600 | 0.044 | 0.179 |
| 5 | 1225.0 | 4.012 | 0.235 | 3.776 | 4.852 | 0.046 | 0.189 |
| 5 | 1235.0 | 4.091 | 0.279 | 3.812 | 4.893 | 0.048 | 0.192 |
| 5 | 1245.0 | 4.247 | 0.283 | 3.964 | 5.076 | 0.050 | 0.199 |
| 5 | 1255.0 | 4.393 | 0.270 | 4.123 | 5.249 | 0.053 | 0.206 |
| 5 | 1265.0 | 4.506 | 0.273 | 4.233 | 5.374 | 0.055 | 0.211 |
| 5 | 1275.0 | 4.479 | 0.272 | 4.208 | 5.370 | 0.056 | 0.210 |
| 5 | 1285.0 | 4.623 | 0.277 | 4.347 | 5.515 | 0.061 | 0.216 |
| 5 | 1295.0 | 4.915 | 0.277 | 4.639 | 5.831 | 0.067 | 0.229 |
| 5 | 1305.0 | 5.004 | 0.302 | 4.702 | 5.915 | 0.071 | 0.233 |
| 5 | 1315.0 | 5.111 | 0.321 | 4.789 | 6.036 | 0.079 | 0.238 |
| 5 | 1325.0 | 5.139 | 0.318 | 4.821 | 6.089 | 0.086 | 0.239 |
| 5 | 1335.0 | 5.304 | 0.323 | 4.982 | 6.284 | 0.089 | 0.247 |
| 5 | 1345.0 | 5.554 | 0.349 | 5.205 | 6.547 | 0.088 | 0.258 |
| 5 | 1355.0 | 5.832 | 0.379 | 5.453 | 6.833 | 0.086 | 0.271 |
| 5 | 1365.0 | 6.032 | 0.388 | 5.644 | 7.057 | 0.086 | 0.280 |
| 5 | 1375.0 | 6.215 | 0.382 | 5.832 | 7.301 | 0.088 | 0.289 |
| 5 | 1385.0 | 6.136 | 0.381 | 5.755 | 7.261 | 0.084 | 0.286 |
| 5 | 1395.0 | 6.816 | 0.404 | 6.412 | 7.964 | 0.091 | 0.316 |
| 5 | 1405.0 | 6.805 | 0.426 | 6.379 | 7.972 | 0.090 | 0.316 |
| 5 | 1415.0 | 7.369 | 0.463 | 6.906 | 8.550 | 0.095 | 0.340 |
| 5 | 1425.0 | 7.139 | 0.497 | 6.641 | 8.328 | 0.091 | 0.330 |
| 5 | 1435.0 | 7.435 | 0.427 | 7.008 | 8.731 | 0.092 | 0.344 |
| 5 | 1445.0 | 7.669 | 0.474 | 7.195 | 8.971 | 0.095 | 0.354 |
| 5 | 1455.0 | 8.120 | 0.505 | 7.615 | 9.429 | 0.102 | 0.373 |
| 5 | 1465.0 | 8.585 | 0.576 | 8.008 | 9.870 | 0.109 | 0.393 |

*continued on next page*

Table C.1: *continued*

| kin | $W$ | $\sigma_{raw}$ | $\sigma_{\mathrm{N}}^{dil}$ | $\sigma_{exp}$ | $\sigma_{Born}$ | stat | syst |
|---|---|---|---|---|---|---|---|
| 5 | 1475.0 | 9.392 | 0.594 | 8.797 | 10.699 | 0.119 | 0.428 |
| 5 | 1485.0 | 8.638 | 0.579 | 8.058 | 10.009 | 0.110 | 0.394 |
| 5 | 1495.0 | 9.451 | 0.591 | 8.860 | 10.850 | 0.118 | 0.430 |
| 5 | 1505.0 | 9.389 | 0.615 | 8.774 | 10.800 | 0.118 | 0.426 |
| 5 | 1515.0 | 10.501 | 0.585 | 9.916 | 11.998 | 0.129 | 0.475 |
| 5 | 1525.0 | 9.817 | 0.585 | 9.231 | 11.352 | 0.124 | 0.445 |
| 5 | 1535.0 | 10.210 | 0.617 | 9.593 | 11.753 | 0.128 | 0.461 |
| 5 | 1545.0 | 10.685 | 0.706 | 9.979 | 12.177 | 0.137 | 0.481 |
| 5 | 1555.0 | 10.592 | 0.689 | 9.903 | 12.149 | 0.136 | 0.477 |
| 5 | 1565.0 | 11.362 | 0.672 | 10.690 | 12.969 | 0.135 | 0.509 |
| 5 | 1575.0 | 11.542 | 0.661 | 10.882 | 13.198 | 0.127 | 0.517 |
| 5 | 1585.0 | 11.994 | 0.788 | 11.206 | 13.564 | 0.131 | 0.534 |
| 5 | 1595.0 | 12.061 | 0.800 | 11.261 | 13.655 | 0.128 | 0.537 |
| 5 | 1605.0 | 12.680 | 0.883 | 11.797 | 14.228 | 0.135 | 0.562 |
| 5 | 1615.0 | 13.160 | 0.838 | 12.321 | 14.790 | 0.136 | 0.582 |
| 5 | 1625.0 | 13.669 | 0.793 | 12.876 | 15.389 | 0.139 | 0.605 |
| 5 | 1635.0 | 13.537 | 0.879 | 12.658 | 15.209 | 0.134 | 0.598 |
| 5 | 1645.0 | 14.184 | 1.006 | 13.178 | 15.774 | 0.144 | 0.624 |
| 5 | 1655.0 | 14.314 | 0.950 | 13.364 | 16.008 | 0.148 | 0.630 |
| 5 | 1665.0 | 15.402 | 0.935 | 14.468 | 17.151 | 0.162 | 0.676 |
| 5 | 1675.0 | 15.646 | 0.931 | 14.715 | 17.443 | 0.167 | 0.685 |
| 5 | 1685.0 | 15.863 | 1.101 | 14.762 | 17.516 | 0.180 | 0.693 |
| 5 | 1695.0 | 16.048 | 0.885 | 15.163 | 17.988 | 0.180 | 0.702 |
| 5 | 1705.0 | 17.047 | 0.946 | 16.101 | 18.947 | 0.202 | 0.743 |
| 5 | 1715.0 | 16.736 | 1.112 | 15.623 | 18.478 | 0.223 | 0.728 |
| 5 | 1725.0 | 17.504 | 1.036 | 16.468 | 19.302 | 0.208 | 0.759 |
| 5 | 1735.0 | 17.442 | 1.062 | 16.380 | 19.203 | 0.220 | 0.755 |
| 5 | 1745.0 | 17.655 | 1.088 | 16.567 | 19.373 | 0.210 | 0.762 |
| 5 | 1755.0 | 18.694 | 1.114 | 17.579 | 20.353 | 0.206 | 0.804 |
| 5 | 1765.0 | 18.677 | 1.141 | 17.536 | 20.273 | 0.204 | 0.802 |
| 5 | 1775.0 | 18.729 | 1.168 | 17.561 | 20.247 | 0.202 | 0.802 |
| 5 | 1785.0 | 19.493 | 1.196 | 18.297 | 20.919 | 0.209 | 0.833 |
| 5 | 1795.0 | 19.909 | 1.224 | 18.685 | 21.230 | 0.211 | 0.849 |
| 5 | 1805.0 | 20.735 | 1.253 | 19.482 | 21.955 | 0.215 | 0.883 |

*continued on next page*

Table C.1: *continued*

| kin | $W$ | $\sigma_{raw}$ | $\sigma_{\mathrm{N}}^{dil}$ | $\sigma_{exp}$ | $\sigma_{Born}$ | stat | syst |
|---|---|---|---|---|---|---|---|
| 5 | 1815.0 | 20.336 | 1.282 | 19.054 | 21.454 | 0.219 | 0.866 |
| 5 | 1825.0 | 21.118 | 1.311 | 19.806 | 22.135 | 0.236 | 0.898 |
| 5 | 1835.0 | 21.617 | 1.341 | 20.276 | 22.532 | 0.246 | 0.920 |
| 5 | 1845.0 | 21.772 | 1.372 | 20.400 | 22.581 | 0.251 | 0.926 |
| 5 | 1855.0 | 22.018 | 1.403 | 20.615 | 22.727 | 0.259 | 0.937 |
| 5 | 1865.0 | 22.510 | 1.434 | 21.076 | 23.115 | 0.269 | 0.959 |
| 5 | 1875.0 | 22.938 | 1.465 | 21.472 | 23.436 | 0.281 | 0.978 |
| 5 | 1885.0 | 23.479 | 1.497 | 21.981 | 23.888 | 0.295 | 1.001 |
| 5 | 1895.0 | 23.253 | 1.606 | 21.648 | 23.490 | 0.278 | 0.995 |
| 5 | 1905.0 | 24.380 | 1.529 | 22.851 | 24.631 | 0.267 | 1.043 |
| 5 | 1915.0 | 24.743 | 1.655 | 23.088 | 24.811 | 0.266 | 1.059 |
| 5 | 1925.0 | 24.856 | 1.650 | 23.206 | 24.878 | 0.269 | 1.065 |
| 5 | 1935.0 | 25.623 | 1.616 | 24.007 | 25.625 | 0.273 | 1.098 |
| 5 | 1945.0 | 25.671 | 1.694 | 23.977 | 25.551 | 0.270 | 1.100 |
| 5 | 1955.0 | 25.803 | 1.692 | 24.111 | 25.644 | 0.280 | 1.106 |
| 5 | 1965.0 | 27.367 | 1.818 | 25.549 | 27.050 | 0.311 | 1.172 |
| 5 | 1975.0 | 27.762 | 1.823 | 25.939 | 27.410 | 0.339 | 1.188 |
| 5 | 1985.0 | 28.463 | 1.772 | 26.691 | 28.134 | 0.391 | 1.218 |
| 6 | 985.0 | 0.325 | 0.035 | 0.290 | 0.299 | 0.040 | 0.020 |
| 6 | 995.0 | 0.273 | 0.016 | 0.257 | 0.265 | 0.032 | 0.017 |
| 6 | 1005.0 | 0.380 | 0.016 | 0.364 | 0.377 | 0.033 | 0.024 |
| 6 | 1015.0 | 0.356 | 0.019 | 0.337 | 0.345 | 0.031 | 0.022 |
| 6 | 1025.0 | 0.300 | 0.048 | 0.252 | 0.265 | 0.027 | 0.018 |
| 6 | 1035.0 | 0.387 | 0.029 | 0.357 | 0.371 | 0.025 | 0.024 |
| 6 | 1045.0 | 0.426 | 0.025 | 0.401 | 0.415 | 0.023 | 0.026 |
| 6 | 1055.0 | 0.388 | 0.030 | 0.358 | 0.375 | 0.021 | 0.023 |
| 6 | 1065.0 | 0.406 | 0.027 | 0.379 | 0.400 | 0.019 | 0.024 |
| 6 | 1075.0 | 0.393 | 0.032 | 0.361 | 0.382 | 0.018 | 0.023 |
| 6 | 1085.0 | 0.435 | 0.028 | 0.406 | 0.432 | 0.017 | 0.026 |
| 6 | 1095.0 | 0.459 | 0.031 | 0.428 | 0.458 | 0.017 | 0.027 |
| 6 | 1105.0 | 0.436 | 0.034 | 0.403 | 0.433 | 0.015 | 0.026 |
| 6 | 1115.0 | 0.465 | 0.035 | 0.429 | 0.465 | 0.015 | 0.027 |
| 6 | 1125.0 | 0.465 | 0.023 | 0.442 | 0.481 | 0.014 | 0.027 |
| 6 | 1135.0 | 0.515 | 0.039 | 0.476 | 0.519 | 0.015 | 0.030 |

*continued on next page*

Table C.1: *continued*

| kin | $W$ | $\sigma_{raw}$ | $\sigma_{\mathrm{N}}^{dil}$ | $\sigma_{exp}$ | $\sigma_{Born}$ | stat | syst |
|---|---|---|---|---|---|---|---|
| 6 | 1145.0 | 0.549 | 0.029 | 0.519 | 0.568 | 0.014 | 0.032 |
| 6 | 1155.0 | 0.522 | 0.029 | 0.493 | 0.546 | 0.013 | 0.030 |
| 6 | 1165.0 | 0.571 | 0.033 | 0.538 | 0.594 | 0.014 | 0.033 |
| 6 | 1175.0 | 0.587 | 0.039 | 0.548 | 0.609 | 0.014 | 0.033 |
| 6 | 1185.0 | 0.631 | 0.044 | 0.587 | 0.654 | 0.014 | 0.036 |
| 6 | 1195.0 | 0.639 | 0.044 | 0.596 | 0.665 | 0.014 | 0.036 |
| 6 | 1205.0 | 0.699 | 0.045 | 0.653 | 0.729 | 0.014 | 0.039 |
| 6 | 1215.0 | 0.694 | 0.051 | 0.642 | 0.724 | 0.014 | 0.039 |
| 6 | 1225.0 | 0.715 | 0.049 | 0.665 | 0.750 | 0.014 | 0.040 |
| 6 | 1235.0 | 0.753 | 0.038 | 0.715 | 0.805 | 0.014 | 0.042 |
| 6 | 1245.0 | 0.759 | 0.047 | 0.712 | 0.808 | 0.015 | 0.042 |
| 6 | 1255.0 | 0.815 | 0.048 | 0.767 | 0.866 | 0.015 | 0.045 |
| 6 | 1265.0 | 0.845 | 0.053 | 0.792 | 0.897 | 0.016 | 0.046 |
| 6 | 1275.0 | 0.888 | 0.062 | 0.825 | 0.935 | 0.017 | 0.048 |
| 6 | 1285.0 | 0.908 | 0.061 | 0.847 | 0.960 | 0.017 | 0.049 |
| 6 | 1295.0 | 0.916 | 0.057 | 0.859 | 0.978 | 0.017 | 0.050 |
| 6 | 1305.0 | 0.949 | 0.065 | 0.884 | 1.006 | 0.019 | 0.051 |
| 6 | 1315.0 | 1.016 | 0.069 | 0.947 | 1.074 | 0.020 | 0.054 |
| 6 | 1325.0 | 0.983 | 0.067 | 0.916 | 1.049 | 0.020 | 0.053 |
| 6 | 1335.0 | 1.055 | 0.062 | 0.993 | 1.129 | 0.022 | 0.056 |
| 6 | 1345.0 | 1.087 | 0.075 | 1.012 | 1.152 | 0.023 | 0.058 |
| 6 | 1355.0 | 1.152 | 0.089 | 1.064 | 1.208 | 0.026 | 0.061 |
| 6 | 1365.0 | 1.148 | 0.074 | 1.074 | 1.224 | 0.026 | 0.061 |
| 6 | 1375.0 | 1.259 | 0.097 | 1.162 | 1.316 | 0.030 | 0.066 |
| 6 | 1385.0 | 1.199 | 0.075 | 1.124 | 1.282 | 0.028 | 0.063 |
| 6 | 1395.0 | 1.240 | 0.060 | 1.180 | 1.346 | 0.030 | 0.065 |
| 6 | 1405.0 | 1.296 | 0.061 | 1.235 | 1.407 | 0.032 | 0.068 |
| 6 | 1415.0 | 1.384 | 0.089 | 1.295 | 1.476 | 0.036 | 0.072 |
| 6 | 1425.0 | 1.427 | 0.079 | 1.348 | 1.538 | 0.036 | 0.074 |
| 6 | 1435.0 | 1.600 | 0.097 | 1.503 | 1.703 | 0.037 | 0.083 |
| 6 | 1445.0 | 1.592 | 0.112 | 1.480 | 1.690 | 0.036 | 0.082 |
| 6 | 1455.0 | 1.677 | 0.130 | 1.547 | 1.766 | 0.037 | 0.086 |
| 6 | 1465.0 | 1.756 | 0.110 | 1.646 | 1.876 | 0.037 | 0.090 |
| 6 | 1475.0 | 1.796 | 0.111 | 1.685 | 1.926 | 0.037 | 0.092 |

*continued on next page*

Table C.1: *continued*

| kin | $W$ | $\sigma_{raw}$ | $\sigma_{\mathrm{N}}^{dil}$ | $\sigma_{exp}$ | $\sigma_{Born}$ | stat | syst |
|---|---|---|---|---|---|---|---|
| 6 | 1485.0 | 1.878 | 0.101 | 1.776 | 2.029 | 0.036 | 0.096 |
| 6 | 1495.0 | 1.970 | 0.118 | 1.852 | 2.117 | 0.039 | 0.101 |
| 6 | 1505.0 | 2.043 | 0.121 | 1.922 | 2.196 | 0.039 | 0.104 |
| 6 | 1515.0 | 2.111 | 0.145 | 1.966 | 2.252 | 0.040 | 0.107 |
| 6 | 1525.0 | 2.158 | 0.146 | 2.012 | 2.309 | 0.041 | 0.109 |
| 6 | 1535.0 | 2.378 | 0.145 | 2.233 | 2.541 | 0.045 | 0.120 |
| 6 | 1545.0 | 2.386 | 0.115 | 2.271 | 2.588 | 0.044 | 0.121 |
| 6 | 1555.0 | 2.420 | 0.162 | 2.259 | 2.587 | 0.046 | 0.122 |
| 6 | 1565.0 | 2.323 | 0.139 | 2.184 | 2.521 | 0.043 | 0.117 |
| 6 | 1575.0 | 2.484 | 0.155 | 2.329 | 2.678 | 0.044 | 0.125 |
| 6 | 1585.0 | 2.723 | 0.179 | 2.544 | 2.903 | 0.047 | 0.136 |
| 6 | 1595.0 | 2.539 | 0.177 | 2.362 | 2.729 | 0.044 | 0.127 |
| 6 | 1605.0 | 2.781 | 0.191 | 2.590 | 2.967 | 0.046 | 0.139 |
| 6 | 1615.0 | 2.829 | 0.182 | 2.647 | 3.034 | 0.046 | 0.141 |
| 6 | 1625.0 | 2.937 | 0.180 | 2.757 | 3.153 | 0.046 | 0.147 |
| 6 | 1635.0 | 3.059 | 0.187 | 2.871 | 3.276 | 0.045 | 0.152 |
| 6 | 1645.0 | 3.175 | 0.180 | 2.995 | 3.408 | 0.043 | 0.158 |
| 6 | 1655.0 | 3.448 | 0.201 | 3.248 | 3.671 | 0.045 | 0.171 |
| 6 | 1665.0 | 3.479 | 0.192 | 3.286 | 3.718 | 0.045 | 0.172 |
| 6 | 1675.0 | 3.492 | 0.203 | 3.289 | 3.725 | 0.044 | 0.173 |
| 6 | 1685.0 | 3.803 | 0.227 | 3.575 | 4.020 | 0.047 | 0.188 |
| 6 | 1695.0 | 3.892 | 0.239 | 3.653 | 4.106 | 0.048 | 0.192 |
| 6 | 1705.0 | 4.035 | 0.235 | 3.800 | 4.263 | 0.049 | 0.199 |
| 6 | 1715.0 | 4.025 | 0.244 | 3.781 | 4.251 | 0.051 | 0.198 |
| 6 | 1725.0 | 4.176 | 0.241 | 3.935 | 4.411 | 0.054 | 0.205 |
| 6 | 1735.0 | 4.535 | 0.258 | 4.277 | 4.757 | 0.058 | 0.222 |
| 6 | 1745.0 | 4.371 | 0.276 | 4.095 | 4.581 | 0.057 | 0.214 |
| 6 | 1755.0 | 4.598 | 0.293 | 4.305 | 4.794 | 0.061 | 0.225 |
| 6 | 1765.0 | 4.671 | 0.287 | 4.384 | 4.880 | 0.063 | 0.228 |
| 6 | 1775.0 | 4.662 | 0.283 | 4.379 | 4.868 | 0.063 | 0.228 |
| 6 | 1785.0 | 4.818 | 0.265 | 4.552 | 5.043 | 0.067 | 0.235 |
| 6 | 1795.0 | 4.928 | 0.303 | 4.625 | 5.121 | 0.070 | 0.240 |
| 6 | 1805.0 | 5.024 | 0.311 | 4.713 | 5.210 | 0.066 | 0.245 |
| 6 | 1815.0 | 5.292 | 0.322 | 4.970 | 5.465 | 0.065 | 0.258 |

*continued on next page*

Table C.1: *continued*

| kin | $W$ | $\sigma_{raw}$ | $\sigma_{\mathrm{N}}^{dil}$ | $\sigma_{exp}$ | $\sigma_{Born}$ | stat | syst |
|---|---|---|---|---|---|---|---|
| 6 | 1825.0 | 5.364 | 0.303 | 5.061 | 5.547 | 0.064 | 0.261 |
| 6 | 1835.0 | 5.663 | 0.348 | 5.315 | 5.799 | 0.066 | 0.275 |
| 6 | 1845.0 | 5.592 | 0.339 | 5.253 | 5.735 | 0.066 | 0.272 |
| 6 | 1855.0 | 6.055 | 0.402 | 5.653 | 6.139 | 0.070 | 0.294 |
| 6 | 1865.0 | 6.062 | 0.400 | 5.661 | 6.144 | 0.071 | 0.294 |
| 6 | 1875.0 | 6.009 | 0.366 | 5.643 | 6.115 | 0.073 | 0.292 |
| 6 | 1885.0 | 6.557 | 0.432 | 6.125 | 6.596 | 0.085 | 0.318 |
| 6 | 1895.0 | 6.427 | 0.465 | 5.962 | 6.430 | 0.091 | 0.311 |
| 6 | 1905.0 | 6.788 | 0.497 | 6.292 | 6.757 | 0.105 | 0.328 |
| 6 | 1915.0 | 7.405 | 0.537 | 6.868 | 7.332 | 0.129 | 0.357 |

# APPENDIX D

# POLARIZED CROSS SECTIONS

In the following, the first column is defined as:

- kin=3 for data at (3.028 GeV, 25°)
- kin=4 for data at (4.018 GeV, 25°)
- kin=5 for data at (5.009 GeV, 25°)
- kin=6 for data at (5.009 GeV, 32°)

The other quantities are the invariant mass $W$ in MeV, and the parallel and perpendicular cross section differences and their respective statistical and systematic uncertainties. The polarized cross section values and the uncertainties are given in pb/MeV.sr.

Table D.1: Polarized Born cross section differences.

| kin | $W$ | $\Delta\sigma_{\parallel}$ | stat | syst | $\Delta\sigma_{\perp}$ | stat | syst |
|---|---|---|---|---|---|---|---|
| 3 | 1050.0 | -0.1323 | 0.7683 | 0.0584 | -2.7675 | 0.6888 | 0.1483 |
| 3 | 1150.0 | -1.5871 | 0.5828 | 0.2577 | 0.1399 | 0.5253 | 0.0078 |
| 3 | 1250.0 | -3.5893 | 0.7489 | 0.4171 | 1.7912 | 0.7818 | 0.1354 |
| 3 | 1350.0 | -3.2291 | 0.7898 | 0.2714 | 2.2066 | 0.9348 | 0.1091 |
| 3 | 1450.0 | -1.8574 | 0.8603 | 0.1175 | 1.6042 | 1.1014 | 0.1917 |
| 3 | 1550.0 | 0.5117 | 1.1218 | 0.1636 | 4.9079 | 1.7230 | 0.4194 |
| 3 | 1650.0 | -2.3193 | 1.1232 | 0.2069 | -1.7933 | 2.3871 | 0.2501 |
| 3 | 1750.0 | -3.1624 | 1.1456 | 0.2247 | -0.7063 | 2.1333 | 0.0928 |
| 3 | 1850.0 | -1.0117 | 1.3682 | 0.0736 | -1.7115 | 2.9103 | 0.3811 |
| 4 | 900.0 | 0.1419 | 0.3482 | 0.0071 | -1.4764 | 0.4456 | 0.0675 |
| 4 | 1000.0 | -0.0361 | 0.3286 | 0.0522 | -0.6013 | 0.4181 | 0.0799 |
| 4 | 1100.0 | 0.2548 | 0.2828 | 0.0039 | -0.7094 | 0.3553 | 0.1342 |
| 4 | 1200.0 | -0.5092 | 0.3886 | 0.0520 | -0.0301 | 0.4256 | 0.0217 |
| 4 | 1300.0 | -0.9771 | 0.6047 | 0.0371 | 0.5060 | 0.5380 | 0.0173 |

*continued on next page*

Table D.1: *continued*

| kin | $W$ | $\Delta\sigma_{\parallel}$ | stat | syst | $\Delta\sigma_{\perp}$ | stat | syst |
|---|---|---|---|---|---|---|---|
| 4 | 1400.0 | -1.4015 | 0.5958 | 0.1161 | 0.9030 | 0.6305 | 0.0772 |
| 4 | 1500.0 | -0.8458 | 0.6252 | 0.0210 | -0.9327 | 0.7776 | 0.1043 |
| 4 | 1600.0 | -0.2091 | 0.7201 | 0.0143 | 0.3327 | 1.0805 | 0.1393 |
| 4 | 1700.0 | 0.6379 | 0.8762 | 0.0869 | 1.6210 | 1.4393 | 0.1137 |
| 4 | 1800.0 | 0.1991 | 1.0227 | 0.3022 | -2.6765 | 1.7865 | 0.0534 |
| 4 | 1900.0 | -0.8308 | 0.9592 | 0.2300 | 4.2149 | 2.2726 | 0.1228 |
| 5 | 900.0 | 0.0185 | 0.0463 | 0.0083 | -0.1066 | 0.0633 | 0.0147 |
| 5 | 1000.0 | 0.0245 | 0.0562 | 0.0068 | -0.0716 | 0.0770 | 0.0183 |
| 5 | 1100.0 | 0.0444 | 0.0559 | 0.0036 | -0.2381 | 0.0764 | 0.0137 |
| 5 | 1200.0 | 0.0227 | 0.0631 | 0.0058 | -0.0443 | 0.0871 | 0.0135 |
| 5 | 1300.0 | 0.0332 | 0.0894 | 0.0003 | -0.0170 | 0.1284 | 0.0170 |
| 5 | 1400.0 | 0.0438 | 0.1153 | 0.0006 | -0.1127 | 0.1716 | 0.0151 |
| 5 | 1500.0 | 0.0020 | 0.1469 | 0.0020 | 0.0476 | 0.2118 | 0.0161 |
| 5 | 1600.0 | -0.0281 | 0.1832 | 0.0083 | 0.1608 | 0.2535 | 0.0005 |
| 5 | 1700.0 | -0.5433 | 0.2397 | 0.1209 | 0.1959 | 0.3304 | 0.0983 |
| 5 | 1800.0 | -0.3138 | 0.3025 | 0.0581 | -0.1331 | 0.4346 | 0.0467 |
| 5 | 1900.0 | 0.4498 | 0.3520 | 0.0369 | 0.5704 | 0.6104 | 0.0759 |
| 6 | 950.0 | -0.0286 | 0.0306 | 0.0004 | -0.0530 | 0.0420 | 0.0058 |
| 6 | 1050.0 | 0.0030 | 0.0204 | 0.0012 | 0.0130 | 0.0283 | 0.0003 |
| 6 | 1150.0 | -0.0007 | 0.0214 | 0.0014 | -0.0838 | 0.0297 | 0.0090 |
| 6 | 1250.0 | 0.0142 | 0.0255 | 0.0005 | 0.0093 | 0.0354 | 0.0009 |
| 6 | 1350.0 | 0.0228 | 0.0335 | 0.0019 | -0.0856 | 0.0460 | 0.0092 |
| 6 | 1450.0 | -0.0519 | 0.0439 | 0.0074 | -0.0450 | 0.0598 | 0.0079 |
| 6 | 1550.0 | -0.0110 | 0.0537 | 0.0035 | 0.0005 | 0.0774 | 0.0008 |
| 6 | 1650.0 | 0.0446 | 0.0667 | 0.0050 | 0.0961 | 0.1053 | 0.0012 |
| 6 | 1750.0 | 0.0191 | 0.0838 | 0.0028 | 0.0333 | 0.1399 | 0.0231 |
| 6 | 1850.0 | -0.1432 | 0.1105 | 0.0154 | 0.3597 | 0.1942 | 0.0332 |

# APPENDIX E

# ASYMMETRIES

In the following, the first column is defined as:

- kin=3 for data at (3.028 GeV, 25°)
- kin=4 for data at (4.018 GeV, 25°)
- kin=5 for data at (5.009 GeV, 25°)
- kin=6 for data at (5.009 GeV, 32°)

The other quantities are the invariant mass $W$ in MeV, and the parallel and perpendicular asymmetries and their respective statistical and systematic uncertainties.

Table E.1: Parallel and perpendicular Born asymmetries.

| kin | $W$ | $A_{\parallel}$ | stat | syst | $A_{\perp}$ | stat | syst |
|---|---|---|---|---|---|---|---|
| 3 | 1050.0 | -0.0003 | 0.0060 | 0.0004 | -0.0230 | 0.0053 | 0.0010 |
| 3 | 1150.0 | -0.0126 | 0.0043 | 0.0014 | 0.0010 | 0.0039 | 0.0000 |
| 3 | 1250.0 | -0.0188 | 0.0039 | 0.0017 | 0.0093 | 0.0041 | 0.0005 |
| 3 | 1350.0 | -0.0160 | 0.0039 | 0.0011 | 0.0109 | 0.0046 | 0.0004 |
| 3 | 1450.0 | -0.0076 | 0.0036 | 0.0004 | 0.0068 | 0.0046 | 0.0006 |
| 3 | 1550.0 | 0.0018 | 0.0039 | 0.0005 | 0.0171 | 0.0061 | 0.0012 |
| 3 | 1650.0 | -0.0076 | 0.0036 | 0.0005 | -0.0059 | 0.0078 | 0.0006 |
| 3 | 1750.0 | -0.0098 | 0.0035 | 0.0006 | -0.0022 | 0.0066 | 0.0002 |
| 3 | 1850.0 | -0.0032 | 0.0043 | 0.0002 | -0.0055 | 0.0091 | 0.0010 |
| 4 | 900.0 | 0.0045 | 0.0127 | 0.0002 | -0.0542 | 0.0156 | 0.0018 |
| 4 | 1000.0 | -0.0015 | 0.0103 | 0.0013 | -0.0190 | 0.0131 | 0.0020 |
| 4 | 1100.0 | 0.0091 | 0.0101 | 0.0001 | -0.0257 | 0.0126 | 0.0038 |
| 4 | 1200.0 | -0.0148 | 0.0112 | 0.0011 | -0.0013 | 0.0122 | 0.0005 |
| 4 | 1300.0 | -0.0215 | 0.0135 | 0.0006 | 0.0110 | 0.0122 | 0.0003 |
| 4 | 1400.0 | -0.0247 | 0.0104 | 0.0015 | 0.0160 | 0.0113 | 0.0010 |

*continued on next page*

Table E.1: *continued*

| kin | $W$ | $A_{\parallel}$ | stat | syst | $A_{\perp}$ | stat | syst |
|---|---|---|---|---|---|---|---|
| 4 | 1500.0 | -0.0110 | 0.0084 | 0.0002 | -0.0128 | 0.0104 | 0.0010 |
| 4 | 1600.0 | -0.0023 | 0.0081 | 0.0001 | 0.0041 | 0.0122 | 0.0012 |
| 4 | 1700.0 | 0.0061 | 0.0083 | 0.0006 | 0.0152 | 0.0136 | 0.0008 |
| 4 | 1800.0 | 0.0017 | 0.0087 | 0.0020 | -0.0224 | 0.0151 | 0.0003 |
| 4 | 1900.0 | -0.0068 | 0.0075 | 0.0014 | 0.0322 | 0.0179 | 0.0007 |
| 5 | 900.0 | 0.0063 | 0.0111 | 0.0014 | -0.0271 | 0.0148 | 0.0025 |
| 5 | 1000.0 | 0.0026 | 0.0087 | 0.0008 | -0.0125 | 0.0118 | 0.0021 |
| 5 | 1100.0 | 0.0060 | 0.0076 | 0.0004 | -0.0321 | 0.0103 | 0.0015 |
| 5 | 1200.0 | 0.0028 | 0.0070 | 0.0005 | -0.0057 | 0.0097 | 0.0011 |
| 5 | 1300.0 | 0.0027 | 0.0076 | 0.0000 | -0.0007 | 0.0109 | 0.0011 |
| 5 | 1400.0 | 0.0025 | 0.0073 | 0.0000 | -0.0074 | 0.0108 | 0.0007 |
| 5 | 1500.0 | 0.0001 | 0.0067 | 0.0001 | 0.0025 | 0.0097 | 0.0006 |
| 5 | 1600.0 | -0.0011 | 0.0065 | 0.0002 | 0.0053 | 0.0090 | 0.0000 |
| 5 | 1700.0 | -0.0164 | 0.0066 | 0.0026 | 0.0062 | 0.0092 | 0.0021 |
| 5 | 1800.0 | -0.0077 | 0.0070 | 0.0011 | -0.0035 | 0.0102 | 0.0009 |
| 5 | 1900.0 | 0.0084 | 0.0073 | 0.0006 | 0.0120 | 0.0127 | 0.0012 |
| 6 | 950.0 | -0.0615 | 0.0423 | 0.0005 | -0.0772 | 0.0571 | 0.0074 |
| 6 | 1050.0 | 0.0051 | 0.0253 | 0.0010 | 0.0121 | 0.0353 | 0.0003 |
| 6 | 1150.0 | 0.0002 | 0.0174 | 0.0009 | -0.0689 | 0.0236 | 0.0056 |
| 6 | 1250.0 | 0.0070 | 0.0146 | 0.0002 | 0.0043 | 0.0202 | 0.0004 |
| 6 | 1350.0 | 0.0091 | 0.0136 | 0.0006 | -0.0349 | 0.0183 | 0.0028 |
| 6 | 1450.0 | -0.0152 | 0.0122 | 0.0015 | -0.0137 | 0.0167 | 0.0016 |
| 6 | 1550.0 | -0.0025 | 0.0104 | 0.0005 | 0.0000 | 0.0150 | 0.0001 |
| 6 | 1650.0 | 0.0064 | 0.0094 | 0.0005 | 0.0123 | 0.0150 | 0.0001 |
| 6 | 1750.0 | 0.0017 | 0.0088 | 0.0002 | 0.0044 | 0.0148 | 0.0019 |
| 6 | 1850.0 | -0.0122 | 0.0093 | 0.0010 | 0.0304 | 0.0166 | 0.0022 |

# APPENDIX F

# SPIN STRUCTURE FUNCTIONS

The spin structure functions $g_1$ and $g_2$ and their respective statistical and systematic uncertainties are listed in Table F.1. Also listed are: the momentum transfer $Q^2$ in GeV$^2$, the invariant mass $W$ in GeV, and the Bjorken variable $x$.

Table F.1: The spin structure functions $g_1^{^3\mathrm{He}}$ and $g_2^{^3\mathrm{He}}$.

| $Q^2$ | $W$ | $x$ | $g_1$ | stat | syst | $g_2$ | stat | syst |
|---|---|---|---|---|---|---|---|---|
| 1.2 | 1.103 | 0.7820 | -.00257 | 0.00190 | 0.00017 | -.00128 | 0.00121 | 0.00001 |
| 1.2 | 1.203 | 0.6799 | -.00941 | 0.00237 | 0.00093 | 0.00378 | 0.00189 | 0.00053 |
| 1.2 | 1.303 | 0.5954 | -.01340 | 0.00360 | 0.00113 | 0.01103 | 0.00380 | 0.00098 |
| 1.2 | 1.403 | 0.5249 | -.01138 | 0.00426 | 0.00101 | 0.00947 | 0.00551 | 0.00065 |
| 1.2 | 1.503 | 0.4657 | -.00468 | 0.00576 | 0.00053 | 0.01144 | 0.00938 | 0.00250 |
| 1.2 | 1.603 | 0.4156 | 0.00072 | 0.00767 | 0.00079 | 0.01463 | 0.01748 | 0.00166 |
| 1.2 | 1.703 | 0.3729 | -.00318 | 0.00994 | 0.00158 | 0.00410 | 0.02695 | 0.00266 |
| 1.2 | 1.803 | 0.3363 | -.00496 | 0.01222 | 0.00296 | -.03792 | 0.03787 | 0.00343 |
| 1.9 | 1.103 | 0.8500 | 0.00012 | 0.00198 | 0.00021 | -.00397 | 0.00205 | 0.00070 |
| 1.9 | 1.203 | 0.7706 | -.00437 | 0.00289 | 0.00048 | 0.00081 | 0.00294 | 0.00023 |
| 1.9 | 1.303 | 0.6995 | -.00668 | 0.00471 | 0.00035 | 0.00557 | 0.00445 | 0.00020 |
| 1.9 | 1.403 | 0.6362 | -.00927 | 0.00479 | 0.00090 | 0.00969 | 0.00595 | 0.00072 |
| 1.9 | 1.503 | 0.5798 | -.00711 | 0.00514 | 0.00023 | -.00699 | 0.00817 | 0.00100 |
| 1.9 | 1.603 | 0.5296 | -.00059 | 0.00602 | 0.00023 | 0.00517 | 0.01218 | 0.00125 |
| 1.9 | 1.703 | 0.4849 | -.00122 | 0.00745 | 0.00178 | 0.01968 | 0.01736 | 0.00281 |
| 1.9 | 1.803 | 0.4451 | -.00645 | 0.00869 | 0.00206 | -.02406 | 0.02313 | 0.00194 |
| 2.6 | 1.103 | 0.8857 | 0.00015 | 0.00107 | 0.00009 | -.00332 | 0.00129 | 0.00033 |
| 2.6 | 1.203 | 0.8212 | -.00085 | 0.00134 | 0.00016 | -.00042 | 0.00165 | 0.00021 |
| 2.6 | 1.303 | 0.7610 | -.00079 | 0.00189 | 0.00010 | 0.00118 | 0.00248 | 0.00024 |
| 2.6 | 1.403 | 0.7052 | -.00096 | 0.00209 | 0.00013 | -.00067 | 0.00341 | 0.00031 |
| 2.6 | 1.503 | 0.6537 | -.00011 | 0.00246 | 0.00007 | 0.00101 | 0.00451 | 0.00040 |
| 2.6 | 1.603 | 0.6064 | 0.00019 | 0.00292 | 0.00008 | 0.00236 | 0.00566 | 0.00003 |

*continued on next page*

Table F.1: *continued*

| $Q^2$ | $W$ | $x$ | $g_1$ | stat | syst | $g_2$ | stat | syst |
|---|---|---|---|---|---|---|---|---|
| 2.6 | 1.703 | 0.5630 | -.00895 | 0.00370 | 0.00172 | 0.00746 | 0.00765 | 0.00229 |
| 2.6 | 1.803 | 0.5233 | -.00435 | 0.00457 | 0.00078 | 0.00560 | 0.01054 | 0.00143 |
| 3.3 | 1.103 | 0.9077 | -.00019 | 0.00053 | 0.00003 | -.00238 | 0.00080 | 0.00010 |
| 3.3 | 1.203 | 0.8536 | 0.00076 | 0.00052 | 0.00003 | -.00113 | 0.00095 | 0.00016 |
| 3.3 | 1.303 | 0.8016 | 0.00121 | 0.00066 | 0.00003 | -.00147 | 0.00151 | 0.00026 |
| 3.3 | 1.403 | 0.7522 | 0.00119 | 0.00105 | 0.00005 | -.00384 | 0.00225 | 0.00011 |
| 3.3 | 1.503 | 0.7055 | 0.00034 | 0.00151 | 0.00002 | 0.00067 | 0.00308 | 0.00007 |
| 3.3 | 1.603 | 0.6616 | 0.00083 | 0.00202 | 0.00015 | 0.00390 | 0.00431 | 0.00051 |
| 3.3 | 1.703 | 0.6205 | 0.00156 | 0.00283 | 0.00010 | -.00578 | 0.00701 | 0.00064 |
| 3.3 | 1.803 | 0.5821 | 0.00311 | 0.00392 | 0.00061 | 0.02353 | 0.01202 | 0.00257 |